ISSN 2078-7405

МІНІСТЕРСТВО ОСВІТИ ТА НАУКИ УКРАЇНИ

РІЗАННЯ ТА ІНСТРУМЕНТИ

В ТЕХНОЛОГІЧНИХ СИСТЕМАХ

100’2024

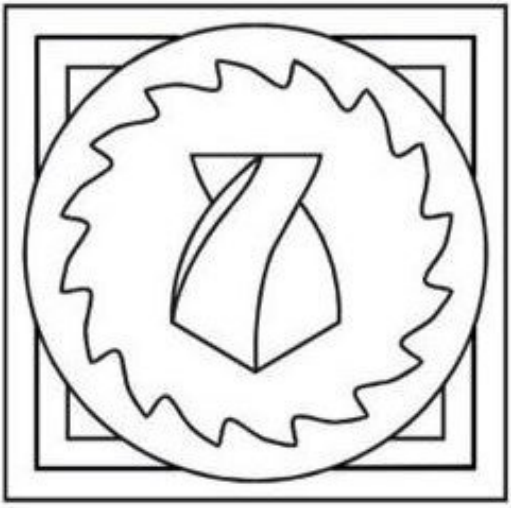

МІНІСТЕРСТВО ОСВІТИ ТА НАУКИ УКРАЇНИ

НАЦІОНАЛЬНИЙ ТЕХНІЧНИЙ УНІВЕРСИТЕТ
«ХАРКІВСЬКИЙ ПОЛІТЕХНІЧНИЙ ІНСТИТУТ»

Ministry of Education & Science of Ukraine
National Technical University
«Kharkiv Polytechnic Institute»

РІЗАННЯ ТА ІНСТРУМЕНТИ в технологічних системах

CUTTING & TOOLS IN TECHNOLOGICAL SYSTEM

Збірник наукових праць
Collection of scientific papers

Заснований у 1966 р. М. Ф. Семко
Found by M. F. Semko in 1966

ВИПУСК № 100
Edition № 100

Харків НТУ «ХПІ» – 2024 – Kharkiv NTU «KhPI»

ISSN (print) 2078-7405
УДК 621.91

Ідентифікатор медіа R30-02559, згідно з рішенням Національної ради України з питань телебачення і радіомовлення від 27.07.2023 р. №598
Друкується за рішенням Вченої ради НТУ "ХПІ",
протокол № 6 від 28 червня 2024 р.

У збірнику представлені наукові статті, в яких розглядаються актуальні питання в області механічної обробки різних сучасних матеріалів із застосуванням високопродуктивних технологій, нових методик, вимірювальних приладів для контролю якості оброблених поверхонь і високоефективних різальних інструментів. Розглядаються аспекти оптимізації та математичного моделювання на різних етапах технологічного процесу.

Для інженерів і наукових співробітників, що працюють в області технології машинобудування, різання матеріалів, проектування різальних інструментів в технологічних системах.

Збірник наукових праць «Різання та інструменти в технологічних системах» включений в Перелік фахових видань України категорії «Б», наказ МОН України від 17.03.2020 р., № 409

Різання та інструменти в технологічних системах/Cutting and Tools in Technological Systems: Збірник наукових праць. – Харків: НТУ «ХПІ», 2024. – Вип. 100. – 210 с.

Адреса редакційної колегії: вул. Кирпичова, 2, Харків, 61002, Національний технічний університет «Харківський політехнічний інститут», кафедра «Інтегровані технології машинобудування» ім. М.Ф. Семка, тел. +38 (057) 706-41-43.

УДК 621.91

UDC 658.511 **doi: 10.20998/2078-7405.2024.100.02**

IMPACT OF QUANTITY DISCOUNT ON PURCHASING COSTS IN BLENDING TECHNOLOGIES

Ágota **Bányai** [0000-0002-2537-7301]

University of Miskolc, 3515 Miskolc-Egyetemváros, Hungary
agota.banyaine@uni-miskolc.hu

Received: 25 March 2024 / Revised: 27 April 2024 / Accepted: 25 May 2024 / Published: 15 June 2024

Abstract. *Blending technologies are important in many sectors of industry, but are most prevalent in the chemical and food industries. They are playing an increasingly important role in the world economy despite the spread of electromobility. Nowadays, in addition to the technological aspects, there is a growing need to look at the logistical aspects, as logistics related costs account for a significant part of the cost of blending technologies. In this research work, the results of the analysis of the impact of quantity discounts, an important aspect of procurement activities related to blending technologies, are presented. A mathematical model is presented that can be used to investigate the impact of quantity discounts of components on profit and product quality. Based on scenario analyses carried out based on the mathematical model, it is demonstrated that the quantity discount can have a significant impact not only on total cost and profit, but also on the quality of the finished blended product.*
Keywords: *blending technologies; cost efficiency; optimisation; quantity discount; product quality.*

1. INTRODUCTION

The chemical and food industries typically use blending technology to produce their products. These blending technologies are becoming increasingly widespread, producing large quantities of high value products. The global fossil fuel consumption in 2022 was 39.413 TWh gas, 52.970 TWh oil and 44.854 coal [1]. This huge amount of fossil energy is generally processed by blending technologies, therefore it is important to improve both technological and logistics processes and blending technologies. Research of the technology and logistics associated with blending technologies is very significant, but the integrated study of technological and logistical aspects is still a less researched area.

The logistics aspects of blending technologies affect procurement, production, distribution and recycling, while manufacturers and service providers have to face both the positive and negative impacts of the fourth industrial revolution, globalisation and digitalisation. In this research paper, the author aims to investigate a fundamental area of procurement logistics. The aim of the research is to develop a mathematical model to investigate the effects of quantity discounts, well known in

procurement logistics, on the quality of products produced using blending technologies. The research work discusses an important topic of blending technologies, because logistics represents an important part of the total costs.

This paper is organized as follows. Section 2 shows the most important research results from both technological and logistics point of view. Section 3 proposes a mathematical model, which makes it possible to analyse the impact of quantity discount of components on the total cost, profit and product quality. Section 4 discusses the results of the numerical analysis of two scenarios, which validates the mathematical model. Conclusions, future research directions and managerial impacts are discussed in Section 5.

2. LITERATURE REVIEW

The research results regarding blending technologies can be divided into two main parts. The first part focuses on technological aspects of blending technologies, while the second part discusses logistics aspects in blending technologies.

The technological researches include a wide range of quality and processing related aspects, for example development of diesel fuel blending technologies using house of quality [2], fusibility and gasification aspect in coal blending technologies [3], automation and digitalization of cotton blending technologies [4], development of novel blending technologies for power generation focusing on biomass blending [5]. As the technological researches shows, the development of blending technologies is important not only from financial aspects, but it has a significant impact on environment [6]. The blending technology can also be researched from stability of final product point of view and stability can be significantly influenced by components [7]. Blending technologies and blending processes are complex, their optimisation can lead to complex NP-hard optimisation problems and the solution of these NP-hard optimisation problems is generally possible by heuristics and metaheuristics, as Cai et al. shows in a research focusing on optimisation of coal blending technologies using quantum particle swarm optimization [8]. Other interesting research works are focusing on online blending [9], mineral processing [10], intensification of flow blending technologies [11], blending technologies and renewable fuel [12], stability in blending [13], extraction processes [14] and melt blending technologies [15].

The logistics aspects of blending technologies include purchasing logistics, production logistics, distribution logistics and recycling logistics, but the mainly researched area is purchasing logistics, because a suitable optimised supply chain can significantly increase the efficiency of blending technologies. The supplier selection problem is extensively discussed in [16]. The author focuses on the global supply chain and discusses the potentials in cross-docking facilities to improve availability and efficiency of material supply in blending technologies. A integrated approach is discussed in [17] focusing on stock size, batch size, transportation,

storage and supply chain structure. The networking potentials of blending technologies are also discussed by researchers [18]. Outsourcing is also an important potential in logistics processes of blending technologies, as a research validates the importance of outsourcing activities in supply chain solutions [19]. However, the mathematical modelling generally leads to complex, NP-hard models, but there are approaches, which shows, that LP models can be also suitable to model logistics aspects of blending technologies [20].

As this short literature review shows, the research of blending technologies is important both from technological and logistics aspects. Within the frame of this article, a purchasing logistics related approach is discussed to show the importance of quantity discount in purchasing and procurement decisions.

3. MATERIALS AND METHODS

Within the frame of this part of the article, the mathematical model for the analysis of the impact of quantity discounts on the purchasing costs for blending technologies is discussed.: The input parameters of the optimization model are the followings:

- specific price of blended products: p_j^*, where $j = 1 \dots j_{max}$,
- specific purchasing price of component *i* for the final products: $p_i(a_i^*)$, where
$$a_i^* = \sum_{i=1}^{i_{max}} a_{ij} \quad (1)$$
and a_{ij} defines the amount of component *i* assigned to final product *j*,
- specific blending cost of component *i* into final product *j*: c_{ij}^T
- quality parameter *k* of component *i*: μ_{ik},
- demand for final product *j*: d_j,
- lower limit for the quality parameter *k* for final product *j*: μ_{jk}^{MIN},
- upper limit for the quality parameter *k* for final product *j*: μ_{jk}^{MAX},
- the total available inventory of component *i* available to be purchased: a_i^{max}.

The objective function of the optimisation of the blending processes is generally a cost function, which defines the minimization of the total cost depending on the specific price of blended products, the purchasing price of components, the amount of purchased components required to blend the final products, and the specific blending cost as follows:

$$C = \sum_{j=1}^{j_{max}} p_j^* + \sum_{i=1}^{i_{max}} \sum_{j=1}^{j_{max}} a_{ij} \cdot \left(p_i(a_i^*) + c_{ij}^T\right) \rightarrow min. \quad (2)$$

The first constraint defines, that it is not allowed to exceed the available upper order limit, which depends on the available component inventory of suppliers:

$$\forall i: \sum_{j=1}^{j_{max}} a_{ij} \leq a_i^{max} \quad (3)$$

The second constraint defines, that it is not allowed to exceed the lower and upper limit of quality parameters predefined for the blended final products:

$$\forall j,k: \mu_{jk}^{MIN} \leq \sum_{i=1}^{i_{max}} a_{ij} \cdot \mu_{ik} \cdot (\sum_{i=1}^{i_{max}} a_{ij})^{-1} \leq \mu_{jk}^{MAX} \quad (4)$$

The third constraint defines, that it is not allowed to exceed the available component specific technological resources:

$$\forall i: \sum_{j=1}^{j_{max}} f_{ij}^{T} \leq f_i^{TMAX} \quad (5)$$

Within the frame of this model, the impact of specific purchasing price is discussed, therefore it is important to define the specific price depending on the order quantity. The first way to define the purchasing price depending on the order quantity is a price function, as follows:

$$\forall i: p_i(a_i^*) = p_i^B - \alpha^{a_i^*} \quad (6)$$

where p_i^B is the initial purchasing cost of component *i*, and α is a discount factor. The second way to define the purchasing price depending on the order quantity is a stepwise function as follows:

$$\forall i: p_i(a_i^*) = \begin{cases} a_i^* \leq h^{a1} \rightarrow & p_i(a_i^*) = p_i^{a1} \\ h^{a1} + 1 < a_i^* \leq h^{a2} \rightarrow & p_i(a_i^*) = p_i^{a2} \\ \dots & \dots \\ h^{g-1} + 1 < a_i^* \leq h^{ag} \rightarrow & p_i(a_i^*) = p_i^{ag} \end{cases} \quad (7)$$

The third way define to define the purchasing price depending on the order quantity is a capacity related function, which defines the specific purchasing price increased by the logistics related costs. One typical type of these logistics related costs is the specific transportation cost depending on the capacity of the transportation resources. Figure 1 shows examples for these three types of specific purchasing price functions.

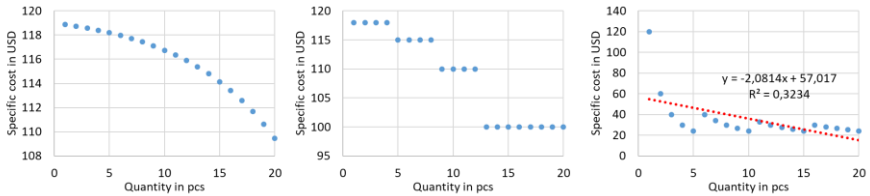

Figure 1 – Specific cost models

The decision variable of the optimization problem is the $A = [a_{ij}]$ assignment matrix, which defines that a_{ij} quantity from component *i* has to be purchased for final product *j*. The supplier selection problem is also an important part of purchasing strategies regarding blending technologies, within the frame of this article the single supplier solution is discussed, but the models are also suitable for multi supplier solution, because it is possible to define products from different suppliers as different products.

4. RESULTS

Within the frame of this chapter, two scenarios will be described to validate the proposed optimization approach to find the optimal purchasing quantity of components for the final products to be blended. Scenario 1 discusses the impact of quantity discount of components on the total price and profit, while scenario 2 focuses on the impact of quantity discount on the quality parameters of final products. In this scenarios, the capacity constraints are not taken into consideration, but in a future research, the connection between constrained available technological resources and quantity discount of components can be also analysed. The scenarios include 5 final products and 5 components, each having 3 quality parameters, which are defined as proportions in percent. All quality parameters have lower and upper limits, but in practical cases, the quality parameters can be constrained either by a lower or by an upper limit and it is not allowed to exceed this lower or upper limit.

Scenario 1: Numerical analysis of a case study focusing on costs

Within the frame of this scenario, the impact of quantity discount on the total cost and profit are described, while quality and capacity related constraints are taken into consideration. Table 1 summarizes the input parameters of components.

Table 1 – Input parameters of components in scenario 1

Input parameters of components	Notation	Component ID				
		C1	C2	C3	C4	C5
Initial purchasing price in USD	p_i^B	3	4	5	6	7
Quantity specific purchasing price	$p_i(a_i^*)$	$p_i^B - (\sum_{j=1}^{j_{max}} d_j)^{-1} \sum_{j=1}^{j_{max}} a_{ij}$				
Quality parameter 1 in %	μ_{i1}	10	12	14	11	9
Quality parameter 2 in %	μ_{i2}	1	2	3	2	4
Quality parameter 3 in %	μ_{i3}	30	34	41	29	52
Available amount in pcs	a_i^{max}	150	20	260	50	150

Table 2 shows the input parameters of final products to be blended.

Table 2 – Input parameters of final products in scenario 1

Input parameters of final products	Notation	Product ID				
		A1	A2	A3	A4	A5
Demand in pcs	d_j	100	90	80	110	55
Specific price in USD	p_j^*	10	10	10	10	10
Lower limit of quantity parameter 1 in %	μ_{j1}^{MIN}	9	9	9	9	9
Upper limit of quantity parameter 1 in %	μ_{j1}^{MAX}	14	14	14	12	14
Lower limit of quantity parameter 2 in %	μ_{j2}^{MIN}	2	2	3	2	2
Upper limit of quantity parameter 2 in %	μ_{j2}^{MAX}	3	4	4	4	3

Lower limit of quantity parameter 3 in %	μ_{j3}^{MIN}	30	34	30	40	30
Upper limit of quantity parameter 3 in %	μ_{j3}^{MAX}	35	52	45	52	40

Based on Table 1 and Table 2, the specific purchasing cost for each component can be described as follows:

- for components C1: $p_1(a_1^*) = 3 - 435^{-1} \sum_{j=1}^{5} a_{1j}$,
- for components C2: $p_2(a_2^*) = 4 - 435^{-1} \sum_{j=1}^{5} a_{2j}$,
- for components C3: $p_3(a_3^*) = 5 - 435^{-1} \sum_{j=1}^{5} a_{3j}$,
- for components C4: $p_4(a_4^*) = 6 - 435^{-1} \sum_{j=1}^{5} a_{4j}$,
- for components C5: $p_5(a_5^*) = 7 - 435^{-1} \sum_{j=1}^{5} a_{5j}$.

The above described scenario is a non-linear optimization problem, which can be solved by nonlinear regression. The optimization led to the results shown in Table 3.

Table 3 – Resulted assignment matrix of the scenario describing the amount of components to be purchased in pcs in scenario 1

Component ID	Product ID				
	A1	A2	A3	A4	A5
C1	46	45	0	30	27
C2	0	0	0	0	0
C3	46	45	80	60	28
C4	8	0	0	0	0
C5	0	0	0	20	0

The quality parameters of final products are shown in Figure 2. As Figure 2 shows, all quality parameters are between the predefined lower and upper limit.

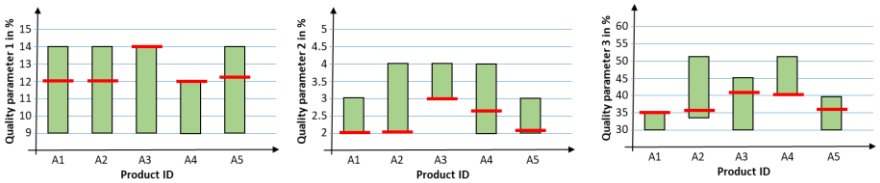

Figure 2 – Quality parameters of final products in scenario 1

In this scenario, the total cost is 1748.1 USD, while the maximized profit is 2601.9 USD. In the case of model without quantity discount, the total purchasing cost would be 178.9 USD higher.

Scenario 2: Comparison of quality parameters with and without quantity discount

In the next scenario, the impact of the quantity discount on the optimized product quality parameters are discussed. As shown in the first scenario, the quantity discount of components has a significant impact on total cost and profit, but it is also important to analyse the impact of quantity discount on quality parameters of final products, as quantity discount may make it worthwhile to order more of certain components, which may lead to a decrease in the quality parameters of the finished products.

Table 4 shows the lower and upper limit of quality parameters for final products. The demands and the specific prices of final products are the same as in the case of scenario 1.

Table 4 – Lower and upper limit of quality parameters for final products in scenario 2

Input parameters of final products	Notation	Product ID				
		A1	A2	A3	A4	A5
Lower limit of quantity parameter 1 in %	μ_{j1}^{MIN}	10	9	7	9	6
Upper limit of quantity parameter 1 in %	μ_{j1}^{MAX}	20	18	20	20	17
Lower limit of quantity parameter 2 in %	μ_{j2}^{MIN}	2	2	3	2	2
Upper limit of quantity parameter 2 in %	μ_{j2}^{MAX}	5	5	5	5	5
Lower limit of quantity parameter 3 in %	μ_{j3}^{MIN}	30	31	34	40	35
Upper limit of quantity parameter 3 in %	μ_{j3}^{MAX}	55	60	50	45	55

Table 5 summarizes the input parameters of components.

Table 5 – Input parameters of components in scenario 2

Input parameters of components	Notation	Component ID				
		C1	C2	C3	C4	C5
Initial purchasing price in USD	p_i^B	10	12	20	8	11
Quality parameter 1 in %	μ_{i1}	10	12	14	11	9
Quality parameter 2 in %	μ_{i2}	1	2	3	2	4
Quality parameter 3 in %	μ_{i3}	30	34	41	29	52
Available amount in pcs	a_i^{max}	200	120	50	350	200

The optimization of scenario 2 led to the results shown in Table 6.

Table 6 – Resulted assignment matrix of the scenario describing the amount of components to be purchased in pcs in scenario 2

Component ID	Product ID				
	A1	A2	A3	A4	A5
C1	0	0	0	0	0
C2	0	0	0	0	0
C3	0	0	0	0	0
C4	95	82	40	57	40
C5	5	8	40	53	15

The quality parameters of final products are shown in Figure 3. As Figure 3 shows, all quality parameters are also between the predefined lower and upper limit.

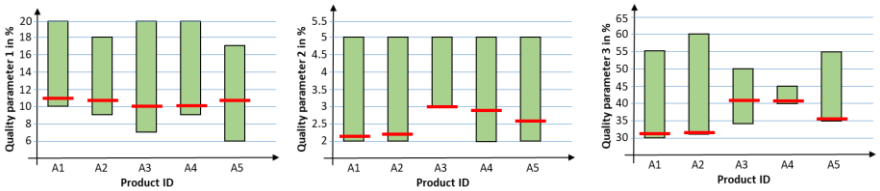

Figure 3 – Quality parameters of final products in scenario 2

In scenario 2, the total cost is 3843 USD, while the maximized profit is 507 USD. Using the following quantity discount model for scenario 2:

$$\forall i: p_i(a_i^*) = p_i^B - \alpha^{a_i^*} \quad (8)$$

where $p_i^B = (10,12,20,8,11)$ and $\alpha = (1.01, 1.001, 1.01, 1.01, 1.005)$, the total profit is 2009.4 USD and the total cost is 2340.6 USD.

In this second part of scenario 2, the quality parameters are also between the lower and upper limits, as shown in Figure 4.

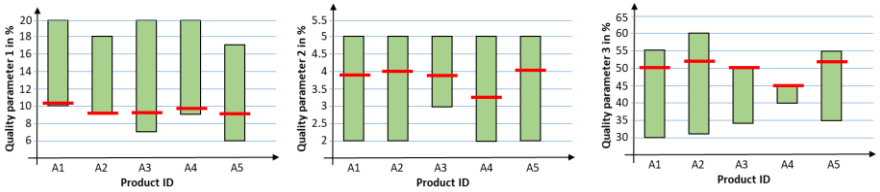

Figure 4 – Quality parameters of final products in scenario 2

As the comparison of quality parameters with and without quantity discount shows, the quantity discount has significant impact on the quality of blended final

products. Figure 5 summarizes the differences of quality parameters with and without quantity discount.

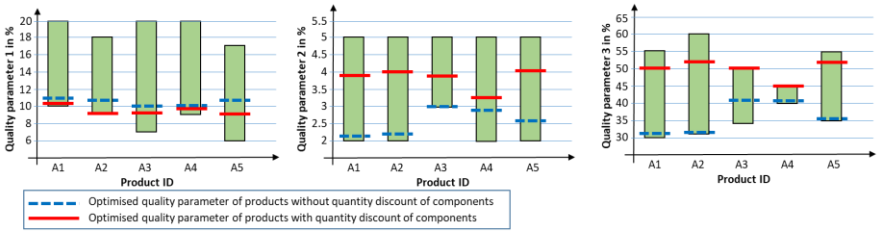

Figure 5 – Comparison of quality parameters of final products in scenario 2 with and without quantity discount of components

As Figure 6 shows, the proportion of optimised quality parameters with and without quantity discount of components can be different, which means, that in the case of scenario 2, quality parameter 1 was lower, while quality parameters 2 and 3 were higher with quantity discount.

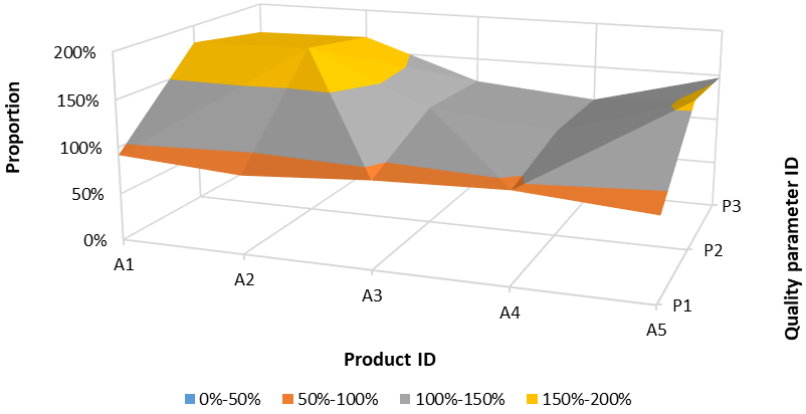

Figure 6 – Proportion of optimised quality parameters in scenario 2 with and without quality discount

5. SUMMARY

Blending technologies are a special field of industrial technologies where the quality parameters of the components significantly determine the quality of the final product, and this significant relationship can usually be defined by means of specific mathematical functions. As evidenced by a number of literature sources and research works, one of the most important research directions for blending technologies is the

investigation of the technological aspects of blending technologies, while there are only few sources in the literature that deal with the logistical aspects of blending technologies. In the present research work, a mathematical model was developed to investigate how the quantity discount on the components that make up the finished product affects the total cost, profit and the impact on the quality and quality parameters of the finished product. Based on the two case studies presented, it can be concluded that the quantity discount has a significant impact on profit, has an impact on the quantity and quality of the components purchased and thus affects the quality of the finished product.

As a future research direction, it is possible to analysed the impact of dynamically changing specific component costs and quantity discounts on the total cost of blending technologies and various purchasing strategies can be defined depending on the complexity of the products, available components, suppliers and cost models.

References: 1. *Our World in Data*: Fossil Fuels. URL: https://ourworldindata.org/fossil-fuels. **2.** *Solikhah, M.D., Karuana, F., Barus, B.R., Amri, K., Wimada, A.R.*: Application of house of quality in assessment of biodiesel - Diesel fuel blending technologies, AIP Conference Proceedings (2023) 2646. https://doi.org/10.1063/5.0114040 **3**. *Xie, Y., Wu, C., Liu, T., Chen, H., Li, H.*: Improving ash fusibility and gasification reactivity of anthracite based on coal blending technology, Clean Coal Technology vol.29(3) (2023) pp. 114–121. https://doi.org/10.13226/j.issn.1006-6772.22040502 **4**. *Wang, M., Wang, J., Gao, W.*: Research progress in computer aided cotton blending technology, Fangzhi Xuebao/Journal of Textile Research vol.44(8) (2023) 225–233. http://doi.org/10.13475/j.fzxb.20220405002 **5**. *Zhou, Y., Zhang, S., Lang, S., Liu, S., Yang, J.*: Research progress of biomass blending technology in pulverized coal furnace for power generation, Clean Coal Technology vol.28(6) (2022) pp. 26–34. https://doi.org/10.13226/j.issn.1006-6772.CC22012502 **6**. *Turner, J.W.G., Leach, F.C.P.*: Using alternative and renewable liquid fuels to improve the environmental performance of internal combustion engines: key challenges and blending technologies, Alternative Fuels and Advanced Vehicle Technologies for Improved Environmental Performance: Towards Zero Carbon Transportation (2022) pp. 57–92. http://doi.org/10.1016/B978-0-323-90979-2.00015-9 **7**. *Yan, S., Wu, Y., Qi, X., Feng, D.*: Study on the blending technology and stability of low sulful marine fuel oil, Petroleum Refinery Engineering vol.51(3) (2021) pp. 5–8. **8**. *Cai, B., Qin, T., Han, Y., Yv, Y.L., Zhao, Z.Y.*: Study on the application of coal blending technology based on quantum particle swarm optimization in large circulating fluidized bed boiler, IOP Conference Series: Earth and Environmental Science vol.354 (2019) 1. https://doi.org/10.1088/1755-1315/354/1/012005 **9**. Li, Z., Xu, K., Xue, Q., Liu, M., Wang, M.: Experimental study of online blending technology for residual marine fuel oil, Petroleum Processing and Petrochemicals vol.49(5) (2018) pp. 92–96. **10**. *Agustinus, A.*: Multi Blending Technology (MBT): Mineral processing method for increasing added value of marginal reserve, IOP Conference Series: Earth and Environmental Science vol.118(1) (2018). https://doi.org/10.1088/1755-1315/118/1/012064 **11**. *Ivanchina, E.D., Dolganov, I.M., Chuzlov, V.A., Belinskaya, N.S.*: Intensification of flow blending technology in the production of motor fuels by the method of mathematical modelling, Chemical Engineering and Processing: Process Intensification vol.122 (2017) pp. 415–424. https://doi.org/10.1016/j.cep.2017.07.015 **12**. *Pearson, R.J., Turner, J.W.G.*: Using alternative and renewable liquid fuels to improve the environmental performance of internal combustion engines: Key challenges and blending technologies, Alternative Fuels and Advanced Vehicle Technologies for Improved Environmental Performance: Towards Zero Carbon Transportation vol.2014 (2014) pp. 52–89. https://doi.org/10.1533/9780857097422.1.52 **13**. *Li, Y., Liu, M., Zhao, D.Z.*: Blending technology and study on the stability of marine fuel, Shiyou Huagong Gaodeng Xuexiao Xuebao/Journal of Petrochemical Universities vol.25(6) (2012) pp. 14–17. https://doi.org/10.3969/j.issn.1006-396X.2012.06.004 **14**. *Yang, M., Zhou, Y., Chen, J., Yu, M., Shi, X.*: Application of genetic algorithm in blending technology for extractions of Cortex Fraxini, Zhongguo Zhongyao Zazhi vol.34(20) (2009) pp. 2594–2598. **15**. *Schut, J.H.*: Novel melt blending technology

commercialized in micro- & nanolayer films, Plastics Technology vol.55(4) (2009) pp. 29–30+45. **16**. *Bányai, Á.*: Supplier selection in supply chain using cross-docking services for blending technology-based production processes, Academic Journal of Manufacturing Engineering vol.21(2) (2023) pp. 101–109. **17**. *Bányai, T., Veres, P.*: Supply Chain Design for Blending Technologies, Sustainability vol.14 (2022) 14. https://doi.org/10.3390/su14148760 **18**. *Nagy, G., Bányai, Á., Illés, B., Glistau, E.*: Analysis of supply chain efficiency in blending technologies, Lecture Notes in Mechanical Engineering vol.2018 (2018), pp. 280–291. https://doi.org/10.1007/978-3-319-75677-6_23 **19**. *Bányai, T.*: Supply chain optimization of outsourced blending technologies, Journal of Applied Economic Sciences vol.12(4) (2017) pp. 960–976. **20**. *Bányai, Á., Illés, B., Schenk, F.*: Supply chain design of manufacturing processes with blending technologies, Solid State Phenomena vol.261 (2017) pp. 509–515. https://doi.org/10.4028/www.scientific.net/SSP.261.509

Агота Баньяї, Мішкольц, Угорщина

ВПЛИВ КІЛЬКІСТНОЇ ЗНИЖКИ НА ЗАКУПІВЕЛЬНІ ВИТРАТИ В ТЕХНОЛОГІЯХ ЗМІШУВАННЯ

Анотація. *Технології змішування (купажування) важливі в багатьох галузях промисловості, але найбільш поширені в хімічній та харчовій промисловості. Вони відіграють все більш важливу роль у світовій економіці, незважаючи на поширення електромобільності. Сьогодні, окрім технологічних аспектів, зростає потреба розглянути логістичні аспекти, оскільки витрати, пов'язані з логістикою, становлять значну частину собівартості технологій змішування. Купажні технології є особливою галуззю промислових технологій, де параметри якості компонентів суттєво визначають якість кінцевого продукту, і цей суттєвий взаємозв'язок, як правило, може бути визначений за допомогою певних математичних функцій. Як свідчить низка літературних джерел та науково-дослідних робіт, одним з найважливіших напрямків досліджень технологій змішування є дослідження технологічних аспектів технологій змішування, в той час як логістичним аспектам технологій змішування в літературі присвячені лише поодинокі джерела. У даній науково-дослідній роботі була розроблена математична модель для дослідження того, як кількісна знижка на компоненти, що входять до складу готового продукту, впливає на загальну собівартість, прибуток і вплив на параметри якості готового продукту. На основі двох представлених тематичних досліджень можна зробити висновок, що кількістна знижка має значний вплив на прибуток, впливає на кількість та якість придбаних компонентів і, таким чином, впливає на якість готової продукції. В якості майбутнього напрямку дослідження може бути аналіз впливу динамічної зміни питомих витрат на компоненти та кількістних знижок на загальну вартість технологій змішування, а також визначити різні стратегії закупівель залежно від складності продукції, доступних компонентів, постачальників та моделей витрат.*

Ключові слова: *технології змішування; економічна ефективність; оптимізація; кількістна знижка; якість продукції.*

UDC 658.511 **doi: 10.20998/2078-7405.2024.100.03**

IMPACT OF DYNAMIC HUMAN AND TECHNOLOGICAL RESOURCE COST ON LOT SIZE OPTIMIZATION

Tamás **Bányai** [0000-0002-0229-4781]

University of Miskolc, 3515 Miskolc-Egyetemváros, Hungary
tamas.banyai@uni-miskolc.hu

Received: 25 March 2024 / Revised: 10 April 2024 / Accepted: 25 April 2024 / Published: 15 June 2024

Abstract. *The design methods of production systems have evolved significantly in recent decades. New methods have emerged that are capable of determining the optimal parameters of production systems operating in increasingly complex environments. The two best known methods for lot sizing problems are the Wagner-Whitin algorithm and the Silver-Meal heuristics. The original versions of these two methods are only suitable for solving simple lot sizing problems, but there are several complex mutations of these methods that allow solving complex lot sizing problems. In the present research, the author presents a modified Wagner-Whitin algorithm that is suitable for solving the lot sizing problem and also for investigating the impact of dynamically changing resource costs. The proposed method is validated through case studies. The case studies demonstrate that the dynamic nature of cost of human resources and technological resources has a significant impact on the solution of lot sizing problems.*
Keywords: *lot sizing; production planning and scheduling; cost minimization; modelling.*

1. INTRODUCTION

Companies are making ever greater efforts to meet customer demand, but they also need to reduce costs while increasing efficiency. Cost reduction involves both resource optimisation and process improvement. Since resource availability is a dynamic phenomenon, resource costs are often a dynamic parameter to be considered when solving production planning problems. In the present research work, the author proposes an improvement of the Wagner-Whitin algorithm (WWA) in order to take into account the dynamically varying cost of resources when solving the lot sizing problem. In the second chapter of the article, a short literature review shows the importance of lot sizing problems, and highlights the importance of WWA-based solutions. In the third chapter a novel WWA-based approach is described, which makes it possible to analyse the impact of dynamic changing costs of human resources and technological resources. In chapter four a case study shows the efficiency of the developed algorithm, while in the last chapter the results are summarized and the potential future research directions are discussed.

2. LITERATURE REVIEW

Kumar et al. [1] analysed various lot sizing strategies including lot for lot, Wagner-Whitin algorithm and Silver-Meal heuristics. Their analysis showed, that these algorithms are suitable to solve dynamic lot sizing problems also in the case when demand surpasses a predicted value. This research validated, that WWA and SMH are suitable for lot sizing problems in uncertain operation environment. Asmal et al. [2] applied WWA and SMH to solve inventory problems when inventories are influenced by dynamic safety stock and lead time due to uncertain logistics. Zhang et al. [3] developed a new extended mixed-integer programming formulation, which makes it possible to take Wagner-Whitin conditions into consideration in order to solve the static joint chance-constrained lot-sizing problem. Kuznetsov and Demidenko [4] focuses on their work on the organization of material resources supply in transport construction, and they showed, that WWA can be used for the problem solution of probabilistic nature of the construction logistics systems. Narkhede and Rajhans described in a research [5] on redesign inventory management strategies, that WWA can be integrated with other lot sizing methodologies. The proposed an integrated Wagner-Whitin & Rank Order Clustering approach (WW&ROC), which could lead to savings in amount of total cost compared to existing purchase strategies and stock-out situations can be also improved. A lot sizing model for two items with imperfect manufacturing process, time varying demand and return rates was proposed by van Zyl and Adetunji [6]. Their research focuses on constrained returns and the potential of secondary use of returns. A modified WWA was supposed to solve the lot sizing problems. Assi and Effanga [7] showed in a research focusing on human resource aspects including recruitment and promotion policies, that a WWA like dynamic programming algorithm can also solve human resource optimization problems. Oca Sánchez et al. [8] discusses in a research work the raw material problems of automotive industry, and showed, that the efficiency of WWA can be improved by the integration of forecast methodologies. Kian et al. [9] described a novel optimization approach for problems with demands exhibiting stationary, increasing and decreasing trends and seasonality. Their proposed solution is a combination and variation of the well known WWA, SMH and least Unit Cost (LUC) approaches. Production planning and facility location can be also integrated as shown by Wu et al. [10] in a research describing the relationship between pricing problems and uncapacitated lot-sizing problems with Wagner-Whitin property. The importance of forecasting and their impact on production planning and scheduling is highlighted in a research by Olesen et al. [11]. Their showed a method to support cost savings by managerial decisions. Gaol and Matsuo [12] focuses on the impact of state-of-the-art technologies on the solution of lot sizing problems. They showed the importance of sensor technologies by simulation supported analysis. Uncertainties are also modelled by Hanafizadeh et al. [13] in a research focusing on the application of WWA. In their research robustness was in the focus. Güner and Tunali [14] showed a novel approach of capacitated lot-sizing problems, which is a special extension of Wagner-Whitin

problems. Other important topics in the field of lot sizing problems were also intensively researched including improvement of existing solution methodologies [15] and they are also focusing on supply chain disruption problems [16], which can also significantly improve the complexity of dynamic lot sizing problems in production processes. This short literature review showed the importance and complexity of lot sizing problems. Following this brief literature review, the paper presents a novel methodology, which takes into consideration of the dynamic resource cost, including human resources and technological resources.

3. MATERIALS AND METHODS

Within the frame of this chapter, a novel, Wagner-Whitin algorithm-based approach will be described, which integrates the dynamic costs of human resources (operators for logistics and technological resources) and technological resources (machine tools). The novelty of the methodology is, that conventional Wagner-Whitin algorithm focuses on the initialization cost of production, on the production cost depending on the quantity and the warehousing cost (inventory), while this approach makes it possible to analyse the impact of time dependent costs of human and technological resources.

The input parameters of the model are the followings:

- C_{IP}: initialization cost of production per time frame,
- C_P: specific production cost,
- C_W: specific warehousing cost,
- L_{OP}: lot size assigned to operators (the operators are assigned to lot size L_{OP} and their specific, time dependent specific cost is defined for this L_{OP} lot size),
- L_{TR}: lot size assigned to technological resources (machine tools, assembly stations), the machines are assigned to lot size L_{TR} and their specific, time dependent specific cost is defined for this L_{TR} lot size),
- D_i: demand in time frame *i*,
- C_i^{OP}. operator cost per operator related lot in time frame *i*,
- C_i^{TR}: technological resource cost per production lot in time frame *i*,
- i_{max}: the total number of time frames.

The algorithm includes i_{max} computational phases. The first phase computes the local optimal production scheduling for the last time frame. The second phase computes the local optimal production schedule for the second last time frames, etc.

As a first step, we can calculate the local optimal production schedule for the last day as follows:

$$C_{imax} = C_{imax}^{imax} = C_{IP} + D_{imax}C_P + \left\lceil \frac{D_{imax}}{L_{OP}} \right\rceil C_{imax}^{OP} + \left\lceil \frac{D_{imax}}{L_{TR}} \right\rceil C_{imax}^{TR} \quad (1)$$

In the second phase, for the predecessor time frame, the local optimal production schedule can be defined as follows:

$$C_{imax-1} = \min\left(C_{imax-1}^{imax-1}, C_{imax-1}^{imax-1-imax}\right) \quad (2)$$

$$C_{imax-1}^{imax-1} = C_{IP} + D_{imax-1}C_P + \left\lceil \frac{D_{imax-1}}{L_{OP}} \right\rceil C_{imax-1}^{OP} + \left\lceil \frac{D_{imax-1}}{L_{TR}} \right\rceil C_{imax-1}^{TR} + C_{imax} \quad (3)$$

$$C_{imax-1}^{imax-1-imax} = C_{IP} + \sum_{i=imax-1}^{imax} D_i(C_P + (i - imax + 1)C_W) + + \left\lceil \frac{\sum_{i=imax-1}^{imax} D_i}{L_{OP}} \right\rceil C_{imax-1}^{OP} + \left\lceil \frac{\sum_{i=imax-1}^{imax} D_i}{L_{TR}} \right\rceil C_{imax-1}^{TR} \quad (4)$$

Eq (2) defines, that in this phase of the algorithm we can choose beteen to potential solutions:

- C_{imax-1}^{imax-1} defines a solution, where within the time frame $imax-1$ only the demand of time frame $imax-1$ is produced,
- $C_{imax-1}^{imax-1-imax}$ defines a solution, where within the time frame $imax-1$ the demands for both time frame $imax-1$ and time frame $imax$ are produced.

We can define a general computational phase for time frame j as follows:

$$C_j = min\,(C_j^j, C_j^{j-(j+1)}, C_j^{j-(j+2)}, \dots, C_j^{j-imax}) \quad (5)$$

$$C_j^j = C_{IP} + D_jC_P + \left\lceil \frac{D_j}{L_{OP}} \right\rceil C_j^{OP} + \left\lceil \frac{D_j}{L_{TR}} \right\rceil C_j^{TR} + C_{j+1} \quad (6)$$

$$C_j^{j-(j+1)} = C_{IP} + \sum_{i=j}^{j+1} D_i(C_P + (i-j)C_W) + \left\lceil \frac{\sum_{i=j}^{j+1} D_i}{L_{OP}} \right\rceil C_j^{OP} + \left\lceil \frac{\sum_{i=j}^{j+1} D_i}{L_{TR}} \right\rceil C_j^{TR} + C_{j+2} \quad (7)$$

$$C_j^{j-(j+2)} = C_{IP} + \sum_{i=j}^{j+2} D_i(C_P + (i-j)C_W) + \left\lceil \frac{\sum_{i=j}^{j+2} D_i}{L_{OP}} \right\rceil C_j^{OP} + \left\lceil \frac{\sum_{i=j}^{j+2} D_i}{L_{TR}} \right\rceil C_j^{TR} + C_{j+3} \quad (8)$$

$$C_j^{j-imax} = C_{IP} + \sum_{i=j}^{imax} D_i(C_P + (i-j)C_W) + \left\lceil \frac{\sum_{i=j}^{imax} D_i}{L_{OP}} \right\rceil C_j^{OP} + \left\lceil \frac{\sum_{i=j}^{imax} D_i}{L_{TR}} \right\rceil C_j^{TR} \quad (9)$$

Figure 1 demonstrates the flowchart of the production schedule optimization. As the flowchart shows, the local optimal solutions for each time frame can be calculated analytical, it means no heuristics or metaheuristics are required to find the optimal solution.

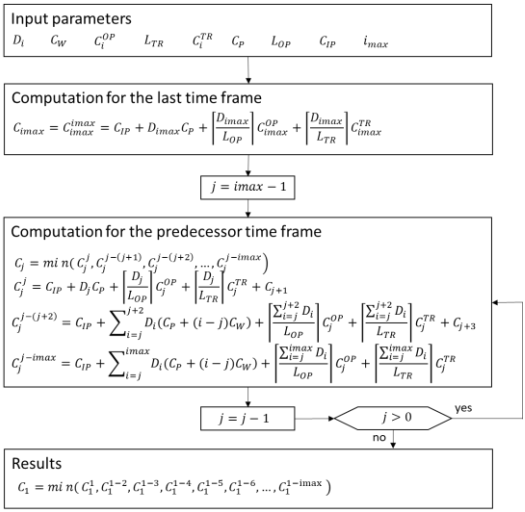

Figure 1 – Layout of the production plant

Within the frame of the next chapter, some numerical examples will validate the above-mentioned approach and show the suitability of the describe methodology to find the optimal production schedule and analyse the impact of dynamic human and technological resource costs.

4. RESULTS

Within the frame of this section, the main results of some numerical studies are summarized. The first scenario analysis focuses on the comparison of conventional lot sizing and the dynamic lot sizing taking the cost of human resources (machine operators) and technological resources (machine tools) into consideration. In the first case study, the results of traditional scheduling and dynamic scheduling are compared over a seven-day time horizon. The time-dependent parameters of the first case study are summarised in Table 1.

Table 1 – Examples for the identification of production lines

Time frames	T1	T2	T3	T4	T5	T6	T7
Demand to be produced	100	105	95	110	94	111	89
Operator cost per operator related lot	7.8	8.2	8.9	7.8	9.7	9.1	8.2
Technological resource cost per production lot	10.2	11.4	12.3	11.1	10.5	10.6	13.4

The initialization cost of production per time frame is $C_{IP} = 500$ €, the specific production cost is $C_P = 3$ €$/pcs$ and the specific warehousing cost is $C_W = 2$ €$/time\ frame$. The lot size assigned to operators is $L_{OP} = 50\ pcs$ and the lot size assigned to technological resources is $L_{TR} = 75\ pcs$.

As the first phase of the optimization, we can compute the total cost for the last time frame as follows:

$$C_7 = C_7^7 = C_{IP} + D_7 C_P + \left\lceil \frac{D_7}{L_{OP}} \right\rceil C_7^{OP} + \left\lceil \frac{D_7}{L_{TR}} \right\rceil C_7^{TR} = 1166.2\ € \tag{10}$$

The second phase of the optimization is to calculate the total cost of the predecessor time frame based on the following equations:

$$C_6 = \min\left(C_6^6, C_6^{6-7}\right) \tag{11}$$

$$C_6^6 = C_{IP} + D_6 C_P + \left\lceil \frac{D_6}{L_{OP}} \right\rceil C_6^{OP} + \left\lceil \frac{D_6}{L_{TR}} \right\rceil C_6^{TR} + C_7 \tag{12}$$

$$C_6^{6-7} = C_{IP} + \sum_{i=6}^{7} D_i (C_P + (i-6) C_W) + \left\lceil \frac{\sum_{i=6}^{7} D_i}{L_{OP}} \right\rceil C_6^{OP} + \left\lceil \frac{\sum_{i=6}^{7} D_i}{L_{TR}} \right\rceil C_6^{TR} \tag{13}$$

$$C_6 = \min \begin{cases} C_6^6 = 2491.7\ € \\ C_6^{6-7} = 2146.2\ € \end{cases} = 2146.2\ € \tag{14}$$

The third phase of the optimization is to calculate the total cost of time frame 5 based on the following equations:

$$C_5 = \min\left(C_5^5, C_5^{5-6}, C_5^{5-7}\right) \tag{15}$$

$$C_5^5 = C_{IP} + D_5 C_P + \left\lceil \frac{D_5}{L_{OP}} \right\rceil C_5^{OP} + \left\lceil \frac{D_5}{L_{TR}} \right\rceil C_5^{TR} + C_6 \quad (16)$$

$$C_5^{5-6} = C_{IP} + \sum_{i=5}^{6} D_i (C_P + (i-5)C_W) + \left\lceil \frac{\sum_{i=5}^{6} D_i}{L_{OP}} \right\rceil C_5^{OP} + \left\lceil \frac{\sum_{i=5}^{6} D_i}{L_{TR}} \right\rceil C_5^{TR} + C_7 \quad (17)$$

$$C_5^{5-7} = C_{IP} + \sum_{i=5}^{7} D_i (C_P + (i-5)C_W) + \left\lceil \frac{\sum_{i=5}^{7} D_i}{L_{OP}} \right\rceil C_5^{OP} + \left\lceil \frac{\sum_{i=5}^{7} D_i}{L_{TR}} \right\rceil C_5^{TR} \quad (18)$$

$$C_5 = \min \begin{cases} C_5^5 = 3344.6 \text{ €} \\ C_5^{5-6} = 3403.2 \text{ €} = 3236.2 \text{ €} \\ C_5^{5-7} = 3236.2 \text{ €} \end{cases} \quad (19)$$

The fourth phase of the optimization is to calculate the total cost of time frame 4 based on the following equations:

$$C_4 = min\,(C_4^4, C_4^{4-5}, C_4^{4-6}, C_4^{4-7}) \quad (20)$$

$$C_4^4 = C_{IP} + D_4 C_P + \left\lceil \frac{D_4}{L_{OP}} \right\rceil C_4^{OP} + \left\lceil \frac{D_4}{L_{TR}} \right\rceil C_4^{TR} + C_5 \quad (21)$$

$$C_4^{4-5} = C_{IP} + \sum_{i=4}^{5} D_i (C_P + (i-4)C_W) + \left\lceil \frac{\sum_{i=4}^{5} D_i}{L_{OP}} \right\rceil C_4^{OP} + \left\lceil \frac{\sum_{i=4}^{5} D_i}{L_{TR}} \right\rceil C_4^{TR} + C_6 \quad (22)$$

$$C_4^{4-6} = C_{IP} + \sum_{i=4}^{6} D_i (C_P + (i-4)C_W) + \left\lceil \frac{\sum_{i=4}^{6} D_i}{L_{OP}} \right\rceil C_4^{OP} + \left\lceil \frac{\sum_{i=4}^{6} D_i}{L_{TR}} \right\rceil C_4^{TR} + C_7 \quad (23)$$

$$C_4^{4-7} = C_{IP} + \sum_{i=4}^{7} D_i (C_P + (i-4)C_W) + \left\lceil \frac{\sum_{i=4}^{7} D_i}{L_{OP}} \right\rceil C_4^{OP} + \left\lceil \frac{\sum_{i=4}^{7} D_i}{L_{TR}} \right\rceil C_4^{TR} \quad (24)$$

$$C_4 = \min \begin{cases} C_4^4 = 4551.8 \text{ €} \\ C_4^{4-5} = 4334.5 \text{ €} \\ C_4^{4-6} = 4613.3 \text{ €} \\ C_4^{4-7} = 4630.8 \text{ €} \end{cases} = 4334.5 \text{ €} \quad (25)$$

The fifth phase of the optimization is to calculate the total cost of time frame 3 based on the following equations:

$$C_3 = min\,(C_3^3, C_3^{3-4}, C_3^{3-5}, C_3^{3-6}, C_3^{3-7}) \quad (26)$$

$$C_3^3 = C_{IP} + D_3 C_P + \left\lceil \frac{D_3}{L_{OP}} \right\rceil C_3^{OP} + \left\lceil \frac{D_3}{L_{TR}} \right\rceil C_3^{TR} + C_4 \quad (27)$$

$$C_3^{3-4} = C_{IP} + \sum_{i=3}^{4} D_i (C_P + (i-3)C_W) + \left\lceil \frac{\sum_{i=3}^{4} D_i}{L_{OP}} \right\rceil C_3^{OP} + \left\lceil \frac{\sum_{i=3}^{4} D_i}{L_{TR}} \right\rceil C_3^{TR} + C_5 \quad (28)$$

$$C_3^{3-5} = C_{IP} + \sum_{i=3}^{5} D_i (C_P + (i-3)C_W) + \left\lceil \frac{\sum_{i=3}^{5} D_i}{L_{OP}} \right\rceil C_3^{OP} + \left\lceil \frac{\sum_{i=3}^{5} D_i}{L_{TR}} \right\rceil C_3^{TR} + C_6 \quad (29)$$

$$C_3^{3-6} = C_{IP} + \sum_{i=3}^{6} D_i (C_P + (i-3)C_W) + \left\lceil \frac{\sum_{i=3}^{6} D_i}{L_{OP}} \right\rceil C_3^{OP} + \left\lceil \frac{\sum_{i=3}^{6} D_i}{L_{TR}} \right\rceil C_3^{TR} + C_7 \quad (30)$$

$$C_3^{3-7} = C_{IP} + \sum_{i=3}^{7} D_i (C_P + (i-3)C_W) + \left\lceil \frac{\sum_{i=3}^{7} D_i}{L_{OP}} \right\rceil C_3^{OP} + \left\lceil \frac{\sum_{i=3}^{7} D_i}{L_{TR}} \right\rceil C_3^{TR} \quad (31)$$

$$C_3 = \min \begin{cases} C_3^3 = 5541.9 \text{ €} \\ C_3^{3-4} = 5472.6 \text{ €} \\ C_3^{3-5} = 5437.8 \text{ €} = 5437.8 \text{ €} \\ C_3^{3-6} = 5952.1 \text{ €} \\ C_3^{3-7} = 6142.1 \text{ €} \end{cases} \quad (32)$$

The sixth phase of the optimization is to calculate the total cost of time frame 2 based on the following equations:

$$C_2 = min\,(C_2^2, C_2^{2-3}, C_2^{2-4}, C_2^{2-5}, C_2^{2-6}, C_2^{2-7}) \quad (33)$$

$$C_2^2 = C_{IP} + D_2 C_P + \left\lceil \frac{D_2}{L_{OP}} \right\rceil C_2^{OP} + \left\lceil \frac{D_2}{L_{TR}} \right\rceil C_2^{TR} + C_3 \quad (34)$$

$$C_2^{2-3} = C_{IP} + \sum_{i=2}^{3} D_i(C_P + (i-2)C_W) + \left\lceil \frac{\sum_{i=2}^{3} D_i}{L_{OP}} \right\rceil C_2^{OP} + \left\lceil \frac{\sum_{i=2}^{3} D_i}{L_{TR}} \right\rceil C_2^{TR} + C_4 \quad (35)$$

$$C_2^{2-4} = C_{IP} + \sum_{i=2}^{4} D_i(C_P + (i-2)C_W) + \left\lceil \frac{\sum_{i=2}^{4} D_i}{L_{OP}} \right\rceil C_2^{OP} + \left\lceil \frac{\sum_{i=2}^{4} D_i}{L_{TR}} \right\rceil C_2^{TR} + C_5 \quad (36)$$

$$C_2^{2-5} = C_{IP} + \sum_{i=2}^{5} D_i(C_P + (i-2)C_W) + \left\lceil \frac{\sum_{i=2}^{5} D_i}{L_{OP}} \right\rceil C_2^{OP} + \left\lceil \frac{\sum_{i=2}^{5} D_i}{L_{TR}} \right\rceil C_2^{TR} + C_6 \quad (37)$$

$$C_2^{2-6} = C_{IP} + \sum_{i=2}^{6} D_i(C_P + (i-2)C_W) + \left\lceil \frac{\sum_{i=2}^{6} D_i}{L_{OP}} \right\rceil C_2^{OP} + \left\lceil \frac{\sum_{i=2}^{6} D_i}{L_{TR}} \right\rceil C_2^{TR} + C_7 \quad (38)$$

$$C_2^{2-7} = C_{IP} + \sum_{i=2}^{7} D_i(C_P + (i-2)C_W) + \left\lceil \frac{\sum_{i=2}^{7} D_i}{L_{OP}} \right\rceil C_2^{OP} + \left\lceil \frac{\sum_{i=2}^{7} D_i}{L_{TR}} \right\rceil C_2^{TR} \quad (39)$$

$$C_2 = \min \begin{cases} C_2^{2} = 6720.2\ € \\ C_2^{2-3} = 6491.5\ € \\ C_2^{2-4} = 6650.6\ € \\ C_2^{2-5} = 6810.4\ € \\ C_2^{2-6} = 7523.2\ € \\ C_2^{2-7} = 7909.2\ € \end{cases} = 6491.5\ € \quad (40)$$

The last phase of the optimization is to calculate the total cost of the first time frame based on the following equations:

$$C_1 = min\ (C_1^1, C_1^{1-2}, C_1^{1-3}, C_1^{1-4}, C_1^{1-5}, C_1^{1-6}, C_1^{1-7}) \quad (41)$$

$$C_1^1 = C_{IP} + D_1 C_P + \left\lceil \frac{D_1}{L_{OP}} \right\rceil C_1^{OP} + \left\lceil \frac{D_1}{L_{TR}} \right\rceil C_1^{TR} + C_1 \quad (42)$$

$$C_1^{1-2} = C_{IP} + \sum_{i=1}^{2} D_i(C_P + (i-1)C_W) + \left\lceil \frac{\sum_{i=1}^{2} D_i}{L_{OP}} \right\rceil C_1^{OP} + \left\lceil \frac{\sum_{i=1}^{2} D_i}{L_{TR}} \right\rceil C_1^{TR} + C_3 \quad (43)$$

$$C_1^{1-3} = C_{IP} + \sum_{i=1}^{3} D_i(C_P + (i-1)C_W) + \left\lceil \frac{\sum_{i=1}^{3} D_i}{L_{OP}} \right\rceil C_1^{OP} + \left\lceil \frac{\sum_{i=1}^{3} D_i}{L_{TR}} \right\rceil C_1^{TR} + C_4 \quad (44)$$

$$C_1^{1-4} = C_{IP} + \sum_{i=1}^{4} D_i(C_P + (i-1)C_W) + \left\lceil \frac{\sum_{i=1}^{4} D_i}{L_{OP}} \right\rceil C_1^{OP} + \left\lceil \frac{\sum_{i=1}^{4} D_i}{L_{TR}} \right\rceil C_1^{TR} + C_5 \quad (45)$$

$$C_1^{1-5} = C_{IP} + \sum_{i=1}^{5} D_i(C_P + (i-1)C_W) + \left\lceil \frac{\sum_{i=1}^{5} D_i}{L_{OP}} \right\rceil C_1^{OP} + \left\lceil \frac{\sum_{i=1}^{5} D_i}{L_{TR}} \right\rceil C_1^{TR} + C_6 \quad (46)$$

$$C_1^{1-6} = C_{IP} + \sum_{i=1}^{6} D_i(C_P + (i-1)C_W) + \left\lceil \frac{\sum_{i=1}^{6} D_i}{L_{OP}} \right\rceil C_1^{OP} + \left\lceil \frac{\sum_{i=1}^{6} D_i}{L_{TR}} \right\rceil C_1^{TR} + C_7 \quad (47)$$

$$C_1^{1-7} = C_{IP} + \sum_{i=1}^{7} D_i(C_P + (i-1)C_W) + \left\lceil \frac{\sum_{i=1}^{7} D_i}{L_{OP}} \right\rceil C_1^{OP} + \left\lceil \frac{\sum_{i=1}^{7} D_i}{L_{TR}} \right\rceil C_1^{TR} \quad (48)$$

$$C_1 = \min \begin{cases} C_1^{1} = 7727.5\ € \\ C_1^{1-2} = 7652.4\ € \\ C_1^{1-3} = 7612.1\ € \\ C_1^{1-4} = 7987.6\ € \\ C_1^{1-5} = 8333.4\ € \\ C_1^{1-6} = 9276.4\ € \\ C_1^{1-7} = 9827.0\ € \end{cases} = 7612.1\ € \quad (49)$$

The above described computation resulted, that within the first time frame the demands of three weeks must be produced, because $C_1 = C_1^{1-3}$. The $C_1 = C_1^{1-3}$ equation resulted that the next production operation must be performed on the fourth time frame, where $C_4 = C_4^{4-5}$, which means, that within the fourth time frame the demands from two weeks must be produced. The $C_4 = C_4^{4-5}$ equation resulted that the next production operation must be performed on the sixth time frame, where

$C_6 = C_6^{6-7}$, which means, that within the sixth time frame the demands from two weeks must be produced.

Figure 2 shows the process of computations and the detailed results of each potential lot-size and scheduling. However, the computation goes backwards, from the last time frame to the first time frame, but after finishing all computations, the optimal lot sizing and scheduling of production can be defined forwards, from the first time frame until the last time frame, as Figure 2 shows.

	Production of demand until time frame						
	1	2	3	4	5	6	7
Time frame 1	7727.5	7652.4	7612.1	7987.6	8333.4	9276.4	9827
Time frame 2		6720.2	6491.5	6650.6	6810.4	7523.2	7909.2
Time frame 3			5541.9	5472.6	5437.8	5952.1	6142.1
Time frame 4				4551.8	4334.5	4613.3	4630.8
Time frame 5					3344.6	3403.2	3236.2
Time frame 6						2491.7	2146.2
Time frame 7							1166.2

Figure 2 – The optimization process and the detailed results of different lot size solutions

Figure 3 demonstrates the cost distribution function including the initialization cost of production, the total production cost, the warehousing cost, the cost of operators and the cost of technological resources.

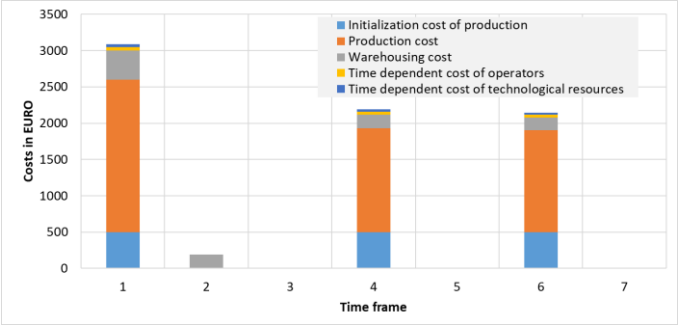

Figure 3 – The cost distribution of the optimal lot sizing

To validate the above mentioned approach, the next phase is to compare the solution of this extended dynamic lot size optimization and the conventional solution of the production scheduling.

The total cost of the conventional solution can be calculated as follows:

$$C_{CONV} = \sum_{i=1}^{7}(D_i C_P + C_{IP} + \left\lceil \frac{D_i}{L_{OP}} \right\rceil C_i^{OP} + \left\lceil \frac{D_i}{L_{TR}} \right\rceil C_i^{TR}) = 8731.5\ € \qquad (50)$$

Figure 4 demonstrates the cost distribution function of the conventional scheduling. As Figure 4 demonstrates, the conventional production scheduling has a

significant higher production initialization cost, because production is initialized in all time frames. The warehousing cost in the case of conventional production scheduling is zero, which means, that in this case we are talking about just-in-time production. The cost of just-in-time production are too high, because the zero inventory costs 1119.4 €.

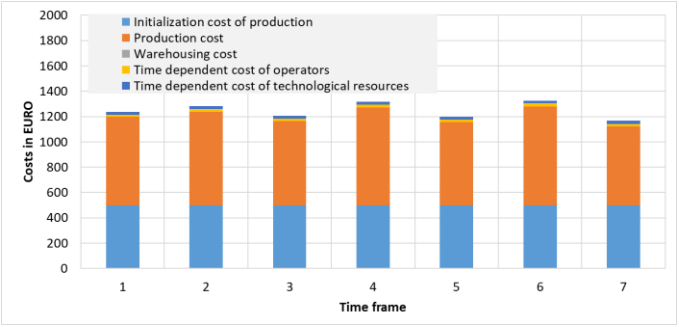

Figure 4 – The cost distribution of the conventional production scheduling

Figure 5 shows the comparison of the total costs of each time frames. In the case of conventional production scheduling, the distribution of the total costs is much more uniform than in the case of optimized production scheduling.

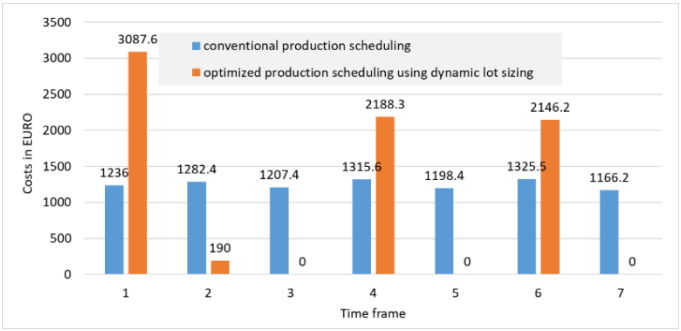

Figure 5 – Cost comparison of conventional and optimized production scheduling

As demonstrated in the case study presented above, the calculation and analysis of dynamic batch sizes is a good way to optimize production processes, as it can lead to significant efficiency gains. The results presented above show that while just-in-time production can be beneficial in terms of storage costs, it is important to consider the cost of achieving these warehousing cost savings. The analysis of the scenario shows, that the dynamic cost of human resources and technological resources can also significantly influence the optimal schedule, because depending on the

fluctuation of specific operator costs and technological resource cost, different schedules can lead to the more cost efficient production schedule.

5. SUMMARY

The efficiency of production processes can be affected by many factors. In order to increase the efficiency of production processes, it is becoming increasingly important to take into account a growing number of parameters. Although the Wagner-Whitin algorithm is an excellent method for determining dynamic batch sizes, there are a number of environmental parameters that cannot be taken into account by current algorithms. In the present research work, a method based on the Wagner-Whitin algorithm is presented which allows to take into account dynamically varying resource costs focusing on both human and technological resources. The applicability of the developed method was demonstrated by means of calculations. The method has been demonstrated through a case study that, compared to conventional production scheduling. The application of the method can lead to significant cost reductions when taking into account the impact of dynamic changes in resource costs. The study confirmed the fact that, although just-in-time production can be very beneficial from an inventory point of view, as just-in-time production can lead to significant inventory cost reductions, these inventory cost reductions can lead to multiple increases for other cost components, and it is therefore important to consider as many environmental parameters as possible in the calculations. In the present research work, the model was tested using deterministic parameters, so a potential future research task could be to develop a stochastic approach.

References: 1. *Kumar, N., Singh, B.J., Khope, P.*: Unleashing an ML-based selection criteria for economic lot sizing in a smart batch-type production system, TQM Journal vol.36(1) (2024) 90–107. https://doi.org/10.1108/TQM-05-2022-0166 **2.** *Asmal, S., Kurniawan, D., Indah, A.B.R., Anshar, A.M., Suradi, S.*: Inventory planning of raw material using Silver Meal and Wagner Whitin Algorithm, Acta Logistica vol.10(4) (2023) 589–596. https://doi.org/10.22306/al.v10i4.437 **3.** *Zhang, Z., Gao, C., Luedtke, J.*: New valid inequalities and formulations for the static joint Chance-constrained Lot-sizing problem, Mathematical Programming vol.199 (2023) 639–669. https://doi.org/10.1007/s10107-022-01847-y **4.** *Kuznetsov, S., Demidenko, O.*: Organization of Material Resources Supply in Transport Construction, Lecture Notes in Networks and Systems vol.509 (2023) 385–394. https://doi.org/10.1007/978-3-031-11058-0_37 **5**. *Narkhede, G., Rajhans, N.*: An integrated approach to redesign inventory management strategies for achieving sustainable development of small and medium-sized enterprises: Insights from an empirical study in India, Business Strategy and Development vol.5(4) (2022) 308–321. https://doi.org/10.1002/bsd2.200 **6**. *van Zyl, A., Adetunji, O.*: A lot sizing model for two items with imperfect manufacturing process, time varying demand and return rates, dependent demand and different quality grades, Journal of Remanufacturing vol.12(2) (2022) 227–252. https://doi.org/10.1007/s13243-022-00110-z **7.** *Assi, P.G., Effanga, E.O.*: Optimal manpower recruitment and promotion policies for the finitely graded systems using dynamic programming Heliyon, vol.7(7) (2021) 07424. https://doi.org/10.1016/j.heliyon.2021.e07424 **8.** *de Oca, S., Montesa, E., Loza-Hernández, L., Loza-Hernández, A.*: Supply of raw materials in an automotive manufacturing company, International Journal of Management and Decision Making vol.20(4) (2021) 323–348. https://doi.org/1504/IJMDM.2021.118541 **9.** *Kian, R., Berk, E., Gürler, Ü., Rezazadeh, H., Yazdani, B.*: The effect of economies-of-scale on the performance of lot-sizing heuristics in rolling horizon basis, International Journal of Production Research vol.59(8) (2021) 2294–2308.

https://doi.org/10.1080/00207543.2020.1730464 **10.** *Wu, T., Shi, Z., Liang, Z., Zhang, X., Zhang, C.*: Dantzig-Wolfe decomposition for the facility location and production planning problem, Computers and Operations Research (2020) 124. https://doi.org/10.1016/j.cor.2020.105068 **11.** *Olesen, J., Pedersen, C.E.H., Knudsen, M.G., Toft, S., Nedbailo, V.*: Joint effcet of forecasting and lot-sizing method on cost minimization objective of a manufacturer: A case study, Applied Computer Science vol.16(4) (2020) 21–36. https://doi.org/10.23743/acs-2020-26 **12.** *Gaol, F.L., Matsuo, T.*: The Simulation of Implications of Sensor Technology on the New Product Development to Solve Lot-Sizing Problems with Fuzzy Approach, Journal of Sensors (2020) 3503895. https://doi.org/10.1155/2020/3503895 **13.** *Hanafizadeh, P., Shahin, A., Sajadifar, M.*: Robust Wagner–Whitin algorithm with uncertain costs, Journal of Industrial Engineering International vol.15(3) (2019) 435–447. https://doi.org/10.1007/s40092-018-0298-y **14.** *Güner, G., Tunali, S.*: Fix-and-optimize heuristics for capacitated lot sizing with setup carryover and backordering, Journal of Enterprise Information Management vol.31(6) (2018) 879–890. https://doi.org/10.1108/JEIM-01-2017-0017 **15.** *Chowdhury, N.T.*: Dynamic Economic Lot-Sizing Problem: A new O(T) Algorithm for the Wagner-Whitin Model, Computers and Industrial Engineering vol.117 (2018) 6–18. https://doi.org/10.1016/j.cie.2018.01.010 **16.** *Sonar, A., MacKenzie, C.A.*: Supply chain disruptions preparedness measures using a dynamic model, Supply Chain Risk Management: Advanced Tools, Models, and Developments (2018) 123–137. https://doi.org/10.1007/978-981-10-4106-8_8

Тамаш Баньяї, Мішкольц, Угорщина

ВПЛИВ ДИНАМІЧНИХ ВИТРАТ НА ЛЮДСЬКІ ТА ТЕХНОЛОГІЧНІ РЕСУРСИ ПРИ ОПТИМІЗАЦІЇ РОЗМІРУ ПАРТІЇ ТОВАРІВ

Анотація. *Методи проектування виробничих систем за останні десятиліття значно еволюціонували. З'явилися нові методи, здатні визначати оптимальні параметри виробничих систем, що функціонують у все більш складних середовищах. Двома найбільш відомими методами для задач на розмір лотів (партій) є алгоритм Вагнера-Вітіна та евристика Сільвера-Міла. Оригінальні версії цих двох методів підходять тільки для вирішення простих задач на розмір лота, але існує кілька складних мутацій цих методів, які дозволяють вирішувати складні задачі розміру партії. На ефективність виробничих процесів може впливати безліч факторів. Для того щоб підвищити ефективність виробничих процесів, все більш важливим стає облік зростаючого числа параметрів. Хоча алгоритм Вагнера-Вітіна є відмінним методом для визначення динамічних розмірів партії, існує ряд параметрів середовища, які не можуть бути враховані сучасними алгоритмами. У даній дослідницькій роботі представлений метод, заснований на алгоритмі Вагнера-Вітіна, який дозволяє враховувати динамічно мінливі ресурсні витрати, орієнтуючись як на людські, так і на технологічні ресурси. За допомогою розрахунків продемонстровано застосовність розробленого методу, який був продемонстрований на конкретному прикладі у порівнянні зі звичайним виробничим плануванням. Застосування методу може призвести до значного зниження витрат при врахуванні впливу динамічних змін витрат на ресурси. Дослідження підтвердило той факт, що, хоча виробництво точно в строк може бути дуже вигідним з точки зору запасів, оскільки виробництво точно в строк може призвести до значного зниження витрат на запаси, яке в свою чергу може призвести до багаторазового збільшення інших компонентів витрат, і тому важливо враховувати якомога більше параметрів навколишнього середовища в розрахунках. У даній дослідницькій роботі модель була перевірена з використанням детермінованих параметрів, тому потенційним майбутнім дослідницьким завданням може бути розробка стохастичного підходу.*

Ключові слова: *розмір партії; планування та складання графіків виробництва; мінімізація витрат; моделювання.*

UDC 62-18. **doi: 10.20998/2078-7405.2024.100.05**

MANUFACTURING SYSTEMS USED IN THE SHIPBUILDING INDUSTRY FROM YEARS 2000 UP TO NOWADAYS

György **Czifra** [0000-0002-4758-0773]

Óbuda University, Budapest, Hungary
czifra.gyorgy@bgk.uni-obuda.hu

Received: 2 April 2024 / Revised: 19 April 2024 / Accepted: 15 May 2024 / Published: 15 June 2024

Abstract. *The continuous growth in demands for product quality and their utility properties in today's competitive environment places increased requirements on activities ranging from pre-production stages to sales completion. From these facts, it is evident that special attention must be paid to material selection, product design, and the construction of individual components, as well as the technologies used in their production and processing. Achieving high technical parameters for products while simultaneously optimizing the cost/performance or cost/utility value ratio compels designers and engineers to explore new progressive materials with high mechanical, chemical, and physical properties. They must also consider technologies that ensure efficient and precise manufacturing*.
Keywords: *shipbuilding; Industry 4.0; manufacturing systems; artificial intelligence.*

1 INTRODUCTION

In shipyards of global significance, both river and sea vessels are currently manufactured for various clients with highly specialized requirements. These vessels are constructed according to the rules of classification societies such as German Lloyd, American Bureau of Shipping, Bureau Veritas, and Lloyd's Register. Like other industrial sectors, the shipbuilding industry faces intense global competition. Labor costs are rising, and the risk of production errors due to the so-called "human factor" is significant. To remain competitive in this challenging environment, shipyards aiming to excel must analyse their current state and develop a strategic plan for the technical preparation of production. Subsequently, they can propose feasible production technologies. Despite dealing with large-scale steel structures, a considerable percentage of shipbuilding processes can be mechanized and automated. These innovations are crucial for maintaining competitiveness in today’s demanding environment.

Mechanization and automation allow for minimizing the impact of the human factor, increasing work productivity, and improving the precision and quality of products. Another positive effect that should not be underestimated is the

enhancement of working conditions for employees in the shipbuilding industry. As the achievable profit directly correlates with production efficiency, most shipyards have adopted modern project and design methods, followed by the implementation of mechanization and automation in production and assembly processes [1].

2 THE SITUATION

The shipbuilding industry faces challenges in transitioning from old, legacy systems to newer, more integrated approaches. On the other hand, here are some challenges that the modern shipbuilding industry must address: [2]

1) Technological Advancements: Keeping up with cutting-edge technologies is crucial. Shipbuilders need to adopt digitalization, automation, and innovative materials to enhance efficiency and reduce environmental impact.
2) Complexity and Customization: Ships are becoming more complex, with specialized designs and features. Meeting customer demands while maintaining cost-effectiveness is a challenge.
3) Supply Chain Management: Coordinating suppliers, managing lead times, and ensuring timely availability of materials and equipment are critical for smooth production.
4) Environmental Regulations: Stricter environmental standards require shipbuilders to design eco-friendly vessels and reduce emissions.
5) Labor Costs and Skills: Labor costs are rising, and skilled workers are essential. Upskilling and attracting talent are ongoing challenges.
6) Global Competition: Asia-Pacific countries (Japan, Korea, and China) dominate shipbuilding. European shipyards face intense competition and must innovate to stay competitive.
7) Risk Management: Making early decisions in ship design can impact costs and project success. Balancing risk and innovation are essential.
8) Sustainability: Shipbuilders must focus on sustainable practices, including recycling, energy efficiency, and minimizing waste.

These challenges highlight the dynamic nature of the shipbuilding industry and the need for continuous adaptation and improvement.

1. Legacy Work Processes: Many shipyards operate with established, traditional work processes. These legacy systems often hinder collaboration due to silos and lack of integration between different departments. For instance, enterprise resource planning (ERP) solutions may not communicate effectively with design tools, leading to inefficiencies.

2. Data Silos: The existence of functional silos creates difficulties in problem-solving. Differences in data structures, formats, and naming conventions

make it challenging to identify and trace issues. This lack of cohesion affects agility and responsiveness to change.

3. Collaboration and Expertise: Shipyards increasingly rely on external contractors and suppliers for various aspects of vessel design and construction. To form an effective ship delivery team, information must be integrated and accessible across the organization.

In summary, the shipbuilding industry must overcome legacy systems, foster collaboration, and embrace integrated information flow to enhance efficiency and quality in ship design and production processes.

The goal of this article is to analyse the current state of automation in design and construction processes within the field of technical production preparation. It aims to establish fundamental principles for designing process with a focus on achieving the highest possible level of automation in this field.

Significant attention must be devoted to the integration of CAD systems and the automated production system to ensure rapid and accurate data transfer. Furthermore, addressing issues related to quality control of finished products and suggesting potential solutions for conflict resolution due to inaccuracies in the environment are essential aspects [3].

3 CREATION OF A COMPLEX MODEL OF THE VESSEL

After considering the factors mentioned earlier, we can conclude that the so-called complex mathematical model of the vessel could be the optimal solution to the problems outlined in the preceding sections. This comprehensive model incorporates all geometrical information, interlinking various parts and components. When changes occur in one area, they necessarily impact other components. By doing so, users receive alerts to correct either the source of the change or initiate a chain reaction of adjustments. This collaborative approach among experts working on the same object ensures continuous relevance and accuracy of shared data within the geometric database [4].

From the perspective of communication between distinct mathematical models, the transmission of information about changes is ensured either in real time or through periodic updates. For users of such computer systems, the communication possibilities mirror those between mathematical models. Each user is assigned specific permissions and design elements, granting them the right to create and modify certain components. Other elements can be viewed but not altered. Users can annotate requested changes on other elements, and the associated owner will implement necessary adjustments after assessing eligibility.

When multiple users collaborate within the same space and simultaneously, a “real-time update” becomes feasible. However, this solution may strain computing devices. From a security and information transfer speed standpoint, this

method remains optimal. Nevertheless, the constant flux of changes and adjustments in an ever-evolving environment can evoke a sense of uncertainty for designers [5].

The concept of a “batch update” system can indeed address the challenges you’ve outlined. This approach involves transmitting new components and elements, along with any changes, to other users at specified time intervals. The interval is carefully chosen to optimize data updates, preventing system overload, and minimizing disruptions caused by constant modifications. Users can then focus on their work without being constantly interrupted by unfinished solution variants. This method strikes a balance between timely updates and maintaining a stable work environment.

Figure 1. Engine room 3D model [1]

4 USE OF THE “CONCURRENT ENGINEERING” METHOD

The “Concurrent Engineering (CE)” method represents the pinnacle of convenience in terms of the volume and type of managed information [1]. In this approach, we utilize what is known as the production model of the spatial vessel. This model encompasses not only geometric data but also associative and parametric relationships, along with what we refer to as non-geometric information.

What does this comprehensive model provide? It offers the technical and logistical details necessary for describing and supporting the design of the complete product—the vessel. Across the entire life cycle of the vessel, it

integrates information from various domains: design, construction, technology, production, logistics, and sales.

The fundamental concept behind the CE system is continuous access to shared data and information. By establishing a robust CE system, we achieve several benefits:

- Reduced Production and Overhead Costs: Streamlining processes leads to cost savings.
- Accelerated Technical Preparation Stage: Faster decision-making and collaboration.
- Shortened Production Cycle: Efficient workflows lead to quicker results.
- Reduced Product Launch Time: Getting the vessel to market promptly.

In summary, the CE method fosters collaboration, optimizes efficiency, and ensures that everyone works with the most up-to-date information.

Advantages of the "concurrent engineering" concept are [1]:

- Product development time: 30-70% reduction
- Design changes needed: 65-90% reduction.
- Time to market: 20-90% reduction
- General quality increased by 200-600%
- Work productivity, efficiency increased by 20-110%
- Business turnover increased by 5-50%
- Return on Assets increased by 20-120%

At first glance, it is evident from the data above that the advantages resulting from the implementation of the Concurrent Engineering (CE) method yield economic outcomes, ensuring a relatively swift return on the necessary investments in this technology.

By transitioning to more advanced computing systems, CE technology opens new possibilities within the realm of virtual reality. Virtual reality represents the pinnacle of interactive design facilitated by CE technology. The fundamental concept involves creating a complex mathematical model — a computer-generated representation — of the vessel. This model not only incorporates geometric and database data but also allows for interactive engagement. In essence, users can interact with the model as if it were a physical prototype, mimicking the behaviour of a real vessel. Unlike a static element, this dynamic model possesses the properties of an actual physical body.

The NUPAS-CADMATIC system for example, implemented in several shipyards, encompasses all the necessary properties, and meets usability criteria for preparing inputs into a flexible production system. This solution, based on NUPAS-CADMATIC, significantly enhances productivity, and leads to an optimal spatial model of the vessel, particularly in areas with limited space. By doing so, it elevates workshop pre-production capabilities, effectively shifting the workload

from shipbuilding to technologically advanced workshop spaces. Ultimately, this approach reduces product transit time and significantly cuts production costs. Thanks to its highly intelligent graphical user interface, the system requires minimal user training [6].

The software solution makes it possible to share design information between individual designers from different professions. The most important design information is public and available to everyone. Such a solution reduces the time for coordinating the location of individual equipment and components of pipeline systems. This increases the quality of the construction solution and the overall quality of the vessel. By using the same system in different areas of construction work, the so-called method of parallel engineering - Concurrent Engineering - becomes a reality [1].

Using this system, components are created only once, it contains their spatial mathematical model. All other component views are derived from that mathematical model and are kept up to date according to pre-defined and set rules. The modification of the component in the model is indicated based on the stated rules, and its other views are updated according to the need and decision of the designer. It means high consistency of construction and correct exact information for production.

The advantage of the production model is that the designer, by defining the component in the model, automatically creates the production data in one step. This means extremely precise and exact information for production, which is always up to date according to the latest construction status. The system enables its freely programmable export generators to forward the necessary information in the required form for other systems, for example, for material management, warehouses, purchasing and logistics, financial evaluation, and the like. In the field of pipeline systems, the creation of a model of pipeline systems is based on an intelligent database, which contains not only the design data of individual components, geometry, but also the logic of mutual connection - pressure class, number of screws, type of seal, etc. Based on this database, connection diagrams of individual pipe systems are created. It is possible to insert only such a component into the schemes, which is included in the database. Of course, the missing component can be added at any time, but first it must be defined with all the necessary properties in the database and then it can be used in the schema. After completing the scheme and verifying the functionality and correctness of the connection, it is possible to start creating a spatial model. The relationship between a spatial model and a wiring diagram is the same as that between diagrams and databases. Only components that have been included in the scheme can be used in the model. Such a solution ensures the unequivocal correctness of the model and its consistency with the functional scheme. All standards, regulations and requirements of the shipyard are stored in the database and are automatically

considered during the creation of the model. By using the CE – Concurrent Engineering method, it is possible to increase the efficiency of material use and effectively use the available space [1].

It is possible to save a lot of time by generating all other information necessary for production from the spatial model, such as isometric drawings of pipe branches, a breakdown of the material used, and a cutting plan. Accurate information for production also contributes to increasing production accuracy and reducing the overall error rate.

What is created while modelling can no longer be called just a geometric model, but due to the complexity of the information contained in it, we speak of a so-called production model - Product Model. In addition to geometric information, this model also contains information on physical properties and technological and production information for production. As an example, it is possible to mention that the places of pipeline transitions through watertight walls are inserted at the stage of creating a spatial model of pipeline systems, but the information about the necessary openings in individual dividing walls becomes part of the geometry of the sheet metal, their geometry is burned on NC automatic burning machines. A change in the pipe system also causes a change in the dividing wall, the change in geometry is reflected in the control program for the movement of the firing head, which ensures a high degree of data consistency for production. Similarly, it is possible to describe the state after checking collisions between individual components or between devices, steel structure and pipe systems. The structure of NUPAS-CADMATIC allows dividing the model into smaller integrated blocks with a precisely defined interface and connection, which enables parallel processing of the created blocks. Of course, it means a significant saving of time, and in the final phase the entire complete model is assembled in one integrated database of the production model of the vessel. The production space model allows you to use the so-called virtual vessel bypass function. It is possible to define the route of a camera or a visitor who can - it is true that without the possibility of intervention in the model and without the possibility of its modification - pass the entire object and see for himself the quality of the technical solutions used. This option is also a great help for the production itself, as it allows you to interactively check and see the model in its real form before production. Another advantage is that changes made in the mathematical model are immediately reflected in the production information [1].

The real benefit of this solution, in addition to the above, is that control programs for DNC burning and bending automata of sheet metal parts, control programs for DNC cutting and bending automata of pipes and profiles, or for others, such as assembly and welding robots, are generated and exported from an accurate mathematical model. The support of the automatic production line by the software consists in supplying the automatic warehouse of semi-finished products

with the necessary information to produce pipe branches, a computer-controlled handling line, a cutter-saw, a pipe marker, and a DNC bending centre. With the generation of isometric drawings of pipe branches, information for direct control of the DNC bending centre is also generated. In addition to information such as branch number, material, surface treatment, number of block or higher assembly, order of assembly, orientation of holes in the flange are contained in the file. Part of this information can be printed on a label and stuck on the pipe branch, respectively in the form of a barcode or in the form of a 2D Data Matrix code, it can be stamped on the surface of the branch. By combining design software with computer-controlled manufacturing, manual handling, and preparation of data for production is eliminated. An important aspect of the mentioned solution is that the information coming from the program already contains technological data.

An optimally designed construction solution results in an optimal production batch, and with such a solution, it is possible to extremely increase the share of workshop preparatory production and reduce the share of expensive, time- and material-intensive modifications directly on the vessel.

In addition to the mentioned information, the system can cooperate with the largest software solutions in the field of purchasing, logistics and material management, and of course also software solutions for production management. Design, technologically correct organization, increase the capacity of the workplace, which will ensure the production of pipeline components based on information from a complex computer model of the vessel, was the scope of the assignment. The results clearly show the feasibility of the proposed solution. The analysis attempted to outline a wide range of problems in the transition of technical preparation from classical manual methods to the most modern, computer-aided methods of competitive engineering. The basis of the solution is a complex mathematical spatial model of the vessel. Expanding this model with structural, material-technological, production information means the creation of the already mentioned production model of the vessel. Based on the created production model, it is possible to formulate the basic requirements for the technological process of production and pipeline branches about securing the automated production system with information.

By using design-construction computer systems, it becomes possible to supply the entire region with custom-made, surface-modified components of pipeline systems, it is possible to separate the design and construction activity from the production of parts, we come to believe that such a project must be effectively applicable and usable [7].

5 RESULTS

The basic goal of our work was to provide an analysis of the current state of the technology of the production of pipe branches in the conditions of a shipyard. Part of our work is also the proposal for the use of new technology for the technical preparation of production and at the same time for the technological preparation of production. Detailed cost analysis, workability analysis and review of the feasibility of the entire project demonstrated the complexity and complexity of the investigated issue.

The basic characteristics of the control system working based on fuzzy logic were presented. A description of the characteristics of the control computer and the control hierarchy of automatic production systems was given. Based on the facts mentioned above, an integrated flexible production system was designed, which can automatically change its production program based on input information without the need to stop work and possibly adjust the used components.

Concrete results and benefits of the solution described above are listed below. Figure 2 shows the number of necessary changes for modelled and non-modelled vessels during manufacturing process.

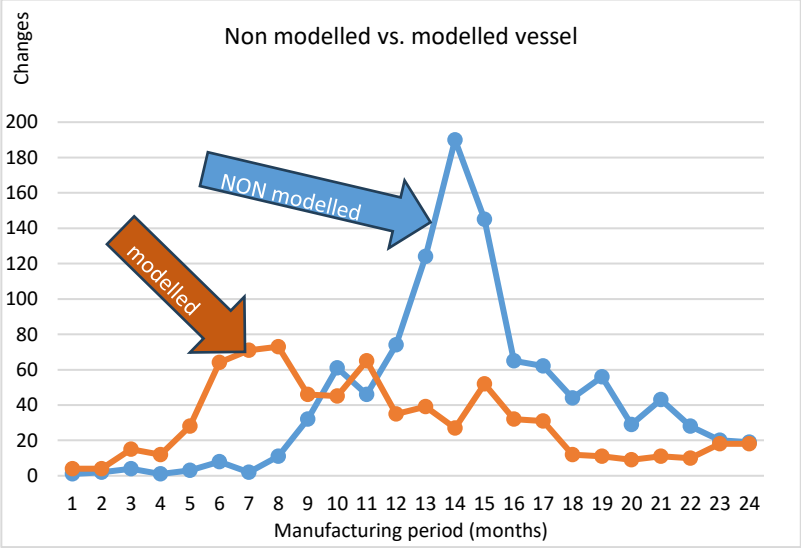

Figure 2. Non-modelled vs. modelled vessel - number of necessary changes during manufacturing process [1].

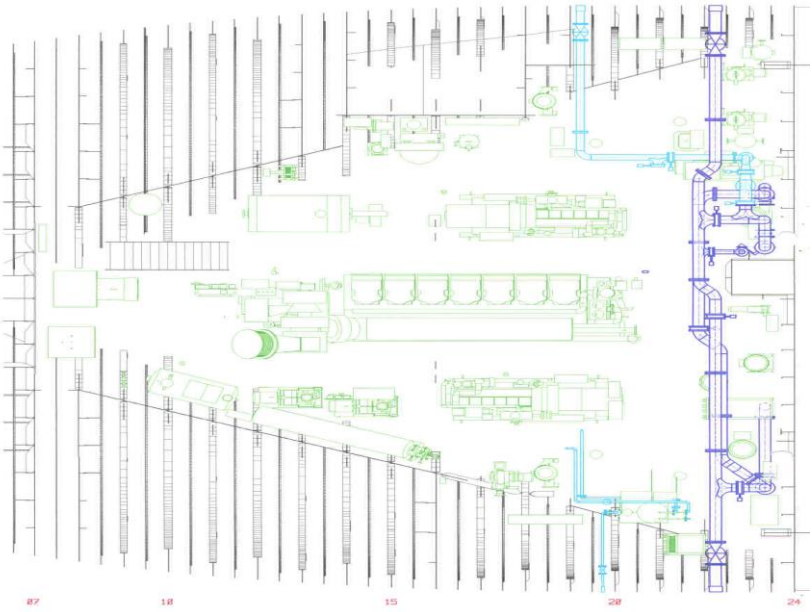

Figure 3. Engine room of a vessel [1].

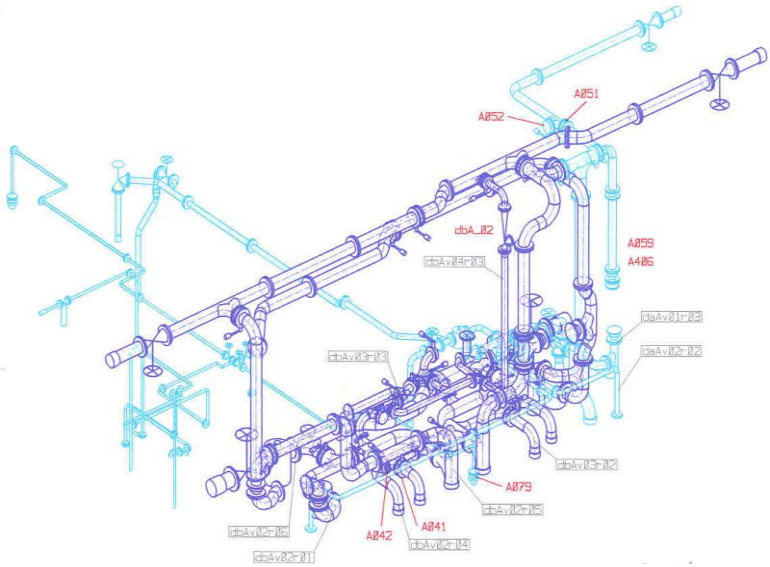

Figure 4. Pipeline systems of a vessel [1].

6 CONCLUSION

The working place of automated production system - APS for pipe systems of vessels is connected to the 3D CAD system for preparing of working documentation for pipe systems. The 3D model of pipe systems is used as a base. From the automated design of 3D model is processed the technological background for production with output applicable straight in the automated production process. The production process is provided by the flexible production system includes subsystems for manipulation, transport, material preparing, production, testing, sorting, and stocking. Automated production line includes numerical controlled daily stock of raw material, computer-controlled workplace for measuring and cutting of pipes. This workplace is connected to the workplace with NC bending machine continuing with numerical controlled welding machine – robot for flange welding. Other workplaces for geometry checking and welding quality verification are included into the automated production line too. The production system is designed based on the actual accessible results of science and research in this field. The production line is characterized as a Flexible Production System – FPS controlled by fuzzy logic. The system can react to the necessary changes of the product assortment. After the change of the control information the system is able immediately to start production of other assortment of products. Our flexible production system is an automated production line, where the change of the product assortment is done by changing of the controlling programs.

References: 1. *Czifra J.; Koloman V.* (2007) Fuzzy logikával vezérelt automatikus gyártórendszer (Fuzzy logic controller automated production system), Műszaki Szemle (EMT) 10(38):81-84. (in Hungarian) **2.** *Iwańkowicz, R.; Rutkowski, R.* (2023) Digital Twin of Shipbuilding Process in Shipyard 4.0. Sustainability, 15:9733. https://doi.org/10.3390/su15129733 **3.** *Okubo Y, Mitsuyuki T.* Ship (2022) Production Planning Using Shipbuilding System Modeling and Discrete Time Process Simulation. Journal of Marine Science and Engineering. 10(2):176. https://doi.org/10.3390/jmse10020176 **4.** *Lee, Y. G., Ju, S., & Woo, J. H.* (2020). Simulation-based planning system for shipbuilding. International Journal of Computer Integrated Manufacturing, 33(6), 626–641. https://doi.org/10.1080/0951192X.2020.1775304 **5.** https://link.springer.com/content/pdf/10.1007/3-540-27032-9_35.pdf **6.** CADMATIC webpage; https://www.cadmatic.com/en/products/cadmatic-hull/ **7.** Concurrent Engineering (CE). Engineering Product Design 13/02/2023 https://engineeringproductdesign.com/knowledge-base/concurrent-engineering/

Дьордь Чіфра, Будапешт, Угорщина

ВИРОБНИЧІ СИСТЕМИ, ЯКІ ВИКОРИСТОВУЮТЬСЯ У СУДНОБУДІВНІЙ ПРОМИСЛОВОСТІ ВІД 2000 РОКУ ДО СЬОГОДЕННЯ

Анотація. *Безперервне зростання вимог до якості продукції та її корисних властивостей у сучасному конкурентному середовищі висуває підвищені вимоги до промисловості, починаючи*

від етапів підготовки виробництва до його завершення і продажів. З цих фактів видно, що особлива увага повинна бути приділена вибору матеріалів, дизайну виробів і конструкції окремих компонентів, а також технологіям, що використовуються при їх виробництві та обробці. Досягнення високих технічних параметрів виробів з одночасною оптимізацією співвідношення витрат і продуктивності або витрат і корисностей змушує конструкторів та інженерів досліджувати нові прогресивні матеріали з високими механічними, хімічними та фізичними властивостями. Вони також повинні враховувати технології, які забезпечують ефективне та точне виробництво. Робоче місце автоматизованої виробничої системи – АВС для трубних систем суден підключено до системи 3D CAD для підготовки робочої документації для трубних систем. Виробничий процес побудови суден забезпечується гнучкою виробничою системою, що включає підсистеми маніпуляцій, транспортування, підготовки матеріалів, виробництва, тестування, сортування та складування. Автоматизована виробнича лінія включає в себе щоденний запас сировини з числовим програмним управлінням, комп'ютеризоване робоче місце для вимірювання і різання труб. Це робоче місце з'єднане з робочим процесом за допомогою згинального верстата з ЧПУ, продовжуючи зварювальним апаратом з числовим програмним управлінням – роботом для зварювання фланців. Інші робочі місця для перевірки геометрії та перевірки якості зварювання також включені в автоматизовану виробничу лінію. Виробнича система проектується на основі актуальних доступних результатів науки і досліджень в даній області. Виробнича лінія характеризується як гнучка виробнича система – ГВС, керована нечіткою логікою. Система може реагувати на необхідні зміни товарного асортименту. Після зміни контрольної інформації система здатна відразу ж приступити до випуску іншого асортименту продукції. Така гнучка виробнича система являє собою автоматизовану виробничу лінію, де зміна асортименту продукції здійснюється шляхом зміни керуючих програм.

Ключові слова: *суднобудування; Індустрія 4.0; виробничі системи; штучний інтелект.*

UDC 621.713.1 **doi: 10.20998/2078-7405.2024.100.04**

INTERPRETATION WORKFLOW OF GEOMETRIC TOLERANCES

Balazs **Mikó** [0000-0003-3609-0290]

Óbuda University, Budapest, Hungary
miko.balazs@bgk.uni-obuda.hu

Received: 2 April 2024 / Revised: 19 April 2024 / Accepted: 25 May 2024 / Published: 15 June 2024

Abstract. *The application of the principles of the geometric product specification (GPS) has increasing importance in the machining industry. The tolerancing process should harmonize the relationship between tolerancing, machining process, measuring and design requirements. The aim of the article is to present the interpretation process and the suggested workflow of geometric tolerances. The dimensional and geometric tolerances are compared, and some critical problems of geometric tolerancing are demonstrated by case studies.*
Keywords: *geometric tolerance; GPS; GD&T; degree of freedom; datum feature*

1 INTRODUCTION

In the production of machine components, we always experience deviations due to a number of factors. Deviations may be singular or recurring, recurring deviations may be permanent or random. The causes of deviations can be explained by changes in the raw material used, changes in the condition of the manufacturing equipment, changes in technology, human factors, environmental influences or the measurement process.

There are several ways to manage deviations from plan. The first is to define a manufacturing technology, a series of processes in the process planning that will gradually, step by step, produce the desired part geometry with the expected accuracy. The second solution is to define tolerances, which are the allowable deviation. We can define macro and micro precision for the geometry design. The macro accuracy of a part can be defined by dimensional and geometric tolerances. Dimensional accuracy refers to the distance between points, while geometric tolerances refer to shape and positional accuracy. A comparison of dimensional and geometric tolerances is provided in Table 1.

The ISO standards define the specifications for dimensional tolerances of mechanical parts [1] by the abbreviated name GPS - geometric product specification. The American ASME standard uses the term GD&T - geometric dimensioning and tolerancing. The aim and the basic principles of the two sets of standards are the

same, but some details can be different. In case of interpretation of the engineering drawing, the detailed understanding of the relevant standards is essential.

The aim of the research is to investigate the tolerancing process, the relationship between tolerancing, machining process, measuring and design requirements. The aim of the article is to present the interpretation process and the suggested workflow of geometric tolerances. Some critical problems are demonstrated by case studies.

Table 1 Comparison of dimensional and geometric tolerances

	Dimensional Tolerances	**Geometric Tolerances**
Definition	Specify the acceptable variations in the numerical values of dimensions, such as length, width, height, or diameter. They focus on the size of individual features.	Specify the allowable variations in the form, orientation, location, and relationship of features. Geometric tolerances are concerned with the shape and spatial arrangement of features
Representation	Usually represented by numerical values indicating the acceptable range of dimensions. For example, a dimension is specified as "25 ± 0.05 mm".	Represented using symbols and feature control frames, indicating the desired geometric relationship and allowable variations.
Focus	Primarily concerned with the size of features, ensuring they fall within specified limits.	Focus on the form and arrangement of features, ensuring that they relate to each other correctly in terms of shape, orientation, and location.
Application	Applied to individual measurements of length, width, height, etc. For example, specifying the length of a shaft or the diameter of a hole.	Applied to relationships between features, ensuring proper alignment, orientation, and form.
Complexity	Generally simpler to specify and interpret, involving straightforward numerical values	Can be more complex as they involve a combination of symbols, datum, and specific instructions to define relationships between features accurately.
Interchangeability	Mainly contribute to the interchangeability of parts by specifying acceptable size variations.	Contribute to both interchangeability and functional relationships between parts by ensuring proper form, orientation, and alignment.

Cost Considerations	Tight dimensional tolerances can increase manufacturing costs, as they require more precise machining and measurement.	Can contribute to cost savings by allowing more flexibility in certain dimensions while ensuring critical relationships for functionality.

2 TOLERANCING PROCESS

The tolerance process should identify the type and value of tolerances required. In this process, several conflicting aspects need to be taken into account. The primary consideration is the function of the part, the role of each geometric element [2][3]. The second aspect is to take into account the manufacturing capabilities [4][5]. The third aspect is the analysis of the assembly relationships and the impact of the propagation of manufacturing defects. The fourth aspect is the consideration of the measurement possibilities [6][7][8]. Finally, these requirements must be indicated on the drawing by means of engineering symbols [1], for which clarity and compliance with engineering standards are essential. The tolerancing of the part therefore sets expectations for the manufacturing and measurement process, taking into account the functional requirements, and thus determines the cost of the part.

For geometric tolerances, whether we are in the design, manufacturing preparation or measurement phase, the following analysis process should be carried out to clarify the interpretation of the tolerance (Figure 1). The interpretation of geometric tolerances is based on standard drawing symbols (Figure 3).

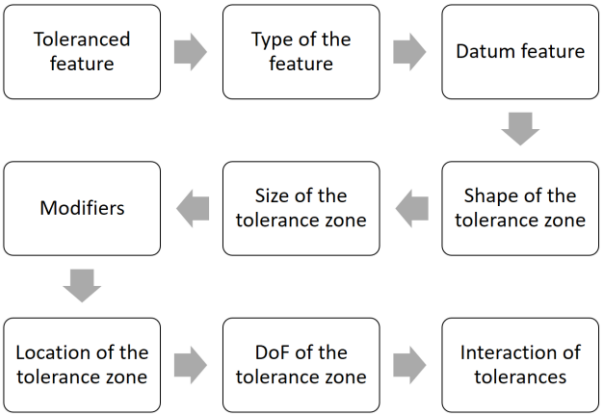

Figure 1. Tolerance analysing process

The first question is what is the *toleranced feature*. The leader and an arrow show this from the tolerance frame (Figure 3a). The direction of the leader can have a modifying effect on the meaning, so accurate application is important. The notation can only point to a physically existing feature, not to a theoretical geometric element (e.g. centre line, plane of symmetry). Indeed, if a centre line is the centre line of several geometric elements (e.g. a stepped hole), it is not possible to determine to which element the specification applies. If the indicator arrow continues along a dimension line, the centre line, plane of symmetry of the marked element is the one to which the specification applies.

Another important aspect of the toleranced element is whether the measuring is technologically feasible. For example, a hole in a sheet metal part theoretically has an axis, but due to the short length of the hole, this can only be measured with a higher uncertainty. The fundamental cause of the measured deviation will be the measuring process. It is therefore necessary to consider the metrological process in the tolerancing process.

The *tolerance type* is indicated by the symbol in the first field of the tolerance frame. ISO 1101 defines 15 types of geometric tolerances, shown in Figure 2. The interpretation of each tolerance is defined in the standard.

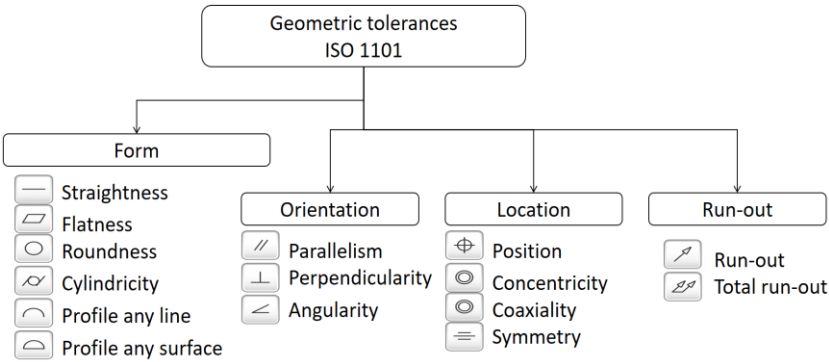

Figure 2. Type of geometric tolerances based on ISO 1101

The next step is to define the *datum feature*. In the tolerance frame, the datum are marked on the right-hand side and must be indicated on the drawing. The datum feature is connected to the surface by a triangle, not an arrow (Figure 3b). The notation rules are the same as for the marking of the toleranced feature, so the marking should not point to a theoretical geometric element. An exception to this is when the points forming the base are also given with base locations (ISO 5459). The locations of the points are given with theoretical dimensions (Figure 3d), which have no tolerance, giving the theoretical dimensions necessary to interpret the tolerance.

For some geometric tolerances, no datum can be used, for others the use of a datum is necessary, while in some cases both with and without a datum can be used (profile any line, profile any surface, position), but the interpretation is modified. If a datum is required, it must be checked that (1) the datum feature is independent of the toleranced element; (2) its indication is on the drawing; (3) it corresponds to the type of tolerance (e.g. perpendicularity tolerance is indeed perpendicular to the toleranced element).

If several datum are applied to a tolerance, the order of these is important. We can talk about primary, secondary and tertiary bases. These are important for the degrees of freedom of the tolerance field (see later). The primary base is usually a planar geometric element, which is, for all intents and purposes, the supporting surface of the element being toleranced. The secondary base is an axis or straight element that gives directional constraint, while the tertiary base is a point element.

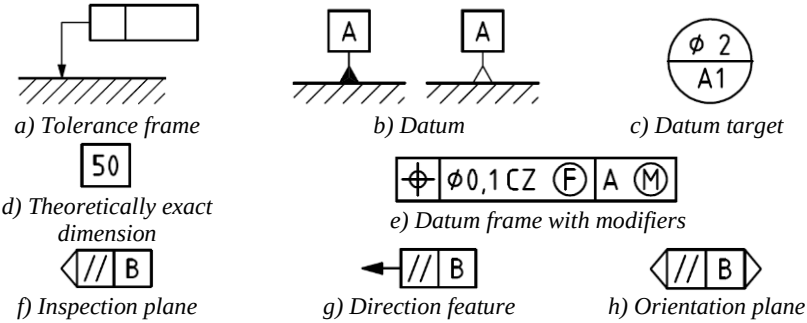

a) Tolerance frame *b) Datum* *c) Datum target*

d) Theoretically exact dimension

e) Datum frame with modifiers

f) Inspection plane *g) Direction feature* *h) Orientation plane*

Figure 3. Some drawing symbols related to geometric tolerances

The next step is to determine the *shape of the tolerance zone*. Depending on the type and nature of the toleranced feature, the tolerance zone can be either planar or three-dimensional. A tolerance field is two parallel elements that envelops the toleranced feature along its entire extent. Where a diameter (Ø) is indicated in the metre of tolerance, the tolerance zone is circular or cylindrical. The type of tolerance and the nature of the toleranced feature determines whether the tolerance can be used with a diameter mark only, without a diameter mark, or with both. In the case of circular and cylindrical tolerances, the tolerance field is in the form of a circular ring or cylindrical ring.

The *size of the tolerance zone* is always given in millimetres (mm) and is the width or diameter of the aforementioned zone. The application of the diameter symbol is depends on the type of the tolerance and the nature of the toleranced feature.

The interpretation of the tolerance can be modified or clarified using a number of *modifiers*. These modifiers can refer to the definition of the associated

geometry (C, G, N, X, T, E); the relationship between several features (CZ, SZ, UF, SIM), the offset of the tolerance field (P, UZ, OZ), the measurement condition for elastic pieces (F), the relationship between geometric and dimensional tolerances (M, L, R). The use of these modifiers provides a high degree of flexibility in the definition of tolerances, but requires careful analysis during measurement. The modifiers cannot be used in all cases and the guidelines of the standard should be followed.

Based on the type of geometric tolerance and the nature of the toleranced element, the *location of the tolerance zone* can be determined. In this context, account shall be taken of any datum, the location and orientation of the drawing markings, or, in their absence, the indicative notations which are mandatory under the standard (Figure 3f, Figure 3g, Figure 3h).

Geometric tolerances are not fixed tolerance zones at a given location, but have a different number of *Degrees of Freedom* (DoF) depending on the type of tolerance, the nature of the element being toleranced and the number of possible bases. These provide the flexibility to adapt to the specific design requirement, determining the most appropriate tolerance at the design stage.

The final step investigated the *interaction* effects between each tolerance. If a toleranced feature is associated with more than one tolerance, the relationship between them is examined. It is possible that the same requirement has been specified in several different ways, so that one of the tolerances is redundant. For example, there are both perpendicularity and parallelism tolerances on the axis of a hole. Specifications may also be found that are conflicting. This means that if one specification is satisfied by the part, the other is not. This can be due to an incorrect choice of tolerance type or tolerance value. The analysis shall determine the value of the degree of freedom of each tolerance field. The tolerance with more degrees of freedom should have a smaller tolerance zone value.

3 CASE STUDIES

The current chapter demonstrates the interpretation process of the geometric tolerancing by case studies.

Figure 4 shows a position tolerancing of a hole. The toleranced feature is the axis of the hole, because the indicator arrow continues along a dimension line. The position tolerance required datum features, which define the theoretical location of the hole. The theoretical position is 55 mm and 70 mm from the *A* and *B* datum.

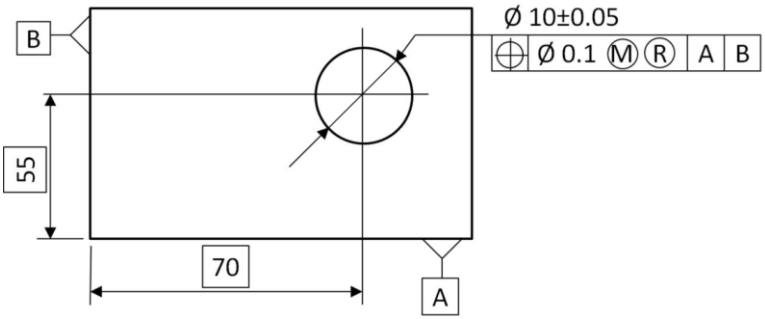

Figure 4. Case study #1 – Position tolerance of a hole with modifiers

The shape of the tolerance zone is a circle or a cylinder, because of the diameter indicator (Ø), and the size is 0.1 mm. The shape of the tolerance zone can also be interpreted as a circle or a cylinder, a kind of uncertainty in the definition of tolerance. The shape of the tolerance zone depends on how deep the hole is. For a sheet metal part, it can be interpreted as 2D geometry, in which case the tolerance field is a circle. If the depth of the hole allows measurements to be made on several levels, the tolerance field is a cylinder as a 3D element.

The tolerance frame contains two modifiers. The first is the maximum material principle, which means, than the current value of the geometric tolerance depends on the dimeson of the hole. The tolerance of 0.1 mm is valid for the maximum material condition (M). In this case, the part contains the most material, so this is the lower limit for a hole (9.95). If the diameter of the manufactured part is larger than this, the position tolerance is increased by this value. If the diameter of the hole is 10.05 mm (upper limit), the value of the tolerance zone is 0.2 mm. The result is a virtual hole in which no hole's contour will intersect any of the elements of the produced series. The reciprocity modifier (R) extends this by allowing the dimensional tolerance of the hole to increase if the hole's position error is smaller than the specified position tolerance. Therefore, if the current position error is 0 mm, the minimum value of the diameter can be 9.85 mm. This is the theoretical value of the previous mentioned virtual hole. The tolerance zone located in the given position, there is no degree of freedom, so this type of geometric tolerance is close to the dimensional tolerancing.

Figure 5a presents an example from the ISO 1101 standard for the position tolerance of a plane surface. The two datum features are the face surface on the right side (A) and the axis of the shaft (B). Let's determine the location of the tolerance zone!

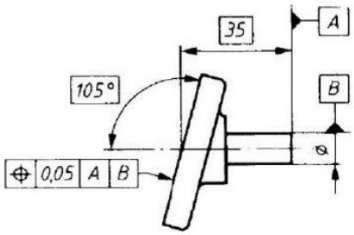

a) Original drawing [1].

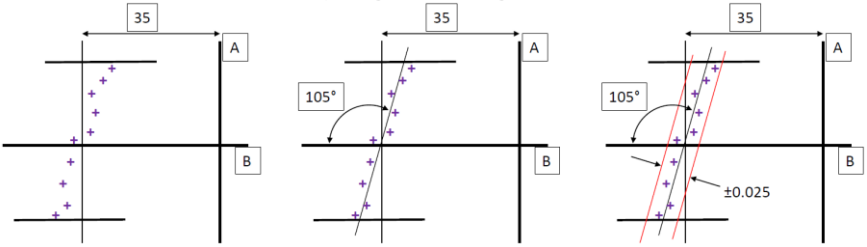

b) *c)* *d)*

Figure 5. Case study #2 – Location of the tolerance zone

First, a parallel plane is drawn at a distance of 35 mm from datum *A* (Figure 5b). After that this plane is rotated 105° about the horizontal, an *A* datum parallel axis passing through the intersection of bases *A* and *B* (Figure 5c). The resulting plane is offset by ±0.025 mm. This indicates the limit of the tolerance zone (Figure 5d). The position tolerance has no degree of freedom, so the points of the toleranced surface must be within this fixed range.

In some cases it is possible to change the degree of freedom of the tolerance zone by specifying the datum. This provides a high degree of flexibility during the design process. The larger the number of degrees of freedom in the tolerance zone, the more stringent the specification. The „profile any surface" tolerance is often used for general tolerancing of parts bounded by free-form surfaces (e.g. injection moulded plastic parts).

Figure 6 shows the "profile any surface" tolerance for different bases. If no base is defined (Figure 6a), the 3D tolerance zone around the part has six degrees of freedom, three linear and three rotational. The surface points of the part must be covered by displacements along these three axes. If a planar datum is defined (Figure 6b), the number of degrees of freedom is reduced, leaving two linear and one rotational possible displacements. This tolerance zone is more strict. If a secondary datum is added (Figure 6c), the tolerance field is reduced by two more degrees of freedom, leaving only one linear displacement possibility. With the addition of a tertiary datum (Figure 6d), all degrees of freedom are removed.

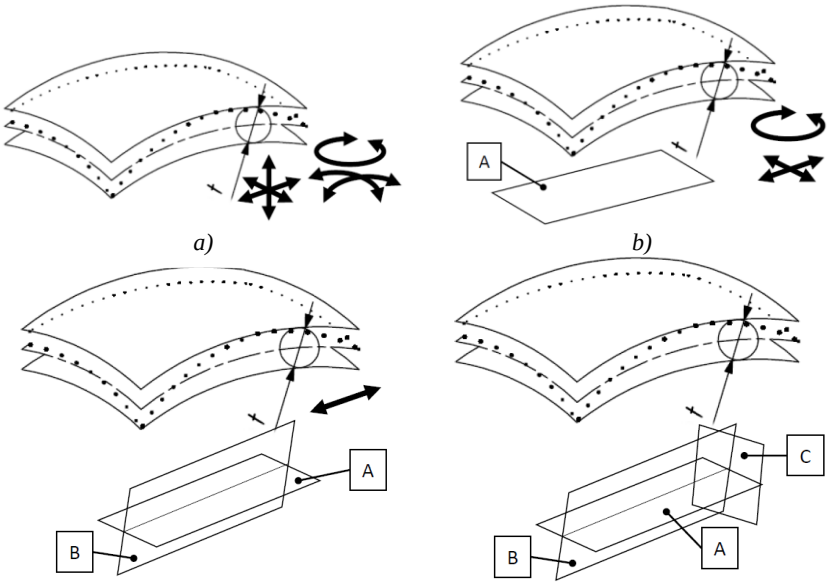

a) *b)* *c)* *d)*

Figure 6. Case study #3 - Profile any surface with datum

The fourth case study shows an example of multiple tolerancing (Figure 7). The drawing in the second example (Figure 5a) is extended with two additional tolerances, an angularity tolerance and a flatness tolerance.

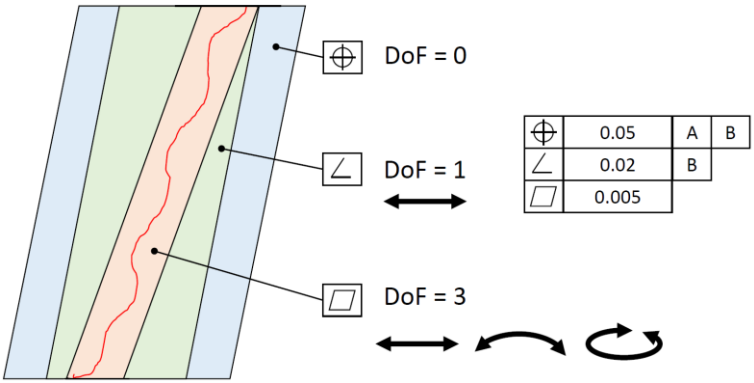

Figure 7. Case study #4 – Multiple tolerances

Position tolerance has no degree of freedom, as we saw earlier. However, the angularity tolerance has one degree of freedom, it can move along the datum *B.*

However, this is only a true degree of freedom if the value of the angularity tolerance is less than the position tolerance, so the angularity tolerance is within the position tolerance. Otherwise, both tolerances cannot be satisfied. It is advisable to adjust the ratio between the two tolerances between 1:3 and 1:5, so that the effect of a smaller tolerance is noticeable in operation, measurement and production.

The flatness tolerance has no datum, so it has three 3D degrees of freedom: one linear and two rotational DoF. The value of the flatness tolerance must be smaller than the value of the angularity tolerance, as explained above. The degrees of freedom can only be used if the other tolerance zone does not constrain it.

4 CONCLUSION

The use of geometrical tolerances is nowadays essential in the design of mechanical engineering components. Consequently, the correct interpretation of the engineering drawings is also required when planning manufacturing and measurement plans.

In this paper, a nine-step workflow has been presented to provide a systematic interpretation of each engineering drawing item. The proposed nine steps are:

1. Define the tolerance feature.
2. Determine the type of tolerance.
3. Determine the datum.
4. Determine tolerance zone shape.
5. Determine the size of the tolerance zone.
6. Interpretation of modifiers.
7. Determine the location of the tolerance zone.
8. Determine the degree of freedom of the tolerance zone.
9. Analyse the interaction between tolerances.

In the future research the machining and measuring circumstances are investigated, in order to support the manufacturing process planning. The geometric tolerance based machine tool accuracy and the GPS based machinability of materials will be investigated and developed.

References. 1. ISO 1101-2017 Geometrical product specifications (GPS) - Geometrical tolerancing - Tolerances of form, orientation, location and run-out. **2.** *Sun W.; Gao Y.* (2022) The rule-based specification of the datum-based model for geometric dimensioning & tolerancing. Procedia CIRP 114:189–196 https://doi.org/10.1016/j.procir.2022.10.026 **3.** *Fengxia Z.* et. al (2015) Research on the intelligent annotation technology of geometrical tolerance based on geometrical product specification (GPS). Procedia CIRP 27: pp. 254 – 259 https://doi.org/10.1016/j.procir.2015.04.074 **4.** *Corrado A.; Polini W.* (2021) Model of geometrical deviations in milling with three error sources. Manufacturing Technology. 21(5): pp. 575–584. https://doi.org/10.21062/mft.2021.078 **5.** *Sultana J., Sztankovics I.* (2023) Roundness error and topography of hard turned surfaces. Cutting & Tools in Technological System 98: pp. 83–92 https://doi.org/10.20998/2078-7405.2023.98.08 **6.** *Gosavi A; Cudney E.* (2012) Form error in precision metrology: a survey of measurement techniques. Quality Engineering 24: pp. 369–380 https://doi.org/10.1080/08982112.2011.652583 **7.** *Li Y; Gu P.* (2004) Free-form surface

inspection techniques state of the art review. Computer-Aided Design 36: pp. 1395–1417 https://doi.org/10.1016/j.cad.2004.02.009 **8.** *Armillotta A.* (2013) A method for computer-aided specification of geometric tolerances. Computer-Aided Design 45: pp. 1604–1616 https://doi.org/10.1016/j.cad.2013.08.007

Балаш Міко, Будапешт, Угорщина

ІНТЕРПРЕТАЦІЯ РОБОЧОГО ПРОЦЕСУ ВИЗНАЧЕННЯ ГЕОМЕТРИЧНИХ ДОПУСКІВ

Анотація. *Застосування принципів геометричної специфікації продукту (ГСП) набуває все більшого значення в обробній промисловості. Процес визначення допуску повинен гармонізувати взаємозв'язок між допуском, процесом механічної обробки, вимірювальними та проектними вимогами. У разі інтерпретації інженерного креслення важливе значення має детальне розуміння відповідних стандартів. Метою дослідження є вивчення процесу визначення допуску, взаємозв'язку між допуском, процесом механічної обробки, вимірювальними та проектними вимогами. Метою статті є представлення процесу інтерпретації та запропонованого робочого процесу геометричних допусків. Деякі критичні проблеми демонструються на прикладах кейсів. Процес допуску повинен визначати тип і значення необхідних допусків. У цьому процесі необхідно враховувати кілька суперечливих аспектів. Першочерговим фактором є функція деталі, роль кожного геометричного елемента. Другим аспектом є врахування виробничих можливостей. Третій аспект - аналіз складальних взаємозв'язків і впливу поширення виробничого браку. Четвертим аспектом є розгляд можливостей вимірювання. Нарешті, ці вимоги повинні бути позначені на кресленні за допомогою інженерних символів, для чого необхідна чіткість і відповідність інженерним нормам. Таким чином, допуск деталі встановлює очікування щодо процесу виготовлення та вимірювання з урахуванням функціональних вимог і, таким чином, визначає вартість деталі. У цій роботі представлений дев'ятиетапний робочий процес, що забезпечує систематичну інтерпретацію кожного елемента інженерного креслення. Запропоновані дев'ять кроків: визначення ознаки допуску, типу допуску, форми зони допуску, розміру зони допуску, тлумачення модифікаторів, визначення місця розташування зони допуску, ступіня свободи зони допуску, аналіз взаємодії між допусками.*

Ключові слова: *геометричний допуск; ГСП;геометричні розміри та допуски; ступінь свободи; вихідна ознака.*

UDC 621.923: 661.65 **doi:10.20998/2078-7405.2024.100.01**

SPECIFIC ENERGY CAPACITY OF PROCESSING AND ENERGY EFFICIENCY FOR PROCESS OF GRINDING WITH WHEELS FROM SUPERHARD MATERIALS

Valerii **Lavrinenko**[1][0000-0003-2098-7992], Volodymyr **Solod**[2][0000-0002-7516-9535], Predrag **Dašić**[3][0000-0002-9242-274X],Yevgeniy **Ostroverkh**[4][0000-0002-8926-1324]

[1]V. Bakul Institute for Superhard Materials NAS Ukraine, Kyiv, Ukraine
[2]Dniprovsk State Technical University, Kamianske, Ukraine
[3]Engineering Academy of Serbia (IAS), Belgrade, Serbia
[4]National Technical University «Kharkiv Polytechnic Institute», Kharkiv, Ukraine
lavrinenko@ism.kiev.ua

Received: 15 February 2024 / Revised: 10 March 2024 / Accepted: 25 April 2024 / Published: 15 June 2024

Abstract. *The analysis of modern research shows that when evaluating the specific energy intensity of the abrasive processing process, one should pay attention not only to the indicators of grinding power and material removal rate, but also to the indicator of the wear of the abrasive tool, which we will show below for the grinding tool made of superhard materials. It is shown that the traditional method of estimating the specific energy capacity based on the ratio of the grinding power to the processing productivity does not provide an adequate solution, since with it the specific heat capacity of processing exceeds the specific heat capacity of melting of the processing material by almost an order of magnitude. Therefore, it is the application of a new approach to the assessment of the specific energy intensity of diamond grinding, taking into account the wear of the working layer of the diamond wheel, and makes it possible to estimate the indicators of the specific energy intensity of grinding and the energy efficiency coefficient. It has been proven that when estimating the specific energy capacity of grinding metal-ceramic composite materials consisting of a low-melting and refractory component, the latent heat capacity of melting of the low-melting component should be taken as the basis. It is shown that the plastic mode of grinding occurs precisely when the specific energy capacity of grinding, taking into account the wear of the wheel, becomes close to the specific heat capacity of melting of a brittle material.*

Keywords: *specific energy capacity of grinding; energy efficiency coefficient; grinding;abrasive tool; wheel of the superhard materials; wear, friction.*

1. INTRODUCTION

Relevant studies have shown that the energy consumed by the processing industry makes up to 37% of the total global energy consumption and produces up

to 21% of greenhouse gas emissions worldwide [1]. At the same time, 20% of energy is used to overcome friction, and 14% of energy loss is caused by wear and tear, including energy to manufacture new parts and idle equipment. In addition, taking into account the cost of maintenance work due to wear, the total cost of costs due to wear is 35% of the cost of overcoming friction [1]. That is, the field of industrial production requires more energy consumption due to the need to overcome friction and wear. In addition, researchers pay great attention to the issue of reducing the energy intensity of machining processes. This is due to the fact that, for example, in the manufacture of engineering products, the specific share of the cost of energy consumption only for processing is from 15 to 25% [2] and increases over time. Thus, the specific share of the energy component in the cost price of machine-building products used to not exceed 5–7%, and over the past decades it has increased to 18–25% [3] and has a tendency to further increase. And this tendency is largely connected with the fact that the achievement of the necessary accuracy of processing requires an increase in the specific energy of processing. Methods for modeling and optimization of parameters of the grinding process were used in works [4-5].

2. MODERN PUBLICATIONS ON ENERGY ISSUES DURING ABRASIVE PROCESSING

Examining the specific energy during material removal processes at the micro-scale offers a deeper comprehension of the energy transfer across various material removal regimes. Breaking down specific energy into sliding, plowing, and cutting components facilitates the examination of how grain properties, process parameters, and mechanical properties impact the energy transfer between different phases of material removal. An inclusive framework for specific energy consumption (SEC) in abrasive cut-off operations by integrating individual models of primary and secondary rubbing energies, specific plowing energy, and specific cutting energy was proposed [6]. The strong correlation observed between the formulated model and empirical data underscores the concept that specific energy consumption (SEC) exhibits asymptotic behavior relative to the material removal rate.

As it is presented in Fig. 1, with the increase in material removal rate, there is a corresponding decrease in specific energy consumption. Mirroring trends are observed in prior studies on grinding operations. The notion of ductility aids in comprehending the overall energy consumption of materials. In ductile materials, the malleability of the workpiece materials resulting from heat generation, along with their higher fracture toughness compared to brittle materials, escalates the

machining challenge, consequently demanding higher specific energy during metal cutting[6]. Hence, the specific energy consumption of ductile materials such as OFC-C10100 and Al-1100 is higherin comparison to other materials operating at the same material removal rate. During the grinding process of hard and less ductile materials, the rate of crack propagation while cutting with abrasive grits increases, thereby decreasing the energy needed to deform the material. Therefore, hard and less ductile materials such as SS201 and Al 7075 require relatively lower specific energy consumption. Among the materials, Inconel-718 exhibits higher specific energy consumption, due to its elevated hardness, increased strength, and greater resistance to cutting[6].

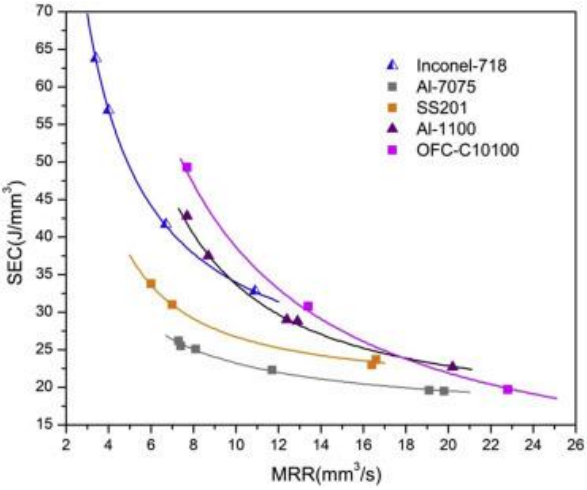

Fig.1. SEC relationship with material removal rate for materials [6].

The critical grinding depth of the ductile-brittle transition (DBT) is a crucial processing parameter that ensures machining of brittle materials in the ductile mode. However, predicting the critical grinding depth is challenging due to the multitude of grain interactions resulting from the random distribution of grains on the wheel. Innovative grinding force and energy model has been developed to anticipate the critical grinding depth, taking into account the random interactions among multiple grains [7]. In order to verify the model's accuracy, experimental validations have been performed on single crystal silicon. During this procedure, the interactions between the grains and the workpiece are examined through the

actual heights of grain protrusions and the random distribution of grains. Addressing this deficiency, paper [7] introduces an analytical model for grinding force and energy to forecast the critical depth of ductile-brittle transition in the grinding of brittle materials (Fig. 2). The surface generation mechanisms during the ductile-brittle transition are thoroughly explored through the utilization of both numerical simulations and experimental techniques. The results indicate that plastic plowing and brittle fracture are the predominant modes of material removal during the grinding of brittle materials. Furthermore, the experimental validation results suggest that the proposed model is able to accurately predict the actual critical grinding depth, with an average deviation of less than 9.2%. At the end, utilizing the proposed model, a thorough investigation is conducted into the impact of grinding conditions on the critical grinding depth. The critical grinding depth rises with higher grinding speed, whereas it decreases with increasing feed speed. Thus, this study not only offers a novel approach for forecasting the critical grinding depth but also advances the comprehension of the ductile-brittle transition mechanism in the machining of brittle materials[7].

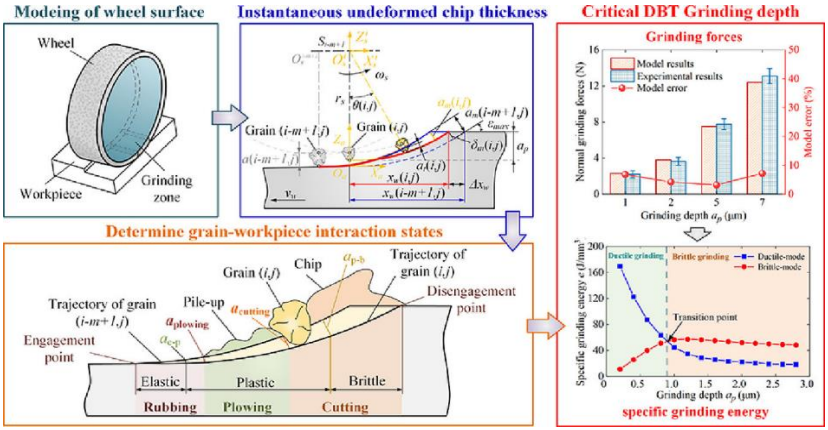

Fig. 2. An analytical grinding force and energy model for predicting the critical DBT depth in grinding of brittle material is proposed in paper [7].

Modeling and quantification of the abrasive processesis challenging task due to the stochastic nature of the abrasive-tool surface characteristics. On the other hand, their macroscopic geometry and motion patterns are typically clearly defined and easily regulated on machine tools. To address this apparent inconsistency, a new integrated modeling framework is established based on the

concept of aggressiveness [8]. It encompasses the diverse geometry and motion patterns of a workpiece in motion, relative to an abrasive surface. The point-aggressiveness, as a dimensionless scalar quantity derived from the vector field of relative velocity and the vector field of abrasive-surface normals, represents the key parameter. This fundamental process parameter directly influences common process outcomes such as specific energy, abrasive-tool wear, and surface roughness. The theory of aggressiveness is experimentally confirmed through its application to various abrasive processes, including grinding, diamond truing, and dressing. In these applications, the aggressiveness number is correlated with the aforementioned measured process outputs. The major issue in grinding crankshafts is to avoid thermal damage caused by grinding, particularly on the sidewalls of the crankpin [8]. The higher temperatures that caused thermal damage primarily rely on the specific energy of grinding, calculated as the ratio of grinding power and material removal rate, $e_G = P_G/Q_G$. As it is presented in Fig. 3b, it is obvious that the aggressiveness number comprehensively captures the geometry and motion characteristics of the process, as indicated by the coefficient of determination close to 1. On the other hand, creating a plot of specific energy versus commonly used process parameters that do not fully consider geometry and motion characteristics, such as grinding equivalent chip-thickness $h_{eq,G}$ (Fig. 3a), might result in misinterpretation of observed variations in measured results.

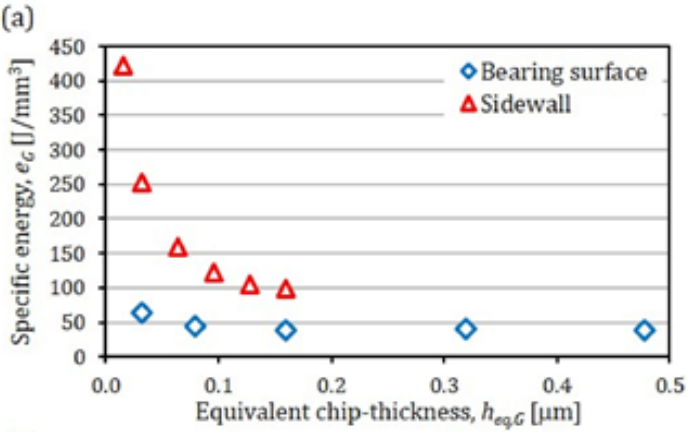

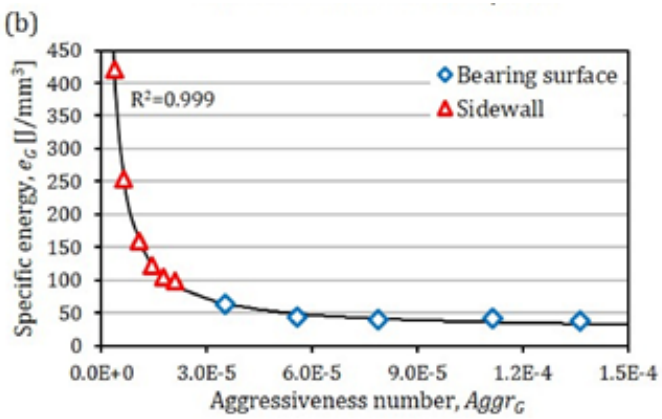

Fig. 3. Grinding specific-energy e_G (a) equivalent chip-thickness and (b) aggressiveness number [8].

3. FORMULATION OF THE PURPOSE OF THE RESEARCH

Summarizing the above short review, we pay attention to the following. The more plastic the processed material is, the greater is the specific energy of its grinding. The specific energy intensity of grinding is affected by the cutting conditions and the conditions for fixing the abrasive grains. With a small equivalent chip thickness and under the conditions of grinding the side surfaces, the specific grinding energy increases significantly due to the increase in the process of friction and wear of the wheel grains. And when grinding support surfaces, the thickness of the chips does not affect and the specific energy of grinding remains unchanged. As a result, it affects the depth of grinding of the ductile-brittle transition, which is an important processing parameter that guarantees the processing of brittle materials in the ductile regime. The above in the articles [1, 6–8] shows that when estimating the specific energy intensity of the abrasive processing process, in addition to the indicators of grinding power and material removal rate, attention should also be paid to the indicator of wear of the abrasive tool, which we will show below for the grinding tool from superhard materials (SHM), which was the purpose of this article.

4. PRESENTING MAIN MATERIAL

We will remind that the main direction of reducing energy costs for physical processes in the cutting zone is the optimization of processing modes according to criteria related to the level of specific energy consumption during cutting. These are [8–10]:

criterion of the minimum specific energy intensity of cutting

$$e = A_{ct}/V = N_{ef}/P_{ct} = N_{ef}/(v \cdot S \cdot t) \rightarrow min \quad (1)$$

where A_{ct} – cutting work; V – is the volume of the cut material layer; N_{ef} – effective cutting power; P_{ct} – cutting performance; v – cutting speed; S – feed; t – cutting depth,

and the criterion of maximum energy efficiency (CEE) of the cutting process

$$K_e = \Delta w \cdot V/N_{ef} = \Delta w/e \rightarrow max \quad (2)$$

where Δw is the specific energy density of the processed material.

In article [11], it was clarified that formula (2) includes the specific energy density of the processed material, which is interpreted as the specific heat of fusion, and the processes of blade processing are interpreted as plastic deformation, and the process of abrasive processing (grinding) – as a physical process of melting. That is, here we see a certain analogy of the specific energy capacity of abrasive processing, as the specific heat capacity of melting of the processed material.

Let's figure out what we know from the literature on abrasive processing processes from the point of view of the specific energy intensity of processing. For example, the authors [8–10] define the specific energy capacity as the ratio of the effective power of processing to its productivity, then $e=\Delta E=N/Q$ (dimension J/m^3). This is characteristic of both blade processing [9] and abrasive processing [8, 10]. As it was shown in the work [1], the calculations according to this formula and the data available in the literature for abrasive processing are included in the range of 20–200 kJ/cm^3. And actually we can see it from the data in Fig. 1 (ranges 20–65 J/mm^3 [4]), Fig. 2 (ranges 20–160 J/mm^3 [7]) and Fig. 3 (the range of 40–60 J/mm^3 for the support surface [8], we will consider the range for the side surface later). The author of the article [1] additionally applied his own data for calculations according to the above formula of the specific energy intensity of grinding (ΔE) of R6M5 steel. It is shown that when grinding R6M5 steel with productivity (Q) of 400 mm^3/min. the power indicator (N) was 0.4 kW, then ΔE = 60 kJ/cm^3, at Q = 1000 mm^3/min and N = 1.4 kW, ΔE = 84 kJ/cm^3, and at Q = 2000 mm^3/min and N = 2.0 kW, ΔE = 60 kJ/cm^3. That is, these data actually coincide with the range indicated above. However, the average specific energy intensity of steel grinding is about 60 kJ/cm^3, and the specific heat of fusion of steel is 0.64

kJ/cm^3. That is, there is a contradiction. At one time, attention was drawn to this in the work [1], where it was shown that the calculation of the specific energy intensity of grinding according to the traditional indicator in relation to the effective power of grinding to the productivity of processing does not completely correspond to reality, it is more energy-intensive than the process of diamond-abrasive processing and exceeds the heat capacity of melting of the processed material by 10 to 100 times. That is, the indicated contradiction is present, and it is especially relevant for the processes of grinding with SHM wheels, which are expensive and require an economically justified application, justified primarily by the reduction of energy costs during processing. In order to find ways to resolve the above-mentioned contradiction, in our opinion, it is more correct to estimate the specific energy consumption of diamond-abrasive processing with SHM wheels due to the additional consideration of the wear of the working layer of the wheel, as indicated in the article [8]. Let's pay attention to the significant increase in the specific grinding energy for processing the side surfaces with a grinding wheel, where the conditions for holding abrasive grains are worse and, as a result, the specific grinding energy increases sharply (see Fig. 3). The formula for determining the specific energy intensity of processing, for grinding processes with SHM wheels, taking into account the wear of the working layer of the SHM wheel, is substantiated in [1] and has the form:

$$e=E_{se}= 2{,}4\cdot 10^7\cdot N_{ef}\cdot q_p/(Q\cdot K\cdot \gamma_{shm}),\ kJ/kg, \quad (3)$$

where: N_{ef} – effective grinding power, kW; q_p – relative consumption of SHM grains in the wheel during grinding, mg/g; Q – grinding productivity, mm^3/min; K – is the relative concentration of SHM grains in the wheel, %; γ_{shm} – SHM grain density, g/cm^3.

Let's return to the energy efficiency indicated above. As we saw from the previous paragraph, for diamond-abrasive processing (grinding) processes, Δw from formula (2) can be interpreted as the specific heat capacity of melting of the processed material, as it occurs in a number of researchers. At the same time, some indicate that the specific energy capacity of the abrasive treatment process should be lower than the heat capacity of melting, others – what is higher, and those that correspond to it. Let's express it for equation (2) as follows: the energy efficiency for the first case must be $K_e > 1$, for the second – $K_e = 1$, and for the third case $K_e \geq 0.8$. That is, here we already get certain initial values of energy efficiency for abrasive processing, and as we can see, it should not be less than 0.8.

Since, as we have shown above, 100 times more heat is pumped into steel during grinding than is needed for its melting, the energy efficiency (CEE) according to formula (2) will be

$$K_e = \Delta w/\Delta E = 0{,}64/60 = 0.01067.$$

As we can see here, the energy efficiency CEE is significantly lower than even the expected minimum efficiency of 0.8 indicated above. That is, there is a contradiction both in the specific energy intensity of grinding and in terms of energy efficiency CEE. Now let's return to the energy efficiency indicated above according to formula (2). As we have seen from the above, for the processes of grinding wheels of superhard materials, Δw can be interpreted as the specific heat capacity of melting of the processed material. But the indicator – e, namely the specific energy intensity of processing, according to the proposed new approach, taking into account the wear of the working layer of the SHM wheel [1], has the form of formula (3) and then the energy efficiency CEE for grinding processes with SHM wheels will have the form:

$$K_e = \Delta w/e = \Delta w \cdot Q \cdot K \cdot \gamma_{shm}/(2{,}4 \cdot 10^7 \cdot N_{ef} \cdot q_p), \quad (4)$$

where: $\Delta w$is the specific heat of melting of the processed material, *kJ/kg*; Q – grinding productivity, mm^3/min; K is the relative concentration of SHM grains in the wheel, %; γ_{shm} – SHM grain density, g/cm^3; N_{ef} – effective grinding power, *kW*; q_p – relative consumption of SHM grains in the wheel during grinding, *mg/g*.

In order to more clearly evaluate the above, let's try, as an example, to first evaluate the temperature level in the surface layer of high-speed cutting steel R6M5 during grinding with cubic boron nitride (cBN) wheels without cooling, when this level will be the highest. And in the future, compare these data with the specific energy capacity of grinding according to formula (3) and the values of energy efficiency according to formula (4) for the process of grinding R6M5 steel with cBN wheels on different connections. Samples of plates made of R6M5 steel measuring 5x30x60 *mm* were ground on a mod universal sharpening machine 3V642 wheels 12A2-45° 125x5x3x32 with different characteristics of their working layer. Grinding modes: wheel speed – 25 *m/s*, longitudinal feed – 2.4 *m/min*, transverse feed – 0.05 *mm/f*. The grinding productivity was 600 mm^3/min. It was found that the highest temperature level in the grinding zone (T_{gr}) is observed in wheels on the metal-polymer bond – V1-13, slightly lower in the ceramic bond K17, noticeably lower in the polymer bond V2-08, and the lowest in the polymer – ceramic connection – PK-03. For comparison, we found the temperature level on the direct surface of the plates when cutting thermocouples during the use of an abrasive wheel made of white electro corundum with the characteristics of an abrasive layer 25A25SM1K8. The temperature in the processing zone here was 750 °C. That is, all the above wheels from cBN are here with a grinding performance of 600 mm^3/min. Do not exceed the ignition temperature of high-speed steel R6M5

(620 °C), in contrast to a wheel made of electro corundum, where such ignition is observed on the treated surface of the steel. This is described in more detail in the article [11].

Now let's return to the issue of energy consumption of grinding and energy efficiency for the above conditions of grinding R6M5 steel with cBN wheels. The calculation of the specific energy capacity according to formulas (2) and (3) is given in the Table 1. Analysis of table data shows the following. The value of the specific energy capacity of grinding according to the traditional indicator, calculated according to the ratio (2), is from 21 to 30 kJ/cm^3, and the value of the specific heat capacity of melting of R6M5 steel is – 0.68 kJ/cm^3, that is, here too we see that as the specific heat of fusion of P6M5 steel is exceeded by at least 30 times during grinding. And in the case when we apply a new approach to the calculation of the value of the specific energy capacity according to formula (3), then here we already see more conscious values. For a wheel with a PK-03 connection, the specific energy capacity of grinding is 72.6% of the specific heat capacity of melting of R6M5 steel, for wheels with connections V2-08 and K17 it actually corresponds to it, and for a wheel with a connection V1-13 already the specific energy capacity of grinding exceeds the specific heat capacity of melting of R6M5 steel by 14.3%. That is, it is the new approach to calculating the specific energy intensity of grinding wheels with SHM that allows it to be adequately evaluated.

Table 1 – Calculation of the specific energy capacity and energy efficiency for the process of grinding R6M5 steel without cooling with different wheels from cBN (source data from work [11]) with productivity Q=600 mm^3/min. (T_{gr} is the temperature value in the grinding zone).

Characteristics of the working layer of the wheel	Effective grinding power, *kW*	T_{gr}, °C	Relative consumption of CBN in the wheel during grinding, *mg/g*	Specific energy capacity of grinding		K_e
				according to relation (2), kJ/cm^3	according to formula (3), *kJ/kg*	
KP 100/80 PK-03 100	0,29	510	1,84	29	61	1,377
KP 80/63 V2-08 100	0,21	525	3,48	21	83	1,012
KP 100/80 K17 100	0,25	605	2,89	25	83	1,012
KP 80/63 V1-13 100	0,30	610	2,80	30	96	0,875

As evidenced by the analysis of the Table. 1 shows a certain correspondence between the temperature in the grinding zone and the indicators of specific energy capacity and energy efficiency. The higher the temperature in the grinding zone, the higher the specific energy capacity and the lower the energy efficiency. At the same time, as we drew attention to in the article [12], when the specific energy capacity of grinding becomes close to the specific heat capacity of melting of a brittle material, a plastic mode of processing occurs. The concept of plasticity, presented in the article [6], helps to understand the total energy costs for processing materials. It is shown that the specific energy consumption during the processing of plastic materials is higher in comparison with other materials at the same rate of material removal. When grinding hard and less plastic materials, the rate of crack growth when cutting with abrasive grains is higher, which reduces energy consumption for material deformation [6]. For this reason, hard and less plastic materials require less specific energy during processing. At the same time, the article [7] proposed an analytical model of grinding force and energy for predicting the critical depth of DBT when grinding brittle material.

Recall that the above referred to more or less homogeneous instrumental materials. And what if our composite tool material consists of components that are quite heterogeneous in terms of thermophysical characteristics, for example, metal-ceramic hard alloys, where there is a relatively low-melting component (cobalt or nickel as a binder) and a refractory component (tungsten or titanium carbides). Accordingly, such components differ significantly among themselves in terms of specific heat of fusion 263 *kJ/kg* (2.31 *kJ/cm*^{3}) for cobalt and 273 *kJ/kg* for nickel (2.43 *kJ/cm*^{3}) and for 1100 *kJ/kg* (4.62 *J/cm*^{3}) for TiC and WC. In order to find out how to estimate the specific energy intensity of grinding such composite materials, we analyzed the data for calculating such energy intensity for hard alloys VK8 and T15K6 (binder - cobalt), as well as tungsten-free hard alloy (TFHA) TN50 (binder - nickel) with the involvement of initial data from work [12] (Table 2).

Table 2 – Calculation of the specific energy capacity for the process of diamond grinding of various tool materials (source data from the work [10]) with a wheel AS6 100/80 V11-2 100 with productivity Q = 525 *mm*^{3}*/min.*

Instrumental material	Effective grinding power, *kW*	Relative consumption of diamond in the wheel during grinding, *mg/g*	Specific energy capacity of grinding	
			according to relation (2), *kJ/cm*^{3}	according to relation (2), *kJ/cm*^{3}
Hard allow – VK8	0,90	0,7	103	82

Hard allow – T15K6	0,70	0,8	80	73
TFHA – TN50	0,70	2,2	80	201

Analysis of data Table 2 shows the following. When calculating the specific energy intensity of grinding according to the ratio (2), the obtained data fall into the already known range of 20–200 *kJ/cm*^{3}. And this means that, for example, in all the given tool materials, the specific energy intensity of grinding exceeds the specific heat of fusion of even their refractory component by 17 to 22 times. But let's pay attention to the fact that VK6, T15K6 and TN50 hard alloys contain a more easily melting binder: VK6 and T15K6 have cobalt, and TN50 have nickel. They are usually the first to be exposed to heat. And this means that calculations of the specific energy intensity of grinding according to the ratio (2) exceed the specific heat of fusion for cobalt by 35–45 times, and for nickel by 33 times. That is, such calculations do not provide an adequate estimate of the specific energy intensity of grinding. Now consider the calculations according to formula (3). As we can see (see Table 2), here the specific energy intensity of grinding does not even reach the specific heat capacity of melting of the binding hard alloy. But on the most difficult-to-process tungsten-free hard alloy TN50, the specific energy capacity of grinding is already approaching the specific heat capacity of melting nickel. The above allowed us to make an assumption that when estimating the specific energy intensity of grinding metal-ceramic composite materials consisting of a low-melting and refractory component (hard alloys), the latent heat capacity of melting of the weakest link, namely the low-melting component, should be taken as a basis.

Now let's consider instrumental mineral ceramics. There are no data on the specific melting energy here either, but there are data on its components: for Al_2O_3 it is 1108 *kJ/kg* [12], and for TiC – 1094 *kJ/kg* [12], i.e., for ceramics it will be Σ 1100 *kJ/kg*. This gives us the opportunity to estimate the specific energy intensity when grinding oxide-carbide ceramics (Table 3). We would like to point out that the calculation of the specific energy intensity of grinding VOK60 ceramics according to the above traditional ratio (2) was 35–45 *kJ/cm*^{3}. That is, it corresponds to the above range. Something else is interesting here. As we have already indicated above, the real specific heat capacity of steel melting is actually 2 orders of magnitude lower than the specific energy capacity of grinding, calculated according to the above-mentioned traditional indicator Δ*E*. And what do we have for oxide-carbide ceramics. The specific heat capacity of its melting is ~1100 *kJ/kg*, i.e., if recalculated, then Σ4.62 *kJ/cm*^{3}. And this means that if the

calculations are carried out according to the traditional indicator ΔE, then for ceramics, as well as for steel, this indicator again significantly exceeds the specific heat of fusion, except that here it is not by 2 orders of magnitude, but only by an order of magnitude. And what really? Let's evaluate this, again, with the involvement of data from work [12] when grinding VOK60 ceramics with different diamond wheels (Table 3). It can be seen that relative to the specific energy of ceramic melting, the specific energy of its diamond grinding according to formula (3) is almost an order of magnitude lower.

Table 3 – Calculation of the specific energy capacity according to formula (2) of the process of grinding VOK60 ceramics with diamond wheels

Characteristics of the working layer of the wheel	Q, mm^3/min	N_{ef}, kW	q_p, mg/g	E_{se}, kJ/kg
AS6 100/80 MO20-2 100	800	0,66	0,53	30,0
AS4 100/80MA V1-13 100	1050	0,65	1,30	55,2

In addition, let's pay attention to the influence of the speed of rotation of the wheel. Consider this when grinding Si_3N_4+B_4C ceramics, which can be used in plates for processing with impact loads and ceramic balls, and is a rather difficult-to-process ceramic (Table 4). As can be seen from the data in the Table 4, reducing the cutting speed also from 30 to 15 *m/s* immediately transfers processing to the mode of increased specific energy capacity, which actually approaches the specific heat capacity of melting, that is, to the plastic mode of grinding.

Table 4 – Grinding indicators of Si_3N_4+B_4C ceramic plates with a productivity of 1000 mm^3/min with diamond wheels 12A2-45° 150x10x3x32 AS4 160/125 V1-13 100

Speed of wheel rotation, *m/s*	q_p, mg/g	N_{ef}, kW	E_{se}, kJ/kg	R_a, μm
30	2,8	0,95	182	0,28
15	14	1,0	960	0,45

5. CONCLUSIONS

1. The analysis of modern research shows that when assessing the specific energy intensity of the abrasive processing process, attention should be paid not only to the indicators of grinding power and material removal rate, but also to the indicator of wear of the abrasive tool.

2. It is shown that the traditional method of estimating specific energy capacity based on the ratio of grinding power to processing productivity does not

provide an adequate solution, since with it the specific heat capacity of processing exceeds the specific heat capacity of melting of processed materials by almost an order of magnitude, and therefore, any diamond processing of ceramics must immediately fall into the plasticity mode, which is not really the case. Therefore, it is the application of a new approach to estimating the specific energy intensity of diamond grinding, taking into account the wear of the working layer of the diamond wheel, and makes it possible to assess the possibility of adequately evaluating the specific energy intensity of grinding and the energy efficiency coefficient.

3. When estimating the specific energy capacity of grinding metal-ceramic composite materials consisting of a low-melting and refractory component (hard alloys), the latent heat capacity of melting of the low-melting component should be taken as a basis.

4. It is shown that the plastic regime occurs precisely when the specific energy capacity of grinding, taking into account the wear of the wheel, becomes close to the specific heat capacity of melting of the processing material.

References: 1. *Jianbiao Du, Hanzhong Liu, Ning Yang, Xiaozhou Chen, Wenjun Zong*. Modification of diamond tool by focused ion beam in dry single-point diamond turning. Applied Surface Science. Volume 637,15 November 2023, 157882. https://doi.org/10.1016/j.apsusc.2023.157882**. 2.** *Myronenko, E.V., Klymenko, H.P., Kalynychenko, V.V.* Obshaja struktura matematicheskoj modeli dlja opredelenia energoefektivnich tehnologicheskih parametrov tokarnoi obrabotki detalei tjazhelogo mashinistroenia. Cutting&Tools in Technological System, 2015, Edition 85. pp. 202–210. **3.** *Lavrinenko,V.I.* To the analysis of the estimate of energy expenditures in the diamond abrasive treatment by wheels from superhard materials. Journal of Superhard Materials, 2022, Vol. 44, No. 4, pp. 285–291. https://doi.org/10.3103/S1063457622040050. **4.** *Usov, A., Tonkonogyi, V., Dašić, P., Rybak, O.* Modelling of temperature field and stress-strain state of the workpiece with plasma coatings during surface grinding. Machines, 2019, Vol. 7, No. 1, Article no. 20. https://doi.org/10.3390/machines7010020. **5.** *Tonkonogyi, V., Dašić, P., Rybak, O., Lysenko, T.* Application of the modified genetic algorithm for optimization of plasma coatings grinding process. Lecture Notes in Networks and Systems (LNNS), 2020, Vol. 76, pp. 199–211. https://doi.org/10.1007/978-3-030-18072-0_23. **6.** *Muhammad RizwanAwan, Hernán A.González Rojas, José I. Perat Benavides. Saqib Hameed, Abrar Hussai, Antonio J. Sánchez Egea*. Specific energy modeling of abrasive cut off operation based on sliding, plowing, and cutting. Journal of Materials Research and Technology. Vol. 18, May–June 2022, pp. 3302-3310. https://doi.org/10.1016/j.jmrt.2022.03.185. **7.** *Zhengding Zheng, Kai Huang, Chuangting Lin, Jianguo Zhang, Ke Wang, Peng Sun, Jianfeng Xu*. Ananalytical force and energy model for ductile-brittle transition in ultra-precision grinding of brittle materials. International Journal of Mechanical Sciences. Vol. 220, 15 April 2022, Article no. 107107. https://doi.org/10.1016/j.ijmecsci.2022.107107. **8.** *Radovan Dražumerič, Jeffrey Badger, Roope Roininen, Peter Krajnik*. On geometry and kinematics of abrasive processes: The theory of aggressiveness. International Journal of Machine Tools and Manufacture. Volume 154, July 2020, Article no. 103567. https://doi.org/10.1016/j.ijmachtools.2020.103567. **9.** *Kalilichenko, V.* Kompeksnij pidhid do znizenniaenergovutrat pru tokarnij obrobci na vazkih verstatah. Materials and Technologies in

Engineering (MTE-2023): Engineering, Materials, Technologies, Transport: Collection of Scientific Reports of the International Conference, Lutsk, Ukraine, May 16-18, 2023 / Compilers: *Oleksandr Povstyanoy, Olha Zaleta, Bohdan* Valetskyi. – Lutsk : Vezha-Druk , 2023. pp. 133–135. **10.** *O.Yermolenko, F.Novikov, A.Yakimov, Y.Babych, A.Toropenko*. Study of the Scaling Effect of Cutting Elements of the Abrasive Wheels' Discretized Working Surface on Geometric and Physical-Mechanical Parameters of the Surface Layer Quality of Ground Parts. In: Tonkonogyi, V., Ivanov, V., Trojanowska, J., Oborskyi, G., Pavlenko, I. (eds) Advanced Manufacturing Processes V. Selected Papers from the 5th Grabchenko's. International Conference on Advanced. Manufacturing Processes (InterPartner-2023), September 5–8, 2023, Odessa, Ukraine. Cham. 409-418. https://doi.org/10.1007/978-3-031-42778-7_38. **11.** *Lavrinenko, V.I.* Krugu z KNB dlja shlifuvannia shvidkorizalnoi stali bez oholodzennia: putoma energoemnist ta energetuchnij koeficient korusnoi dii. Superhardmaterials. 2024. № 2. pp. 89–97. **12.** *Lavrinenko, V.I., Solod, V.Yu., Muzychka, D.H., Ostroverkh Ye.V.* Perehid vid plastuchnogo rezimyalmaznogo slifyvannia keramiku do plavlennia ta osobluvostii plavleniia instrumentalnih keramik. Collection of scholarly papers of Dniprovsky State Technical University (Technical Sciences). № 1 (42) 2023. pp. 48–58. https://doi.org/10.31319/2519-2884.42.2023.6.

Валерій Лавріненко, Київ, Україна, Володимир Солод, Кам'янське, Україна, Предраг Дашич, Белград, Сербія, Євгеній Островерх, Харків, Україна

ПИТОМА ЕНЕРГОЄМНІСТЬ ОБРОБКИ ТА ЕНЕРГЕТИЧНИЙ КОЕФІЦІЄНТ КОРИСНОЇ ДІЇ СТОСОВНО ПРОЦЕСІВ ШЛІФУВАННЯ КРУГАМИ З НАДТВЕРДИХ МАТЕРІАЛІВ

Анотація. *Аналіз сучасних досліджень свідчить про те, що чим більш пластичним є оброблюваний матеріал, тим більшою є питома енергія його шліфування. На питому енергоємність шліфування також впливають умови різання і умови закріплення абразивних зерен. Сучасні дослідження свідчать і про те, що при оцінці питомої енергоємності процесу абразивної обробки кругами з надтвердих матеріалів слід звертати увагу крім показників ефективної потужності шліфування і швидкості зйому матеріалу, також і на показник зносу абразивного інструменту, що нами далі і буде показано для шліфувального інструменту з надтвердих матеріалів (алмазів та кубічного нітриду бору). Доведено, що традиційний метод оцінки питомої енергоємності за відношенням потужності шліфування до продуктивності обробки не дає адекватного рішення, оскільки при ньому питома теплоємність оброблення майже на порядок перевищує питому теплоємність плавлення обробного матеріалу. Тому, саме застосування нового підходу до оцінки питомої енергоємності алмазного шліфування з урахуванням зношування робочого шару алмазного кругу, і дає можливість оцінити показники питомої енергоємності шліфування та енергетичний коефіцієнт корисної дії. Доведено, що при оцінці питомої енергоємності шліфування мінерало- та металокерамічних композитних матеріалів (оксидно-карбідних керамік та твердих сплавів), що складаються з низькоплавкої та тугоплавкової складової, за основу потрібно приймати приховану теплоємність плавлення саме низькоплавкої складової. Показано, що пластичний режим шліфування виникає саме тоді, коли питома енергоємність шліфування з урахуванням зносу кругу стає близькою до питомої теплоємності плавлення низькоплавкої складової крихкого матеріалу.*

Ключові слова: *питома енергоємність шліфування; енергетичний коефіцієнт корисної дії; шліфування; абразивний інструмент; круги з надтвердих матеріалів; знос; тертя*.

UDC 621.914.22 **doi: 10.20998/2078-7405.2024.100.07**

INFLUENCE OF FEED RATE ON THE DYNAMIC PROPERTIES OF THIN-WALLED PART DURING END-MILLING

Sergei **Dyadya** [0000-0002-7457-7772], Olena **Kozlova** [0000-0002-3478-5913], Eduard **Brukhno** [0000-0001-5526-073X], Denys **Yakhno** [0009-0009-2816-9397], Daria **Karamushka** [0009-0007-3114-0996]

National University «Zaporizhzhya Polytechnic», Zaporizhzhya, Ukraine
kozlova@zntu.edu.ua

Received: 11 April 2024 / Revised: 23 April 2024 / Accepted: 20 May 2024 / Published: 15 June 2024

Abstract. *When selecting cutting modes for end-milling of thin-walled parts from hard-to-machine materials, their influence on machining stability must be considered. To do this, it is necessary to understand the types of vibrations that operate and the conditions under which they arise. Research has shown that different types of vibrations operate sequentially during cutting and only for a certain of time. During end-milling, forced and accompanying free oscillations operates due to the short duration of cutting. Their influence on the stability of the cutting process depends on the speed zone in which the milling takes place. The most unfavorable is the third speed zone of vibrations, where accompanying free vibrations of high intensity occur. Cutting speeds for machining parts from hard-to-machine materials fall precisely within this zone. The intensity of vibrations is influenced by the dynamic properties of the part. During end-milling of thin-walled parts, these properties are characterized by the amplitude and frequency of accompanying free vibrations, which exceed the natural frequency of the part's free vibrations. In other words, cutting modes alter the dynamic properties of the part. Some researchers focus on utilizing the damping properties of the feed. Therefore, the aim of this paper was to determine how the feed affects the dynamic properties of the part during cutting. A universal stand was used for the investigation, which allows for the creation of various dynamic characteristics of the processed sample and recording its motion laws during milling on an oscillogram. The research results showed that the feed, as an element of cutting modes, influences the dynamic properties of the part during cutting. It creates a variable layer that is being cut. Therefore, during the cutting time, the frequency and amplitude of accompanying free vibrations change during both up- and down milling. The feed affects the dynamic stiffness. Increasing the feed increases the dynamic stiffness of the part. This leads to a reduction in the amplitude of accompanying free vibrations during milling in the third speed zone of vibrations. The results presented in the article have practical significance for technologists in the aviation manufacturing industry. They help to better understand the physical processes occurring during milling and develop optimal processing strategies for thin-walled parts, which have high requirements for dimensional accuracy and surface quality.*

Keywords: *milling; milling cutter; thin-walled part; feed rate per tooth; oscillogram; accompanying free oscillations.*

1. INTRODUCTION

Thin-walled components, widely used in the construction of aviation products, attract special attention from technologists due to the close relationship between cutting conditions and high-intensity vibrations that occur during machining and affect its productivity, tool stability, dimensional accuracy, and surface quality [1].

To establish favorable cutting conditions, petal diagrams of stability [2–4] are utilized. Additionally, the distribution of vibrations across zones, depending on the ratio between the natural frequency of the component's vibrations and the frequency of forced vibrations [5, 6], allows for the analysis of milling conditions prior to processing, and also evaluate surface roughness [7, 8].

In some cases, the obtained results do not match expectations due to uncertainties regarding vibrations embedded in the calculations [9–13]. This is due to the fact that the pattern of oscillations and their dependence on cutting time is not taken into account. Studies [14] have shown that the following sequence of oscillations is observed during cutting. When the tool is plunged, forced vibrations appear. The accompanying free oscillations (AFO) are superimposed on them [14], which persist for several milliseconds before damping out. Then the system adjusts and steady-state self-oscillations occur. This oscillation sequence occurs during turning or face milling when the cutting time is long. However, during end milling of thin-walled components, the intermittent nature of cutting results in cutting times measured in a few milliseconds. This affects the fact that only forced oscillations are effective, which are imposed by the AFO. It is their intensity that most significantly influences the formation of the machined surface. It is worth noting that the distribution of vibrations during end milling into speed zones [15] allows determining, based on initial data during technological preparation, under what conditions machining will occur. Among the five speed zones, the third speed zone of vibrations is the most unfavorable for stable milling. It is the only one with high intensity AFO, while they are absent in other zones. However, it is precisely the third speed zone of vibrations that corresponds to milling of parts from hard-to-machine materials. Therefore, the search for an answer to the question of what influences the properties of the part during cutting is relevant, as the intensity of vibrations depends on them. It is known that the period of AFO during cutting is different from the period of free vibrations during idle motion [16]. It decreases. Thus, by connecting the part to the tool through cutting conditions, it is possible to influence its new properties through chip formation. Researchers focus on utilizing the damping properties of the feed [17]. Therefore, the task of determining how exactly the feed rate affects this becomes relevant.

2. EXPERIMENTS AND DISCUSSION OF RESULTS

For the investigation, a universal stand was utilized [15], which allows for the creation of various dynamic characteristics of the workpiece and recording the laws of its motion during milling on an oscillogram.

The investigation of the feed rate's influence on the dynamic characteristics of the workpiece was conducted during up and down-milling in the third speed zone

with conditions that lead to the occurrence of high-intensity AFO. The initial data for the study are provided in Table 1.

Table 1- The initial data for conducting the research

The material of the workpiece being machined	Steel 3
The material of the milling cutter's cutting edge	Hard alloy
The stiffness of the elastic element of the part, j_{ee}, N/m	1746562
Free oscillation frequency of the elastic element of the part, f_{foee}, Hz	512
The stiffness of the milling cutter, f_{mc}, N/m	23986111
Free oscillation frequency of the milling cutter, f_{fomc}, Hz	1776
The diameter of the milling cutter, d_{mc}, mm	30
The number of teeth of the milling cutter, z	1
The helix angle of the milling cutter's tooth, ω, deg	0
Feed rate, S_z, mm/tooth	0.05; 0.1; 0.2; 0.3
The spindle rotation speed, n, rpm	355
The radial depth of cut, a_o, mm	0.3
The axial depth of cut, a_p, mm	4

The analysis of the workpiece motion during milling was conducted using fragments of oscillograms during cutting [15]. Based on these, dynamic characteristics such as the period T_{afo} and amplitude R_2 of accompanying free oscillation were determined. These were measured after straightening the oscillogram fragment using a Savitzky-Golay filter, as well as the maximum static deflection (Δ_{max}).

Figures 1-4 depict fragments of oscillograms during up and down-milling with various feed rates and checked parameters.

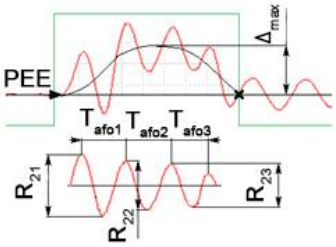

Up-milling

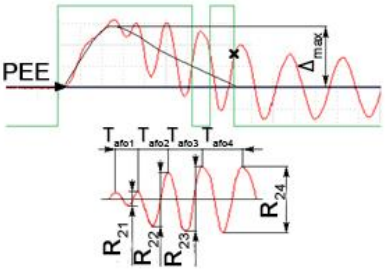

Down-milling

PEE - position of elastic equilibrium; ► - tool entry point into the part; × - tool exit point from the part

Figure 1 - Fragments of the oscillogram of part vibrations during milling with a feed rate of S_z = 0.05 mm/tooth

Based on the measurement results of the part's vibration parameters during cutting, Tables 2-5 were constructed.

Table 2 - The parameters of the part's vibrations during milling with a feed rate of S_z = 0.05 mm/tooth

The parameters	The feed direction	
	Up-milling	Down-milling
T_{afo1}, 10^{-3} s	1.64	0.84
T_{afo2}, 10^{-3} s	1.76	1.12
T_{afo3}, 10^{-3} s	1.44	1.28
T_{afo4}, 10^{-3} s	-	1.48
f_{afo1}, Hz	609	1190
f_{afo2}, Hz	568	892
f_{afo3}, Hz	694	781
f_{afo4}, Hz	-	675
R_{21}, mm	0.086	0.019
R_{22}, mm	0.069	0.076
R_{23}, mm	0.061	0.092
R_{24}, mm	-	0.093
Δ_{max}, мм	0.065	0.094

The data in Table 2 indicate that the dynamic properties of the part during cutting are different from its properties before cutting. Moreover, they change throughout the cutting process with varying depth of cut. During up-milling, after plunging, the frequency of AFO is 16% higher than the natural frequency of the part. As the thickness of the layer to be cut increases, the AFO frequency increases by another 12% by the end of the cut. In down-milling, after after plunging with the maximum depth of cut, the frequency of AFO exceeds the natural frequency of the part by 57%. However, with the minimum depth of cut towards the end of cutting, the frequency of AFO decreases by 43%. Due to the differences in cutting in the shaping zone of the machined surface (at the beginning of cutting for up-milling and at the end of cutting for down-milling), the frequency of AFO during down-milling is 10% higher than during up-milling.

The amplitude of AFO decreases by 29% from the beginning to the end of cutting during up-milling, while during down-milling, it increases by 79% due to negative attenuation [18].

The maximum deflection of the part, which characterizes the action of the radial component of the cutting force, is 30% less during up-milling than during down-milling.

A characteristic feature of the feed rate's influence on the dynamic properties of the part during cutting is the dynamic stiffness index k_{dyn}, which indicates how much the dynamic stiffness differs from the static stiffness and is determined by the formula:

$$k_{dyn} = \frac{2\Delta_{max}}{R_2}.$$

During up-milling: k_{dyn} = 1.51.
During down-milling: k_{dyn} = 2.02.

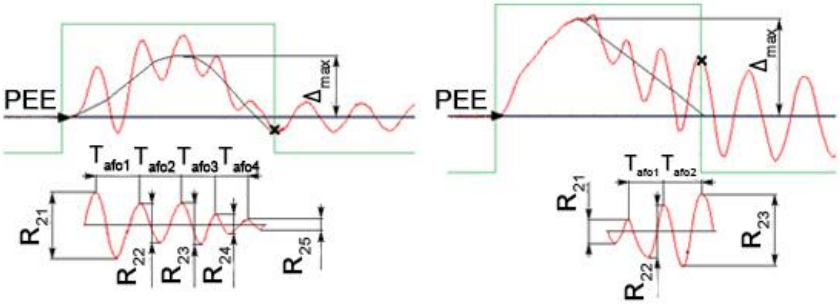

Up-milling Down-milling

Figure 2 - Fragments of the oscillogram of part vibrations during milling with a feed rate of S_z = 0.1 mm/tooth

Table 3 - The parameters of the part's vibrations during milling with a feed rate of S_z = 0.1 mm/tooth

The parameters	The feed direction	
	Up-milling	Down-milling
T_{afo1}, 10^{-3}, s	1.72	1.24
T_{afo2}, 10^{-3}, s	1.52	1.44
T_{afo3}, 10^{-3}, s	1.24	-
T_{afo4}, 10^{-3}, s	1.24	-
f_{afo1}, Hz	581	806
f_{afo2}, Hz	657	694
f_{afo3}, Hz	806	-
f_{afo4}, Hz	806	-

R_{21}, mm	0.088	0.032
R_{22}, mm	0.049	0.071
R_{23}, mm	0.054	0.099
R_{24}, mm	0.026	-
R_{25}, mm	0.012	-
Δ_{max}, мм	0.076	0.133

When up-milling with a feed rate of S_z = 0.1 mm/tooth, the frequency of AFO after plunging is 12% higher than the natural frequency of the part. By the end of cutting, it further increases by 28%. During down-milling with the same feed rate, the frequency of AFO after plunging is 36% higher than the natural frequency of the part. However, it decreases by 14% by the end of cutting. Moreover, the frequency of AFO in the shaping zone of the machined surface is 16% higher during down-milling than during up-milling.

The amplitude of AFO decreases by 86% from the beginning to the end of cutting during up-milling, while during down-milling, it increases by 68%.

The maximum deflection of the part during up-milling is 42% less than during down-milling.

The dynamic stiffness index during up-milling is k_{dyn} =1.73, while during down-milling, it is k_{dyn} = 2.69.

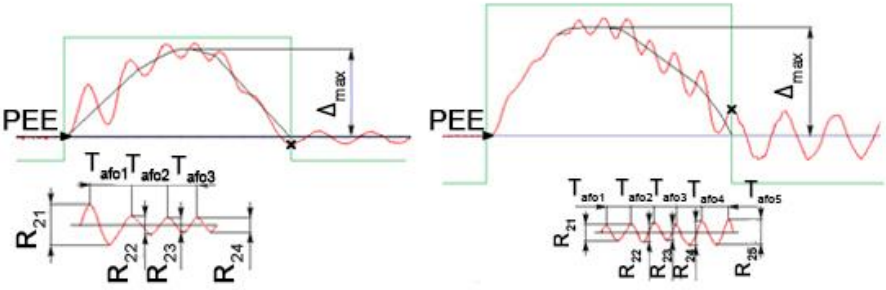

Up-milling Down-milling

Figure 3 - Fragments of the oscillogram of part vibrations during milling with a feed rate of S_z = 0.2 mm/tooth

When up-milling with a feed rate of S_z = 0.2 mm/tooth, the frequency of AFO after plunging is 20% higher than the natural frequency of the part. By the end of cutting, it further increases by 28%. During down-milling, the frequency of AFO after plunging is 55% higher than the natural frequency of the part. However, it decreases by 27% by the end of cutting. Moreover, the frequency of AFO in the

formation zone of the machined surface is 23% higher during down-milling than during up-milling.

The amplitude of AFO decreases by 75% from the beginning to the end of cutting during up-milling, while during down-milling, it increases by 37%. It is worth noting that vibrations during cutting with an amplitude ($R_2/2$) up to 0.02 mm can be favorable for chip formation [19]. Such values were obtained during down-milling with a feed rate of S_z = 0.2 mm/tooth.

The maximum deflection of the part during up-milling is 20% less than during down-milling.

The dynamic stiffness index during up-milling is k_{dyn} = 4.35, while during down-milling, it is k_{dyn} = 8.91.

Table 4 - The parameters of the part's vibrations during milling with a feed rate of S_z = 0.2 mm/tooth

The parameters	The feed direction	
	Up-milling	Down-milling
T_{afo1}, 10^{-3}, s	1.56	0.88
T_{afo2}, 10^{-3}, s	1.40	0.88
T_{afo3}, 10^{-3}, s	1.12	0.96
T_{afo4}, 10^{-3}, s	-	1.04
T_{afo5}, 10^{-3}, s	-	1,2
f_{afo1}, Hz	641	1136
f_{afo2}, Hz	714	1136
f_{afo3}, Hz	892	1041
f_{afo4}, Hz	-	961
f_{afo5}, Hz	-	833
R_{21}, mm	0.057	0.022
R_{22}, mm	0.023	0.027
R_{23}, mm	0.020	0.020
R_{24}, mm	0.014	0.027
R_{25}, mm	-	0.035
Δ_{max}, мм	0.124	0.156

When up-milling with a feed rate of S_z = 0.2 mm/tooth, the frequency of AFO after plunging is 20% higher than the natural frequency of the part. By the end of cutting, it further increases by 28%. During down-milling, the frequency of AFO after plunging is 55% higher than the natural frequency of the part. However, it decreases by 27% by the end of cutting. Moreover, the frequency of AFO in the formation zone of the machined surface is 23% higher during down-milling than during up-milling.

The amplitude of AFO decreases by 75% from the beginning to the end of cutting during up-milling, while during down-milling, it increases by 37%. It is worth noting that vibrations during cutting with an amplitude (R_2/2) up to 0.02 mm can be favorable for chip formation [19]. Such values were obtained during down-milling with a feed rate of S_z = 0.2 mm/tooth.

The maximum deflection of the part during up-milling is 20% less than during down-milling.

The dynamic stiffness index during up-milling is k_{dyn} = 4.35, while during down-milling, it is k_{dyn} = 8.91.

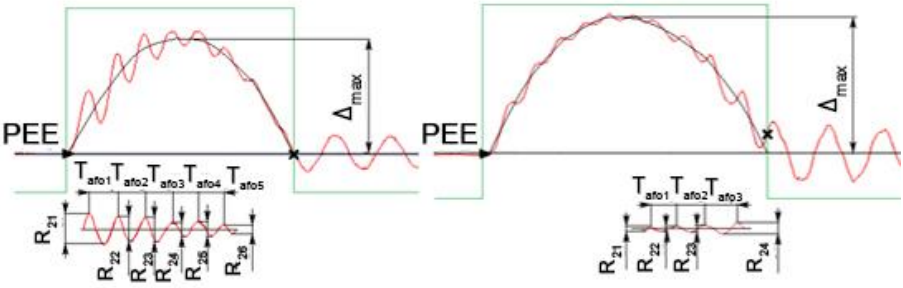

Up-milling Down-milling

Figure 4 - Fragments of the oscillogram of part vibrations during milling with a feed rate of S_z = 0.3 mm/tooth

Table 5 - The parameters of the part's vibrations during milling with a feed rate of S_z = 0.3 mm/tooth

The parameters	The feed direction	
	Up-milling	Down-milling
T_{afo1}, 10^{-3}, s	1.04	0.88
T_{afo2}, 10^{-3}, s	0.96	0.92
T_{afo3}, 10^{-3}, s	0.96	1.12
T_{afo4}, 10^{-3}, s	0.92	-
T_{afo5}, 10^{-3}, s	0.92	-
f_{afo1}, Hz	961	1136
f_{afo2}, Hz	1041	1086
f_{afo3}, Hz	1041	892
f_{afo4}, Hz	1086	-
f_{afo5}, Hz	1086	-

R_{21}, mm	0.045	0.003
R_{22}, mm	0.039	0.007
R_{23}, mm	0.032	0.010
R_{24}, mm	0.019	0.017
R_{25}, mm	0.020	-
R_{26}, mm	0.012	-
Δ_{max}, мм	0.156	0.187

When up-milling with a feed rate of S_z = 0.3 mm/tooth, the frequency of AFO after plunging is 42% higher than the natural frequency of the part. By the end of cutting, it further increases by 11%. During down-milling, the frequency of AFO after plunging is 55% higher than the natural frequency of the part. However, it decreases by 21% by the end of cutting. Moreover, the frequency of AFO in the in the formation zone of the machined surface is 7% lower during down-milling than during up-milling.

The amplitude of AFO decreases by 73% from the beginning to the end of cutting during up-milling, while during down-milling, it increases by 82%.

During conventional milling with a feed rate of S_z = 0.3 mm/tooth, the amplitude of AFO is less than 0.02 mm.

The maximum deflection of the part during up-milling is 16% less than during down-milling.

The dynamic stiffness index during climb milling is k_{dyn} = 6.93, while during conventional milling, it is k_{dyn} = 22.

The research results indicate that the feed rate S_z during up and down-milling affects the part's properties during cutting due to its influence with the thickness of the cut layer. For all feed rate values, the frequency of AFO is higher than the natural frequency of the part.

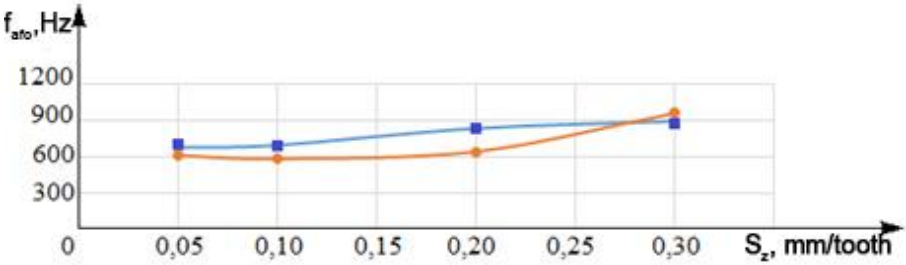

● – up-milling; ■ – down-milling

Figure 5 - Dependency of AFO frequency on feed rate

Correlation coefficient between AFO frequency and feed rate is 0.87 for up-milling and 0.98 for down-milling. These dependencies are described by the following regression equations:

- for up-milling:

$$f_{afo} = 1392{,}5 \cdot S_z + 471{,}71. \quad (2)$$

- for down-milling:

$$f_{afo} = 937{,}63 \cdot S_z + 621{,}14. \quad (3)$$

Increasing the thickness of the cut layer, in addition to affecting the frequency of AFO, also influences the amplitude of AFO, which decreases in this case (Fig. 6).

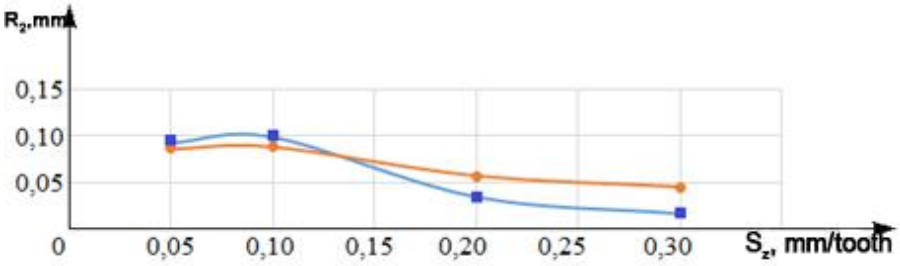

● – up-milling; ■ – down-milling

Figure 6 – Dependency of AFO amplitude on feed rate

Correlation coefficient between AFO amplitude and feed rate is (-0.96) for up-milling and (-0.94) for down-milling. These dependencies are described by the following regression equations:

- for up-milling:

$$R_2 = -0{,}1858 \cdot S_z + 0{,}0992. \quad (3)$$

- for down-milling:

$$R_2 = -0{,}3525 \cdot S_z + 0{,}1183. \quad (4)$$

Increasing the thickness of the cut layer with increasing feed rate increases the static squeeze of the part during cutting Δ_{max}. Due to the differences in milling, it is larger in the down-milling than during up-milling (Fig. 7). This is influenced by the thickness of the layer at the beginning of cutting. It is greatest during down-milling and least during up-milling. Therefore, the radial component of the cutting force is more significant during down-milling. The squeeze of the part, with the same stiffness, will be greater in this case than during up-milling.

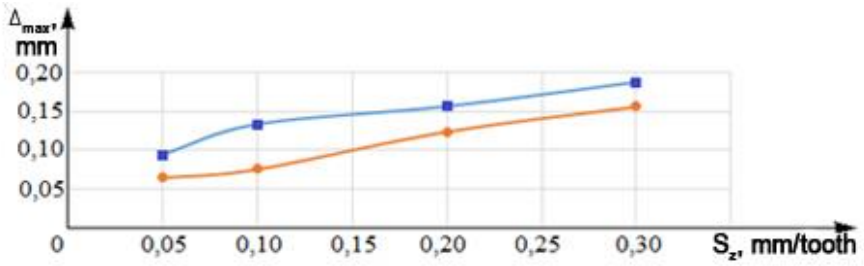

• - up-milling; ■ – down-milling

Figure 7 - Dependence of workpiece compression on feed rate

Furthermore, with an increase in feed rate, dynamic stiffness increases (Fig. 8). The correlation between them in up-milling is 0.98, and in down-milling it is 0.96. This influences the reduction of AFO intensity with an increase in feed rate.

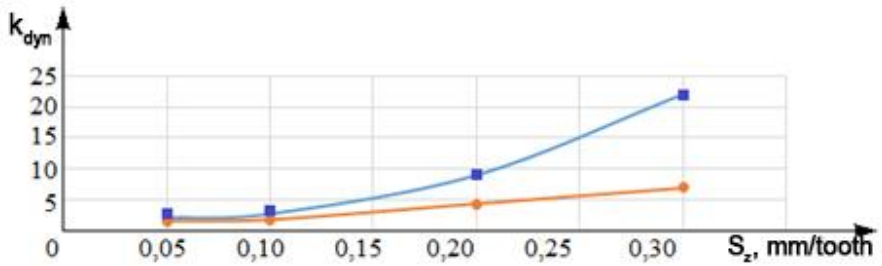

• - up-milling; ■ – down-milling

Figure 8 - Dependence of dynamic stiffness on feed rate

The regression equation for face milling:

$$k_{dyn} = 40{,}201 \cdot S_z^2 + 8{,}5869 \cdot S_z + 0{,}8025. \quad (6)$$

The regression equation for peripheral milling:

$$k_{dyn} = 336{,}94 \cdot S_z^2 - 38{,}081 \cdot S_z + 3{,}0946. \quad (7)$$

3. CONCLUSIONS

The dynamic properties of the workpiece during cutting manifest themselves in the form of frequency and amplitude of accompanying free vibrations. As demonstrated by conducted research, the feed rate, as an element of cutting conditions, affects them.

The AFO frequency during cutting is higher than the natural frequency of the workpiece by (16-47)% in up-milling and by (36-55)% in down-milling. The variable layer being cut during end-milling affects the chatter frequency, which changes from tool engagement to exit by up to 28%. Due to the characteristics of up- and down-milling, the AFO frequency increases when using the former feed direction and decreases when using the latter.

The feed rate affects the dynamic stiffness of the workpiece during cutting, which increases with its increment. This influences the fact that with an increase in feed rate, the AFO frequency increases and its amplitude decreases. The dynamic stiffness is greater in down-milling than in up-milling.

The positive influence of the feed rate in reducing vibration intensity is beneficial for machining rigid workpieces. However, when milling thin-walled components, the radial cutting force component increases with feed rate increment. This negatively impacts machining accuracy due to the reduction in cutting depth caused by workpiece squeezing.

References: **1**. *Munoa, J., Beudaert, X., Erkorkmaz, K. et al.*: Active suppression of structural chatter vibrations using machine drives and accelerometers, CIRP Annals 64(1), pp. 385–388, 2015. **2**. *Altintas, Y., Engin, S., Budak, E.* Analytical Stability Prediction & Design for Variable Pitch Cutters, Journal of Manufacturing Science & Engineering 1998-1024, pp. 141–148, 2022. **3**. *Gradiš˘eka, J., Kalveramb, M., Inspergerc, T., Weinertb, K., Ste´pa´nc, G. Edvard et al.*: On stability prediction for milling, International Journal of Machine Tools & Manufacture 45, pp. 769–781, 2005. **4**. *Altintas, Y.*: Critical Review of Chatter Vibration Models for Milling, Autonome Produktion, pp. 39–60, 2004. **5**. *Stupnytskyy, V.*: Simulation Studies of High-Speed Machining, Lecture notes in mechanical engineering, pp. 1–13, 2022. **6**. *Alexander, I.*: Milling stability improvement through novel prediction and suppression techniques, doctoral thesis, Universitat de Girona, 2015. 287 p. **7**. *Nagy, A., Kundrak, J., Miskolc*: Changes in the values of roughness parameters on face-milled steel surface, Cutting and Tools in Technological Systems 92, pp. 85–95, 2020. **8**. *Kundrák, J., Nagy, A., Miskolc, Markopoulos, A.P., Karkalos, N.E., Skondras-Giousios, D.*: Experimental study on surface roughness of face-milled parts with round insert at various feed rates, Cutting and Tools in Technological Systems 92, pp. 96–106, 2020. **9**. *Kai, Ch.*: Machining Dynamics. Springer-Verlag London Limited, 2009, 341 p. **10**. *Jinbo, N., Jinting, X., Fei, R., Yuwen, S., Dongming, G.*: A short review on milling dynamics in low-stiffness cutting conditions: Modeling and analysis, Journal of Advanced Manufacturing Science and Technology,1, 2020004, 2021. **11**. *Honeycutt, A., Schmitz, T.*: Milling bifurcations: A review of literature and experiment, Journal of Manufacturing Science and Engineering 140(12):120801, 2018. **12**. *Totis, G., Insperger, T., Sortino, M. et al.*: Symmetry breaking in milling dynamics, International Journal of Machine Tools and Manufacture 139, pp. 37–59, 2019. **13**. *Li, H., Chen, Y.*: Machining Process Monitoring, Handbook of Manufacturing Engineering and Technology, pp. 1–34, 2014. **14**. *Vnukov, Y., Dyadya, S., Kozlova, O., Trishyn, P., Zubarev, A.*: Influence of cutting time on types of oscillations during blade processing, Ukrainian Journal of Mechanical Engineering and Materials Science, 9(1), pp. 53–66, 2023. **15**. *Vnukov, Y., Dyaya, S., Kozlova, Ye., Logominov, V., Chernovol, N.* Self-oscillations when milling thin-walled elements of parts. Zaporizhzhia: ZNTU; 2017. 208 p. **16**. *Belikov, S., Germashev, A., Logominov, V., Kozlova, E., Kryshtal, V.*: Features of end milling of complex profile thin-walled parts, New materials and technologies in metallurgy and engineering 2, pp. 107–113, 2017. **17**. *Beudaert, X., Franco, O., Erkorkmaz, K., Zatarain, M.*: Feed drive control tuning considering machine dynamics and chatter stability, CIRP Annals Manufacturing Technology 69, pp. 345–348, 2020. **18**. *Dyadya, S., Kozlova, O., Tryshyn, P., Brukhno, E., Yakhno, D.*: Influence of radial depth of cut on initial conditions

of oscillations during end-milling of thin-walled parts Cutting and Tools in Technological Systems 99, pp. 153–164, 2023. **19**. *Dyadya, S., Kozlova, Ye., Germashev, A., Logominov V.*: Simulation of the machining surface after end milling with self-oscilations, Cutting& Tools in Technological System 94, pp. 19–27, 2021.

Сергій Дядя, Олена Козлова, Едуард Брухно, Денис Яхно, Дарія Карамушка

ВПЛИВ ПОДАЧІ НА ДИНАМІЧНІ ВЛАСТИВОСТІ ТОНКОСТІННОЇ ДЕТАЛІ ПРИ КІНЦЕВОМУ ФРЕЗЕРУВАННІ

Анотація. *При призначенні режимів різання для кінцевого фрезерування тонкостінних деталей з важкооброблюваних матеріалів треба враховувати їх вплив на сталість обробки. Для цього треба знати, які види коливань діють і за яких умов вони виникають. Виконаними дослідженнями встановлено, що при різанні різні види коливань діють послідовно і тільки певний час. При кінцевому фрезеруванні через короткочасність різання виникають вимушені та супроводжуючі вільні коливання. Їх вплив на сталість процесу різання залежить від того, в якій швидкісній зоні коливань буде проходити фрезерування. Найбільш несприятливою є третя швидкісна зона коливань. Тільки в ній діють супроводжуючі вільні коливання великої інтенсивності. Швидкості різання для обробки деталей з важкооброблюваних матеріалів припадають саме на цю зону. На інтенсивність коливань впливають динамічні властивості деталі. При кінцевому фрезеруванні тонкостінних деталей вони характеризуються амплітудою та частотою супроводжуючих вільних коливань, які більше за частоту вільних коливань деталі. Тобто режими різання змінюють динамічні властивості деталі. Деякі дослідники зосереджуються на використанні демпфуючих властивостей подачі. Тому метою даної роботи було визначення того, яким чином подача впливає на динамічні властивості деталі при різанні. Для дослідження використовувався універсальний стенд, за допомогою якого можливо створювати різні динамічні характеристики зразка, який обробляється та записувати на осцилограмі закони його руху при фрезеруванні. Результати досліджень показали, що подача, як елемент режимів різання, впливає на динамічні властивості деталі при різанні. Вона створює змінний шар, який зрізається. Тому на протязі часу різання частота і амплітуда супроводжуючих вільних коливань при зустрічному і попутному фрезеруванні змінюються. Подача впливає на динамічну жорсткість. При збільшенні подачі динамічна жорсткість деталі збільшується. Це призводить до зменшення амплітуди супроводжуючих вільних коливань при фрезеруванні в третій швидкісній зоні коливань. Наведені у статті результати мають практичне значення для технологів у галузі авіаційного виробництва. Вони допомагають краще розуміти фізичні процеси, що відбуваються під час фрезерування, та розробляти оптимальні стратегії обробки тонкостінних деталей, до яких висуваються високі вимоги щодо точності розмірів та якості поверхні.*

Ключові слова: *фрезерування; фреза; тонкостінна деталь; подача на зуб; осцилограма; супроводжуючі вільні коливання.*

UDC 621.91.01 **doi: 10.20998/2078-7405.2024.100.06**

COMPARISON OF CUTTING TOOL GEOMETRIES BASED ON CUTTING FORCES AND ROUGHNESS OF HARD TURNED SURFACES

Viktor **Molnár** [0000-0002-4156-9987], Gergely **Szabo** [0000-0001-8191-5410]

University of Miskolc, 3515 Miskolc-Egyetemváros, Hungary
molnar.viktor@mail.uni-miskolc.hu

Received: 15 November 2023 / Revised: 10 March 2024 / Accepted: 25 April 2024 / Published: 15 June 2024

Abstract. *Surface quality and energy consumption are two widely studied topics of hard machining. Due to the increasing need of companies for new, more efficient materials, tools and procedures, their manufacturers or suppliers have to deliver innovative solutions from time to time. In this study the latest development of a hard turning insert manufacturer is used in comprehensive machining experiments to show how the new tool (a wiper insert) behaves compared to its standard counterpart. Based on surface roughness and machining force measurement and analysis, this efficiency is proved by quantitative results: the wiper geometry ensures significantly better surface quality, while the energy consumption of the used machine tool is considerably lower.*
Keywords: *surface topography; cutting force; hard turning.*

1. INTRODUCTION

The high quality of machined components plays a significant role in the planning of production process, and can be achieved, among other approaches, by a comprehensively planned technological process that ensures suitable surface quality and part accuracy. To remain competitive, the latest innovation must be used in machining technology, which in the world of machining metallic materials means new machines, materials, procedures, jigs and tools. In hard turning, cutting tools are continuously being developed by their manufacturers and a wide range of applications is covered by various solutions concerning tool materials or geometries [1].

3D surface roughness analysis is a developing are of qualifying functional surfaces. The 3D topography parameters provide more information about the analyzed surface than 2D because of the number of detected points. At the same time, a wider range of reliable parameters are available [2, 3]. 3D measurement is not so efficient than the 2D one but it is widely applied by high-tech companies [4]. The 3D analysis can also provide information about the effectiveness of the applied

cutting procedure [5]. Not only the innovative variants of turning and grinding [6-8] but also relative new technologies have been analyzed recently by topography studies, such as additive techniques [9, 10] or precision milling [11].

Cutting force analysis provides the basis for rough estimation about the energy consumption of a machine tool. Numerous studies have been published in precision hard machining [12, 13] and within that, hard turning topics; and the majority of them focus on the efficiency of the technology [14, 15], the surface integrity [16, 17] and part accuracy [18], the prediction of tool life or physical phenomena of the cutting process [19–21]. Many of the studies focus on the appropriate selection of technological data [22–24].

In this study the results of a machining experiment are introduced. The roughness of the machined cylindrical surfaces and the machining forces were measured and analyzed. The machining was carried out by standard insert and then by its wiper counterpart. The goal was to determine whether the wiper insert provides lower energy consumption due to the lower cutting forces and favorable surface quality due to the lower values of surface roughness. For the force measurement the cutting force (F_c), passive force (F_p) and feed force (F_f) were analyzed. For the roughness measurement the arithmetic mean height (S_a) 3D topography parameter was analyzed.

2. EXPERIMENTAL METHOD

In the machining experiment 18 external cylindrical surfaces (S1 – S18) with diameter 60 mm were hard turned by two variants (standard and wiper) of a turning insert type 4NC-CNGA 12048. The machined material was case hardened 16MnCr5 steel, the applied machine tool was a hard machining centre type EMAG VSC 400 DDS. The hard turning experiment was carried out dry. In the experiment the depth-of-cut (a_p) was fixed at 0.2 mm; the cutting speed (v_c) and the feed rate (f) were varied. The experimental plan and the applied technological data are demonstrated in Table 1.

Table 1. Experimental plan

Insert	feed rate, f [mm/rev]	cutting speed, v_c [m/min]		
		120	180	240
Standard	0.04	S1	S7	S13
	0.12	S2	S8	S14

	0.2	S3	S9	S15
Wiper	0.04	S4	S10	S16
	0.12	S5	S11	S17
	0.2	S6	S12	S18

For the force measurement, a 3-channel dynamometer, type Kistler 5011 was used. After acquisition, the data were processed by the MATLAB software.

After machining, the surfaces were scanned by a 3D topography measuring and analyzing equipment type ALTISURF 520. The applied sensor was a confocal chromatic one type CL2 of which resolution is 0.012 μm in z and 1 μm in x and y directions. The evaluated area of each surface was 2 × 2 mm, which resulted in 2 million detected points. The applied cut-off lengths were 0.08; 0.25; and 0.8 mm according to the specifications of ISO 25178. The raw data were processed and analyzed by the software Altimet Premium and Origin Lab.

The material was case hardened before machining, the microstructure of it was martensitic with HRC hardness 60–63.

3. RESULTS OF FORCE MEASUREMENT AND SURFACE TOPOGRAPHY ANALYSIS

The three components of the machining force were analyzed separately: cutting, feed and passive force. All three of them showed significant differences when the feed rate or the tool geometry were varied. Varying the cutting speed resulted in only a slight difference in the force components. The F_c cutting force values varied between 41.9 and 142.7 N and between 37.7 and 122.7 N when the standard or wiper insert was used, respectively. The force values slightly decreased with the increase of cutting speed. The percentage difference between two consecutive cutting speed values changed by 0.3–6.4%. The F_c values increased by the increase of the feed rate. When the standard insert was used, two consecutive force component values changed by 44–126%; and when the wiper insert was used, these changes varied between 41 and 107%. This means that the F_c force component ranges were closer to each other when the machining was carried out by wiper insert.

In Fig. 1 the F_c values are demonstrated. At the applied cutting speed levels the F_c values decreased by 4.5–15.9% when the wiper insert was used compared to the results of the standard insert. The decreases were more emphasized at higher feed rates: 14–15.9%. This means that lower cutting forces can be reached with the wiper insert compared to the standard tool geometry.

The F_p passive force values varied between 70.3 and 163.1 *N* and between 65.2 and 126.3 *N* when the standard or wiper insert was used, respectively. The force values slightly decreased with the increase of cutting speed. The percentage difference between two consecutive cutting speed values changed by 0.2–7.3%. The F_p values increased with the increase of the feed rate. When the standard insert was used, two consecutive force component values were changed by 28–69%; and when the wiper insert was used, these changes varied between 24 and 48%.

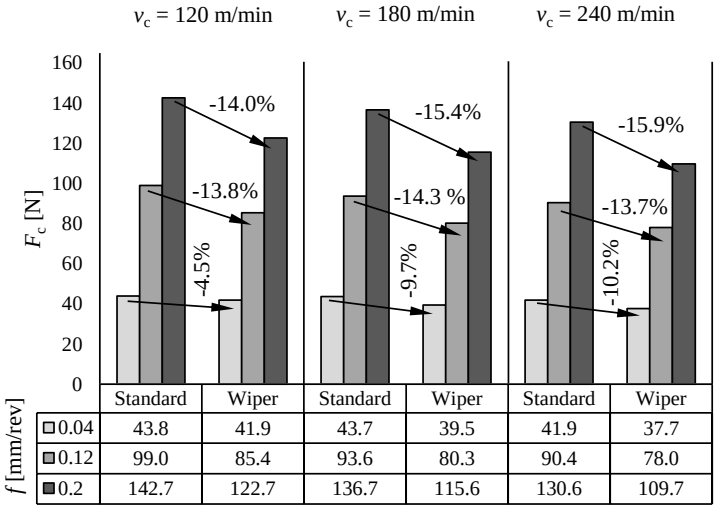

f [mm/rev]	Standard	Wiper	Standard	Wiper	Standard	Wiper
0.04	43.8	41.9	43.7	39.5	41.9	37.7
0.12	99.0	85.4	93.6	80.3	90.4	78.0
0.2	142.7	122.7	136.7	115.6	130.6	109.7

Figure 1. Cutting force (F_c) values of hard turning

In Fig. 2 the F_p values are demonstrated. At the applied cutting speed levels the F_p values decreased by 7.2–23.9% when the wiper insert was used compared to the results of the standard insert. The decreases were more emphasized at higher feed rates: 20.7–23.9%. This means that compared to the standard tool geometry, lower cutting forces occur when the wiper insert is used. Compared to the F_c cutting force component values; the F_p passive force values are significantly higher, which is one of the main characteristics of hard turning. The reason for this is the negative rake angle designed for hard turning inserts.

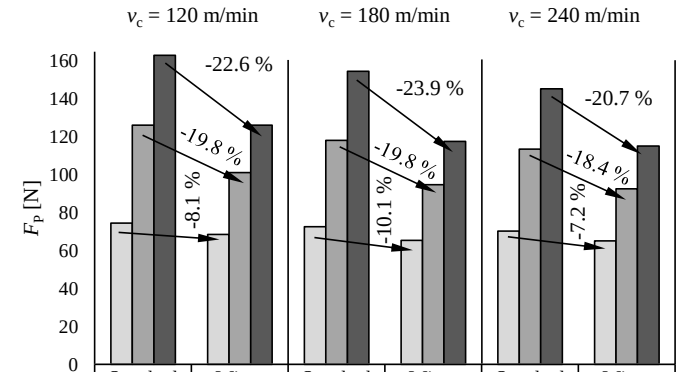

f [mm/rev]	Standard	Wiper	Standard	Wiper	Standard	Wiper
0.04	74.6	68.6	72.7	65.4	70.3	65.2
0.12	126.2	101.2	118.2	94.8	113.6	92.7
0.2	163.1	126.3	154.7	117.7	145.4	115.3

Figure 2. Passive force (F_p) values of hard turning

The F_f feed force values varied between 24.4 and 50.5 *N* and between 18.2 and 37.3 *N* when the standard or wiper insert was used, respectively. The force values slightly decreased with the increase of cutting speed. The percentage difference between two consecutive cutting speed values changed by 0.2–15.3%. The F_f values increased with the increase of the feed rate. When the standard insert was used, two consecutive force component values changed by 14–56%; and when the wiper insert was used, these changes varied between 12 and 47%.

In Fig. 3 the F_f values are demonstrated. At the applied cutting speed levels the F_f values decreased by 22.3–33% when the wiper insert was used compared to the results of the standard insert. The decreases were more emphasized at the middle feed rate (f = 0.12 mm/rev) than in the cases of the lowest and the highest cutting speed levels (120 and 240 m/min): 32.6 and 33%, respectively; and was 32.9% lower at the highest feed rate (f = 0.2 mm/rev) in the case of the 180 mm/rev cutting speed level. This also means that lower cutting forces can be achieved with the wiper insert than with the standard tool geometry. Compared to the F_c and F_p force component values; the F_f feed force values are significantly lower.

The most commonly used topography parameter, the arithmetic mean height (S_a), was analyzed to obtain information about the connection between that and the introduced force components. S_a values varied between 0.07 and 1.34 µm. Although these values resulted from an experiment where the applicability ranges of two

technological parameters (v_c and f) were set, technological parameters that result in lower topography values are recommended in precision finish operations.

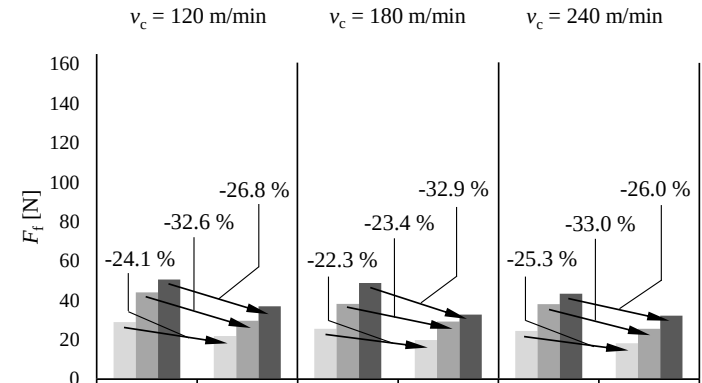

f [mm/rev]	Standard	Wiper	Standard	Wiper	Standard	Wiper
0.04	28.9	21.9	25.5	19.8	24.4	18.2
0.12	44.0	29.7	38.1	29.2	38.1	25.5
0.2	50.5	37.0	48.8	32.7	43.4	32.1

Figure 3. Feed force (F_f) values of hard turning

In many of the cases the S_a values decreased slightly with the increase of cutting speed; however, this technological parameter cannot be the basis of S_a minimization. At the same time, the S_a values decreased significantly with the decrease of feed rate. When the feed rate decreased from the highest (0.2 mm/rev) to the lowest (0.04 mm/rev) value, the S_a values decreased by 90–93% and by 64–81% when the standard or wiper insert were used, respectively.

In Fig. 4 the S_a values are given. In most of the cases the S_a values decreased when the wiper insert was applied. At the 0.2 mm/rev feed rate this decrease was between 67 and 74% and at 1.12 mm/rev between 69 and 74%. At the lowest feed rate (0.04 mm/rev) the decrease was between 13 and 46% for the two higher cutting speeds; however, at the lowest (120 m/min) a 50% decrease was obtained for the S_a value.

In Figs. 5 and 6 the connections between the S_a topography values and the force components are demonstrated. When the standard insert was used, the S_a values formed well-separated areas based on the feed rates. At the same time, similar areas can be observed for the different force components. It can be stated that the lowest

S_a values can be reached at 0.04 mm/rev feed rate and at this level, all the force components are minimal (Fig. 5).

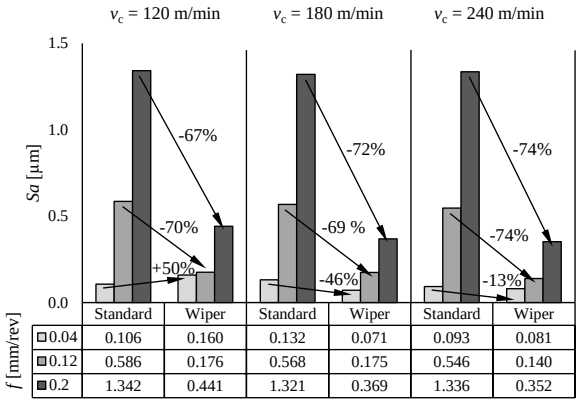

f [mm/rev]	Standard	Wiper	Standard	Wiper	Standard	Wiper
0.04	0.106	0.160	0.132	0.071	0.093	0.081
0.12	0.586	0.176	0.568	0.175	0.546	0.140
0.2	1.342	0.441	1.321	0.369	1.336	0.352

Figure 4. Arithmetic mean height (*Sa*) values of hard turned surfaces

When the wiper insert was used, such clear areas cannot be designated (Fig. 6). The S_a values can be separated clearly only at the highest feed rate, but the F_p and F_c values are nearly identical at this level. The most easily separable area for the force components is that belonging to the lowest feed rate; however, in this case the S_a values form an overlapping set with values belonging to the middle feed rate. This means that the technological parameter-based planning strategy is not as obvious as when using the standard insert. Similar results were found by Nagy [25].

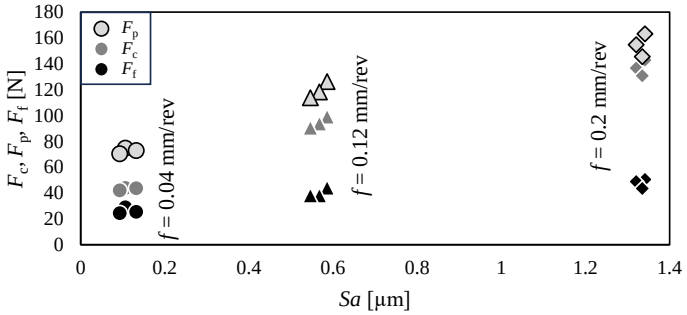

Figure 5. Connections between the S_a values and the force components when standard insert was applied

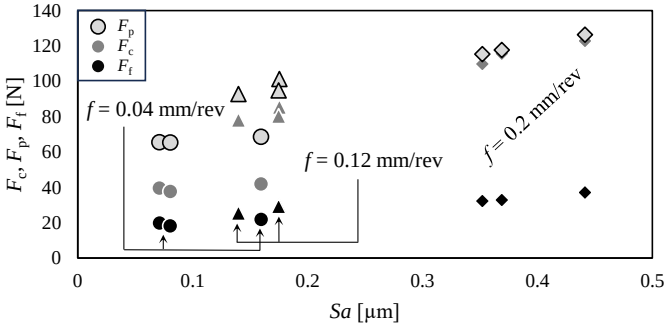

Figure 6. Connections between the S_a values and the force components when wiper insert was applied

Apart from the not perfectly clear technological data-based area designation, it can also be stated that the use of the wiper insert leads to significantly lower machining forces and the technological parameter values that result in the lowest force values also provide the lowest S_a values. This means that high-quality surfaces can be machined using low machining forces, i.e. energy consumption is reduced.

4. CONCLUSIONS

In the introduced machining experiments, where two variants of a cutting insert (standard and wiper) were compared, the technological parameter values v_c and f were varied in the ranges recommended by the tool manufacturer. The following findings were obtained. The lowest cutting force (F_c), passive force (F_p) and feed force (F_f) values were obtained at the highest cutting speed (240 m/min) and the lowest feed rate (0.04 mm/rev) when the depth-of-cut was fixed. The lowest *Sa* topography values (lower than 0.1 μm) were obtained at the lowest feed rate and at 180 and 240 m/min cutting speeds. These results are valid in the analyzed technological data ranges.

References: 1. *Kundrak, J ; Nagy, N* Influences of the technological parameters on the surface twist in grinding, Cutting and Tools in Technological System 86, pp.103–110, 2016. **2.** *Elbah, M., Laouici, H., Benlahmidi, S., Nouioua, M., Yallese, M.*: Comparative assessment of machining environments (dry, wet and MQL) in hard turning of AISI 4140 steel with CC6050 tools, International Journal of Advanced Manufacturing Technology 105, pp.2581–2597, 2019. **3**. Li, S., Chen, T., Qiu, C., Wang, D., Liu, X.: Experimental investigation of high-speed hard turning by PCBN tooling with strengthened edge, International Journal of Advanced Manufacturing Technology 92, pp.3785–3793, 2017. **4**. *Kundrak, J., Nagy, A., Markopoulos, A.P., Karkalos, N.E.*: Investigation of surface roughness on face milled parts with round insert in planes parallel to the feed at various cutting speeds, Cutting and Tools in Technological

System 91, pp.87–96, 2019. **5.** *Karkalos, N.E., Karmiris-Obratanski, P., Kurpiel, S., Zagorski, K., Markopoulos, A.P.*: Investigation on the surface quality obtained during trochoidal milling of 6082 aluminum alloy, Machines 9, art no 75, 2021. **6.** *Zhao, T., Zhou, J.M., Bushlya, V., Stahl, J.E.*: Effect of cutting edge radius on surface roughness and tool wear in hard turning of AISI 52100 steel, International Journal of Advanced Manufacturing Technology 91, pp.3611–3618, 2017. **7.** *Gao, H., Ma, B., Singh, R.P., Yang, H.*: Areal surface roughness of AZ31B magnesium alloy processed by dry face turning: an experimental framework combined with regression analysis, Materials 13, art no 2303. 2020. **8.** *Grzesik, W., Zak, K., Kiszka, P.*: Comparison of surface textures generated in hard turning and grinding operations, Procedia CIRP 13, pp.84–89, 2014. **9.** *Charles, A., Elkaseer, A., Thijs, L., Hagenmeyer, V., Scholz, S.*: Effect of process parameters on the generated surface rough-ness of down-facing surfaces in selective laser melting, Applied Sciences, 9, art no 1256, 2019. **10.** *Sanaei, N., Fatemi, A.*: Analysis of the effect of surface roughness on fatigue performance of powder bed fusion additive manufactured metals, Theoretical and Applied Fracture Mechanics 108, art no 102638, 2020. **11**. *Lu, X., Hu, X., Jia, Z., Liu, M., Gao, S., Qu, C., Liang, S.Y.*: Model for the prediction of 3D surface topography and surface roughness in micro-milling Inconel 718, International Journal of Advanced Manufacturing Technology 94, pp.2043–2056, 2017. **12.** *Kundrak, J., Fedorovich, V., Pyzhov, I., Ostroverkh, Y., Pupan, L.*: Numerical simulation of grain concentration effect on output indicators of diamond grinding, Lecture Notes in Mechanical Engineering, Advanced Manufacturing Processes IV, pp. 165–175, 2022. **13.** *Kundrak, J., Fedorovich, V., Markopoulos, A.P., Pyzhov, I., Ostroverkh, Y.*: Theoretical assessment of the role of bond material during grinding of superhard materials with diamond wheels, Machines 10(7), art no 543, 2022. **14.** *Agarwal, S., Suman, R., Bahl, S., Haleem, A., Javaid, M., Sharma, M.K., Prakash, C., Sehgal, S., Singhal, P.*: Optimisation of cutting parameters during turning of 16MnCr5 steelusing Taguchi technique, International Journal on Interactive Design and Manufacturing, art no 00933, 2022. **15.** *Kovalev, V., Klymenko, G., Vasylchenko, Y., Shapovalov, M.*, Antsiferova, O., Maiskykh, I.: Results of industrial testing of carbide cutting tools by pulsed magnetic field treatment and the effect on the increase of the cutting process efficiency, Cutting and Tools in Technological System 95, pp.3–12, 2021. **16.** *Grzesik, W.*: Prediction of the functional performance of machined components based on surface topography: state of the art, Journal of Materials Engineering and Performance 25(10), pp. 4460–4468, 2016. **17.** *Naylor, A.; Talwalkar, S.C.; Trail, I.A.; Joyce, T.J.* : Evaluating the surface topography of pyrolytic carbon finger prostheses through measurement of various roughness parameters, Journal of Functional Biomaterials 9, art no 9, 2016. **18.** *Turmanidze, R., Popkhadze, G., Inasharidze, K.*: Improving the performance characteristics of human hip-joint implants by increasing the quality of processing and geometric accuracy of their spherical surfaces, Cutting and Tools in Technological System 93, pp.103–113, 2020. **19**. *Velazquez Corral, E., Wagner, V., Jerez Mesa, R., Delbe, K., Lluma, J., Travieso Rodriguez, J.A., Dessein, G.*: Wear resistance and friction analysis of Ti6Al4V cylindrical ball burnished specimens with and without vibration assistance, International Journal of Advanced Manufacturing Technology 130, pp. 551–562, 2023. **20.** *Szlachetka, O., Witkowska-Dobrev, J., Baryla, A.; Dohojda, M.*: Low-density polyethylene (LDPE) building films – Tensile properties and surface morphology, Journal of Building Engineering 44, art no 103386, 2021. **21.** *Krolczyk, J.B., Maruda, R.W., Krolczyk, G.M., Wojciechowski, S., Gupta, M.K., Korkmaz, M.E.*: Investigations on surface induced tribological characteristics in MQCL assisted machining of duplex stainless steel, Journal of Materials Research and Technology 18, pp. 2754–2769, 2022. **22.** *Kumar, R., Seetharamu, S., Kamaraj, M.*: Quantitative evaluation of 3D surface roughness parameters during cavitation exposure of 16Cr–5Ni hydro turbine steel, Wear 320, pp.16–24, 2014. **23.** *Mesicek, J., Ma, Q.P., Hajnys, J., Zelinka, J., Pagac, M., Petru, J.; Mizera, O.*: Abrasive surface finishing on SLM 316L parts fabricated with recycled powder, Applied Sciences 11, art no 2869, 2021. **24.** *Kundrak, J., Morgan, M., Mitsyk, A.V., Fedorovich, V.A., Grabchenko, A.I.*: Mathematical simulation of the vibration treatment of parts in a liquefied abrasive working medium, International Journal of Advanced Manufacturing Technology 120 (7-8), pp.5377–5398, 2022. **25.** *Nagy, N.*: Experimental

investigation of tribology-related surface topography parameters and hardness of 16MnCn5 case hardened steel, Cutting and Tools in Technological System 98 pp. 73-82, 2023.

Віктор Мольнар, Гергель Сабо, Мішкольц, Угорщин

ПОРІВНЯННЯ ГЕОМЕТРІЇ РІЖУЧОГО ІНСТРУМЕНТУ НА ОСНОВІ СИЛ РІЗАННЯ І ШОРСТКОСТІ ТОЧЕНИХ ПОВЕРХОНЬ

Анотація. *У токарній обробці загартованих сталей ріжучі інструменти постійно розробляються їх виробниками, і широкий спектр застосування охоплюється різними рішеннями, що стосуються інструментальних матеріалів або геометрії. У цьому дослідженні представлені результати експерименту з механічної обробки. Вимірювали та аналізували шорсткість оброблюваних циліндричних поверхонь та зусилля обробки. Механічна обробка здійснювалася стандартною вставкою, а потім її аналогом після доводки. Мета полягала в тому, щоб визначити, чи забезпечує вставка після доводки менше енергоспоживання за рахунок менших сил різання та сприятливу якість поверхні за рахунок нижчих значень шорсткості поверхні. Для вимірювання сили були проаналізовані сила різання (F_c), пасивна сила (F_p) і сила подачі (F_f). Для вимірювання шорсткості було проаналізовано параметр 3D топографії середнього арифметичного значення висоти (S_a). Для вимірювання сили використовувався 3-х канальний динамометр типу Kistler 5011. Після отримання, дані були оброблені програмним забезпеченням Matlab. Після механічної обробки поверхні були відскановані за допомогою 3D обладнання для вимірювання та аналізу топографії типу Altisurf 520. Застосований сенсор був конфокальним хроматичним типу CL2, роздільна здатність якого становить 0,012 мкм у z та 1 мкм у напрямках x та y. Оцінена площа кожної поверхні становила 2 × 2 мм, що призвело до 2 млн виявлених точок. Застосована довжина зрізу становила 0,08; 0.25; і 0,8 мм згідно зі специфікаціями ISO 25178. Необроблені дані були оброблені та проаналізовані програмним забезпеченням Altimet Premium та Origin Lab. Матеріал перед механічною обробкою був загартований, мікроструктура його була мартенситною з твердістю HRC 60–63. Були отримані наступні результати. Найнижчі значення сили різання (F_c), пасивної сили (F_p) і сили подачі (F_f) були отримані при найбільшій швидкості різання (240 м/хв) і найнижчій швидкості подачі (0,04 мм/об) при фіксованій глибині різання. Найнижчі значення топографії S_a (нижче 0,1 мкм) були отримані при найменшій швидкості подачі і при швидкостях різання 180 і 240 м/хв. Ці результати справедливі в аналізованих діапазонах технологічних даних.*

Ключові слова: *рельєф поверхні; сила різання; жорстке токарне оброблення.*

UDC 621.9.042 **doi: 10.20998/2078-7405.2024.100.08**

ALUMINUM MATRIX COMPOSITES ALTERNATIVE FOR BRAKE ROTOR APPLICATIONS

Afraa **Khattab** [0009-0001-8698-1043], Csaba **Felhő** [0000-0003-0997-666X]

University of Miskolc, 3515 Miskolc-Egyetemváros, Hungary
csaba.felho@uni-miskolc.hu

Received: 29 March 2024 / Revised: 28 April 2024 / Accepted: 27 May 2024 / Published: 15 June 2024

Abstract. *This literature overview examines the capacity of using aluminum matrix composites (AMCs) rather than conventional grey solid iron in brake rotor packages. Driven by the preference for lighter and more environmentally friendly vehicles, AMCs offer several benefits, including decreased weight, advanced thermal properties, superior put-on resistance, and an optimized breaking system. Studies have concluded that AMCs can gain weight reductions of up to 60% compared to cast iron, resulting in stepped-forward gas performance and automobile management. Besides exhibiting superior thermal conductivity and lower thermal enlargement, it results in better heat dissipation and a reduced danger of warping and cracking. The advantage of using ceramic reinforcements, which include SiC, Al2O3, and B4C, is that they can enhance the damage resistance of AMCs, leading to a longer service life for brake rotors. The review covers various elements of AMC brake rotor development, Starting with manufacturing strategies (stir casting, ultrasonic-assisted stir casting, and squeeze casting), which are powerful techniques for producing extremely good AMC rotors, then the thermal traits, which are so essential due to their thermal conductivity, thermal expansion, and heat dissipation in brake rotor overall performance, Finally, the tribological residences affect load, sliding pace, and floor roughness on the wear and friction of AMC rotors. Brake pad compatibility is so vital in breaking systems, that deciding on suitable brake pad materials, containing non-asbestos organic (NAO) pads, can optimize performance with AMC rotors. These traits can be computationally analysed by using finite element evaluation and different numerical methods to predict the thermal and mechanical behaviour of AMC brake rotors. The review emphasizes that AMCs maintain great promise as next-era manufacturing for brake rotors, offering a balance of weight reduction, stepped-forward thermal control, and more advantageous wear resistance. Further research and improvement are necessary to optimize fabric composition, production strategies, and brake pad compatibility to improve the capacity of AMCs in brake structures.*
Keywords: *Brake Rotors; Aluminum Matrix Composites (AMCs); Tribology; Brake pads.*

1. Introduction

Automobiles use disc brake systems to slow down or stop. The system consists of a disc rotor, a pair of brake pads, and a caliper with a piston. This process is highly efficient and reliable, making disc brake systems the preferred choice for modern automobiles. The frictional heat generated by the rotor and pads is essential in converting the car's kinetic energy into thermal energy, effectively slowing or stopping the vehicle [1].

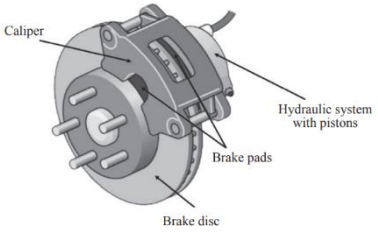

Figure 1 – Hydraulic disc braking system [2].

Gray cast iron is the ideal material for manufacturing brake discs due to its impressive range of properties. It has excellent thermal conductivity, maintains its material stability even at elevated temperatures, and exhibits commendable wear resistance [3]. Gray iron is a practical choice for mass production due to its affordability and the simplicity of the casting process [3].

Gray iron's relatively high density is a major disadvantage as it increases the overall weight of the vehicle, negatively impacting fuel efficiency and CO_2 emissions, as well as the vehicle's handling dynamics, often resulting in poorer performance [4]. However, despite this, gray iron remains a popular choice for its cost-effectiveness and ease of use in manufacturing. The high density of brake rotors is a significant disadvantage as it increases the weight of the vehicle, negatively impacting fuel efficiency, CO_2 emissions, and handling dynamics, often resulting in poorer performance. The weight of the brake rotors is a crucial factor in both conventional and electric vehicles as it significantly contributes to the overall weight of the chassis. The automotive industry is confidently researching and adopting lighter materials for disc brake rotors to significantly improve efficiency and performance. This decisive shift aims to enhance vehicle efficiency and handling by reducing unsprung weight to expertly meet the evolving demands of modern transportation [5, 6].

Aluminum alloys are an excellent choice for manufacturing due to their unique physical properties, including low density, minimal thermal expansion, high thermal conductivity, and strong corrosion resistance [7, 8]. Aluminum alloys are a highly valued choice for the automotive industry due to their high specific strength and excellent corrosion resistance, making them cost-effective and ideal for high-volume production. Our research and development in aluminum-based metal matrix composites (AMCs) have shown great promise for use in brake rotors. This is because traditional cast-iron brake rotors have a major limitation of relatively low resistance to scuffing and seizing, as noted in Reference 6. Our AMCs are a confident alternative to address these challenges [9].

AMCs offer significant benefits over gray cast iron for brake rotor applications, particularly in terms of thermal conductivity, density, and specific strength. Their superior properties make AMCs an appealing option that can potentially improve brake rotor performance and efficiency. Ongoing research and development in this area suggests that AMCs will soon become a more common material in brake rotor manufacturing, offering a balance between strength, weight, and thermal properties [10]. To improve resistance to galling and seizure, AMCs are strengthened with hard synthetic ceramic materials, such as SiC, Al_2O_3, B_4C, SiO_2, and TiO_2. The integration of these ceramic reinforcements with the base aluminum matrix is optimized for various automotive applications, ensuring their effectiveness [11, 12].

Hybrid aluminum-metal matrix composites (HAMCs) outperform single-reinforced AMCs, especially in mechanical and tribological aspects. HAMCs incorporate secondary reinforcements, such as industrial by-products or agricultural wastes like fly ash, red mud, sugarcane bagasse ash, rice husk ash, bean ash, and cow dung ash, providing numerous advantages. HAMCs are the superior choice for automotive applications due to their lower density, reduced manufacturing costs, and lighter weight compared to primary reinforcements. They combine the desirable properties of AMCs with the added benefits of cost-effectiveness and sustainability [9].

2. Methods for Creating Aluminum Matrix Composite Rotor Discs

Aluminum is the ideal material for manufacturing rotor discs due to its ease of casting and suitability for large-scale production (Chebolu et al., 2022). The stir casting process is a highly effective and efficient method for producing low-cost, high-quality aluminum matrix composite (AMC) brake rotors. This technique involves mechanically stirring molten metal to uniformly distribute ceramic particles that are either micron- or nano-sized throughout the aluminum matrix. Aluminum is the ideal material for manufacturing rotor discs due to its ease of casting and suitability for large-scale production [13]. The stir casting process is an effective and efficient method for producing low-cost, high-quality aluminum matrix composite (AMC) brake rotors. This technique involves mechanically stirring molten metal to uniformly distribute micron- or nano-sized ceramic particles throughout the aluminum matrix [14, 15].

Mohanavel and colleagues improved stir casting techniques to produce aluminum alloy AA 7178/Si_3N_4 composites. The study found that the distribution of Si_3N_4 within the matrix plays a critical role in determining the composite's properties, particularly its tensile strength. To optimize the mechanical characteristics, it is imperative to uniformly distribute Si_3N_4 particles throughout the AA7178 alloy matrix. This will significantly improve the strength and performance of the composite [16]. Ul Haq et al. demonstrated that adding silicon nitride (Si_3N_4) in

proportions ranging from 0–8 wt% to AA7075 aluminum alloy significantly improves its hardness, compression strength, and wear resistance. At an 8 wt% Si_3N_4 level, the alloy showed up to a 20% increase in hardness and a 50% boost in compression strength. Additionally, wear resistance improved significantly, with a 37% reduction at 10 N loads and a 61% decrease at 50 N loads. The coefficient of friction (CoF) ranged from 0.10 to 0.30. It increased with Si_3N_4 content up to 4 wt% and then decreased. These results demonstrate that AA7075-Si_3N_4 composites, particularly those with higher Si_3N_4 content, are highly suitable for brake rotor applications [17].

Stir casting has made significant advancements in recent years [18], especially with the introduction of ultrasonic-assisted techniques and the use of nano-sized ceramic particles as reinforcements [16]. The application of ultrasonic waves during the casting process has been found to greatly improve the uniform distribution of these nanoparticles within the molten aluminum alloy [19]. This breakthrough holds immense potential for enhancing the quality and performance of AMC brake rotors [13, 14]. Ultrasonic-assisted stir casting has been extensively researched in the field of materials science and has been proven to enhance mechanical properties and wear resistance. This technique has shown promise in brake rotor manufacturing, an area traditionally dominated by die casting, which has been the industry standard for many years [20, 21, 22].

Researchers have explored a new manufacturing method called ultrasonic squeeze-assisted stir casting [20] instead of conventional methods. This method was successfully used to produce aluminum matrix composite (AMC) brake discs, as demonstrated in a specific study (shown as Figure 2). The technique described in this study combines ultrasonic stirring and squeeze casting principles to confidently produce superior AMC brake discs [23].

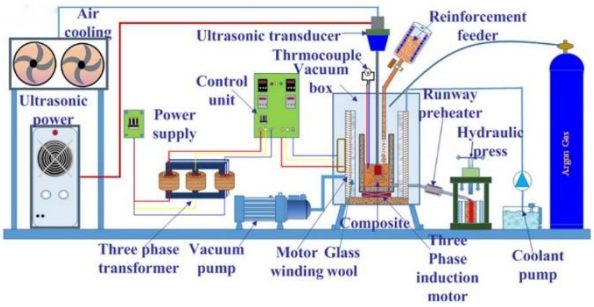

Figure 2 –Recommended stir casting furnace design [23].

The use of ultrasonic vibrations in the stir casting process results in a more uniform distribution of reinforcing particles in the aluminum matrix, leading to better bonding between the matrix and the reinforcement. The end product's mechanical characteristics are significantly enhanced. The squeeze casting process achieves a denser and more refined microstructure in the brake discs, enhancing their performance and wear resistance. The combination of squeeze-assisted stir casting and ultrasonics represents an innovative approach that significantly advances the field of automotive braking systems. This approach produces high-quality aluminum matrix composite (AMC) disc brakes that are more efficient and have a longer lifespan [24].

Lo et al. presents advanced methods for improving aluminum metal matrix composite (Al MMC) brake rotors using squeeze casting (SC). This technique improves reinforcement incorporation, high temperature performance and potentially reduces cost. SC increases the maximum operating temperature (MOT) of Al MMCs by using specific aluminum alloys, more reinforcement, and magnesium alloying. Al MMCs offer over 60% weight reduction compared to cast iron, along with superior thermal conductivity, reducing stress and hot spots. AMCs exhibit superior resistance to thermal shock and fatigue due to their low modulus and thermal expansion. They also exhibit superior tensile strength, damping, and wear resistance compared to cast iron, making them an excellent choice for brake rotor applications.

Kumar conducted a stir-casting research study to produce an aluminum hybrid metal matrix composite (AlHMMC) consisting of 3% alumina and 3% graphite. The objective of the study was to determine the wear resistance of AlHMMC compared to the base alloy for automotive applications. Based on the analysis of various factors such as load, sliding velocity and distance, the study confirms that AlHMMC has superior wear resistance compared to the base alloy. Although the wear rate of AlHMMC increases with load and distance, it is still lower than that of Al6061. This result shows that AlHMMC has various advantages over Al6061 in different tribological applications. Furthermore, the study showed that the wear rate of AlHMMC decreases with increasing sliding velocity up to 4.18 m/s. However, it increases with distance. These results demonstrate the potential of AlHMMC for use in various automotive applications due to its superior wear resistance. As the sliding distance increases, the wear resistance of AlHMMC improves significantly, ranging from 20% to 50% compared to the Al6061 alloy. This improvement is attributed to the combined effects of applied load and sliding velocity. The key to this performance improvement is the integration of hard ceramic reinforcements (Al_2O_3) and soft solid lubricants (graphite) into the AlHMMC composition [25].

The results of the next study are highly significant for the automotive industry, especially for disk applications. These results demonstrate the competence and expertise of the researchers in this field. The results clearly demonstrate that hybrid

metal matrix composites (HMMCs) can significantly improve wear properties and facilitate weight reduction in brake systems. The HMMCs are expertly produced by a two-step stir-casting process in which aluminum alloy (AA2219) is melted and reinforcing materials such as SiC, Al_2O_3 and wollastonite are added. The resulting mixture is then poured into sand molds to form the composites [26].

Madan and his team are investigating the use of radial functional grading to improve disk performance. This technique, although not extensively covered in the existing literature, has been shown to be effective in improving disk performance. The study uses a powder metallurgy process to fabricate Al-SiC-based discs with three and five layers in which the concentration of SiC particles varies radially. Finite element analysis is used to thoroughly investigate the stress distribution in these wafers. The fabrication of the functionally graded material was successful. The uniform distribution of SiC and the seamless transition between layers without cracks or voids demonstrate the success of the process. The material also exhibits reduced grain size and increased hardness with a higher SiC content, making it an ideal candidate for use in various types of machines, such as power transmission and energy storage devices. This study presents a powder metallurgy method for producing functionally graded materials that have significant advantages for various industrial applications [27].

A metal matrix composite (MMC) has been successfully synthesized using the stir-casting technique. The composite consisted of an LM13 aluminum alloy base reinforced with silicon nitride (Si_3N_4) and graphite (Gr). The wear rate was significantly reduced as the sliding distance increased, demonstrating the superior performance of the composite. The LM13/Si_3N_4/Gr MMC was fabricated using the LM13 aluminum alloy for its superior wear resistance properties. Si_3N_4 and graphite were selected as reinforcing agents for their high temperature stability and lubricating properties, respectively. LM13 was melted in a controlled argon atmosphere to avoid unwanted atmospheric reactions during the manufacturing process. The LM13 alloy was melted, and 12 wt% Si_3N_4 and 3 wt% graphite, preheated to 250°C, were carefully added to the melt. The mixture was stirred at a constant speed of 200 rpm for five minutes to ensure uniform distribution of the reinforcements throughout the alloy. Once uniform dispersion was achieved, the molten composite was poured into a preheated mold 20 mm in diameter and 100 mm long. It was then allowed to cool and solidify at room temperature [23].

3. Components for Aluminum Matrix Composite Rotor Discs

3.1. Aluminum Matrix Substances:

3.1.1 Aluminum Metal Matrix composite AMC:

Aluminum alloys are an excellent choice for the automotive industry due to their low density, high strength-to-density ratio, and remarkable thermal

conductivity. They are particularly favored for various vehicle components where weight reduction and heat management are essential. Despite these advantages, there are challenges associated with using aluminum alloys for brake disc applications. To make these alloys a viable alternative to grey cast iron, it is crucial to improve their maximum operating temperature and wear resistance. While grey cast iron is often preferred due to its cost-effectiveness and performance under high-stress conditions, these alloys have the potential to surpass it with the right improvements. It is worth noting that the original text is supported by sources [28, 29].

Rettig and his team developed a new hyper-eutectic aluminum alloy named EDERALSI using a unique low-pressure die-casting technique. The composition of this innovative brake disc is detailed in Table 1. The high strength of this alloy is primarily attributed to its evenly distributed high silicon content. The uniform distribution of silicon particles and consistent grain sizes contribute significantly to the inherent strength of the alloy. This composition does not require post-processing temperature treatments or fiber incorporation to enhance its strength characteristics, simplifying the manufacturing process and making it an environmentally sustainable option. Moreover, the durability of the alloy obviates the necessity for supplementary surface treatments, underscoring its eco-friendly attributes and streamlining the manufacturing process [30]. The EDERALSI alloy offers three significant advantages over traditional grey cast iron used in brake discs. Firstly, it achieves a substantial weight reduction of up to 60%, which is a crucial factor in automotive design as lower weight can lead to improved fuel efficiency and overall vehicle performance. Secondly, this alloy maintains consistent frictional properties across a broad range of temperatures, ensuring reliable braking performance under varying operating conditions.

Table 1 – the material properties of Ederalsi and grey cast iron [30].

Elements	Weight %
Silicon	16-20
Magnesium	0.2- 0.7
Copper	0.3
Titanium	0.06- 0.1
Iron	0.2
Strontium	0.001
Aluminium	Balamce

Mann and colleagues confidently utilized the stir casting process to successfully produce a new hyper-eutectic AMC brake rotor material. This study showcases the competence and expertise of the researchers in developing a superior brake rotor material. The material, which consisted of LM 30 alloy as the matrix and was reinforced with natural mineral corundum (Al_2O_3) particles measuring 74 μm,

demonstrated an average stable wear rate 7% lower than that of traditional cast iron brake materials at a contact pressure of 1.8 MPa. The corundum particles played a crucial role in enhancing the strength of the AMC. They acted as a barrier to fracture propagation and reduced surface delamination, resulting in a significant increase in the wear resistance of the AMC brake disc material. Moreover, brake rotors made from this AMC material were approximately 60% lighter than their cast iron counterparts, which can greatly improve overall vehicle efficiency. This technical advancement represents a practical improvement in automotive design [31].

3.1.2 Aluminum Metal Matrix composite AMC:

Singh et al. introduced Al6061/SiC/Gr, an advanced metal matrix composite material, to enhance the efficiency of conventional car braking systems. Our team confidently assessed the performance and effectiveness of these rotors through detailed finite element analysis. The simulation results clearly indicate that the hybrid Al6061/SiC/Gr composite brake rotor has the potential to replace traditional cast iron brake discs. Table 2 presents the material properties of the composites used in the finite element analysis for a comprehensive understanding [32].

Table 2 – Material properties of new AI based HMMC and cast iron.

	Density (kg/m^3)	Young' Modulus E (MPa)	Poisons Ratio	Specific Heat ($J.Kg^{-1}.K^{-1}$)	Thermal Conductivity (W/m ºC)	Thermal Expansion Coefficient (K^{-1})	Hardness by Vickers (N/ mm2)
AL/ $SiC_{12\%}$ /$Gr_{5\%}$	2815	114	0.24	820	125	$2.3^{-0.5}$	101.7
Cast Iron	7150	119	0.27	460	52	$1.2^{-0.5}$	225

Ferraris and colleagues conducted a study on the feasibility of using aluminum alloys and composites as a substitute for cast iron or steel in the manufacturing of disc brake rotors. The study found that brake discs made from SiC/Al composites exhibited highly promising results, demonstrating their potential as a wear-resistant layer for brake discs in passenger cars. The study confirms that SiC/Al discs can withstand applied stresses and maintain an acceptable coefficient of friction (CoF). Furthermore, their heat dissipation behavior is comparable to that of conventional rotor materials. The significance of silicon (Si) in aluminum alloys utilized for rotor discs is also emphasized. Alloys containing silicon are ideal for this application because they can withstand high temperatures without experiencing galling or

seizure. Additionally, silicon's high thermal conductivity enhances heat dissipation from the brake surface, significantly reducing the likelihood of warping and cracking even in the most extreme conditions [33].

Awe et al. explores the potential of a lightweight SICAlight rotor as a replacement for traditional, gray-cast iron brake discs in future electric vehicle applications. The composite, consisting of AlSi9Mg0.6 and 20 wt% SiC particles, exhibits positive braking performance, minimal wear, low corrosion, reasonable durability, and favorable noise behavior. Extensive testing, including dynamometer and vehicle evaluations, demonstrates the benefits of the SICAlight rotor, such as lower particulate emissions compared to standard gray-cast iron rotors. In collaboration with disc and pad manufacturers, the study evaluates the performance of the aluminum rotor with compatible pads under electrified vehicle conditions. Comparisons with reference cast iron rotors show reduced PM10 emissions (78% reduction) for SICAlight rotors, highlighting potential benefits for battery electric vehicles, including weight reduction, reduced unsprung mass, and lower energy consumption. The corrosion resistance of SICA discs is also superior, indicating a reduced potential for noise, vibration, harshness, and PM emissions compared to GCI discs [34]. Where Sangeethkumar develops hybrid metal matrix composites (HMMC) for automotive rotor disc applications. The composites reinforce aluminum alloy AA2219 with silicon carbide (SiC), aluminum oxide (Al_2O_3), and wollastonite ($CaSiO_3$) to significantly improve wear properties and reduce the weight of cast iron disc brake rotors. The researchers conducted pin-on-disc wear tests and hardness tests to evaluate the tribological performance of the composites. The results clearly demonstrate that increasing the SiC and wollastonite content in the composite leads to a lower wear rate and improved wear resistance. Moreover, the composites with higher SiC and Al_2O_3 content exhibit superior wear characteristic [26].

Kumar's study analyzes AA5052/ZrB_2 composites and highlights a proportional increase in wear as sliding distance increases, a key consideration for brake rotor life. The study also identifies significant variations in the coefficient of friction, which is critical for consistent brake performance. A notable discovery is the escalation of wear rate and coefficient of friction with increasing sliding speed and load, marking a shift from mild to severe wear under extreme conditions. This finding is critical for the design of robust brake rotors capable of handling high-speed, high-load situations. In addition, the study suggests that tailoring the ZrB_2 content in composites can fine-tune their wear and friction characteristics, making them suitable for demanding applications such as brake rotors [35].

3.1.3 Titanium alloy

Qu's research clearly demonstrates that the oxygen diffusion (OD) process significantly improves the friction and wear properties of Ti-6Al-4V titanium alloys

for truck disk brake rotors. In fact, the results indicate that OD-treated Ti-6Al-4V (OD-Ti64) outperforms other titanium materials, including untreated Ti-6Al-4V, titanium-based metal matrix composites (MMCs), and thermally spray-coated titanium alloys. OD-Ti64 maintained an optimal friction coefficient of 0.35-0.50, even at high disk surface temperatures near 600°C, and displayed enhanced wear resistance, surpassing both untreated Ti-6Al-4V and titanium-based composites in durability [36].

In another search, Blau et al focused on two commercial titanium alloys, four experimental titanium-based composites with hard particles, and a titanium alloy that had undergone thermal spray coating [37]. The study found that the friction coefficients were influenced by the type of counter face material, whether semi-metallic or highly metallic, and by the temperature of the friction-induced wear track, which in some cases exceeded 800°C. Interestingly, the wear rates for the titanium metal matrix composites were higher than those of conventional cast iron but significantly lower than those of two of the titanium alloys tested. Of the materials tested, the thermally spray-coated titanium disk showed the least wear, highlighting its potential as a viable option for a lightweight, corrosion-resistant brake rotor material. This finding suggests a promising direction for future research and development in the field of automotive braking systems [38].

3.2 Reinforcement materials

Reinforced aluminum matrix composites (AMCs) offer several improved properties over monolithic aluminum alloys [39]. The effectiveness of AMCs, particularly in brake rotor applications, is largely influenced by the type of reinforcement used [40]. Various reinforcements such as SiC, Al_2O_3 and B_4C as well as natural minerals rich in alumina, silica and aluminum silicate are commonly used to improve the mechanical and tribological properties of AMC brake discs [41].

Hybrid AMCs (HAMCs) with dual reinforcement outperform single particle reinforced AMCs, especially in terms of wear resistance, thermal conductivity, and mechanical properties. The reinforcing particles primarily reinforce the matrix phase. Typically, a concentration of 5–10% is effective for micron-sized reinforcing particles. Even the addition of 5% nanoparticles can result in significant improvements in both mechanical and tribological properties. [42]. SiC is the most used synthetic reinforcement material in AMC rotor disks due to its effectiveness in improving the overall performance of the composite [43].

Sadagopan and his team developed an AMC brake disc made of AA6061 reinforced with 20% SiC. To improve its strength, hardness and wear resistance, the fabricated AMC brake disc was subjected to a meticulous three-step heat treatment process including solution annealing, quenching and age hardening. The AMC disc material exhibited a uniform wear pattern on its contact surface, resulting in a lower wear rate and coefficient of friction (CoF) compared to traditional cast iron discs. A

notable feature of these discs was the varying concentration of SiC particles in different layers, which contributed to their improved performance. The AMC disc showed superior braking efficiency and heat dissipation compared to conventional gray cast iron. The study analyzed the discs and found a lower temperature distribution, indicating the potential for longer brake disc life. This underscores the effectiveness of the AMC material in improving brake disc performance and durability [44].

Venkatachalam and colleagues investigated the use of dual reinforcement in AA6082, specifically combining 5 wt% SiC with 5 wt% fly ash and 5 wt% basalt. Their results showed that the Al/SiC/basalt composites have great potential as Hybrid Aluminum Matrix Composite (HAMC) materials for brake disc applications. The effective wetting of the reinforced particles within the aluminum alloy is critical to the performance and integrity of the composite. This property is responsible for the potential of the material [45].

Bracamonte and his team developed a novel sandwich structure for AMC brake rotors. The structure includes a thin, wear-resistant Al-SiC composite surface layer and an underlying aluminum alloy known for its high thermal conductivity. Their research showed that the tribological properties of the AMC surface layers were significantly affected by the temperature-pressure profile used during the manufacturing process. The process played a critical role in achieving a uniform distribution of Al and SiC particles or the formation of a distinctive mottled or vein-like microstructure. When compared to traditional cast iron rotors, the AMC brake rotors showed remarkable performance improvements. These improvements included minimal wear, no dust emissions, significantly reduced temperatures during braking, and extended service life. These advances highlight the potential of AMC brake rotors as a superior alternative in terms of both environmental friendliness and operational efficiency [46].

The interaction between the solid matrix and the reinforcement in composites can be explained by two types of bonding [47] : chemical and physical bridging. Physical bonding is characterized by relatively low bonding energy and involves hydrogen bonding and van der Waals forces [40]. On the other hand, chemical bonding provides high bonding energy due to processes such as chemical reactions and diffusion. These processes create a distinct interface. The strength of an aluminum matrix composite (AMC) is determined by three main factors: load carrying capacity, dislocation density, and the Orowan strengthening mechanism. In addition, the strength of AMCs can be improved by processes such as quenching and work hardening, which modify the properties of the material and contribute to its structural integrity [48].

Natarajan introduced a motorcycle brake rotor made of a 20% silicon carbide (SiC) reinforced aluminum matrix composite (AMC) combined with Al 6061. The goal of this combination is to reduce heat generation and unsprung mass, which in

turn improves vehicle handling. The rotor has increased strength, stiffness and improved high temperature performance. After being cast, machined, and heat treated, the mechanical and thermal properties of the AMC rotor are proven to be suitable for motorcycle applications. Wear tests have shown that the AMC rotor outperforms traditional cast iron (CI) rotors. Notably, the AMC rotor is 56% lighter than its CI counterpart, resulting in improved braking efficiency and reduced risk of brake fading. This makes it a promising option for high performance applications [44].

The metal-ceramic hybrid brake disc, weighing 4.8 kg, is a novel invention that combines carbon-silicon-carbide (C/SiC) friction segments with an aluminum backing. The design of this disc was created by Opel et al using Finite Element Analysis (FEA) and has proven to be effective in bringing a 1.8-ton vehicle to a complete stop from a speed of 200 km/h. This disc requires less C/SiC material than standard C/SiC brake discs, making it more efficient and lightweight. The disc was tested with LowMet, C/SiC, and C/C pads during emergency conditions and it was found that C/SiC pads had the best balance of coefficient of friction and wear rate, making them the most suitable choice [49, 50]

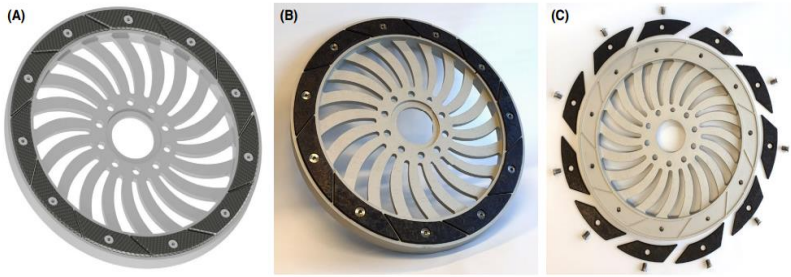

Figure 3 – final design of the metal- ceramic hybrid brake disc (outer diameter = 410): (a) rendering of cad design, (b) photo of built prototype, (c) carrier body with friction segments and correspondent screws [50].

In one hand, Fan et al. investigated the importance of selecting appropriate filler materials for friction blocks in high-speed train brakes. The goal was to optimize wear characteristics and minimize noise and vibration. Three different fillers were used sequentially: a Cu-based powder metallurgy material, a composite material, and a Mn-Cu damping alloy. The results showed that the filler material has a significant effect on the wear behavior at the brake interface and the friction-induced vibration characteristics. The Mn-Cu damping alloy was found to be particularly effective in reducing friction-induced vibration and noise in the brake

system, resulting in the lowest noise levels compared to other systems. The wear debris behavior of the fill materials and the interface wear characteristics are the primary influencers of friction-induced vibration and noise in the brake system [51].

Su et al introduce a novel SiCp/Al-20Si-3Cu functionally graded material (FGM) for brake disks. It demonstrates superior wear and friction properties compared to traditional cast iron (HT250) under various loads and speeds. Our research is significant due to its innovative material composition, detailed analysis of wear mechanisms, and potential to enhance brake system performance and safety in the automotive industry. It offers insights into how the distribution of SiC particles affects performance, shows a transition in wear mechanisms with changing conditions, and highlights the FGM's potential as a more effective and durable material for brake disk applications [52].

Singhal and his team also researched the performance of SiC particle-reinforced functionally graded material (FGM) for brake disk applications. The study demonstrates the impact of SiC particle distribution on performance, revealing a shift in wear mechanisms under varying conditions. The findings underscore the potential of FGM as a superior and long-lasting material for brake disk applications. The composites were fabricated with a porosity level of approximately 1.74%. The HAMCs with Sn and Gr demonstrated wear resistance within 6% of the commercial grey cast iron commonly used in automotive brake rotors [53].

The liquid metallurgy method was used to develop a hybrid composite consisting of LM13, 12 wt.% silicon nitride (Si_3N_4), and 3 wt.% graphite (Gr). The wear behavior of the composite was evaluated using a pin-on-disc tribometer, which revealed that the wear rate increased with both the load and sliding velocity. This increase in wear rate was attributed to the stress induced by the load causing the Si_3N_4 particles to fracture and damaging the aluminum matrix. Silicon nitride was chosen as the primary reinforcement due to its exceptional ability to maintain structural integrity even at high temperatures. Additionally, graphite was selected as the secondary reinforcement for its outstanding thermal and electrical conductivity. The morphological analysis depicted in Figure 4 revealed that the average size of silicon nitride particles was 5 μm, while that of graphite particles was 2 μm. A higher wear rate was observed with an increase in sliding velocity, primarily due to the abrasive action caused by the dislodged Si_3N_4 particles [54].

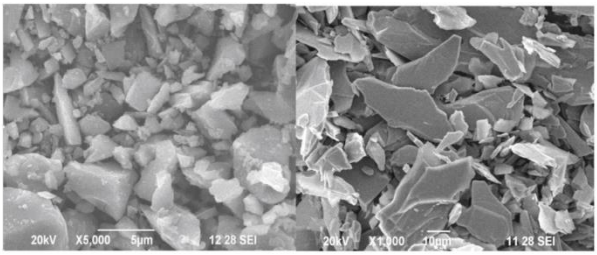

(a) Graphite **(b)** Silicon Nitride

Figure 4 – SEM morphology (a) Graphite, (b) Silicon nitride [54].

Omran and colleagues researched sustainable material science by incorporating recycled elements into their work. They focused on hindalium, a recycled Al-Mg-Si alloy, and enhanced its properties by adding silicon carbide (SiC) particles. The investigation revealed a significant improvement in the alloy's mechanical properties. The addition of SiC particles to the hindalium alloy at a concentration of 15% increases the material's hardness by 14%. The research notes a 17% reduction in wear rate in comparison to the original hindalium alloy, which sets a precedent in the utilization of recycled materials for high-end applications, marrying sustainability with technological advancement [55].

This study of Du et al. addresses the critical issue of reducing vehicle mass to lower fuel usage and greenhouse gas emissions in automotive engineering. The creation of aluminum metal matrix composite (Al-MMC) brake discs that are lightweight and high-performing is examined. The investigation focuses on Al-Si alloys fortified with varying proportions and dimensions of silicon carbide particles (SiCp). Lanthanum (La) and Cerium (Ce) are incorporated into the Al-MMC to fortify the aluminum matrix and enhance the brake discs' ability to withstand high temperatures, such as those encountered during prolonged braking periods. The creation of intermetallic phases through the addition of La and Ce further strengthens the composite. The inclusion of SiCp particles in larger sizes and a broader range enhances thermal endurance and ease of processing of the composite. The material demonstrates a twofold increase in compression peak strength while retaining its malleability [56].

In the other hand, Wang et al. found that the incorporation of nano-sized particles of silicon carbide (n-SiC) by powder metallurgy significantly improves the peak hardness and the aging hardening process of 2014 Al alloy composite materials. This discovery has important implications to produce automotive components, particularly brake rotors. Transmission electron microscopy (TEM) was used to accurately identify key precipitation phases, including $Al_5Cu_2Mn_3$ and θ' (Al_2Cu),

as well as the rarely seen Ω phase in aluminum metal matrix composites without silver (Ag). The higher dislocation density resulting from the thermal expansion coefficient mismatch between n-SiC and the 2014 Al matrix can be confidently attributed to the increase in aging kinetics and peak hardness. Composite materials have great potential to produce high-performance automotive parts, such as brake rotors, due to their ability to provide improved hardness and aging properties [57].

In the study of Lei and his team [58], the team compared three carbon/carbon (C/C) composites with varying compositions for brake rotors. The composites included rough laminar pyrocarbon, resin-derived carbon, and a mixture of both. The study clearly demonstrated that resin-derived carbon significantly increased wear rate without notably affecting friction coefficient, which had a negative impact on rotor durability and maintenance. The composites exhibited consistent friction coefficients at different speeds, but wear rates varied. However, it is important to note that the rough laminar pyrocarbon composite exhibited the least wear, indicating greater durability and a potentially longer service life. On the other hand, the carbon composite derived solely from resin wore down the fastest [59], suggesting a shorter lifespan in brake rotors.

4. Thermal Characteristics

Thermal analysis is critical in assessing the reliability of systems and components, especially those subjected to temperature cycling and thermal stress. In the case of aluminum metal matrix composites (AMCs), thermal analysis focuses on investigating the thermal behavior and response of the material to temperature changes, such as temperature distribution, heat transfer, and heat flux [60].

During braking, friction generates heat that raises the temperature of the brake rotor [61]. The ability of a material to rapidly dissipate heat is critical for effective high-temperature braking. Therefore, brake rotors must have high thermal conductivity, high thermal deformation resistance, and a low coefficient of thermal expansion [62]. Evaluation of these thermal properties is critical for any brake rotor disc alloy or composite. However, there are few studies that focus on these critical thermal properties of brake rotors [63].

Thermal conductivity is the rate at which heat passes through a material per unit thickness per unit area for each unit of temperature difference [64]. It can be evaluated using thermal or laser flash analyzers. The coefficient of thermal expansion, which indicates how a material's dimensions change with temperature changes, can be measured with a dilatometer. This instrument is essential for investigating the thermal properties of brake rotors, including thermal strain and thermal expansion [65].

In their study of the thermal dissipation capabilities of a high aluminum matrix composite (HAMC) brake disc, Gupta and colleagues used an LM27 alloy reinforced

with 15% rutile and sillimanite as shown in table 3. Their research focused on thermal conductivity, strain, and coefficient of expansion. The disc produced by HAMC showed significant resistance to thermal expansion due to the effective interfacial bonding between the matrix and the reinforcements. As a result, it exhibited superior thermal conductivity and lower thermal strain and expansion coefficient compared to rotors made of traditional gray cast iron [66].

Table 4 –Thermal properties of density of LM27 alloy, DRP-15 composite, and the commercial material.

Property	Materials		
	LM27 alloy	DRP- 15 compositr	Commercial brake rotor material
Thermal conductivity at 25 ºC, k (W/ mK)	154.42 ± 0.36	141.65 ± 0.81	55.82 ± 0.31
Thermal strain ε_t (* 10^{-3})	1.01 ± 0.17	0.57 ± 0.17	0.37 ± 0.08
Coefficient of thermal expansion CTE (* 10^{-6} /ºC^{-1})	18.95 ± 0.17	11.09 ± 0.017	7.12 ± 0.08
Density (g/ cm^3)	2.77 ± 0.004	2.82 ± 0.006	6.92 ± 0,005

Thermal analysis is critical in assessing the reliability of systems and components, especially those subjected to temperature cycling and thermal stress. In the case of aluminum metal matrix composites (AMCs), thermal analysis focuses on investigating the thermal behavior and response of the material to temperature changes, such as temperature distribution, heat transfer, and heat flux. During braking, friction generates heat that raises the temperature of the brake rotor. The ability of a material to rapidly dissipate heat is critical for effective high-temperature braking. Therefore, brake rotors must have high thermal conductivity, high thermal deformation resistance, and a low coefficient of thermal expansion. Evaluation of these thermal properties is critical for any brake rotor disc alloy or composite. However, there are few studies that focus on these critical thermal properties of brake rotors [67].

Thermal conductivity is the rate at which heat passes through a material per unit thickness per unit area for each unit of temperature difference. It can be evaluated using thermal or laser flash analyzers. The coefficient of thermal expansion, which indicates how a material's dimensions change with temperature changes, can be measured with a dilatometer. This instrument is essential for investigating the thermal properties of brake rotors, including thermal strain and thermal expansion [68].

Adebisi and her team conducted a study of a passenger car braking system, analyzing a stir-cast AMC brake rotor made of AA6061 alloy with 20% SiC and

comparing it to a cast iron rotor using thermal imaging. The rotors were mounted on a stand and monitored with an IR thermal camera for thermographic analysis. The AMC rotor showed uniform thermal dispersion and a 25% higher heat dissipation rate at brake pressures ranging from 1.5 to 2.0 MPa compared to the cast iron rotor. This was attributed to the superior thermal conductivity of the AMC material [69].

Separately, Jayaraj and colleagues investigated the thermal properties of an LM9 alloy reinforced with multi-walled carbon nanotubes (MWCNTs) at various weight fractions. The thermal conductivity of the stir-cast composites was evaluated using the hot disk technique. The MWCNTs present in the matrix acted as foreign particles, creating thermal barriers that impeded heat movement and reduced the thermal conductivity of the AMCs [70].

In the study conducted by Singh et al, they performed transient thermal analysis on brake disks to study heat flow and temperature variations. The results showed that while the cast iron heated up to a lower temperature of 98°C, the Al6061/SiC/Gr composite reached a higher temperature of 230°C. However, it is important to note that the maximum operating temperature of Al6061/SiC/Gr was below the maximum tolerance of the composite, which was 525°C. The Al6061/SiC/Gr material has high thermal conductivity, which allows for effective heat dissipation and reduces hot spot formation. This results in better temperature uniformity and can help minimize or eliminate thermal failures in brake pads and rotors, ultimately increasing their operational reliability compared to cast iron [32]. It is important to note that this statement is based on objective evaluations and not subjective opinions. This results in better temperature distribution and can help minimize or eliminate thermal failures in brake pads and rotors, ultimately improving their operational reliability compared to cast iron [26]

In their study, Firouz and colleagues [71] developed automotive brake rotors using Al-9Si-SiC and Al-12Si-SiC composites. The composites were reinforced with 10 or 20 weight percent SiC particles by stir casting. The resulting rotors exhibited a uniform distribution of SiC particles and a refined grain structure, which improved their overall microstructure. When exposed to temperatures ranging from room temperature to 350°C, the Al-12Si composites exhibited significantly lower coefficients of thermal expansion and minimal residual strain. In addition, the research included thermal fatigue testing of these composites against conventional cast iron rotors over 80 cycles. Analysis after these cycles, including hardness evaluation, microstructural examination, and X-ray diffraction, indicated that the composite rotors maintained consistent strain and temperature profiles during both the heating and cooling phases without hysteresis loops or residual strain. The crystalline structure of the composite rotors improved with thermal cycling, while that of the cast iron rotors deteriorated over time. This study highlights the potential of AlSi-SiC composites as superior materials for automotive brake rotors due to their

improved thermal stability and fatigue resistance compared to standard cast iron options.

Sharma et al. analyze the impact of heat treatment on the LM30 aluminum matrix composites reinforced with sillimanite. The composites had varying sillimanite content (3–15 wt.%) and particle sizes. They were treated through T4 and T6 methods. The increases in sillimanite content led to an improvement in hardness. Both T4 and T6 treatments resulted in better wear resistance and reduced friction. Specifically, the T6-treated composite with 15 wt.% sillimanite at 200°C showed a significant reduction in wear rate and friction coefficient by 70% and 52%, respectively, which is clear to show in figure 5. The composites had wear properties like those of grey cast iron. This suggests that they could serve as a lightweight alternative to heavy-cast iron in automotive parts like brake rotors [72].

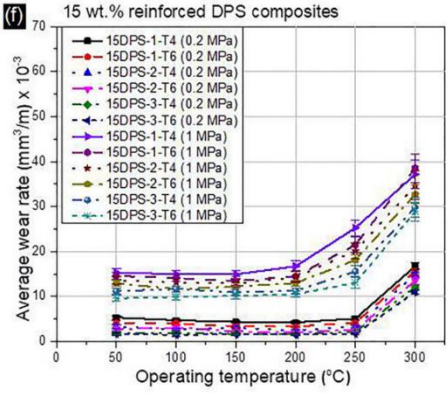

Figure 5 – Average wear rate versus operating temperature for heat treated 15DPS AMCs [72].

5. Tribological properties

Understanding the tribological behavior of Aluminum Matrix Composite (AMC) brake rotors is critical because it is influenced by several factors. The most important of these are the applied load and the sliding speed, both of which have a significant impact on the efficiency of the brake rotor. As a result, numerous studies have focused on these parameters to evaluate the wear and coefficient of friction (COF) rates of AMC brake rotors. The equation used to calculate the wear rate is.

$$K = \frac{\Delta m}{\rho F_n D}$$

Wear is the gradual degradation of material caused by continuous relative motion between two contacting surfaces. It is quantified as wear loss, which is the volume or mass loss of a material during a test period. The rate of wear can be determined using a specific formula. The wear rate 'r' is calculated from the mass loss before and after the wear test (Δm), the density of the material (ρ), the applied normal load (F_n) and the sliding distance (D). This calculation is critical for evaluating the durability and efficiency of AMC brake rotors under various operating conditions [24].

In a tribological evaluation using a small-scale dynamometer, Alnaqi and colleagues compared rotors made of AMC and gray cast iron. The study focused on Al6082 and AMC (Al6061/40% SiC) rotors, the latter having an alumina coating applied by plasma electrolyte oxidation. This coating increased the hardness of the AMC rotors and reduced their wear rates, resulting in a coefficient of friction (COF) in line with industry standards [73].

Lyu et al investigated the friction properties of an Al-SiC AMC brake disc using a pin-on-disc tribometer and non-asbestos organic (NAO) brake pads. They found that this AMC disc exhibited similar friction characteristics to conventional cast iron discs due to a self-generated protective tribo-layer that improved wear resistance [28].

Ahmad et al evaluated the wear and friction characteristics of AMC and cast-iron brake discs using a pin-on-disc tribometer. The AMC samples, consisting of AA242 with 30% Al_2O_3, showed a slight variation in CoF that was more pronounced at higher loads. This difference was attributed to the softer nature of the aluminum alloy compared to cast iron, resulting in increased surface roughness and wear [74].

Daoud and colleagues evaluated the wear and friction characteristics of A359-20 vol% SiC AMC rotors against commercial brake pads. They found that AMCs consistently outperformed cast iron in terms of CoF, which is critical for effective braking. The addition of SiC and Si to the AMC rotors contributed significantly to their superior strength, hardness, and wear resistance. This is due to the ability of the SiC particles to carry most of the wear load and increase the overall toughness of the composite. The reference remains unchanged [75].

Tan and colleagues conducted dynamometer tests on hybrid aluminum metal matrix composite (HAMC) brake rotors for rail vehicles. The results of the study suggest that HAMC brake rotors could be a promising alternative to conventional brake rotors in the rail industry. The discs, consisting of an A357/SiC MMC top layer fused to an AA6082 aluminum alloy base by friction stir processing, exhibited superior wear and friction performance. Capable of withstanding temperatures as high as 240°C, these rotors provide a consistent coefficient of friction, demonstrating their potential to replace traditional heavy iron and steel rotors on trains operating at 120 km/h. The presence of Third Body Films (TBFs) plays a critical role in reducing direct disc-pad contact, thereby reducing the incidence of cracking and debris

generation. This resulted in fewer surface grooves, less AMC layer degradation and less wear loss, which ensured a stable coefficient of friction [76].

Jiang and his team investigated the friction and wear characteristics of SiC3D/Al brake disks paired with graphite (G)/SiC brake pads using a smaller-scale dynamometer designed for high-speed train applications. They found that SiC3D/Al-G/SiC tribocouples outperformed traditional iron-steel pairs by offering lower operating temperatures, stable friction, and improved durability. The mechanically mixed layer formed during the sliding process significantly affected the wear and friction properties of the tribocouple, leading to its improved performance [77].

Baig et al. conducted a study of the tribological behavior of an aluminum composite reinforced with submicron Al_2O_3 particles used as a brake rotor material. The study compared the friction and wear properties of this composite with those of conventional gray cast iron rotors under dry sliding conditions with semi-metallic brake linings, as shown in the figure. The results indicate that the Al_2O_3-reinforced composite exhibits lower wear rates than gray cast iron, particularly at lower braking force intensities. In addition, the use of Al_2O_3 reinforcement results in reduced brake pad wear even at higher intensities due to its superior heat dissipation. The inclusion of submicron Al_2O_3 particles increase the wear resistance of the rotor and extends its life. In addition, the Al_2O_3 particles improve the friction and stability characteristics of the material, potentially lowering the coefficient of friction for smoother braking. The fine particles provide a more uniform distribution within the aluminum matrix, resulting in consistent friction behavior. In addition, the Al_2O_3 reinforcement aids in heat dissipation, improving the thermal stability of the rotor and maintaining performance during extensive braking [5].

6. Influence of Brake Pads on Aluminum Matrix Composite Disc

The effect of brake pad materials on the performance of Aluminum Matrix Composite (AMC) rotors is a critical factor in brake system performance [2]. Research indicates that Non-Asbestos Organic (NAO) pads are more suitable for use with aluminum rotors than low-steel or semi-metallic pads [78]. NAO materials are particularly notable for their ability to develop protective third body tribological layers under higher loads, resulting in a lower coefficient of friction and consistent wear rate [28, 30].

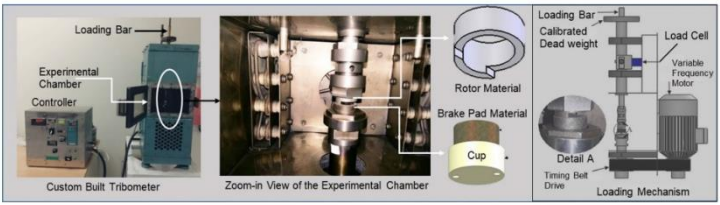

Figure 6 – Photograph of the Tribometer with Pad-on-Disc wear test configuration used in the wear experiments along with the schematic of the loading mechanism [5].

Nakanishi et al. aimed to improve fuel efficiency by reducing vehicle weight through the use of aluminum metal matrix composite (Al-MMC) brake rotors and pads [79]. They ensured that the braking performance and wear resistance of the Al-MMC system matched those of conventional cast iron systems by optimizing the amount and particle size ratio of hard particles in both the rotor and pad [80]. The researchers rigorously tested the wear resistance of the newly developed brake pad. The evaluation consisted of repeating 1000 braking cycles at different temperatures, starting from an initial speed of 50 km/h and a deceleration rate of 1.5 m/s^2 as shown in figure 7. To measure the changes in thickness of the pad need to evaluate its wear resistance [81]. The results were compared with those obtained with a conventional ferrous cast (FC) brake rotor and pad combination [82].

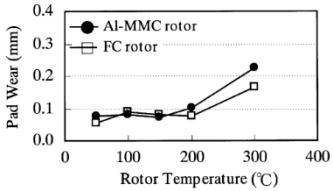

Figure 7 – Pad wear per 1000 braking times[79] .

Zhang and his team have developed a brake rotor composite that consists of 56% foam ceramics and 44% aluminum alloy. They have conducted rigorous tests on an Optimal SRV machine using a phenolic resin brake pad to thoroughly investigate the impact of temperature and load, between 32 N to 128 N, on friction and wear. The composite has shown predictable friction fade with increasing temperature, followed by remarkable over recovery on cooling [41]. The wear rates have also increased with temperature. The tests were meticulously carried out at both 100°C and 250°C. At 250°C, both friction and wear were significantly higher than

at 100°C. Scanning electron microscopy has revealed that the wear was mainly caused by two-body wear [83].

Agbeleye investigates the properties of brake pads made from aluminum 6063 alloy blended with 5–30% clay (Al-clay composites), produced through stir casting. Clay particle size in the composites is 250 microns. Using Denison T62HS pin-on-disc tests, the study assesses the composites' wear behavior under dry sliding conditions. Results show that composites with 10–25% clay content significantly enhance tensile strength, hardness, and wear resistance, with optimal performance at 15% clay. The wear rate is influenced by both load and sliding speed [84]. These Al-clay composites, especially with 15–25% clay, exhibit wear and friction characteristics on par with conventional semi-metallic brake pads [85].

Österle et al. present in their research a detailed analysis of frictional interfaces and coatings on a semi-metallic polymer matrix composite (PMC) brake pad. The focused ion beam (FIB) technique is expertly employed to examine the topmost layers at the micro-contact regions of the brake pad. The frictional material of the brake pad is a blend of a metallic polymer matrix composite and is expertly paired with a cast iron rotor as shown in the next figure. The brake pad is composed of up to three distinct layers [41], each with its own unique composition. These layers consist of a thin friction film made of metal oxides and a sulfur-rich amorphous phase, a layer filled with wear debris, and a heavily distorted layer, especially when a metal particle is used as the base [86]. The analysis confidently indicates the accumulation of iron oxide particles from wear and the adhesion of copper and sulfur on the pad's surface. Furthermore, it highlights the transfer of zinc onto the cast iron rotor [87].

The research of Venugopal et al. investigates the use of magnesium (Mg) composites reinforced with Ni-P-coated alumina and silicon carbide microparticles for brake pad applications [88]. These composites are produced using a special stir-squeeze process. To test their suitability for brake systems, the study uses a tribometer in which the Mg composite acts as a pin against a stainless-steel disk, mimicking the brake pad-rotor interaction. Key findings show that coating the reinforcements significantly reduces the porosity of the composite and increases its hardness and compressive strength. The wear resistance of these Mg composites is comparable to that of conventional brake pad materials, highlighting their potential as effective friction materials in automotive braking systems working in conjunction with rotors [41].

The study of et al. Darmawan examines the wear rates of brake pads in the LRV Series 1100, utilizing both regenerative and pneumatic braking systems. Its goal is to forecast brake pad longevity and uncover reasons for wear rate disparities between motor and trailer bogie brake pads. Through linear regression of maintenance and field data, it predicts brake pad life spans—2039 for McA and McB bogies and 2029 for trailer bogies—noting that braking method impacts wear rates. The findings

underline how braking force and friction influence pad durability, which is crucial for optimizing maintenance and enhancing safety. This analysis aids the rotor desk in strategic planning for maintenance and replacements, potentially lowering costs and ensuring safety by adapting maintenance to actual wear trends.[89, 20].

7. Impact of Surface Texture (R_a) on Rotor Disc

In tribological studies, it is critical to understand the effect of surface roughness, commonly referred to as R_a, on the performance of Aluminum Matrix Composite (AMC) brake rotors [75]. To evaluate the wear rate and friction characteristics of the disc materials, it is necessary to measure the surface roughness of both the disc and pad material before and after tribological testing. To evaluate the wear rate and friction characteristics of the disk materials, it is necessary to measure the surface roughness of both the disk and pad material before and after tribological testing. This helps us to obtain accurate and reliable results. Prior to testing, it is important to ensure that the AMC brake disc and pad material have consistent R_a values [90].

Research has shown that the surface roughness of AMC brake rotors tends to increase significantly after being subjected to dynamometer testing [73]. This increase is attributed to the weakening of the alloy matrix at the contact surface due to the high temperatures experienced during testing. It is also useful to measure the surface roughness of the protective tribofilm formed on the disk. This helps to verify the consistency of the coefficient of friction (CoF) under varying load conditions. Understanding the effect of surface roughness on AMC discs is critical to optimizing brake performance and durability. This is discussed in reference [28].

Biswas et al. investigated the development, characterization, and application of Al-Mg_2Si composites in motorcycle disc brake rotors. The performance of Al-Mg_2Si composites was compared with traditional materials such as cast iron and stainless steel using the Digital Logic Method (DLM) for material selection. In a simulated motorcycle disc brake scenario, the Al-20wt% Mg_2Si composite and steel rotors were evaluated. The technical performance index of the Al-Mg_2Si composite was 73.65, slightly lower than that of steel at 78.10. However, the Energy Efficiency Index (EEI) of the composite was significantly lower at 31.79 compared to 100 for steel. Notably, the composite had significantly lower CO_2 and CO emissions of 0.087 and 0.0026 g/km, respectively, compared to steel's 0.276 and 0.0082 g/km [91].

Alnaqi studied the effects of alumina coatings applied via plasma electrolytic oxidation (PEO) on AA6082 aluminum alloy (Al-Alloy) and 6061/40SiC aluminum metal matrix composite (Al-MMC) brake rotors, focusing on friction and high-temperature performance. The PEO process improves adhesion, uniformity, and surface hardness, with Al-Alloy achieving higher micro-hardness (1400 HV) than Al-MMC (980 HV). Al-Alloy rotors show superior thermal and frictional performance, handling over 500°C, while Al-MMC rotors have reduced heat

tolerance. Coated rotors maintain acceptable friction coefficients (0.28 to 0.34). Al-Alloy rotors keep consistent coating thickness, unlike Al-MMC. Both rotor types develop a 2–4 mm transfer layer. However, alumina-coated Al-Alloy rotors fail above 550°C due to mechanical and thermal stress. Improvements could involve metallurgical changes or design modifications like ventilated discs [73].

In a novel study, laminate composite brake material designed for high-speed train braking systems was developed using powder metallurgy. This material has a bilayer structure consisting of prefabricated tribofilm (PTF, oxide-based) and metal-based materials. We evaluated the friction and wear performance of this brake pad, focusing on variations in PTF layer thickness, against a steel rotor disk. Tests were conducted using a TM-I type dynamometer at initial braking speeds (IBS) ranging from 50 to 350 km/h. The results showed that the PTF pad maintained stable friction and wear rates over a wide range of IBS (50–250 km/h) suitable for high-speed train applications. Key to its performance is the protective friction film formed on the pad's worn surface during braking, which is enhanced by the PTF layer, providing a larger, flatter contact area compared to metal-based materials. This film contributes to the pad's consistent friction performance and wear rate [92].

Synák et al. study the automotive brake components (rotors and pads) at different price points to determine if they effectively convert kinetic energy into thermal energy without overheating. It combines driving and laboratory tests to evaluate stopping distance, deceleration, steering effort, braking force, temperature, and corrosion resistance. The results show that while all brakes perform well under standard conditions, the least expensive brakes may underperform under intense or prolonged use [93].

8. Computational Examination of Aluminum Matrix Composite Brake Discs

Numerical analysis is used in brake system design to predict thermal aspects such as friction pressure distribution, surface heat flow, brake temperature distribution, radial surface temperature, and thermal stress [94]. Effective management of the conversion of kinetic energy to frictional heat at the disc can improve braking efficiency. This can be achieved through ideal rotor design and the use of superior heat dissipating materials. Heat transfer in brakes is primarily by conduction and convection, with radiation playing a minor role (5-10%). Research typically includes analysis of both transient thermal and structural aspects. However, the integration of fluid analysis for heat convection with thermal simulations provides a more comprehensive approach, especially under different braking conditions, such as prolonged, single emergency, and repeated braking events [95].

Pranta and colleagues conducted innovative research to redesign ventilated disc brake rotors. They incorporated unique curved vents, holes, and slots (as shown in

Figure 10) using Solidworks. Their analysis in ANSYS showed that these novel designs outperformed conventional disc brake rotors in terms of performance, achieving higher braking forces while avoiding cracking and buckling during operation [96].

Ali et al. analyzed the thermo-mechanical dynamics of brake rotors and pads during braking using ANSYS finite element software. They examined both full and vented disk interfaces within the braking system. The results showed a rapid temperature increase followed by a decrease after sustained braking, which was attributed to the disc brake design. Despite variations in friction coefficients, the deformation of the disc pad remained largely unchanged [97].

Nong and colleagues recommend the use of aluminum metal matrix composites (AMCs) in brake discs, especially for high-speed train applications where energy efficiency is a priority. They first determined heat convection coefficients using Solidworks 2014 flow simulation, which informed their CFD-based design. The subsequent thermal analysis used these coefficients as initial conditions. The study analyzed the use of radially vented SiC3D/Al alloy brake rotors, which were found to significantly improve airflow around and through the rotor. This improved airflow effectively dissipated frictional heat, resulting in a temperature reduction of up to 14%. The high thermal conductivity of the discs also resulted in a more uniform temperature distribution across the rotor. A peak temperature of 471.08°C was recorded at the 70-second mark near the outer regions of the friction surface, as shown in Figure 11. This underscores the suitability of the material for high-speed rail applications [98].

This study analyzes disc brake rotors, using finite element analysis (FEA) to compare aluminum alloy and aluminum matrix nanocomposite (AMNC) rotors at 70 km/h emergency braking. Key findings include: AMNCs' superior strength-to-weight ratio, aluminum alloy's max heat flux at 8 W/mm² versus AMNC's 16.28 W/mm², aluminum alloy's max deformation at 0.19 mm compared to AMNC's 0.05 mm, and AMNC's max von Mises stress at 184 MPa, slightly higher than aluminum alloy's 180 MPa. This suggests AMNCs as a viable alternative for disc brake rotor materials, Results of the ANSYS modal analysis are presented for the aluminum alloy and AMNC discs [99, 100].

Kumar et al use the grey relational analysis (GRA) to improve the specific wear resistance and friction coefficient of AlHMMC. Using the Grey Relational Analysis (GRA) approach, the study reveals distinct influences on the friction coefficient of Al6061 alloy and its hybrid composite, AlHMMC. For Al6061, the sliding distance, followed by sliding velocity and applied load, are key factors in that order. Conversely, for AlHMMC, the order of influence is applied load (43.67%), sliding velocity (42.51%), and then sliding distance [35].

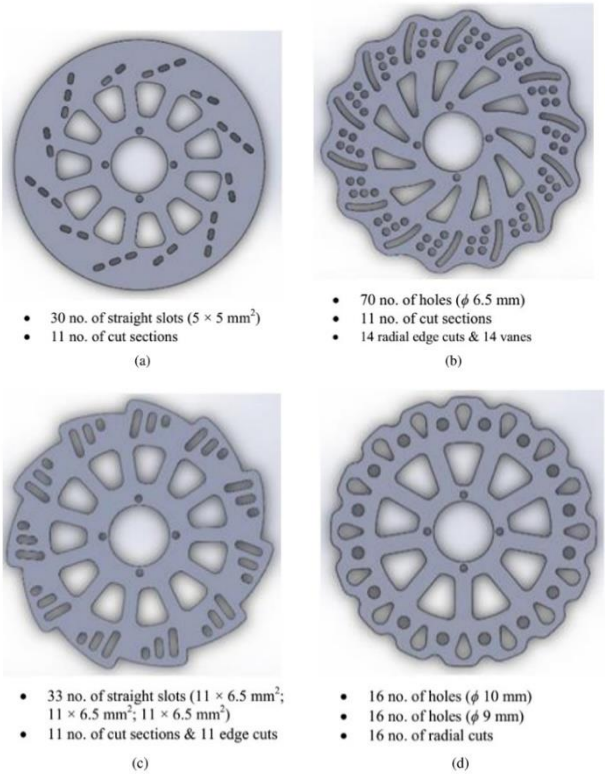

Figure 8 – Diagramof(a)Basemodel, (b)modifiedmodel1(MM1), (c)modifiedmodel2(MM2) and(b)modifiedmodel3 (MM3) with description [98].

The specific wear rate in another study analysis using GRA-ANOVA highlights that sliding velocity impacts Al6061 and AlHMMC by 39.57% and 42.51%, respectively. However, the applied load has a more pronounced effect on AlHMMC for all sliding distances. In summary, while both Al6061 and AlHMMC are influenced by similar factors, the order and magnitude of these influences differ significantly between the two materials [45].

References:

1. *G. Riva, G. Valota, G. Perricone, J. Wahlström*. "An FEA approach to simulate disc brake wear and airborne particle emissions," Tribol. Int. 2019. vol. 138, pp. 90–98. doi: 10.1016/j.triboint.2019.05.035.
2. *D. Viderščak et al.* "Influence of Brake Pad Properties to Braking Characteristics," Promet – TrafficTransportation. 2022. vol. 34. no. 1. pp. 91–102. doi: 10.7307/ptt.v34i1.3846. **3.** *W. Li., X. Yang., S. Wang., J. Xiao., Q. Hou*. "Comprehensive Analysis on the Performance and Material of Automobile

Brake Discs," Metals. 2020. vol. 10. no. 3. p. 377. doi: 10.3390/met10030377. **4.** *M. K. Wasekar., M. P. Khond.* "A Composite Material an alternative for manufacturing of Automotive Disc Brake: A Review," IOP Conf. Ser. Mater. Sci. Eng. 2021. vol. 1126. no. 1. p. 012067. doi: 10.1088/1757-899X/1126/1/012067. **5.** *M. M. A. Baig., A. M. Al-Qutub., I. M. Allam., F. Patel., A. S. Mohammed*. "Tribological Performance of Sub-Micron Al2O3-Reinforced Aluminum Composite Brake Rotor Material," Arab. J. Sci. Eng. 2021. vol. 46. no. 3. pp. 2691–2700. doi: 10.1007/s13369-020-05179-x. **6.** *J. Wahlström., V. Matejka., Y. Lyu., A. Söderberg*. "Contact Pressure and Sliding Velocity Maps of the Friction, Wear and Emission from a Low-Metallic/Cast-Iron Disc Brake Contact Pair," Tribol. Ind. 2017. vol. 39. no. 4. pp. 460–470. doi: 10.24874/ti.2017.39.04.05. **7.** *K. K. Alaneme., T. M. Adewale., P. A. Olubambi.* "Corrosion and wear behaviour of Al–Mg–Si alloy matrix hybrid composites reinforced with rice husk ash and silicon carbide," J. Mater. Res. Technol. 2014. vol. 3. no. 1. pp. 9–16. doi: 10.1016/j.jmrt.2013.10.008. **8.** *R. Manikandan, T. V. Arjunan, A. R. Nath O. P.* "Studies on micro structural characteristics, mechanical and tribological behaviours of boron carbide and cow dung ash reinforced aluminium (Al 7075) hybrid metal matrix composite," Compos. Part B Eng. 2020. vol. 183. p. 107668. doi: 10.1016/j.compositesb.2019.107668. **9.** *Y. K. Singla., R. Chhibber., H. Bansal., A. Kalra*. "Wear Behavior of Aluminum Alloy 6061-Based Composites Reinforced with SiC, Al2O3, and Red Mud: A Comparative Study," JOM, 2015. vol. 67, no. 9. pp. 2160–2169. doi: 10.1007/s11837-015-1365-0. **10.** *A. Rehman., S. Das., G. Dixit*. "Analysis of stir die cast Al–SiC composite brake drums based on coefficient of friction," Tribol. Int. 2-12. vol. 51. pp. 36–41. doi: 10.1016/j.triboint.2012.02.007. **11.** *R. M., D. S*. "Synthesis of Al-TiO2 Composites through Liquid Powder Metallurgy Route," Int. J. Mech. Eng. 2014, vol. 1. no. 1. pp. 12–15. doi: 10.14445/23488360/IJME-V1I1P103. **12.** *P. S. Reddy., R. Kesavan., B. Vijaya Ramnath*. "Investigation of Mechanical Properties of Aluminium 6061-Silicon Carbide, Boron Carbide Metal Matrix Composite," Silicon, 2018. vol. 10. no. 2. pp. 495–502. doi: 10.1007/s12633-016-9479-8. **13.** *R. Chebolu., R. Nallu., and R. Chanamala*. "Experimental investigation on mechanical behavior of as cast Zn-Al-Cu/SiC/TiB 2 hybrid metal matrix composite by ultrasonic assisted stir casting technique," Eng. Res. Express. 2022. vol. 4. no. 2. p. 025040. doi: 10.1088/2631-8695/ac71f7. **14.** *R. Harichandran., N. Selvakumar*. "Effect of nano/micro B4C particles on the mechanical properties of aluminium metal matrix composites fabricated by ultrasonic cavitation-assisted solidification process," Arch. Civ. Mech. Eng. 2016. vol. 16. no. 1. pp. 147–158. doi: 10.1016/j.acme.2015.07.001. **15.** *S. Soltani, R. Azari Khosroshahi, R. Taherzadeh Mousavian, Z.-Y. Jiang, A.* Fadavi Boostani, and D. Brabazon, "Stir casting process for manufacture of Al–SiC composites," Rare Met. 2017. vol. 36. no. 7. pp. 581–590. doi: 10.1007/s12598-015-0565-7. **16.** *V. Mohanavel., M. Ravichandran.* "Optimization of Parameters to Improve the Properties of AA7178/Si3N4 Composites Employing Taguchi Approach," Silicon. 2022. vol. 14. no. 4. pp. 1381–1394. doi: 10.1007/s12633-020-00917-0. **17.** *M. I. Ul Haq., A. Anand.* "Dry Sliding Friction and Wear Behavior of AA7075-Si3N4 Composite," Silicon. 2018. vol. 10. no. 5. pp. 1819–1829. doi: 10.1007/s12633-017-9675-1. **18.** *R. Arunachalam et al.* "Optimization of stir–squeeze casting parameters for production of metal matrix composites using a hybrid analytical hierarchy process–Taguchi-Grey approach," Eng. Optim. 2019. pp. 1–18. doi: 10.1080/0305215X.2019.1639693.
19. *C. U. Atuanya., V. S. Aigbodion.* "Evaluation of Al–Cu–Mg alloy/bean pod ash nanoparticles synthesis by double layer feeding–stir casting method," J. Alloys Compd. 2014 vol. 601. pp. 251–259. doi: 10.1016/j.jallcom.2014.02.086. **20.** *P. Madhukar., N. Selvaraj., C. S. P. Rao., G. B. Veeresh Kumar*. "Enhanced performance of AA7150-SiC nanocomposites synthesized by novel fabrication process," Ceram. Int. 2020. vol. 46, no. 10. pp. 17103–17111. doi: 10.1016/j.ceramint.2020.04.007. **21.** *S. Mahanta., M. Chandrasekaran., S. Samanta., C. Sasikumar*. "Fabrication of Al7075-B4C-fly ash hybrid nanocomposites by ultrasonic assisted stir casting and tensile analysis," presented at the INTERNATIONAL CONFERENCE ON MATERIALS, MANUFACTURING AND MACHINING 2019, Tamilnadu, India, 2019, p. 020026. doi: 10.1063/1.5117938. **22.** *T. B. Rao.* "Microstructural, mechanical, and wear properties characterization and strengthening mechanisms of Al7075/SiCnp composites processed through ultrasonic cavitation assisted stir-casting," Mater. Sci. Eng. A. 2021. vol. 805. p. 140553. doi: 10.1016/j.msea.2020.140553. **23.** *A. Ramanathan., P. K. Krishnan., R. Muraliraja*.

"A review on the production of metal matrix composites through stir casting – Furnace design, properties, challenges, and research opportunities," J. Manuf. Process. 2019. vol. 42, pp. 213–245. doi: 10.1016/j.jmapro.2019.04.017. **24.** *P. K. Dinesh Kumar., S. Darius Gnanaraj*. "Aluminium-Silicon based Metal Matrix Composites for brake rotor applications: a review," Eng. Res. Express. 2023. vol. 5. no. 2. p. 022002. doi: 10.1088/2631-8695/accdb6. **25.** *M. Kumar., M. M. A., V. Baskaran., K. H. Ramji.* "Effect of sliding distance on dry sliding tribological behaviour of Aluminium Hybrid Metal Matrix Composite (AlHMMC): An alternate for automobile brake rotor – A Grey Relational approach," Proc. Inst. Mech. Eng. Part J J. Eng. Tribol. 2016. vol. 230. no. 4. pp. 402–415. doi: 10.1177/1350650115602724. **26.** *E. Sangeethkumar., M. Jaikumar., K. M. N. Sridath., V. Ramanathan., R. Sathyamurthy*. "Tribological study on hybrid metal matrix composites for application in automotive sector," Mater. Res. Express. 2019. vol. 6. no. 5. p. 055703. doi: 10.1088/2053-1591/ab0579. **27.** *R. Madan., S. Bhowmick.* "Fabrication and microstructural characterization of Al-SiC based functionally graded disk," Aircr. Eng. Aerosp. Technol. 2023. vol. 95. no. 2. pp. 292–301. doi: 10.1108/AEAT-03-2022-0096. **28.** *Y. Lyu., J. Wahlström., M. Tu., U. Olofsson.* "A Friction, Wear and Emission Tribometer Study of Non-Asbestos Organic Pins Sliding Against AlSiC MMC Discs," Tribol. Ind. 2018. vol. 40. no. 2. pp. 274–282, Jun. 2018, doi: 10.24874/ti.2018.40.02.11. **29.** *P. B. Pawar., R. M. Wabale., A. A. Utpat.* "A Comprehensive Study of Aluminum Based Metal Matrix Composites: Challenges and Opportunities," Mater. Today Proc. 2018. vol. 5. no. 11. pp. 23937–23944, 2018. doi: 10.1016/j.matpr.2018.10.186. **30.** *M. Rettig et al.* "Carbidic Brake Rotor Surface Coating Applied by High-performance-laser Cladding," in EuroBrake 2020 Technical Programme, FISITA. 2020. doi: 10.46720/eb2020-mds-025. **31.** *V. S. Mann., O. P. Pandey.* "Effect of Dual Particle Size Corundum Particles on the Tribological Properties of LM30 Aluminium Alloy Composites for Brake Rotor Applications," Arab. J. Sci. Eng. 2021. vol. 46. no. 12, pp. 12445–12463. doi: 10.1007/s13369-021-05939-3. **32.** *M. Singh et al.* "Design and Analysis of an Automobile Disc Brake Rotor by Using Hybrid Aluminium Metal Matrix Composite for High Reliability," J. Compos. Sci. 2023. vol. 7. no. 6. p. 244. doi: 10.3390/jcs7060244. **33.** *M. Ferraris et al.* "SiC particle reinforced Al matrix composites brazed on aluminum body for lightweight wear resistant brakes," Ceram. Int. 2022. vol. 48. no. 8. pp. 10941–10951. doi: 10.1016/j.ceramint.2021.12.313. **34.** *S. Awe.* "Sustainable aluminium brake discs and pads for electrified vehicles," in Proceedings of the FISITA - Technology and Mobility Conference Europe 2023, Barcelona, Spain: FISITA. 2023. doi: 10.46720/eb2023-tst-020. **35.** *N. Kumar., G. Gautam., R. K. Gautam., A. Mohan., S. Mohan.* "Wear, friction and profilometer studies of insitu AA5052/ZrB2 composites," Tribol. Int. 2023. vol. 97. pp. 313–326. doi: 10.1016/j.triboint.2016.01.036. **36.** *J. Qu., P. J. Blau., B. C. Jolly.* "Oxygen-diffused titanium as a candidate brake rotor material," Wear. 2019. vol. 267. no. 5–8. pp. 818–822. doi: 10.1016/j.wear.2008.12.044. **37.** *P. J. Blau., B. C. Jolly., J. Qu., W. H. Peter., C. A. Blue.* "Tribological investigation of titanium-based materials for brakes," Wear. 2007. vol. 263. no. 7–12. pp. 1202–1211. doi: 10.1016/j.wear.2006.12.015. **38.** *M. Kindrachuk et al*. "Wear-friction properties of friction pairs in disc-pad brakes," East.-Eur. J. Enterp. Technol. 2023. vol. 4. no. 12 (124). pp. 56–61. doi: 10.15587/1729-4061.2023.285699. **39.** *P. K. Yadav., G. Dixit., B. Kuriachen., M. K. Verma., S. K. Patel., R. K. Singh.* "Effect of Reinforcements and Abrasive Size on High-Stress Tribological Behaviour of Aluminium Piston Matrix Composites," J. Bio- Tribo-Corros. 2020. vol. 6. no. 1. p. 23. doi: 10.1007/s40735-019-0317-6. **40.** *A. Baradeswaran., A. Elaya Perumal.* "Influence of B4C on the tribological and mechanical properties of Al 7075–B4C composites," Compos. Part B Eng. 2013. vol. 54. pp. 146–152. doi: 10.1016/j.compositesb.2013.05.012. **41.** *U. V. Saindane., S. Soni., J. V. Menghani*. "Recent research status on modern friction materials-an Overview," IOP Conf. Ser. Mater. Sci. Eng. 2020. vol. 810. no. 1. p. 012067. doi: 10.1088/1757-899X/810/1/012067. **42.** *K. L. Zheng., X. S. Wei., B. Yan., P. F. Yan.* "Ceramic waste SiC particle-reinforced Al matrix composite brake materials with a high friction coefficient," Wear. 2020. vol. 458–459. p. 203424. doi: 10.1016/j.wear.2020.203424. **43.** *B. Subramaniam., B. Natarajan., B. Kaliyaperumal., S. J. S. Chelladurai.* "Investigation on mechanical properties of aluminium 7075 - boron carbide - coconut shell fly ash reinforced hybrid metal matrix composites," China Foundry. 2018. vol. 15. no. 6. pp. 449–456. doi: 10.1007/s41230-018-8105-3. **44.** *S. P., H. K. Natarajan., P. K. J*. "Study of silicon carbide-reinforced aluminum matrix composite brake rotor

for motorcycle application," Int. J. Adv. Manuf. Technol. 2018. vol. 94. no. 1–4. pp. 1461–1475. doi: 10.1007/s00170-017-0969-7. **45.** *G. Venkatachalam., A. Kumaravel.* "Mechanical Behaviour of Aluminium Alloy Reinforced with Sic/Fly Ash/Basalt Composite for Brake Rotor," Polym. Polym. Compos. 2017. vol. 25. no. 3. pp. 203–208. doi: 10.1177/096739111702500304. **46.** *L. Bracamonte., J. Withers., T. Smith*. "Lightweight, Wear Resistant, High Thermal Conductivity Metal Matrix Composite Brake Rotors," presented at the Brake Colloquium & Exhibition - 36th Annual. Oct. 2018. pp. 2018-01–1879. doi: 10.4271/2018-01-1879. **47.** *M. Afiefudin., R. D. Widodo., R. Rusiyanto.* "Fabrication and Characterization of Asbestos Free Brake Pads Composite using Elaeocarpus Ganitrus as Reinforcement," Automot. Exp. 2023. vol. 6. no. 2. pp. 359–371. doi: 10.31603/ae.9367. **48.** *Z. Zhang., D. L. Chen.* "Contribution of Orowan strengthening effect in particulate-reinforced metal matrix nanocomposites," Mater. Sci. Eng. A. 2008. vol. 483–484. pp. 148–152. doi: 10.1016/j.msea.2006.10.184. **49.** *M. M. Jalilvand., Y. Mazaheri*. "Effect of mono and hybrid ceramic reinforcement particles on the tribological behavior of the AZ31 matrix surface composites developed by friction stir processing," Ceram. Int. 2020. vol. 46. no. 12. pp. 20345–20356. doi: 10.1016/j.ceramint.2020.05.123. **50.** *T. Opel., N. Langhof., W. Krenkel.* "Development and tribological studies of a novel metal‐ceramic hybrid brake disc," Int. J. Appl. Ceram. Technol. 2022. vol. 19. no. 1. pp. 62‐74. doi: 10.1111/ijac.13826. **51.** *Z. Y. Fan et al*. "Effect of Surface Modification on the Tribological Properties of Friction Blocks in High-Speed Train Brake Systems," Tribol. Lett. 2021. vol. 69. no. 1, p. 27. doi: 10.1007/s11249-021-01402-4. **52.** *B. Su, H. G. Yan., J. H. Chen., P. L. Zeng., G. Chen., C. C. Chen.* "Wear and Friction Behavior of the Spray-Deposited SiCp/Al-20Si-3Cu Functionally Graded Material," J. Mater. Eng. Perform. 2013. vol. 22. no. 5. pp. 1355–1364. doi: 10.1007/s11665-012-0409-7. **53.** *V. Singhal., O. P. Pandey*. "Wear and Friction Behavior of Gr/Sn Solid Lubricated Dual Reinforced AMCs," Silicon. 2022. vol. 14. no. 10. pp. 5629–5645. doi: 10.1007/s12633-021-01343-6. **54.** *N. Raj., N. Radhika.* "Tribological Characteristics of LM13/Si3N4/Gr Hybrid Composite at Elevated Temperature," Silicon. 2019. vol. 11, no. 2, pp. 947–960. doi: 10.1007/s12633-018-9893-1. **55.** *S. H. Omran., M. M. Al-Masoudy., O. H. Hassoon., M. A. Fayad*. "Optimization of mechanical wear resistance for recycled (Al-Mg-Si) reinforced SiC composite material using PM method," Curved Layer. Struct. 2022. vol. 9, no. 1. pp. 295–303. doi: 10.1515/cls-2022-0023. **56.** *A. Du et al*. "The Influence of Ce, La, and SiC Particles Addition on the Formability of an Al-Si-Cu-Mg-Fe SiCp-MMC," Materials. 2022. vol. 15. no. 11. p. 3789. doi: 10.3390/ma15113789.
57. *Z. Wang et al.* "Aging Behavior of Nano-SiC/2014Al Composite Fabricated by Powder Metallurgy and Hot Extrusion Techniques," J. Mater. Sci. Technol. 2016. vol. 32. no. 10. pp. 1008–1012. doi: 10.1016/j.jmst.2016.07.011. **58.** *B. Lei., M. Yi., H. Xu., L. Ran., Y. Ge., K. Peng.* "Effect of Resin-Derived Carbon on the Friction Behavior of Carbon/Carbon Composites," Tribol. Lett. 2011. vol. 41. no. 2. pp. 371–378. doi: 10.1007/s11249-010-9723-0. **59.** *S. Liu., C. Martin., D. Lashmore., M. Schauer., C. Livermore*. "Carbon nanotube torsional springs for regenerative braking systems," J. Micromechanics Microengineering. 2015. vol. 25. no. 10. p. 104005. doi: 10.1088/0960-1317/25/10/104005. **60.** *F. Talati., S. Jalalifar*. "Investigation of Heat Transfer Phenomena in a Ventilated Disk Brake Rotor with Straight Radial Rounded Vanes," J. Appl. Sci. 2008. vol. 8. no. 20. pp. 3583–3592. doi: 10.3923/jas.2008.3583.3592. **61.** *A. A. Araújo Filho., A. Yu. Petrov.* "Higher-derivative Lorentz-breaking dispersion relations: a thermal description," Eur. Phys. J. C. 2021. vol. 81. no. 9. p. 843. doi: 10.1140/epjc/s10052-021-09639-y. **62.** *H. Tian et al.* "Significant improvement of thermal and tribological performance with polyimide as the matrix of paper‐based friction materials," Polym. Compos. 2022. vol. 43. no. 4. pp. 2303‐2317. doi: 10.1002/pc.26541. **63.** *G. Sayeed Ahmed., S. Algarni*. "Design, Development and FE Thermal Analysis of a Radially Grooved Brake Disc Developed through Direct Metal Laser Sintering," Materials. 2018. vol. 11. no. 7. p. 1211, Jul. doi: 10.3390/ma11071211. **64.** *X. Liu et al.,* "3D Hydrogel Evaporator with Vertical Radiant Vessels Breaking the Trade‐Off between Thermal Localization and Salt Resistance for Solar Desalination of High‐Salinity," Adv. Mater. 2022. vol. 34. no. 36. p. 2203137. doi: 10.1002/adma.202203137. **65.** *S. Polenz et al*. "Development of a System for Additive Manufacturing of Ceramic Matrix Composite Structures Using Laser Technology," Materials. 2021. vol. 14. no. 12. p. 3248. doi: 10.3390/ma14123248. **66.** *R. Gupta.,*

S. Sharma., T. Nanda., O. P. Pandey. "Wear studies of hybrid AMCs reinforced with naturally occurring sillimanite and rutile ceramic particles for brake-rotor applications," Ceram. Int. 2020. vol. 46. no. 10. pp. 16849–16859. doi: 10.1016/j.ceramint.2020.03.262. **67.** *P. Samal., P. R. Vundavilli., A. Meher., M. M. Mahapatra*. "Recent progress in aluminum metal matrix composites: A review on processing, mechanical and wear properties," J. Manuf. Process. 2020. vol. 59. pp. 131–152. doi: 10.1016/j.jmapro.2020.09.010. **68.** *V. Saravanan., P. R. Thyla., S. R. Balakrishnan*. "A low cost, light weight cenosphere–aluminium composite for brake disc application," Bull. Mater. Sci. 2016. vol. 39. no. 1. pp. 299–305. doi: 10.1007/s12034-015-1134-2. **69.** *A. A. Adebisi., Md. A. Maleque., Q. H. Shah*."Performance assessment of aluminium composite material for automotive brake rotor," Int. J. Veh. Syst. Model. Test. 2014. vol. 9. no. 3/4. p. 207. doi: 10.1504/IJVSMT.2014.066501. **70.** *A. Jayaraj., Ch. V. K. N. S. N. Moorthy., V. S. N. Venkataramana., S. Jaikumar., V. Srinivas*. "Corrosion, mechanical and thermal properties of aluminium alloy metal matrix nano composites (AA-MMNCs) with multi-walled carbon nanotubes," SN Appl. Sci. 2020. vol. 2. no. 7. p. 1259. doi: 10.1007/s42452-020-3081-9. **71.** F. M. Firouz., E. Mohamed., A. Lotfy., A. Daoud., M. T. Abou El-Khair, "Thermal expansion and fatigue properties of automotive brake rotor made of AlSi–SiC composites," Mater. Res. Express. 2020. vol. 6. no. 12. p. 1265d2. doi: 10.1088/2053-1591/ab6129. **72.** *S. Sharma., T. Nanda., O. P. Pandey*. "Heat treatment T4 and T6 effects on the tribological properties of sillimanite mineral-reinforced LM30 aluminium alloy composites at elevated temperatures," Proc. Inst. Mech. Eng. Part J J. Eng. Tribol. 2022. vol. 236. no. 5. pp. 946–959. doi: 10.1177/13506501211036543. **73.** *A. A. Alnaqi., S. Kosarieh., D. C. Barton., P. C. Brooks., S. Shrestha*. "Material characterisation of lightweight disc brake rotors," Proc. Inst. Mech. Eng. Part J. Mater. Des. Appl. 2018. vol. 232. no. 7. pp. 555–565. doi: 10.1177/1464420716638683. **74.** *F. Ahmad., S. H. J. Lo., M. Aslam., A. Haziq*. "Tribology Behaviour of Alumina Particles Reinforced Aluminium Matrix Composites and Brake Disc Materials," Procedia Eng. 2013. vol. 68. pp. 674–680. doi: 10.1016/j.proeng.2013.12.238. **75.** *A. Daoud., M. T. Abou El-khair*. "Wear and friction behavior of sand cast brake rotor made of A359-20vol% SiC particle composites sliding against automobile friction material," Tribol. Int. 2010. vol. 43. no. 3. pp. 544–553. doi: 10.1016/j.triboint.2009.09.003. **76.** *D. Tan et al*. "Evaluation of the wear resistance of aluminium-based hybrid composite brake discs under relevant city rail environments," Mater. Des. 2022. vol. 215. p. 110504. doi: 10.1016/j.matdes.2022.110504. **77.** *L. Jiang et al*. "Fabrication, microstructure, friction and wear properties of SiC3D/Al brake disc−graphite/SiC pad tribo-couple for high-speed train," Trans. Nonferrous Met. Soc. China. 2019. vol. 29. no. 9. pp. 1889–1902. doi: 10.1016/S1003-6326(19)65097-1.
78. *S. Panchenko., J. Gerlici., G. Vatulia., A. Lovska., V. Ravlyuk., J. Harusinec*. "Studying the load of composite brake pads under high-temperature impact from the rolling surface of wheels," EUREKA Phys. Eng. 2023. no. 4. pp. 155–167. doi: 10.21303/2461-4262.2023.002994. **79.** *H. Nakanishi*. "Development of aluminum metal matrix composites (Al-MMC) brake rotor and pad," JSAE Rev. 2002. vol. 23. no. 3. pp. 365–370. doi: 10.1016/S0389-4304(02)00203-5. **80.** *N. Kalel., B. Bhatt., A. Darpe., J. Bijwe*. "Role of binder in controlling the noise and vibration performance of brake-pads," Proc. Inst. Mech. Eng. Part J. Automob. Eng. 2023. vol. 237. no. 13. pp. 3200–3213. doi: 10.1177/09544070221123729. **81.** *Z. Guo., J. Zuo., J. Ding., X. Wang*. "Friction Coefficient Characteristics of Typical Subway Brake Shoes and Brake Pads in Service," J. Phys. Conf. Ser. 2023. vol. 2542. no. 1. p. 012007. doi: 10.1088/1742-6596/2542/1/012007. **82.** *H. Yavuz*. "An Experimental Case Study on The Comparison of The Use of Micronized Quartz and Alumina in Brake Pads," Türk Doğa Ve Fen Derg. 2023. vol. 12. no. 3. pp. 9–14. doi: 10.46810/tdfd.1291333. **83.** *S. Y. Zhang., S. G. Qu., Y. Y. Li., W. P. Chen*. "Two-body abrasive behavior of brake pad dry sliding against interpenetrating network ceramics/Al-alloy composites," Wear. 2010. vol. 268. no. 7–8. pp. 939–945. doi: 10.1016/j.wear.2009.12.004. **84.** S. Wang, Z. Yu, J. Wang, and S. Chen, "Research on CNN-LSTM Brake Pad Wear Condition Monitoring Based on GTO Multi-Objective Optimization," Actuators. 2023. vol. 12. no. 7. p. 301. doi: 10.3390/act12070301. **85.** *A. A. Agbeleye., D. E. Esezobor., S. A. Balogun., J. O. Agunsoye., J. Solis., A. Neville*. "Tribological properties of aluminium-clay composites for brake disc rotor applications," J. King Saud Univ. - Sci. 2020. vol. 32. no. 1. pp. 21–28. doi: 10.1016/j.jksus.2017.09.002. **86.** *O. Kliuiev., V. Makarenko., Y. Mieshkov., O. Voitovych*. "Experimental studies of truck transport brake pads materials friction properties," Collect. Sci.

Works State Univ. Infrastruct. Technol. Ser. Transp. Syst. Technol. 2023. no. 41. pp. 35–44. doi: 10.32703/2617-9059-2023-41-3. **87.** W. Österle and I. Urban, "Friction layers and friction films on PMC brake pads," Wear. 2004. vol. 257. no. 1–2. pp. 215–226. doi: 10.1016/j.wear.2003.12.017. **88.** *S. Venugopal, L. Karikalan., R. Kumar*. "Experimental Investigations on the Effect of Reinforcement Coating on Magnesium Composites for Automotive Brake Pad," Adv. Mater. Sci. Eng. 2022. vol. 2022. pp. 1–9. doi: 10.1155/2022/7604681. **89.** *B. I. Darmawan., K. Iwan*. "ANALISIS LAJU KEAUSAN BRAKE PAD TERHADAP DISC BRAKE KERETA LISTRIK LRV SERI 1100," J. Konversi Energi Dan Manufaktur. 2023. vol. 8. no. 2. doi: 10.21009/JKEM.8.2.4. **90.** *F. Karaca., E. Unal., I. Can*. "Investigation of braking performance and thermal effect of sintering of brake pads with Al2O3 additive," Therm. Sci. 2022. vol. 26. no. Spec. issue 1. pp. 67–73. doi: 10.2298/TSCI22S1067K. **91.** P. Biswas., M. K. Mondal. "Evaluation of a Cast Al-Mg2Si Composite for Automobile Disk-Brake Rotor Application," J. Mater. Eng. Perform., Oct. 2023, doi: 10.1007/s11665-023-08760-1. **92.** X. Zhang et al., "Tribological Properties of Laminate Composite Brake Material for High-Speed Trains," Tribol. Trans. 2022. vol. 65. no. 4. pp. 579–591. doi: 10.1080/10402004.2022.2057376. **93.** *F. Synák., L. Jakubovičová., M. Klačko*. "Impact of the Choice of Available Brake Discs and Brake Pads at Different Prices on Selected Vehicle Features," Appl. Sci. 2022. vol. 12. no. 14. p. 7325. doi: 10.3390/app12147325. **94.** *S. Kerrouz., T. Tamine., M. Bouchetara*. "Numerical Simulation of the Elastic Behavior of the Automotive Brake Disc in Dry Sliding Contact With the Pads," WSEAS Trans. Appl. Theor. Mech., vol. 17, pp. 215–225, Dec. 2022, doi: 10.37394/232011.2022.17.26. **95.** *A. Karnik., M. D. Gudela., A. Sawant., S. M. Auti*. "Numerical Analysis of Different Design Iterations of a Brake Disk," presented at the Automotive Technical Papers, Jan. 2021. pp. 2020-01–5215. doi: 10.4271/2020-01-5215. **96.** *M. H. Pranta., M. S. Rabbi., S. C. Banik., M. G. Hafez., Y.-M. Chu*. "A computational study on structural and thermal behavior of modified disk brake rotors," Alex. Eng. J. 2022. vol. 61. no. 3. pp. 1882–1890. doi: 10.1016/j.aej.2021.07.013. **97**. *B. Ali*. "Finite Element Analysis of Automotive Disk Brake and Pad in Frictional Model Contact:," Int. J. Manuf. Mater. Mech. Eng. 2015. vol. 5. no. 4. pp. 32–62. doi: 10.4018/IJMMME.2015100103. **98.** *X. D. Nong., Y. L. Jiang., M. Fang., L. Yu, C. Y. Liu*. "Numerical analysis of novel SiC3D/Al alloy co-continuous composites ventilated brake disc," Int. J. Heat Mass Transf. 2017. vol. 108. pp. 1374–1382. doi: 10.1016/j.ijheatmasstransfer.2016.11.108. **99.** P. *Sivaprakasam., E. Abebe., R. Čep., M. Elangovan*. "Thermo-Mechanical Behavior of Aluminum Matrix Nano-Composite Automobile Disc Brake Rotor Using Finite Element Method," Materials. 2022 vol. 15. no. 17. p. 6072, Sep. doi: 10.3390/ma15176072. **100.** *M. Nouby., K. Srinivasan*. "Simulation of the structural modifications of a disc brake system to reduce brake squeal," Proc. Inst. Mech. Eng. Part J. Automob. Eng. 2011. vol. 225. no. 5. pp. 653–672. doi: 10.1177/2041299110394515.

Афраа Хаттаб, Чаба Фельхо, Мішкольц, Угорщина

АЛЬТЕРНАТИВНЕ ЗАСТОСУВАННЯ АЛЮМІНІЄВИХ МАТРИЧНИХ КОМПОЗИТІВ ДЛЯ ГАЛЬМІВНИХ ДИСКІВ

Анотація. *У цьому огляді літератури розглядається можливість використання алюмінієвих матричних композитів (АМК) замість звичайного сірого чавуна в пакетах гальмівних дисків. Керуючись перевагою більш легких та екологічних транспортних засобів, АМК пропонують кілька переваг, включаючи зменшену вагу, покращені теплові властивості, чудову стійкість до корозії та оптимізовану систему руйнування. Дослідження дійшли висновку, що АМК можуть зменшити вагу до 60% порівняно з чавуном, що призводить до поступового підвищення продуктивності газу та управління автомобілем. Крім того, що він демонструє чудову теплопровідність і менше теплове збільшення, він призводить до кращого розсіювання тепла та зменшує небезпеку деформації та розтріскування. Перевага використання керамічних підсилювачів, які включають SiC, Al_2O_3 і B_4C, полягає в тому, що вони можуть підвищити стійкість до пошкоджень АМК, що призводить до більш тривалого терміну служби гальмівних*

дисків. Огляд охоплює різні елементи розробки гальмівного диска АМК, починаючи з виробничих стратегій (лиття з перемішуванням, лиття з перемішуванням за допомогою ультразвуку та лиття під тиск), які є потужними технологіями для виробництва надзвичайно хороших дисків АМК, потім теплові характеристики, які є такими важливими через їх теплопровідність, теплове розширення та розсіювання тепла в загальному циклі експлуатації гальмівного диска, нарешті, Трибологічні показники впливають на навантаження через швидкість ковзання та шорсткість поверхні на знос та тертя дисків АМК. Сумісність гальмівних колодок настільки важлива для систем тертя, що вибір відповідних матеріалів гальмівних колодок, наприклад, які містять неазбестові органічні (НАО) речовини, може оптимізувати експлуатаційну продуктивність дисків АМК. Ці характеристики можуть бути проаналізовані обчислювальним шляхом використання оцінки кінцевих елементів та різних чисельних методів для прогнозування теплової та механічної поведінки гальмівних дисків АМК. В огляді підкреслюється, що АМК зберігають великі перспективи як виробництво гальмівних дисків наступної ери, пропонуючи баланс зниження ваги, ступінчастий термоконтроль і більш вигідну зносостійкість. Необхідні подальші дослідження та вдосконалення для оптимізації складу структури, стратегій виробництва та сумісності гальмівних колодок для покращення експлуатаційних показників АМК в гальмівних конструкціях.

Ключові слова: *гальмівні диски; алюмінієві матричні композити (АМК); трибологія; гальмівні колодки.*

UDC 621.923.74 **doi: 10.20998/2078-7405.2024.100.09**

ANALYSIS OF THE ABBOTT-FIRESTONE CURVE ON A DIAMOND-BURNISHED SURFACE

Szilárd **Smolnicki**, Gyula **Varga** [0000-0003-3810-2881]

University of Miskolc, 3515 Miskolc-Egyetemváros, Hungary
gyulavarga@uni-miskolc.hu

Received: 25 March 2024 / Revised: 21 April 2024 / Accepted: 26 May 2024 / Published: 15 June 2024

Abstract. *In the research we provide a brief overview of the context of the topic, starting from the issues of energy efficiency and environmental awareness and sustainable development, through the positive properties of alternative forms of processing such as diamond burnishing, to the examination of the surface finish, which plays a key role in the relationship between surface quality and diamond burnishing. In the first chapter of this paper, the science of sustainable development, industrial ecology and its different systems models are presented, leading to the three pillars of sustainable development. In the same chapter, we touch on the relationship between energy- and eco-efficiency, their characteristics, recent research results and impacts. We present the dimensions and material quality of the test piece on which the tests were carried out. This will be followed by a description of the technological characteristics of the turning and diamond-burnishing processes. The characteristics and usefulness of the Abbott-Firestone curve are listed, and the improvement factors and K-coefficients are calculated. In the third section, experimental results are presented by examining the data of the Abbott-Firestone surface curves, which are presented using both the improvement factors and the K-coefficients to draw conclusions by examining the different technological parameters. We conclude our study by summarizing the results of our research.*

Keywords: *energy efficiency; sustainable development; slide diamond burnishing; surface finish.*

1. Energy efficiency issues

1.1. About sustainable development

Industrial ecology, also known as the science of sustainability, is primarily concerned with the harmonisation of natural and industrial systems, based on a wide range of objective information on the performance of and interrelations between the two systems [1]. Its history goes back to the middle of the 20th century, when a report published in 1972 predicted unsustainable demand and production, a worldwide increase in pollution, depletion of natural resources, widespread malnutrition, and a growing world population [2]. In 1987, the report of the commission chaired by Gro Harlem Brundtland defined sustainable development as development that meets the needs of the present without compromising the ability

of future generations to meet their own needs [3]. Then in 1989, Schaltegger and Sturm examined sustainable development in an eco-efficiency approach, the idea being that goods and services are of greater value if they produce less waste and pollution [4]. The 1992 United Nations Conference on Environment and Development in Rio de Janeiro produced the “Agenda 21” report, one paragraph of which stated that 'achieving the goals of environmental quality and sustainable development will require efficiency in production and changes in consumption patterns, with a focus on optimising resource use and minimising waste' [5].

Industrial ecology is thus how humanity can approach and maintain consumer needs in the face of continuous economic, cultural, and technological development; while the concept requires that an industrial system be considered in harmony with, rather than in isolation from, its surrounding systems [1]. Its essence can be illustrated by presenting three different system models, as shown in Figure 1. Type I is a linear system, where resources are implanted in unlimited quantities, which are disposed of as waste after use. In a Type II system, on the other hand, internal cycles are created and there will be significant internal reuse of materials, so that the amount of material entering and leaving the system can be limited. In a Type III system, full material cycling is achieved, where only energy input is required [1].

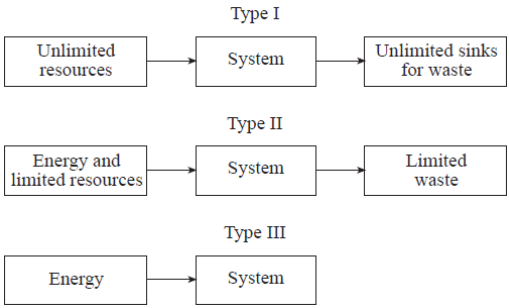

Figure 1. Industrial ecology system types [6]

Sustainable development is not a recent concept, but its achievement still seems very far away even today. The reasons for this are to be found in its three pillars, as shown in Figure 2. Aligning society, the environment and the economy is not easy, and changes in any one of them can upset the balance, because development wants to be liveable, equitable and eco-efficient at the same time.

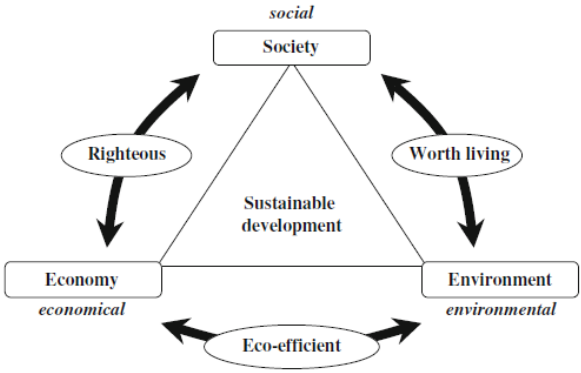

Figure 2. The three pillars of sustainable development [7]

1.2. From energy efficiency to eco-efficiency

The eco-efficiency of a process resolves an apparent contradiction through appropriate innovations and approaches: it "seeks development that allows for an increase in well-being for all while reducing the use of nature" [1].

The reasons for pursuing eco-efficiency are summarised in the following list [8, 9]:

- to attract the attention of companies by encouraging them to innovate,
- to encourage innovation to stimulate innovation, to overcome market failures, external costs, public goods provision, information, and adaptation gaps,
- generate knowledge about likely resource efficiency gaps and potential areas for improvement,
- create and stabilise demand for environmental improvements,
- levelling the playing field in transition periods between technological development paths,
- increasing the likelihood of a new direction of technological development,
- maintaining the policy function of more stringent measures in cases where the state of the environment continues to deteriorate, or new negative external costs emerge.

Eco-efficient perceptions are also leading companies to rethink quality. By recycling and reusing materials that were previously accepted as by-products in processes, they unleash the power of innovation and quality management, for example in waste management, so that the redistributed knowledge base can be used in the actual production itself, as a by-product of change, such as the replacement or reuse of production inputs, increased process yields, careful monitoring and maintenance, and product improvement [10].

To summarise, seven essential guidelines for eco-efficiency can be distinguished [11]:

- reducing the material intensity of goods and services,
- reducing the intensity of goods and services,
- reducing the dispersion of toxic substances,
- reduce the recyclability of materials,
- maximise the sustainable use of renewable resources,
- extend the durability of products,
- increase the service intensity of products.

In addition to these guidelines, indirect elements such as a new perspective on human needs and quality of life, recognition of the capacity limits of ecosystems, and the continuous development of the concept to reflect its dynamic nature are also important [10].

The environmental equivalent of the concept of zero defects in quality insurance is nothing less than zero emissions of hazardous or potentially hazardous substances from a facility or product. Although this is almost impossible, the eco-efficient approach seeks to minimise waste emissions [11]. Practice shows that these guidelines are often in sync with consumer needs, as the size of electronic devices tends to decrease with the development of computing, while the proliferation of digital storage devices (flash drives, hard disks) will eventually eliminate paper-based documentation.

The standard DIN EN ISO 14045 deals with the assessment of eco-efficiency, an approach that can be applied to the assessment of the relationship between certain economic values and the environmental impact of manufacturing processes and systems. The assessment consists of five phases [12, 13]:

(1) definition of purpose and scope,
(2) environmental assessment,
(3) product system value assessment,
(4) quantification of eco-efficiency and
(5) interpretation.

The purpose and scope statement (1) defines the purpose of the eco-efficiency evaluation, the target audience, and the intended use of the results. The environmental assessment (2) is used to determine the potential environmental impact of the product system. The product system value assessment (3) considers the whole life cycle of the product system by assessing the value or desirability of the functional, monetary or other values assigned. In quantifying eco-efficiency (4), the ratio between the results of the environmental assessment and the assessment of the value of the product system is determined in accordance with the definition of the objective and scope [12, 13]. However, the perspective from which the ratio of environmental impact to product quality is ultimately interpreted (5) may differ.

Some research refers to eco-efficiency as eco-productivity, since many economists consider the environment (including natural resources) as a factor of production, and thus formulate eco-productivity as the welfare output of goods and services per unit of environment consumed [14]. The inverse of this, eco-intensity, is closer to the engineering approach, and refers to the use of natural resources per unit of welfare output [1].

Nor are the basic concepts of thermodynamics true in this case, since market conditions are determined by people's capricious preferences (e.g. a torn pair of jeans is more valuable than a spotless pair), which therefore changes the demand function and prices. Furthermore, since companies link their performance evaluation to environmental performance, it is worthwhile to choose a measure of eco-productivity in terms of $\frac{CO_2}{kg}$ or $\frac{resource}{kg}$ [14].

2. Surface machining and roughness measurement

2.1. Characteristics of the test piece

After a theoretical overview, we now turn to the experiments, for which a special axial part designed for this purpose was machined, the technical drawing of which is shown in Figure 3. The part was designed with six cylindrical surfaces where measurements can be taken and was manufactured on machine tools at the workshop of the Institute of Manufacturing Science of the University of Miskolc. A total of four pieces were made.

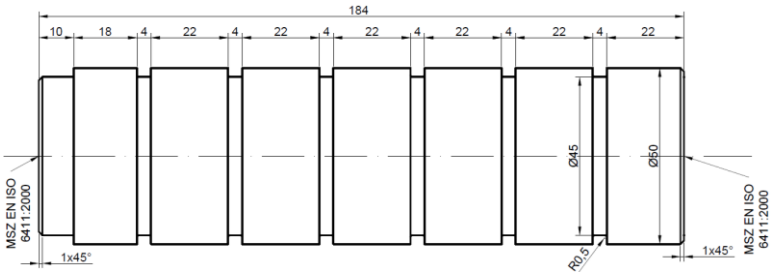

Figure 3. Technical drawing of the test specimen

The material used for the machining was austenitic stainless chromium-nickel steel alloy with a fabricated structure, designated 1.4307 (further designations: X2CrNi18- 9/304L/S30403), which has good corrosion resistance properties and is well suited to cold forming and welding. Due to its excellent anti-fouling properties, resistance to oxidation and easy cleanability, it is often used for food processing equipment (brewing, dairy, wine making), kitchen equipment and

appliances and chemical equipment (containers, heat exchangers, soap making). Its chemical composition is summarised in Table 1 [15].

Table 1. Chemical composition (at 20 °C) - DIN 10088-1:2005 [15]

Element	**Fe**	**C**	**Si**	**Mn**	**P**	**S**	**N**	**Cr**	**Ni**
%	66.8-71,3	≤0.03	1	2	0.045	0.015	≤0.11	17.5-19.5	8-10.5

The yield strength of an alloy $R_{p0,2} \geq 210\ MPa$; its tensile strength $R_m = 520 - 700\ MPa$, while its elongation at break is $A \geq 45\%$. Its density $\rho = 7.9\ kg/dm^3$, its hardness is $160 - 190\ HB$.

2.2. Features of turning

Machining started with sawing the parts to size, then continued with the centre hole on the left side of the part and the machining of the diameter for the clamping on the EU-400-01 lathe. This was followed by longitudinal turning in =Ø50 mm, and then the plunge-cutting starting from the right end of the part every 22 mm.

The technological parameters of the lathe were set up as follows for the surfaces to be measured:

- $v_c = 1.3875 \left[\frac{m}{s}\right]; f = 0.05\ \frac{mm}{revolution}$

In total, 24 surfaces (4 test pieces, 6-6 surfaces per test piece) were turned under the same conditions.

2.3. Features of diamond burnishing

Diamond burnishing used to replace low productivity and costly machining operations (grinding, mirror finishing, polishing) as a finishing operation for high precision and low roughness working surfaces. The advantage of diamond tools is that they have a very low coefficient of friction when friction is applied to metal surfaces, which allows the surface to be polished to low roughness [16].

After turning, the test pieces were not immediately machined by diamond burnishing, but roughness measurements were taken beforehand to compare them with the results of diamond burnishing to obtain a more accurate picture of the effectiveness of diamond burnishing. The methodology of the comparison and the roughness measurements are described in the following chapters.

The diamond burnishing was carried out using the same EU-400-01 type EU-400-01 lathe with a clamped burnishing tool. The head of the burnishing tool was a single-grain diamond, and the machining conditions are schematically illustrated in Figure 4 [17]. In the figure, 1 is the workpiece, 2 the burnishing tool, 3 the burnishing insert, 4 the tool clamp and 5 the diamond tip.

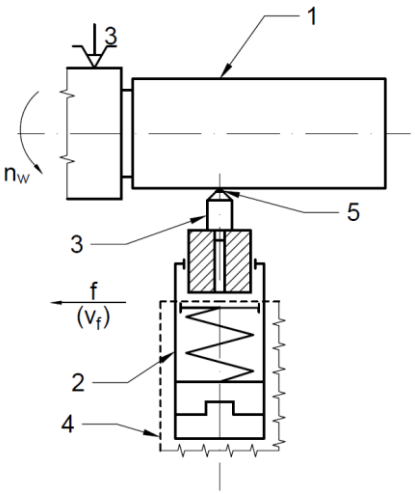

Figure 4. Schematic diagram of diamond burnishing [17]

During surface burnishing, the reduction of surface roughness and the hardening of the surface layer is caused by the sliding friction between the diamond tool and the workpiece surface, which is much harder than the material to be machined [18].

The technological data for diamond burnishing were different for each surface, which were the result of combinations of rate of rotation, feed rate and burnishing force exerted by the burnishing tool. These combinations are summarised in Table 2. The marking of the surfaces was grouped by hexadecimal using the test pieces. Two calculated values were also added to the table, the burnishing speed – formula (1) – and the machining power – formula (2).

$$v_v = d \cdot \pi \cdot n \left[\frac{m}{s}\right] \quad (1)$$

$$P = F \cdot v_v \quad (2)$$

Table 2. Technological data for diamond burnishing

Serial Nr.	$f\left[\frac{mm}{rev}\right]$	$n\left[\frac{1}{min}\right]$	$v_v\left[\frac{m}{s}\right]$	$F\ (N)$	$P\ (W)$
1-1	0.05	265	0.6938	120	83.25
1-2	0.05	265	0.6938	100	69.38
1-3	0.05	265	0.6938	80	55.50
1-4	0.05	265	0.6938	60	41.63
1-5	0.05	265	0.6938	40	27.75
1-6	0.05	265	0.6938	20	13.88

2-1	0.1	265	0.6938	120	83.25
2-2	0.1	265	0.6938	100	69.38
2-3	0.1	265	0.6938	80	55.50
2-4	0.1	265	0.6938	60	41.63
2-5	0.1	265	0.6938	40	27.75
2-6	0.1	265	0.6938	20	13.88
3-1	0.05	375	0.9817	120	117.81
3-2	0.05	375	0.9817	100	98.17
3-3	0.05	375	0.9817	80	78.54
3-4	0.05	375	0.9817	60	58.90
3-5	0.05	375	0.9817	40	39.27
3-6	0.05	375	0.9817	20	19.63
4-1	0.1	375	0.9817	120	117.81
4-2	0.1	375	0.9817	100	98.17
4-3	0.1	375	0.9817	80	78.54
4-4	0.1	375	0.9817	60	58.90
4-5	0.1	375	0.9817	40	39.27
4-6	0.1	375	0.9817	20	19.63

2.4. Measurement of surface roughness

The concept of surface quality encompasses the deformations, roughness and waviness of the machined surface [19]. In the following, the main 2D and 3D roughness metrics are presented, so that we can then compare the individual characteristics based on certain considerations. These are given in micrometres.
The characteristics of the Abbott-Firestone Curve (AFC) are described in ISO 13565, which divides the surface curve into peak, core and valley zones [20]. Accordingly, there are three surface roughness characteristics that provide information on the material content of the surface. These are:

- R_k: core roughness depth
- R_{pk}: reduced peak height
- R_{vk}: reduced valley height

As shown in Figure 5, each parameter is a projection of the material portion curve. The core roughness depth of the profile is obtained where the slope of the barrel surface curve is the smallest. This forms the peak zone to the left and the valley zone to the right, which have a significant slope

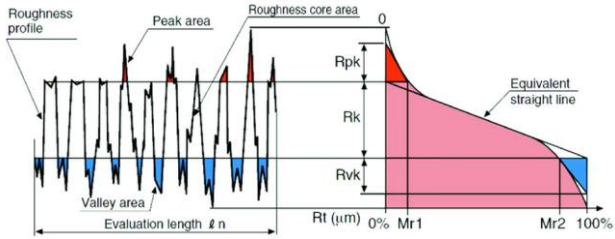

Figure 5. Abbott-Fireston Curve parameters for 2D case [20]

Due to the sensitivity to outliers, and parameters R_{pk} and R_{vk} can be considered as reduced values of the R_{pkx} and R_{vkx} characteristics. The peak zone and the are the initial material portion values of the valley zone in percent. The small value of the former and the large value of the latter represent the ideal load-bearing capacity of the machined surface [20]. These characteristics provide information about the subsequent load-bearing capacity of the machined parts [21].

The history of 3D surface characterization dates to the 1980s, when K.J. Stout and his team at Coventry Polytechnic developed a hardware system and supporting software that became the prototype for the first commercially available software package by providing a wide range of surface visualization techniques. The development of the technology did not go smoothly, as instrument manufacturers believed 3D topography was a 'scientific curiosity' and had no place in industry [22]. After initial wing-boning, the next milestone came in 1990 when, with the support of the European Community, a report of more than 300 pages was published by the University of Birmingham, which proposed the use of 14 3D surface roughness parameters describing the functional, spatial and amplitude properties of the surface. The first touch probe manufacturer was Somicronic, which made a wide range of parameters available on its system. The 'Birmingham 14' parameters were then installed on Somicronic's 3D surface tester in 1996, which included a standard file format that could be transferred to other computer systems [22]. In parallel with European research, advances were also being made in the USA, notably in the development of optical interferometric systems. The main instrument manufacturers were WYKO and ZYGO, whose instruments were capable of extremely fast 3D surface measurements for the capabilities of the time, using techniques such as vertical scanning interferometry or extended range interferometry, while achieving sub-nanometre resolution. At the beginning of the 2000s, instruments using triangulation and confocal techniques began to appear, for example from a company called Scantron [22].

The parameters of the Abbot-Firestone curve are effective for tribological applications [23]. Here, too, the setting of the correct parameters during measurement is crucial [24]. The characteristics of the previously described 2D

Abbott-Firestone curve can also be investigated in the 3D case. For 3D features, Heidari and Yan presented a similar diagram (Figure 6) [25].

These are as follows:

- S_k: core height
- S_{pk}: reduced peak height
- S_{vk}: reduced valley height

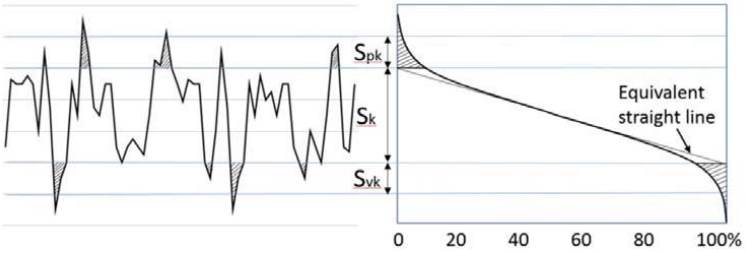

Figure 6. Definition of parameters S_{pk}, S_k and S_{vk} in a bearing area curve [25]

As in the 2D case, the S_{mr1} characteristic defines the boundary between the peak zone and the core zone, while the S_{mr2} portion of material defines the boundary between the core zone and the valley zone.

The surface roughness was measured with an AltiSurf®520 roughness measuring device, located in the Metrology Laboratory of the Institute of Manufacturing Sciences of the University of Miskolc. The measuring machine can move along three perpendicular x-y-z motorised DC axes at 200 mm per axis. Its maximum speed is 40 mm/sec, up to a scale of 0.1 μm [26].

A detailed analysis of the surface topography was performed using the AltiMap software provided with the measuring machine. Among several sensors of the machine, the non-contact interferometric triangular laser was used.

2.5. Calculation of the improvement factors

The improvement factors are used to look for parameters of diamond burnishing where, in addition to the machining being adequate in terms of energy efficiency, the greatest improvement in surface quality after turning was achieved with diamond burnishing.

The required improvement factor is calculated using equation (3), which is a percentage value that gives the improvement in surface quality due to diamond burnishing. This is necessary because the turning process produces surfaces of different quality, which are the starting points for diamond burnishing. The formula is a generalisation formula, with the 'x' replacing the letters 'R' used for 2D surface finishes and 'S' for 3D finishes, and the 'y' generalising the subscripts for the different gauge types.

$$IX_y = \frac{X_{y;turning} - X_{y;burnishing}}{X_{y;burnishing}} \cdot 100\ [\%] \quad (3)$$

2.6. Calculation of K-coefficients

The values of the individual features of the Abbott-Firestone curve do not necessarily give an indication of the quality and properties of the surface, but their relative values, their ratios, their percentage distribution may be of more interest in the context of diamond burnishing. For this purpose, so-called K-coefficients are calculated using the formulas (4)–(9) [27].

$$K_{Rk} = \frac{R_k}{R_k + R_{pk} + R_{vk}} \quad (4)$$

$$K_{Rpk} = \frac{R_{pk}}{R_k + R_{pk} + R_{vk}} \quad (5)$$

$$K_{Rvk} = \frac{R_{vk}}{R_k + R_{pk} + R_{vk}} \quad (6)$$

$$K_{Sk} = \frac{S_k}{S_k + S_{pk} + S_{vk}} \quad (7)$$

$$K_{Spk} = \frac{S_{pk}}{S_k + S_{pk} + S_{vk}} \quad (8)$$

$$K_{Svk} = \frac{S_{vk}}{S_k + S_{pk} + S_{vk}} \quad (9)$$

For example, formula (4) illustrates in percentage form the core roughness depth (R_k) of the roughness profile ($R_k + R_{pk} + R_{vk}$) with respect to the total roughness profile.

3. The analysis of the abbott-firestone curve

3.1. Improvement factors for the surface roughness characteristics of the abbott-firestone curve

The repeatedly mentioned Abbott-Firestone curve characteristics are plotted as a function of feed rate, burnishing speed and burnishing force for comparison with the improvement factors calculated in the previous chapter. To better follow the plots, trend lines were plotted for each data point set, which resulted in mostly similar curves.

In the graphs of the core part of the roughness profile (Figure 7), the magnitude of the improvement factor increases steadily with increasing burnishing force until it reaches a maximum point from which it starts to decrease. This is consistent with our previous observations for the other surface roughness metrics. The plots - especially the plot analysing the 3D parameter - also show that for the

same burnishing rates (red-blue and green-yellow trend lines) the maximum position of the curves, i.e. the burnishing force, is the same, but they differ only in the values of the improvement factor.

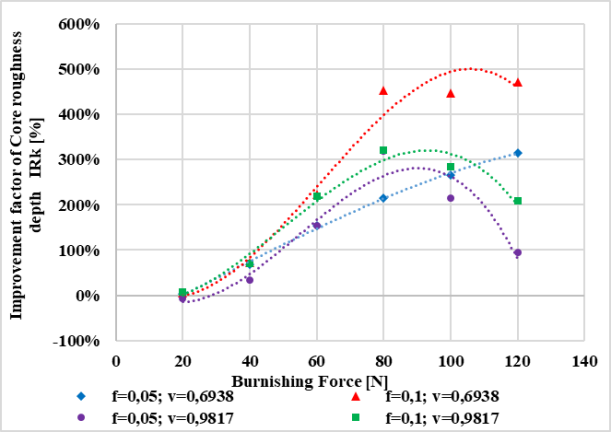

a)

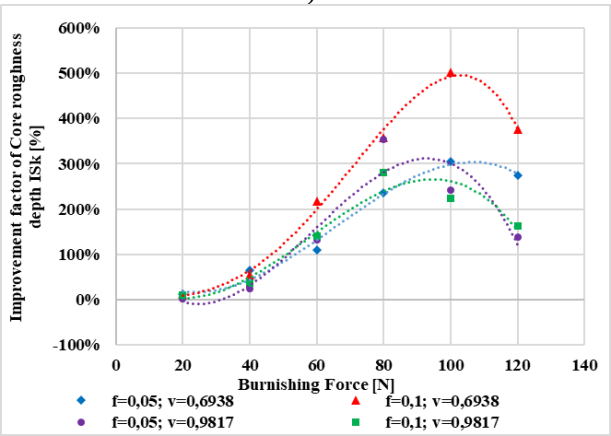

b)

Figure 7. Improvement factor of the core roughness depth as a function of burnishing speed, feed rate and burnishing force, a) 2D case b) 3D case

The improvement factors of the reduced peak height show a much larger variation depending on the variation of the technological parameters (Figure 8). The reduced peak height represents the top of the profile, proportional to the material portion of the core zone and the valley zone. This factor is better evaluated only for the 3D case, as the 2D data did not give a valuable picture of the subject. It can be

observed that at the minimum feed rate and burnishing speed (blue trend line), the improvement factor increased steadily with increasing burnishing force, whereas at the maximum values of these parameters (green trend line), increasing burnishing force even worsened the peak part of the roughness profile over time. On the other hand, for the minimum-maximum combination of values (red, yellow trend lines), the improvement factor was again at its maximum value, with a similar slight improvement above 70-80 N of burnishing force.

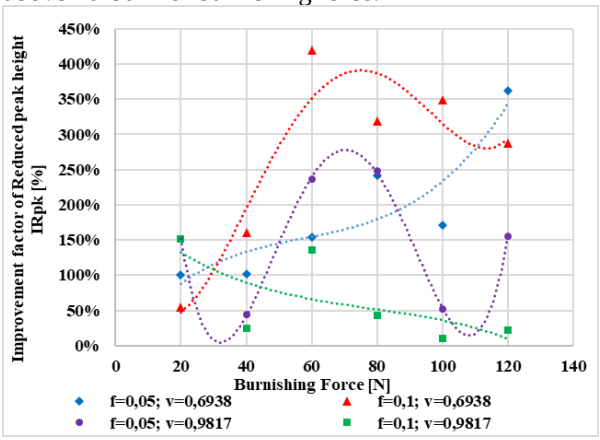

a)

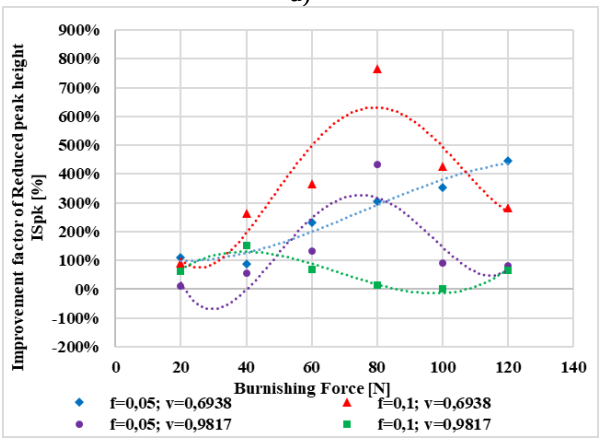

b)

Figure 8. Improvement factor of the reduced peak height as a function of burnishing speed, feed rate and burnishing force, a) 2D case b) 3D case

As with the peak section, the improvement factors in the valley portion of the Abbot-Firestone curve varied quite a bit with changes in process parameters (Figure 9). The valley portion of the barrel surface provides feedback from the deepest layers of the surface. As in the peak part of the profile, again relying only on the 3D metric, it can be observed that increasing the burnishing force first has a negative effect on the improvement factor (negative values also occur), while reaching a minimum point, the highest burnishing forces already improve the valley part of the barrel surface curve to a large extent. From this, therefore, we can draw the important conclusion that the deepest "valleys" on the surface are in fact only reduced by diamond burnishing when sufficiently high forces are applied.

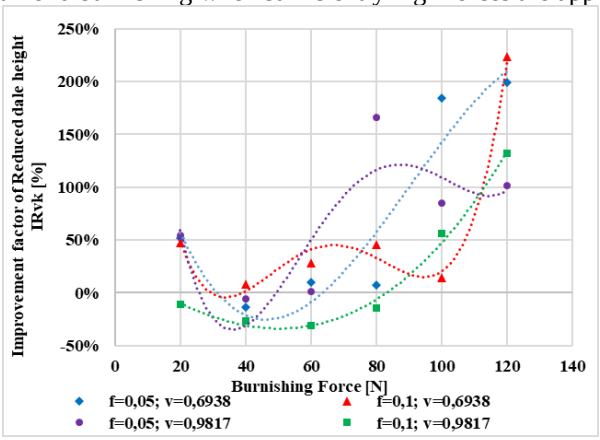

a)

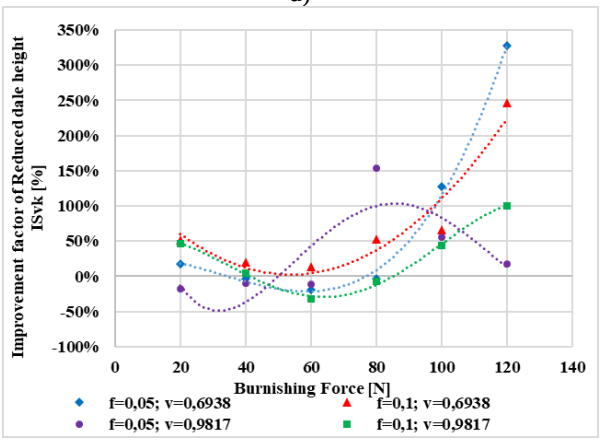

b)

Figure 9. Improvement factor of the reduced valley height as a function of burnishing speed, feed rate and burnishing force, a) 2D case b) 3D case

3.2. K-coefficients of the surface roughness characteristics of the abbott-firestone curve

The K-coefficients calculated in the previous chapter are plotted as a function of the burnishing force in the following figures. First, let us consider the core roughness depth to the roughness profile, as shown in the 2D and 3D cases in Figure 10. In both dimensions, similar conclusions can be drawn from the plotted trend lines, as diamond burnishing after turning has reduced the proportion of this part in the surface profile by 10-20% except for the smallest burnishing force. It is also seen that the ratio has a minimum at 60 and 80 [N], from where the ratio starts to increase with further increase of the burnishing force. This suggests that too high and burnishing force no longer improves the surface quality.

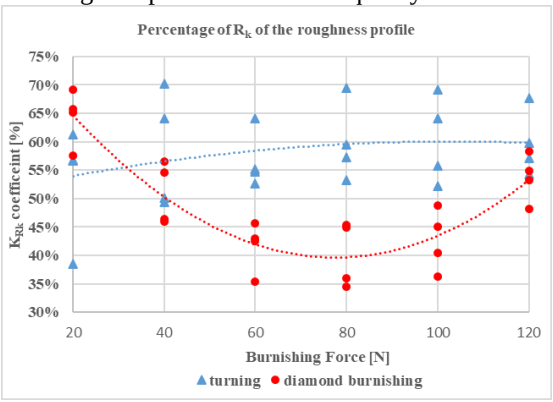

a)

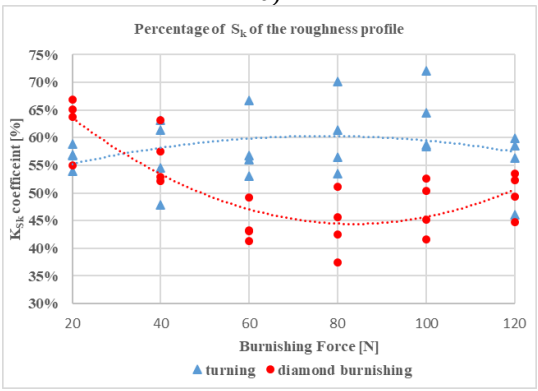

b)

Figure 10. Percentage of the core roughness depth of the roughness profile in the Abbott-Firestone curve as a function of the burnishing force, a) 2D case b) 3D case

And if we recall formula (2), where the power requirement for diamond burnishing was calculated as the product of the burnishing power and the burnishing speed, we can see that in this case, lower burnishing power not only requires better surface quality, but also lower power, which is a clear objective in terms of sustainability and energy efficiency. Following the core part, the reduced peak height of the roughness profile was investigated, as shown in Figure 11, also for 2D and 3D cases. We found, as shown in the figures, that the peak portion of the barrel surface curve was also reduced by 8-10% by diamond burnishing, interestingly just except for the highest burnishing force. Again, this is positive feedback, as our goal in diamond burnishing is to reduce this portion, to "fill in" the valley portion of the roughness profile, thus making the surface more compact. As the lower burnishing force was also more favourable for the surface quality, the energy efficiency principles are also satisfied, as lower power requirements resulted in better surface quality parameters.

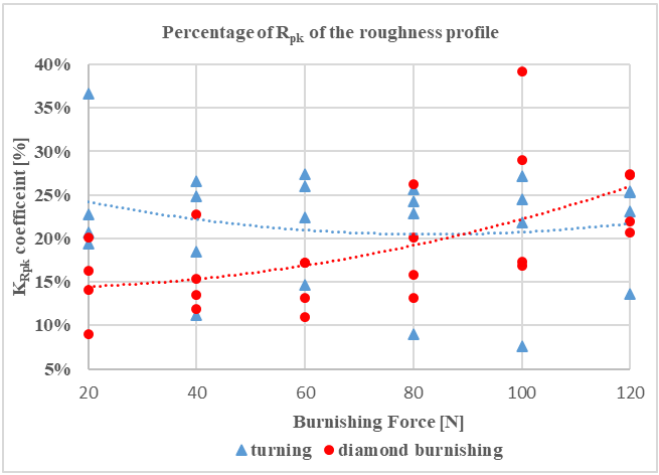

a)

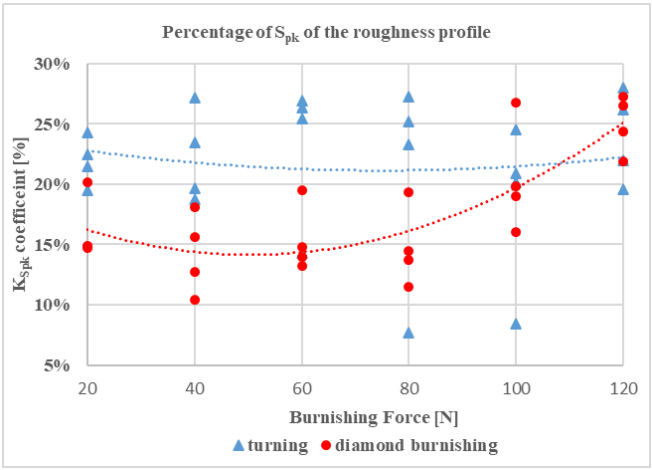

b)

Figure 11. Percentage of the reduced peak height of the roughness profile in the Abbott-Firestone curve as a function of the burnishing force, a) 2D case b) 3D case

Finally, look at Figure 12, where the ratio of the valley portion of the roughness profile is examined in 2D and 3D. In contrast to the previous two cases, our aim is to increase the proportion of the valley section in diamond burnishing, and as can be seen in the figure, this is achieved in almost all cases, in some cases improving the proportion by 20%. It can also be seen that, again, the best results are obtained for the 60-80 [N] burnishing forces, i.e. those where the valley section will have the highest proportion of the roughness profile. Considering this in the context of energy efficiency, we can also conclude that it satisfies its principles.

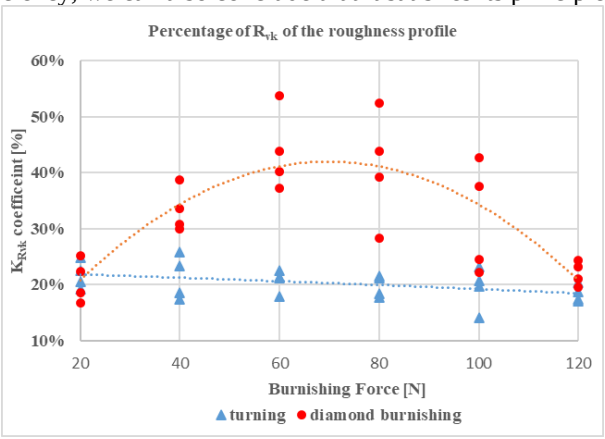

a)

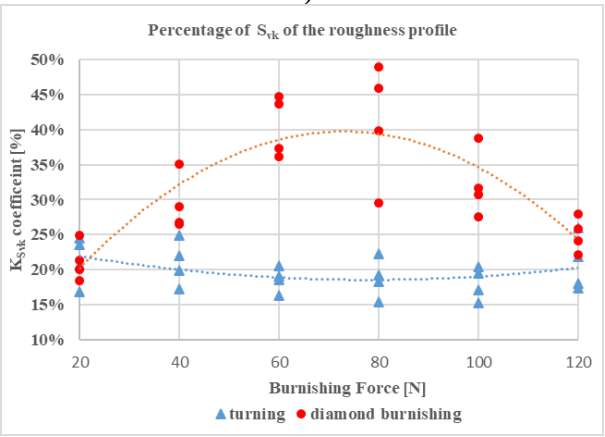

b)

Figure 12. Percentage of the reduced valley height of the roughness profile in the Abbott-Firestone curve as a function of the burnishing force, a) 2D case b) 3D case

4. Summary

In the research we provided an overview of the context of the topic, starting from the issues of energy efficiency, environmental awareness, and sustainable development. We examined the positive properties of alternative machining methods, such as diamond burnishing, and looked at the substrate surface, which is key to the relationship between surface quality and diamond burnishing. In the first part of the paper, we introduced the science of sustainable development, industrial ecology, and its various systems models, and then turned to the three pillars of sustainable development. The relationship between energy and eco-efficiency, their characteristics and recent research results were discussed. In the next section, we described the dimensions and material quality of the test specimens that were tested. The technological characteristics of the turning and diamond-burnishing processes were then presented. The characteristics and usefulness of the barrel Abbott-Firestone curves were discussed in detail and the improvement factors and K-coefficients were calculated. In the third part, we have presented in detail the experimental results obtained by examining the data of the Abbott-Firestone curves. Using the improvement factors, we could see from the diagrams of the core part of the roughness profile that as the burnishing force is increased, the improvement factor increases steadily until it reaches a maximum point from which it starts to decrease. By examining the valley part of the profile, we have seen that the deepest "valleys" in the surface are only reduced by diamond burnishing when a sufficiently

high force is applied. However, by also looking at the K-coefficient data, we found that lower burnishing forces often favour surface quality over higher burnishing forces, which also reduces the power requirements of machining, creating optimal energy efficiency during diamond burnishing. Our aim was to reduce the peak or core fraction and increase the valley fraction in diamond burnishing, and as we have seen in the figures, we have achieved this in almost all cases, in some cases improving the ratios by 20%. In all cases, the best results were obtained with burnishing forces of 60-80 [N], with both lower and higher burnishing forces worsening the ratios. These results therefore fully satisfy the main energy efficiency guidelines.

References: **1**. *P. Bartelmus, S. Moll, S. Bringezu, S. Nowak, R. Bleischwitz*: Translating sustainable development into practice: a 'patchwork' of some new concepts and an introduction to material flows analysis in: Emiel F.M. Wubben (ed.) Green and Competitive: Ending the Stalemate, Chapt. 1, pp. 1–38, Edward Elgar Publishing. 2004. **2.** *D.H. Meadows, J. Randers, D.L. Meadows:* The limits to growth. Chelsea Green Publishing, USA. 2004. **3.** Brundtland Commission: Our Common Future. Oxford University Press, Oxford, UK. 1987. **4.** *S. Schaltegger, A. Sturm:* Ökologieinduzierte Entscheidungsprobleme des Managements: Ansatzpunkte zur Ausgestaltung von Instrumenten. WWZ-Discussion Paper No. 8914. 1989. **5.** UN (United Nations): Earth Summit. Agenda 21. The United Nations Programme of Action from Rio., (Ed.) United Nations Department of Public Information New York. 1992. **6.** *B.R. Allenby*: Industrial Ecology – Policy Framework and Implementation, Englewood Cliffs, NJ: Prentice Hall. 1999. **7.** *C. Herrmann:* Ganzheitliches Life Cycle Management - Nachhaltigkeit und Lebenszyklusorientierung in Unternehmen. Springer Verlag, Berlin, Germany. 2010. **8.** *M.E. Porter, C.v.d. Linde:* 'Green and Competitive: Ending the Stalemate', in E.v.d. Wubben (ed.), The Dynamics of the Eco-Efficient Economy, Cheltenham, UK and Northampton, MA: Edward Elgar, pp. 33–55. 2001. **9.** *R. Bleischwitz:* 'Governance of Eco-Efficiency in Japan – An Institutional Approach', International Asian Quarterly, 34 (1–2), 107–26. 2003. **10.** *R. Bleischwitz, P. Hennicke:* Eco-efficiency, regulation and sustainable business: Towards a governance structure for sustainable development. pp. 1–228. ESRI Studies Series on the Environment, Germany 10.4337/9781845420574.00001. 2004. **11.** *L.D. DeSimone, F. Popoff:* Eco-Efficiency: The Business Link to Sustainable Development, vol. 1, 1 ed., The MIT Press. 2000. **12.** DIN EN ISO 14040: Umweltmanagement - Ökobilanz - Grundsätze und Rahmenbedingungen (ISO 14040:2006). Beuth Verlag, Berlin, Germany. 2009. **13.** DIN EN ISO 14045, Umweltmanagement - Ökoeffizienzbewertung von Produktsystemen - Prinzipien, Anforderungen und Leitlinien (ISO 14045:2012). Beuth Verlag, Berlin, Germany. 2012. **14.** *R. Heijungs:* From thermodynamic efficiency to eco-efficiency. In: Huppes, G., Ishikawa, M. (eds) Quantified Eco-Efficiency. Eco-Efficiency in Industry and Science, vol 22. Springer, Dordrecht. 2007. **15.** https://www.inoxservice.hu/upload/inline/adatlapok/durvalemezek/ 1.4307%20-%20ADATLAP.pdf (2024. 04. 15) **16.** *L. Gribovszki*, Mechanical processing (Tankönyvkiadó, Budapest, pp. 418-421. 1977. (In Hungarian) **17.** *G. Varga, S. Smolnicki, M. Babič, W. Caesarendra*, Energy Efficiency Analysis When Grinding and Diamond Burnishing of Components, In: Gençyılmaz, M. Güneş; Durakbasa, Numan M. (ed.-s.) Towards Industry 5.0: Selected Papers from ISPR2022, Cham, Switzerland, Springer International Publishing pp. 378-396. 2023. **18.** *V. Ferencsik*, Analytical analysis of the theoretical surface roughness in the case of burnishing of cylindrical workpiece, Rezanie i Instrument v Tehnologiceskikh Sistemakh / Cutting and Tool in Technological Systems 99 pp. 101–109, (2023). **19.** https://perfor.hu/erdesseg_67 (2024. 04. 15.) **20.** *I. Szalóki, S. Sipos, Z.J. Viharos:* Analysis of the milled surface structure of syntactic metal foams. In: Proceedings of 8th International Engineering Symposium at Bánki (IESB 2016). Óbudai Egyetem, Budapest, pp. 1–21. ISBN 978-615-5460-95-1. 2016. (In Hungarian) **21.** *D. Kubatova, M. Melichar*: Roughness Evaluation Using Abbott-Firestone Curve

Parameters, Proceedings of the 30th DAAAM International Symposium, pp. 0467–0475, B. Katalinic (Ed.), Published by DAAAM International, ISBN 978-3- 902734-22-8, ISSN 1726-9679, Vienna, Austria. 2019. **22.** *L. Blunt, X. Jiang*: Advanced Techniques for Assessment Surface Topography: Development of a Basis for 3D Surface Texture Standards "Surfstand", Kogan Page Science, pp. 1–355. 2003. **23.** *I. Sztankovics*: Preliminary Study on the Function-Defining 3D Surface Roughness Parameters in Tangential Turning. International Journal of Integrated Engineering 15: 7 pp. 72–81. 2023. **24.** *A. Nagy*: Investigation of the effect of areal roughness measurement length on face milled surface topographies. Cutting and Tools in Technological System, (94), pp.: 60–69. 2021. https://doi.org/10.20998/2078-7405.2021.94.07, **25.** *M. Heidari, J. Yan:* Fundamental characteristics of material removal and surface formation in diamond turning of porous carbon. International Journal of Additive and Subtractive Materials Manufacturing, 1 (1), pp.: 23–41. 2017. **26.** https://www.altimet.fr/?page_id=236&lang=en (2024. 04. 15.) **27.** *M. Tomov, P. Karolczak, H. Skowronek, P. Cichosz, M. Kuzinovski:* Mathematical Modelling of Core Roughness Depth During Hard Turning. In: Królczyk, G., Niesłony, P., Królczyk, J. (eds) Industrial Measurements in Machining. IMM 2019. Lecture Notes in Mechanical Engineering. Springer, Cham. 2020. https://doi.org/10.1007/978-3-030-49910-5_1

Сілард Смольницькі, Дьюла Варга, Мішкольц, Угорщина

АНАЛІЗ КРИВОЇ ЕББОТА-ФАЙЄРСТОУНА НА ПОЛІРОВАНІЙ АЛМАЗНИМ ВИГЛАДЖЕННЯМ ПОВЕРХНІ

Анотація. *У дослідженні ми надали огляд контексту теми, починаючи з питань енергоефективності, екологічної свідомості та сталого розвитку. Ми розглянули позитивні властивості альтернативних методів обробки, таких як алмазне полірування, і звернули увагу на поверхню підкладки, яка є ключовим фактором у взаємозв'язку між якістю поверхні та алмазним поліруванням. У першій частині статті ми представили науку сталого розвитку, промислову екологію та її різні системні моделі, а потім звернулися до трьох стовпів сталого розвитку. Було обговорено взаємозв'язок між енергетичною та екологічною ефективністю, їхні характеристики та останні результати досліджень. У наступному розділі ми описали розміри та якість матеріалу дослідних зразків, які були випробувані. Потім були представлені технологічні характеристики процесів точіння та алмазного вигладжування. Детально обговорено характеристики та корисність кривих Еббота-Файрстоуна, а також розраховано коефіцієнти покращення та К-коефіцієнти. У третій частині ми детально представили експериментальні результати, отримані при вивченні даних кривих Еббота-Файрстоуна. Використовуючи коефіцієнти поліпшення, ми могли бачити з графіків основної частини профілю шорсткості, що зі збільшенням сили полірування коефіцієнт поліпшення неухильно зростає, поки не досягне максимальної точки, з якої він починає зменшуватися. Вивчаючи долинні частини профілю, ми побачили, що найглибші "долини" на поверхні зменшуються за допомогою алмазного полірування вигладженням лише за умови застосування досить високої сили. Однак, проаналізувавши дані про коефіцієнт К, ми виявили, що менші зусилля полірування часто сприяють поліпшенню якості поверхні, ніж більші зусилля, що також знижує енергоспоживання при обробці, створюючи оптимальну енергоефективність під час алмазного полірування. Наша мета полягала в тому, щоб зменшити частку піків або серцевини і збільшити частку долини при алмазному вигладжувальному поліруванні, і, як ми бачимо на рисунках, ми досягли цього майже у всіх випадках, в деяких випадках покращивши співвідношення на 20%. У всіх випадках найкращі результати були отримані при силі притискання 60-80 [H], причому як менші, так і більші сили притискання погіршували співвідношення. Таким чином, ці результати повністю задовольняють основним рекомендаціям з енергоефективності.*

Ключові слова: *енергоефективність; сталий розвиток; вигладжувальне алмазне полірування; обробка поверхні.*

UDC 621.9.048 **doi: 10.20998/2078-7405.2024.100.10**

FINITE ELEMENT ANALYSIS OF CHANGING OF STRESS CONDITION CAUSED BY DIAMOND BURNISHING

Viktoria **Ferencsik** [0000-0002-8673-1095]

University of Miskolc, 3515 Miskolc-Egyetemváros, Hungary
ferencsik.viktoria@uni-miskolc.hu

Received: 22 March 2024 / Revised: 21 April 2024 / Accepted: 28 May 2024 / Published: 15 June 2024

Abstract. *The article is aspected to the finite element modelling of stress in subsurface layer of aluminium alloy workpiece during diamond burnishing process. This cold forming process is a simple, cost-effective finishing method that can be used to improve surface integrity and provide compressive residual stress. Available with these, durability and quality enhancement of the components can be reached, but improperly chosen burnishing parameters can distort the efficiency of the plastic deformation process. In order to optimize this, a 2D FEM model is created including the real surface integrity of the workpiece which was measured with AltiSurf 520 surface roughness measuring device. The method is simulated using DEFORM-2D software, corresponding to the numerical values of burnishing parameters implemented in practice as well, thereby allowing a comparative analysis with the results of X-ray diffraction measurement.*
Keywords: *finite element modelling; diamond burnishing; surface integrity; plastic deformation.*

1. Introduction

As a result of the development of engineering technology, new opportunities and methods are constantly being developed to examine individual material structure changes. However, most of these are impossible to implement on a low budget, which is why it is important to study the individual procedures at a theoretical level, for example using the finite element method, which has already been dealt with in numerous publications in many machining fields [1-5]. Moreover, in industrial practice, the quality requirements of parts subjected to fatigue include the value and distribution of the residual stress near the surface, which can sometimes only be measured by destructive testing, so FEM is also an ideal solution in this case.

Several researchers have worked on modelling surface hardening processes, Yen et al. successfully established 2D and 3D models of roller burnishing and even though the 3D model shown more realistic surface deformation, the refined 2D model seems to predict the residual stresses better than the 3D model [6]. In the work of Amini et al., the 3D model of ball burnishing process was created in ANSYS considering the topography of the initial surface. 3D surface parameters and residual

stresses (in axial and tangential directions) were analysed and the publication also pointed out that the friction coefficient between the tool and workpiece in the modelling is not negligible [7]. Felho and Varga also taken into account the original surface roughness [8], such as Borysenko et al., indeed, in their examination the diamond tool was scanned and used for the FEM simulation in Advant Edge [9]. The study of Balland et al. shows the diversity of applicable programs as they used ABAQUS to investigate the topology of surface with periodic irregularities stressed by rolling contact [10]. In another work on the same topic [11], they draw attention to the importance of meshing during the simulation, not only from the point of view of cost in computing time.

In this paper a 2D FEM model for ball burnishing process is established to examine the effect of it on the changing of stress conditions. The apply of this method makes it possible to reduce some or all the high costs of experimental testing.

2. Implementation of surface burnishing

When external cylindrical surfaces are burnished, plastic deformation occurs as a result of the interaction between the forming element, i.e. the static contact between the tool and the workpiece, during the sliding friction (Fig. 1). No chips, sparks or dust are produced during machining, and the need for coolant is minimal or even eliminated, so environmentally friendly and cost-effective machining can be realized [11-13].

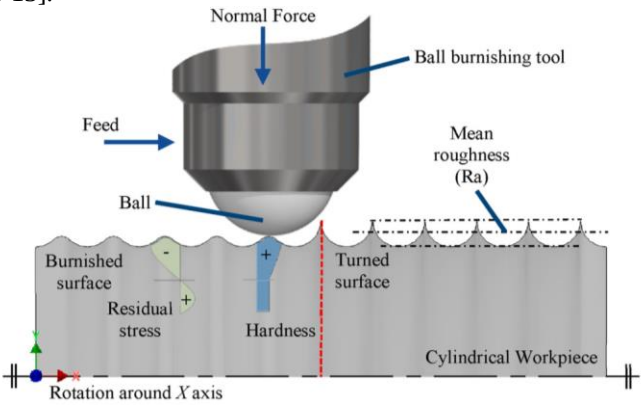

Figure 1. Schematic illustration of burnishing treatment [14]

The purpose of its application is to improve the quality of the surface and increase service life of the component, which is achieved by increasing the hardness of the sub-surface layer and reducing surface roughness [15, 16].

In this experiment the burnishing operation was realized on Optimum OPTIturn L-series 440 flatbed CNC lathe with 3.5 mm radius PCD tool, applying F = 20 N burnishing force, f = 0.001 mm/rec burnishing feed and v = 15 m/min burnishing speed and the kinematic viscosity of the applied manual dosing oil was $\nu = 70$ mm^2/s. The surface of the workpiece was pre-machined by finishing turning set at $f_1 = 0.2$ than $f_2 = 0.15$ mm/rev.
In addition, before and after burnishing, measuring process of residual stress was implemented on an X-ray diffraction measuring machine type Stresstech Xstress 3000 G3R, which realizes non-destruction test.

3. Simulation of burnishing process

Finite element model of diamond burnishing treatment was simulated by DEFORM FE code, creating a 2D model as it has faster runtime, smaller model sizes and simpler boundary conditions than 3D versions.
The burnishing tool was modelled as a rigid sphere with 3.5 mm radius and the surface of the workpiece is based on the physical surface. Before burnishing, the real workpiece was measured on a 4 mm long distance with Altisurf 520 topography measuring device and the surface points were imported to the code. Since the results of the preliminary simulations show that the procedure is effective up to 0.15-0.17 mm below the surface, I have set the thickness of the workpiece to 0.2 mm to further simplify the model.
A critical point in finite element modelling is the decomposition of the workpiece into mesh elements, since the size distribution of these is a key determinant of the accuracy of the simulation results. With the reduced test thickness, I was able to achieve an edge length of 0.02 mm for the four-node mesh elements used near the surface, with sufficient computation time. The tool and the meshed workpiece are illustrated in Figure 2.

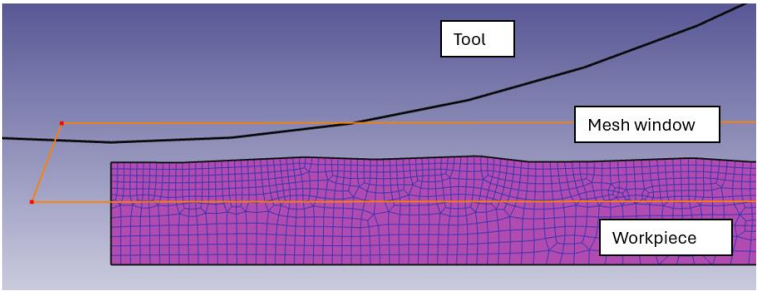

Figure 2. A section of 2D FEM model of burnishing

As a result of the burnishing force exerted by the tool, small plastic deformations are created on and near the surface of the workpiece. To describe these small

deformations, the points of the flow curve taken experimentally must be approximated by a function in the finite element space. In the simulations, "power law" relation provided by the program was used to define the yield stress with deformation, which is described by formula (1), where $\bar{\sigma}$ is the flow stress.

$$\bar{\sigma} = c\bar{\varepsilon}^{n}\dot{\bar{\varepsilon}}^{m} + y \quad (1)$$

, where:

c	material constant,	c = 121,228
$\bar{\varepsilon}$	effective plastic strain,	
$\dot{\bar{\varepsilon}}$	effective strain rate,	
n	strain exponent,	n = 0,266076
m	strain rate exponent,	m = 1,12487
y	initial value	y = 50,0003 MPa

The kinematics of the tool was modelled after the real kinematics of the of the process, according to Stöckmann and Putz [17], Rodriguez et al. [18], Felho and Varga [19]. In the simulation workpiece was fixed at the bottom and sides, firstly the tool is moved down vertically until it reaches the precalculated indentation depth [20], then moved to the initial position. Next, the tool is horizontally moved with the displacement value of the burnishing feed and loads again the surface of the workpiece. This cycle should be repeated at least 8 times [15, 17, 19], this simulation has been built accordingly as well.

4. Results and discussion

Configuration shown in Fig. 3 was used to evaluation of the simulation, where the first contact between the tool and the workpiece can be seen. Since, the procedure was simplified to two-dimensions, it is not possible to interpret stress in the tangential direction, only axial stresses (Stress – X) can be examined.

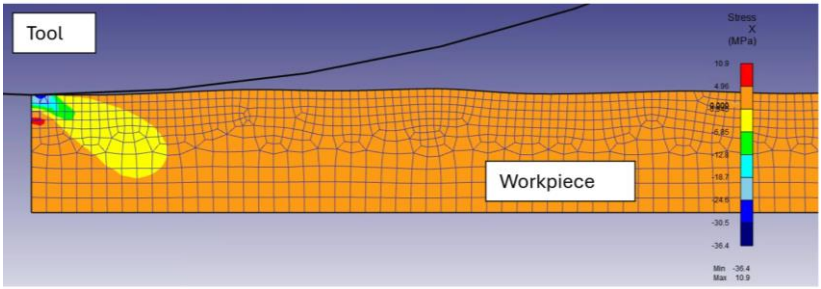

Figure 3. Changing of stress conditions during the first contact

As it was mentioned, the process of "loading-unloading-displacement" was repeated for 8 times and Fig. 4. shows the distribution of the residual stress for each full loading step according to the 0.001 mm step over distance.

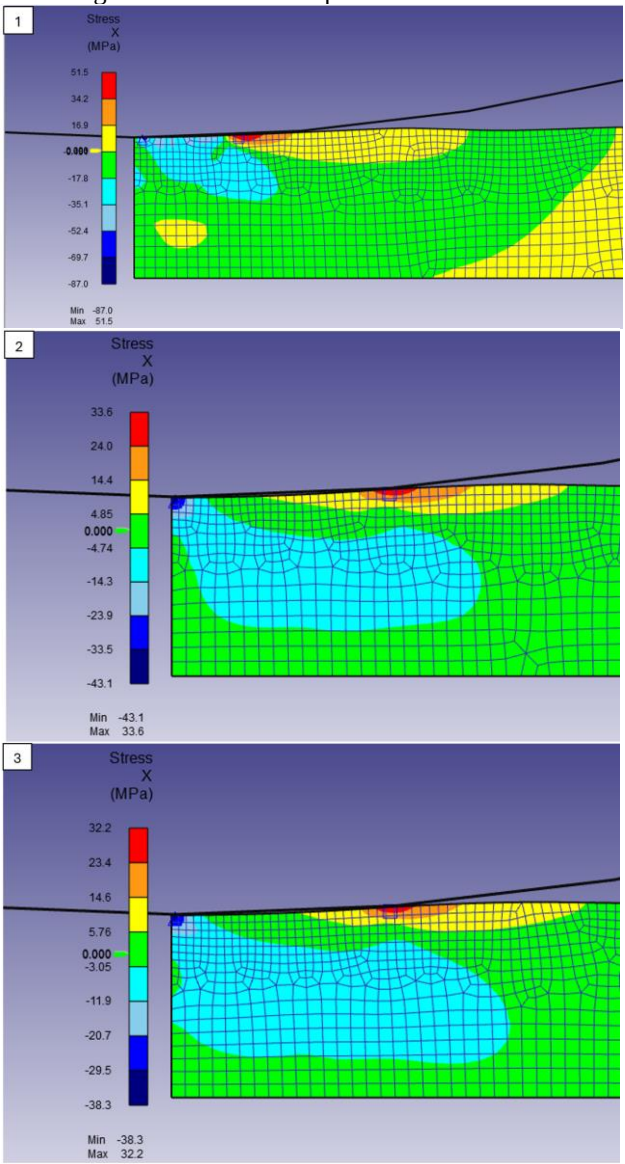

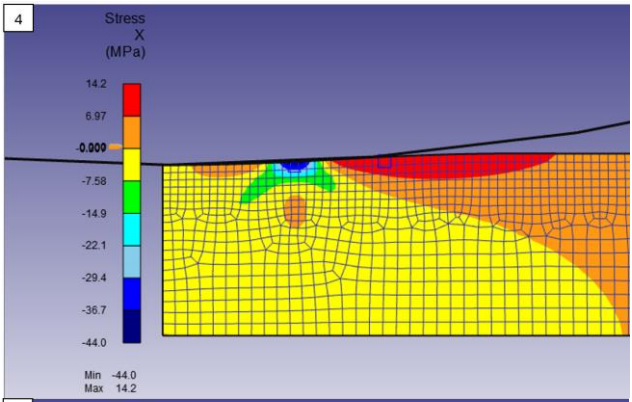
4
Stress
X
(MPa)
14.2
6.97
-0.000
-7.58
-14.9
-22.1
-29.4
-36.7
-44.0
Min -44.0
Max 14.2

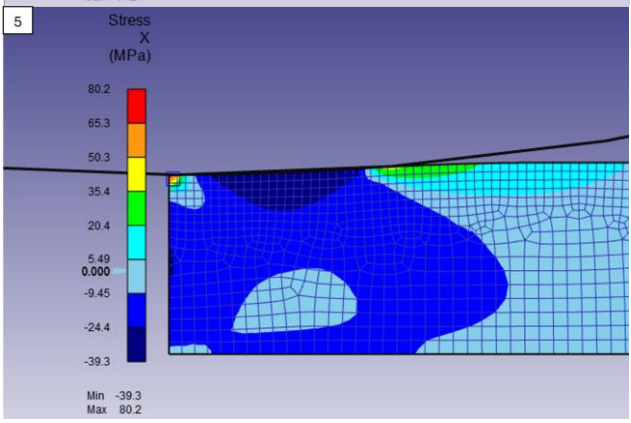
5
Stress
X
(MPa)
80.2
65.3
50.3
35.4
20.4
5.49
0.000
-9.45
-24.4
-39.3
Min -39.3
Max 80.2

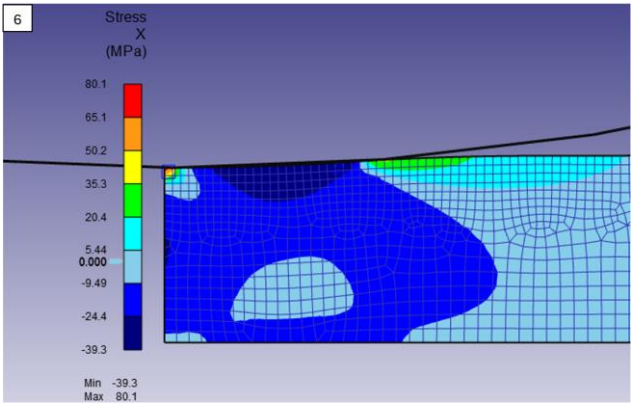
6
Stress
X
(MPa)
80.1
65.1
50.2
35.3
20.4
5.44
0.000
-9.49
-24.4
-39.3
Min -39.3
Max 80.1

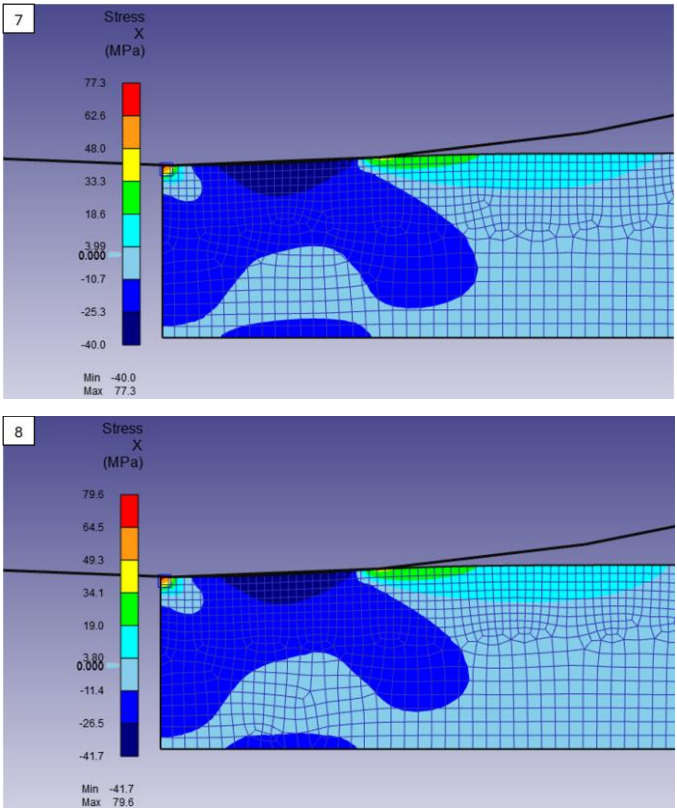

Figure 4. Changing of stress conditions during the first contact

The results of X-ray diffraction measurement showed that the burnished surface has between (-88.6) -(-138.6) MPa compressive residual stress. Compared these values with the FEM simulation results, where this range is between (-38.3) – (-87.0) MPa, it can be observed that these values match only in the case of first tool indentation. One of the possible explanations for this could be that a denser mesh necessary to set and/or the material quality of the workpiece under test is not selected from the FE program library (Al-6061-O, COLD), but is based on the real value by examining the real yield strength.

The physical stress measurement does not provide information on how the residual stress is distributed; this phenomenon can be available at the simulation. Accordingly, as the burnishing progresses, the compressive residual stress distribution increases, however, its value changes unfavourably, it relaxes excessively, which leads to the conclusion that the value of the burnishing feed rate

is too low. This is significant because by increasing this parameter setting, time and cost can be saved both in terms of concrete machining and simulation calculation.

Based on this, my future plans definitely include the creation of a more realistic model to study the effect of the process on the stress conditions at increased feed rate.

References: 1. *I. Sztankovics*: FEM Analysis of the Impact Conditions of the Insert in Face Milling, MultiScience – XXXIII. MicroCAD International Multidisciplinary Scientific Conference , pp. 1–8, 2019. **2.** *C. Felho, I. Sztankovics, Z. Maros, K. Kun-Bodnar*: FEM Simulation of the Flange Turning in the Production of Aluminium Aerosol Cans, Manufacturing Technology 23, pp. 810–818, 2023. **3.** *I. Sztankovics, G. Varga*: FEM Analysis of the Burnishing Process of X5CrNi19-10 Stainless Steel, Rezanie i Instrument v Tehnologiceskikh Sistemakh / Cutting and Tool in Technological Systems, 97, pp. 137–144, 2022. **4.** *T. Emmer, F. Welzel, D. Borysenko, V. Voropai*: Development of the Mathematical Model Smoothing while Using FEA, Rezanie i Instrument v Tehnologiceskikh Sistemakh / Cutting and Tool in Technological Systems, 90, pp. 58–68, 2019. **5.** *V. Fedorovich, I. Pyzhov, I. Voloshkina*: Modeling of the Process of Vibratory Grinding by Finite Element Method, Rezanie i Instrument v Tehnologiceskikh Sistemakh / Cutting and Tool in Technological Systems, 90, pp. 136–150, 2019. **6.** *Y.C. Yen, P. Sartkulvanich, T. Altan*: Finite Element Modelling of Roller Burnishing Process, Engineering, Material Science, pp. 1–4, 2005 **7.** *C. Amini, R. Jerez-Mesa, J.A. Travieso-Rodriguez, J. Lluma, A. Estevez-Urra*: Finite Element Analysis of Ball Burnishing on Ball-End Milled Surfaces Considering Their Original Topology and Residual Stress, Metals 638, pp. 1–16, 2020. **8.** *C. Felho, G. Varga*: 2D FEM Investigation of Residual Stress in Diamond Burnishing, Journal of Manufacturing and Materials Processing 123, pp. 1–16, 2022. **9.** *D. Borysenko, F. Welzel, B. Karpuschewski, J. Kundrak, V. Voropai:* Simulation of the Burnishing Process on Real Surface Structures, Precision Engineering 68, pp. 166–173, 2021. **10.** *P. Balland, L. Tabourot, F. Degre, V. Moreau:* Mechanics of the Burnishing Process, Precision Engineering 37, pp. 129–134, 2012. **11.** *P. Balland, L. Tabourot, F. Degre, V. Moreau:* An Investigation of Mechanics of Roller Burnishing Though Finite Element Simulation and Experiments, International Journal of Machine Tools & Manufacture 365, pp. 29–36, 2013. **12.** *A. Skoczylas, K. Zaleski:* Selected Properties of the Surface Layer of C45 Steel Parts Subjected to Laser Cutting and Ball Burnishing, Materials 3429, pp. 1–19, 2020. **13.** *A. Saldana-Robles, H. Plascencia-Mora, E. Aguilera-Gomez, A. Saldana-Robles, A. Marquez-Herrera, J.A. Diosdado-De la Pena:* Influence of Ball Burnishing on Roughness, Hardness and Corrosion Resistance of AISI 1045 Steel, Surface & Coatings Technology 339, pp. 191–198, 2018. **14.** *E. Becerra-Becerra, C.O. Aguilera Ojada, A. Saladana-Robles, J.F. Reveles-Arredondo, J. Barco-Burgos, A. Vidal-Lesso:* A Review of Numerical Simulation of Ball Burnishing Process, Finite Elements in Analysis and Design 218, pp. 1–19, 2023. **15.** *M. Posdzich, R. Stöckmann, F. Morczinek, M. Putz:* Investigation of a Plain Ball Burnishing Process on Differently Machined Aluminium EN AW 2007, MATEC Web of Conferences 190, pp. 1–19, 2018. **16.** *D. Vukelic, D. Miljanic, S. Randjelovic, I. Budak, D. Dzunic, M. Eric, M. Pantic:* **A** Burnishing Process Based on the Optimal Depth of Workpiece Penetration, Material and Technology 47, pp. 43–51, 2013. **17.** *R. Stöckmann, M. Putz:* Modelling of Surface Formation Mechanism during Burnishing of Aluminium, Procidia CIRP 82, pp. 450–454, 2019. **18.** *A. Rodriguez, L.N. Lopez de Lacalle, A. Celeya, A. Lamikiz, J. Albizuri:* Surface Improvement of Shafts by the Deep Ball-Burnishing Technique, Surface & Coatings Technology 206, pp. 2817–2824. 2012. **19.** *C. Felho, G. Varga:* 2D FEM Investigation of Residual Stress in Diamond Burnishing, Journal of Manufacturing and Materials Processing 123, pp. 1–16. 2022. **20.** *V. Ferencsik:* Analytical Analysis of the Theoretical Surface Roughness in the Case of Burnishing of Cylindrical Workpiece, Rezanie i Instrument v Tehnologiceskikh Sistemakh / Cutting and Tool in Technological Systems, 99, pp. 101–109. 2023.

Вікторія Ференчик, Мішкольц, Угорщина

СКІНЧЕННО-ЕЛЕМЕНТНИЙ АНАЛІЗ ЗМІНИ НАПРУЖЕНОГО СТАНУ ПОВЕРХНІ, ВИКЛИКАНОГО АЛМАЗНИМ ВИГЛАДЖУВАННЯМ

Анотація. *Статтю присвячено скінченно-елементному моделюванню напружень у підповерхневому шарі заготовки з алюмінієвого сплаву в процесі алмазного вигладжування. Цей процес холодного формоутворення є простим, економічно ефективним методом обробки, який можна використовувати для покращення цілісності поверхні та забезпечення залишкових напружень стиснення. З ними можна досягти довговічності та підвищення якості компонентів, але неправильно підібрані параметри вигладжування можуть спотворити ефективність процесу пластичної деформації. Для того, щоб оптимізувати це, створюється 2D FEM-модель, що включає реальну цілісність поверхні заготовки, яка була виміряна за допомогою приладу для вимірювання шорсткості поверхні AltiSurf 520. Метод моделюється за допомогою програмного забезпечення DEFORM-2D, що відповідає реалізованим на практиці числовим значенням параметрів вигладжування, що дозволяє проводити порівняльний аналіз з результатами рентгенівських дифракційних вимірювань. Результати рентгенівського дифракційного вимірювання показали, що полірована поверхня має від (-88,6) до (-138,6) МПа компресійне залишкове напруження. Порівнюючи ці значення з результатами моделювання МСЕ, де цей діапазон знаходиться в межах (-38,3) –(-87,0) МПа, можна помітити, що ці значення збігаються лише у випадку першого відступу інструменту. Одне з можливих пояснень цього може полягати в тому, що більш щільна сітка, необхідна для встановлення та/або якості матеріалу випробовуваної заготовки, не вибирається з бібліотеки програми FE (Al-6061-O, COLD), а базується на реальному значенні шляхом вивчення реальної межі текучості. Вимірювання фізичного напруження не дає інформації про те, як розподіляється залишкове напруження; Це явище може бути доступне при моделюванні. Відповідно, у міру вигладжування збільшується розподіл залишкових напружень стисненні, однак його величина змінюється несприятливо, надмірно зменшується, що призводить до висновку про занадто низьку величину швидкості подачі вигладжування. Це важливо, оскільки, збільшуючи цей параметр, можна заощадити час і кошти як з точки зору механічної обробки, так і з точки зору імітаційного розрахунку.*

Ключові слова: *скінченно-елементне моделювання; алмазне вигладжування; цілісність поверхні; пластична деформація.*

UDC 621.767 **doi: 10.20998/2078-7405.2024.100.11**

AN EXPERIMENTAL INVESTIGATION OF THE MECHANICAL PROPERTIES OF FUSED FILAMENT FABRICATED NYLON-CARBON FIBER COMPOSITES

Ioannis T. **Christodoulou** [1][0000-0003-1860-6839], Vasiliki E. **Alexopoulou** [1][0000-0003-4068-9810], Angelos P. **Markopoulos** [1,2][0000-0002-3754-5202]

[1]National Technical University of Athens, School of Mechanical Engineering, Laboratory of Manufacturing Technology, Heroon Polytechniou 9, 15780 Athens, Greece
[2]AGH University of Kraków, Department of Manufacturing Systems, Faculty of Mechanical Engineering and Robotics, 30-059 Krakow, Poland
amark@mail.ntua.gr

Received: 28 March 2024 / Revised: 26 April 2024 / Accepted: 28 May 2024 / Published: 15 June 2024

Abstract. *Additive Manufacturing (AM) is a rapidly growing field in both the researching and the industrial world, as it produces highly customized and geometrically complex objects. The most well-known AM technology for plastics is Fused Filament Fabrication (FFF), in which a thermoplastic filament is melted and extruded through a nozzle on the printing bed. A wide variety of printing parameters affect the quality of the printed objects, such as printing speed, infill density, infill pattern, build orientation, layer height, etc. In literature, there is already extended research of the impact of the printing parameters on the mechanical properties of the most common thermoplastics, such as ABS and PETG. However, the development of advanced thermoplastic materials, such as Nylon composites reinforced with carbon fibers (Nylon-CF), requires a further investigation of the effect of the printing parameters on those advanced composites. In the current study, an in-depth correlation of all the major printing parameters (infill pattern, infill density, dual line infill and printing speed) with all the major mechanical properties (tensile strength, compressive strength and bending strength) of Nylon-CF is carried out.*
Keywords: *Fused Filament Fabrication (FFF); Nylon-Carbon Fiber (Nylon-CF); tensile strength; compressive strength; bending strength.*

1. Introduction

Additive Manufacturing (AM) has become a very popular field for both the researching and the industrial world, due to its ability to give lightweight products with high customization and geometrical complexity [1]. In AM, the final product is fabricated with layer-by-layer deposition of melted material on a printing bed. According to the printing material, different AM technologies have been developed, such as Laser Powder Bed Fusion (LPBF) for metals and

developed, such as Laser Powder Bed Fusion (LPBF) for metals and Stereolithography (SLA) and Fused Filament Fabrication (FFF) for thermoplastics [2].

Specifically, in Fused Filament Fabrication (FFF), a thermoplastic filament is melted and then extruded through a nozzle on the printing bed [3]. In order to control the quality of the printed object, several printing parameters should be fine-tuned. Such parameters are printing speed, infill density, infill pattern, build orientation, layer height, raster angle, extrusion temperature, nozzle diameter and air gap, etc. [4].

Most of the papers in literature investigate the effect of these parameters on the mechanical properties of the most conventional thermoplastic materials, such as ABS and PETG. Es-Said et al. [5] printed with FFF ABS samples with different raster angles. They observed that the highest strength is achieved for 0^o, whereas 45^o and 90^o lead to layers delamination. Ashtankar et al. [6] examined the effect of building orientation on the tensile and compressive strength of FFF-produced ABS samples. They observed that by increasing the orientation from 0^o to 90^o, both tensile and compressive strength are reduced. Baich et al. [7] studied how infill density (low density, high density and double density) affects tensile, compressive and bending strength of FFF-printed ABS specimens. Higher strength is achieved by the high-density samples, whereas higher compressive and bending strength is achieved by double-density samples. Durgashyam et al. [8] fabricated with FFF PETG samples and observed that a combination of low layer height, high infill density and medium feed rate leads to higher tensile strength, whereas a combination of low infill density, low layer height and medium feed rate results in the best flexural properties. Yadav et al. [9] fabricated with FFF ABS, PETG and 50%ABS-50%PETG specimens. The results showed that the tensile strength is, mostly, affected by the extrusion temperature and the infill density. Srinivasan et al. [10] showed that in case of FFF-printed PETG specimens, increased infill density, increases tensile strength and decreases surface roughness.

Although there is, in literature, an in-depth investigation of the effect of printing parameters to the mechanical properties of the most well-known thermoplastic materials, such as ABS and PETG, there is a need to extent these mechanical properties investigations and into more advanced thermoplastic materials, which have started to gain a significant space into the industry, due to their superior mechanical properties. Such a material is the Nylon-Carbon Fiber (Nylon-CF). Nylon-CF is a composite filament of nylon polymer, blended with carbon fibers and demonstrates enhanced strength, stiffness and durability properties. These properties make Nylon-CF appropriate for multiple applications, such as prototyping, tooling and end-use products for aerospace and automotive industries. For this reason, researchers have started to study the mechanical properties of Nylon-CF

FFF-printed products. De Toro et al. [11] carried out experiments with FFF-printed Nylon-CF and showed that infill density has the most crucial role in both tensile and bending properties, whereas infill pattern affects mainly the bending behaviour. León-Becerra et al. [12] investigates the effect of build orientation on the roughness of FFF-fabricated Onyx (short carbon-filled fiber nylon) samples. The lowest roughness was observed in the flat print orientation. Sedlacek et al. [13] developed with FFF and compared pure PA6 nylon and PA6 with short carbon fibers. They showed that carbon fibers affect the strength and the heat deflection of the specimens. The research, till now, regarding FFF-fabricated Nylon-CF is very interesting, but it is not so extended like in other more conventional materials. So, in order to better understand the mechanical behaviour of FFF-fabricated Nylon-CF, all the major printing parameters should be correlated with all the major mechanical properties of Nylon-CF.

The target of this paper is to correlate and optimize all the major printing parameters (infill pattern, infill density, dual line infill and printing speed) with all the major mechanical properties (tensile strength, compressive strength and bending strength) of Nylon-CF.

2. Experimental Methods

The Nylon-CF samples were fabricated by the FFF-printer FlashForge® Creator 3 (Zhejiang Flashforge 3D Technology Co., Ltd.). The Nylon-CF filament was the Ultrafuse® PAHT CF15 (BASF 3D Printing Solutions BV), which is a high-performance 3D printing filament. The samples were fabricated and tested according to the ASTM D638-14, ASTM D695-15 and ASTM D790-15 standards for tensile strength, compressive strength and flexural strength tests, respectively. All the mechanical tests were carried out on an Instron® 4482 machine, which has a maximum loading capacity of 100 [kN].

For the Design of Experiments (DOE), Taguchi method was implemented, as shown in the Tables 1 (tensile strength) and Table 2 (compressive and flexural strength), below:

Table 1 Design of Experiments (DOE) for the tensile strength tests.

Factor / Run	Infill Pattern	Infill Density (%)	Infill Line Multiplier
1	Grid	5	1
2	Grid	15	2

3	Grid	25	3
4	Lines	5	2
5	Lines	15	3
6	Lines	25	1
7	Triangular	5	3
8	Triangular	15	1
9	Triangular	25	2

Table 2 Design of Experiments (DOE) for the compressive and flexural strength tests.

Factor / Run	Infill Pattern	Infill Density	Printing Speed	Infill Line Multiplier
1	Grid	5	25	1
2	Grid	15	50	1
3	Grid	25	75	1
4	Triangular	5	25	1
5	Triangular	15	50	1
6	Triangular	25	75	1
7	Lines	5	50	1
8	Lines	15	75	1
9	Lines	25	25	1
10	Grid	5	75	2
11	Grid	15	25	2
12	Grid	25	50	2

13	Triangular	5	50	2
14	Triangular	15	75	2
15	Triangular	25	25	2
16	Lines	5	75	2
17	Lines	15	25	2
18	Lines	25	50	2

According to the aforementioned standards, 5 samples, for each one of the experiments in Tables 1 and 2, were tested and the mean value of these 5 samples was extracted as a result.

The rest printing parameters were fixed for all the experiments (Table 3):

Table 3 Fixed printing parameters.

Printing Parameter	**Fixed Value**
Nozzle Diameter	0.6 [mm]
Layer Height	0.32 [mm]
Printing Temperature	270 [^{o}C]
Part Orientation	Horizontal
Shells	2
Build Plate Temperature	130 [^{o}C]

3. Results and Discussion

This study systematically investigates the mechanical properties of Nylon-Carbon Fiber composites fabricated using Fused Filament Fabrication (FFF) under varied printing parameters. The results highlight distinct trends across tensile, compressive, and flexural strengths, which are essential for optimizing the use of Nylon-CF in engineering applications.

Tensile Tests:

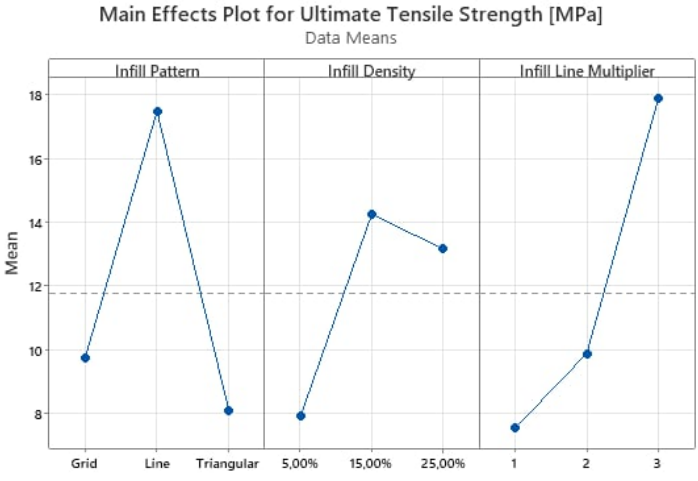

Figure 1. Main Effects Plot for Ultimate Tensile Strength

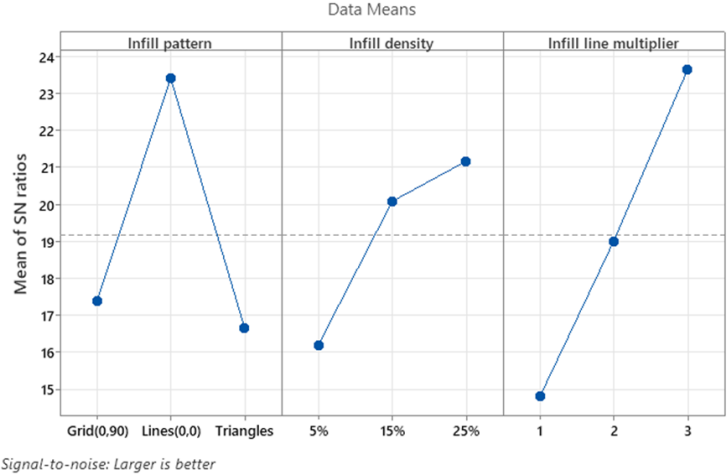

Figure 2. SN plots for Main Effects

The analysis of the tensile strength of Nylon-Carbon Fiber composites fabricated using Fused Filament Fabrication (FFF) reveals critical insights into the influence of printing parameters on mechanical performance. Given Figure 1, notably, the main effects plots indicate that the 'lines' infill pattern yields the highest

tensile strength. This outcome is intuitive, given that the lines were aligned with the direction of the tensile force during testing, thereby enhancing the load-bearing capacity of the composite. Surprisingly, the optimal infill density for maximizing tensile strength is found to be 15%, rather than the denser 25% option. This suggests a balance between material density and structural integrity, where too much density might introduce flaws or stress concentrations. Additionally, the infill line multiplier of 3 emerges as the most beneficial, significantly improving strength by adding two extra lines to the infill, thus reinforcing the composite structure. These findings underscore the complex interplay of infill pattern, density, and line multiplier in optimizing the tensile properties of FFF-manufactured Nylon-CF composites, offering valuable directions for tailoring material properties through precise control of printing parameters. The analysis of the Signal-to-Noise (S/N) ratios for the tensile strength of the Nylon-Carbon Fiber composites further, as showed in Figure 2, corroborates the findings from the main effects plot. The S/N ratios, which emphasize the robustness and reliability of the tensile strength under various experimental conditions, also highlight the lines infill pattern as particularly effective. This consistency between the S/N ratios and the main effects plot underscores the strength stability provided by the line orientation, which aligns with the tensile force direction. Furthermore, the optimal infill density at 15% and the superior performance of the three-line multiplier in the S/N analysis echo the main effects findings, demonstrating that these settings not only enhance mean strength but also minimize variability in performance.

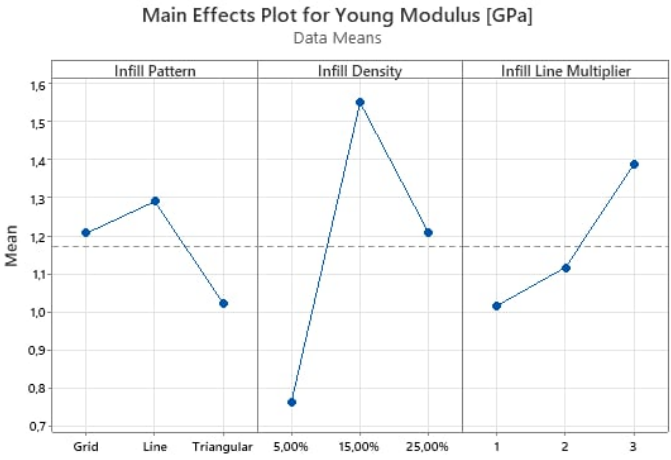

Figure 3. Main Effects Plot for Young Modulus

Figure 4. Main Effects Plot for SN ratios (Young modulus)

The examination of Young's Modulus for the tensile properties of Nylon-Carbon Fiber composites fabricated via Fused Filament Fabrication (FFF) presents intriguing results that align with trends observed in tensile strength. The main effects plot distinctly shows that the 'lines' infill pattern is superior, achieving an impressive modulus of 13 MPa. This pattern likely provides more continuous load-bearing paths along the tensile test direction, effectively improving the elastic response of the material. Furthermore, similar to the findings for tensile strength, an infill density of 15% is identified as optimal for maximizing Young's Modulus. This suggests that a medium density facilitates a balance between flexibility and rigidity, which is crucial for optimizing the elastic properties of the material. Additionally, the three-line multiplier once again proves to be most effective, likely due to its enhancement of the composite's internal structure, making it more resistant to elastic deformation. Consistently, the Signal-to-Noise (S/N) ratios for Young's Modulus reinforce these conclusions. The S/N plots follow the same patterns as the main effects, demonstrating that the 'lines' infill pattern, 15% infill density, and three-line multiplier not only maximize the mean modulus but also ensure stability and consistency across test conditions. These findings confirm the robustness of these parameter settings in enhancing the elastic properties of the composites, providing a reliable basis for parameter selection in the fabrication of FFF-manufactured Nylon-CF composites.

ANOVA Analysis:

Table 3. Analysis of Variance for Ultimate Tensile Strength

Source	Seq SS	Contribution	Adj SS	Adj MS	F-Value	P-Value
Infill Line Multiplier	117.076	48.54 %	117.076	58.5378	119.36	0.008
Infill Patterns	82.324	34.13 %	82.324	41.1622	83.93	0.012
Infill Percentage %	40.821	16.92 %	40.821	20.4104	41.62	0.023
Error	0.981	0.41 %	0.981	0.4904		
Total	241.202	100.00%				

Contribution: displays the percentage that each factor (Source) in the ANOVA table contributes to the total sequential sum of squares (Seq SS). Higher percentages indicate that the factor contributes more to the response variance. In the ANOVA table, the contribution rate of "infill pattern" factor is 34.13%, "infill density" factor is 16.92% and "infill line multiplier" factor is 48.58%, the contribution rate of "Error" factor is 0.41%.

F-value: A large F-value means that the effect of this factor is large compared to the variance of the error. Also, the larger the value, the more important this factor is in influencing the process response. Thus, F values can be used to classify the factors. An F value less than one means that the effect of the factor is less than the model error. An F value greater than two means that the factor is not small enough, while greater than four means that the effect of the factor is quite large. In the ANOVA table, the F values for the factors in order of ranking their effect from largest to smallest are "infill line multiplier" with an F value of 119.36, "infill pattern" with 83.93 and "infill density" with 41.62 respectively.

P-value: P-value is a probability that measures the evidence against the null hypothesis. Lower probabilities provide stronger evidence against the null hypothesis. To determine whether the relationship between the response and each term in the model is statistically significant, the P-value of the term is compared to the significance level for the null hypothesis evaluation. The null hypothesis asserts that there is no relationship between the term and the response. Typically, a significance level of α=0.05 works well. A significance level of 0.05 indicates a 5% risk of concluding that a relationship exists when in fact it does not.

P-value $\leq$ 0.05: The relationship is statistically significant.

If the p-value is less than or equal to the significance level, we can conclude that there is a statistically significant relationship between the response variable and the term.

P-value > 0,05: The relationship is not statistically significant

If the p-value is greater than the significance level, we cannot conclude that there is a statistically significant relationship between the response variable and the term. The model can be re-fitted without the term.

In the ANOVA table the P value of the factor "infill line multiplier" is 0.008 < 0.05, the factor " infill pattern" is 0.012 < 0.05 and the factor "infill density" is 0.023 < 0.05 therefore we conclude that all the factors are statistically significant.

Table 4. Analysis of variance for Young Modulus

Source	Seq SS	Contribution	Adj SS	Adj MS	F-Value	P-Value
Infill Line Multiplier	45.352	44.00%	45.352	22.6761	46.99	0.021
Infill Patterns	22.799	22.12%	22.799	11.3995	23.62	0.041
Infill Percentage %	33.953	32.94%	33.953	16.9763	35.18	0.028
Error	0.965	0.94%	0.965	0.4825		
Total	103.069	100.00%				

From Table 2, on the other hand, for maximizing the elasticity measure, the contribution of infill density comes second after the infill line multiplier factor, while all factors have a large effect and are statistically significant.

Compression Tests:

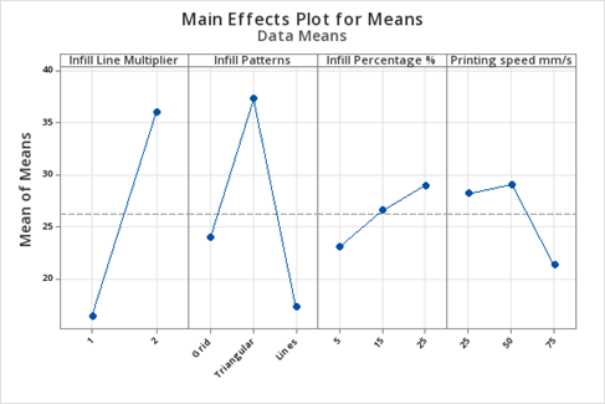

Figure 5. The primary effects of the processing parameters on the compressive strength of the produced specimens were analyzed using Taguchi's L18 array DOE. The average compressive strength of the fabricated specimens is represented by the dashed gray line.

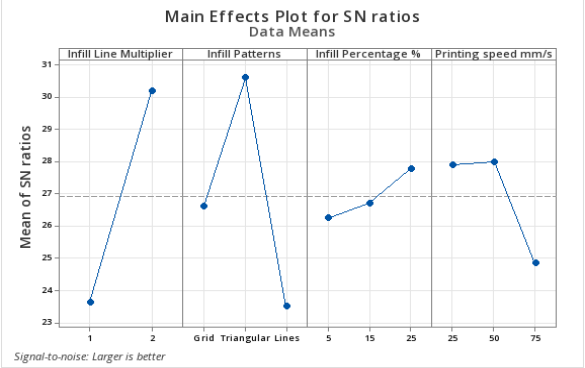

Figure 6. The graphs demonstrate the primary impacts of the processing factors on the compressive strength signal-to-noise ratio. The dashed gray line indicates the average signal-to-noise ratio of all the manufactured specimens

The study examines how different processing factors of Fused Deposition Modeling (FDM) affect the compressive strength of the specimens. Figure 5 shows the graphs of each processing parameter. The findings suggest that the percentage of infill and printing speed have a minimal impact on the resultant compressive strength of the specimens. Augmenting the infill % leads to a marginal augmentation in the compressive strength of the specimen, in line with the anticipated linear correlation, since it provides additional material to counteract the applied stress. Similarly, there is a nearly direct correlation between printing speed and compression strength of the specimens, where an increase in printing speed results in a decrease in compression strength. This phenomenon can be explained by the potential of greater printing speeds to diminish material deposition, leading to a subsequent decrease in adhesion between the layers. The infill pattern is identified as the parameter that has the most significant influence on the compression strength. More precisely, the triangle infill design produces the greatest compression strength values, whilst the grid and linear infill patterns produce the lowest values. The infill line multiplier has the second highest impact on the resultant compression strength. Augmenting the infill line multiplier leads to a proportional augmentation in the infill percentage of the specimen, resulting in a bigger mass of the specimen. This setting enhances the rigidity of the infill material. In order to optimize the Signal-to-Noise (S/N) ratio and improve the consistency of compression strength measurements for the specimen, it is advisable to utilize a double infill line, a triangle infill pattern, a 25% infill percentage, and a printing speed of 50 mm/s. The parameters described are anticipated to result in the greatest level of consistency in the compression strength of the specimens, as shown in Figure 6.

For Compressive Yield Strength, the Figures 7 and 8 are presented below,

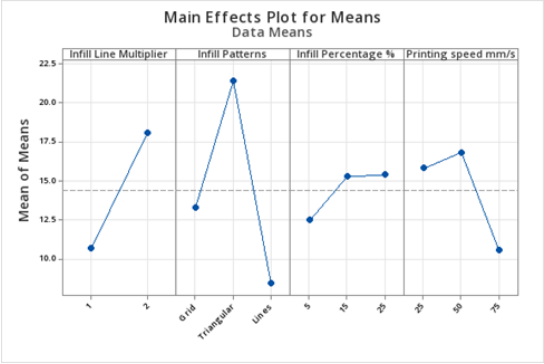

Figure 7. Plots of the main effects of the processing parameters on the compressive yield strength of the fabricated specimens investigated using Taguchi's L18 array DOE, the dashed gray line represents the average compressive yield strength of the fabricated specimens

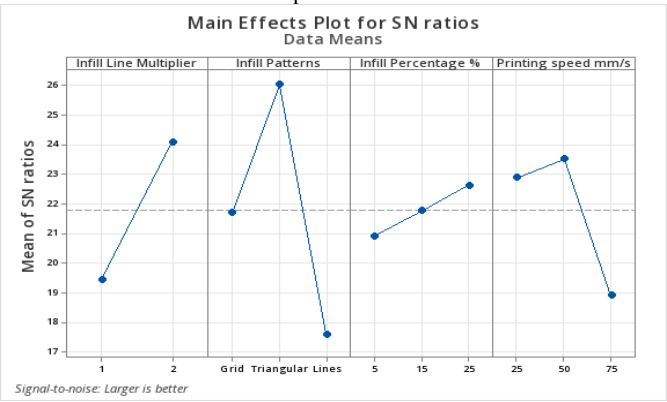

Figure 8. Plots of the main effects of the processing parameters on compressive yield strength S/N ratio, the dashed gray line represents the average S/N ratio of all the fabricated specimens.

The findings suggest that the processing factors have a comparable effect on the yield strength as they do on the compression strength. Infill patterns have an equal impact on both the yield strength and compression strength, as well as on the elastic modulus. The triangle infill pattern achieved the highest maximum yield strength, as shown in Figure 7. The strength of the material improves proportionally with the increase in infill percentage. However, there is no substantial further improvement in the yield strength beyond a 15% infill percentage. In contrast, increased printing speeds have an adverse impact on the strength of the material. According to Figure 8, the Signal-to-Noise (S/N) ratio for yield strength is maximized when the same processing parameters are used.

Table 5. Analysis of Variance for Compressive strength

Source	Seq SS	Contribution	Adj SS	Adj MS	F-Value	P-Value
Infill Line Multiplier	193.120	41.04%	193.120	193.120	24.11	0.001
Infill Patterns	151.497	32.19%	151.497	75.748	9.46	0.005
Infill Percentage %	7.334	1.56%	7.334	3.667	0.46	0.645
Error	80.103	17.02%	80.103	8.010		
Total	470.601	100.00%				

Table 6. Analysis of variance for compressive yield strength

Source	Seq SS	Contribution	Adj SS	Adj MS	F-Value	P-Value
Infill Line Multiplier	96.902	21.16%	96.902	96.902	15.15	0.003
Infill Patterns	213.444	46.61%	213.444	106.722	16.69	0.001
Infill Percentage %	8.870	1.94%	8.870	4.435	0.69	0.522
Error	63.943	13.96%	63.943	6.394		
Total	457.919	100.00%				

Contribution: This indicates the proportionate contribution, expressed as a percentage, of each factor (source) in the ANOVA table to the overall sequential sum of squares (Seq SS). Greater percentages indicate a higher level of contribution from the factor to the variation in the response. The ANOVA table displays the contribution percentages of the components as follows: "Infill line multiplier" contributes 41.04%, "Infill patterns" contributes 32.19%, "Infill percentage" contributes 1.56%, "Printing speed" contributes 8.19%, and the remaining 17.02% is attributed to mistake.

The ANOVA table displays the F-values for the components, listed in descending order of their influence: "Infill line multiplier" has the greatest F-value of 24.11, followed by "Infill patterns" with 9.46, "Printing speed" with 2.41, and "Infill percentage" with 0.46. The ANOVA table shows that the P-value for the factor "Infill line multiplier" is 0.001 and for "Infill patterns" is 0.005. Both of these values are less than the significance level of 0.05, showing that both factors are statistically significant. The remaining factors have P-values exceeding 0.05, indicating that they lack statistical significance.

3-point Bending Test:

Figure 9. Plots illustrating the impact of processing factors on the flexural strength of the fabricated specimens were analyzed using Taguchi's L18 array Design of Experiments (DOE). The dashed gray line indicates the average flexural strength of the fabricated specimens.

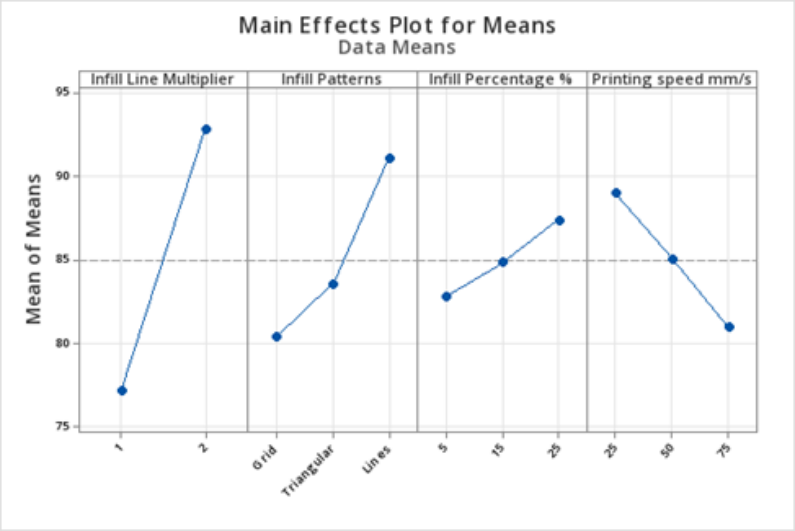

Figure 10. The plots illustrate the primary impacts of the processing factors on the flexural strength signal-to-noise (S/N) ratio. The dashed gray line indicates the average S/N ratio of all the produced specimens.

The flexural test results are presented in Figure 9, displaying the mean values obtained from each of the five repeated specimens. The parameters examined in this study include the flexural fracture stress and flexural strength, Flexural Strength, and the energy required to produce the specimens. For the signal-to-noise ratio, a bigger value is preferable. The signal-to-noise ratio (S/N ratio) is employed to maximize these desired mechanical properties.

The study examines how different processing factors of Fused Deposition Modeling (FDM) affect the flexural strength of the specimens. Figure 9. The charts of each processing parameter are shown. The findings suggest that the impact of the infill percentage and printing speed on the flexural strength of the specimens is less significant compared to the other parameters. Higher infill percentages lead to a proportional increase in the flexural strength of the specimen, since it introduces additional material to withstand the applied load. Similarly, there is a nearly direct correlation between printing speed and compression strength of the specimens, where an increase in printing speed results in a decrease in compression strength.

This phenomenon is ascribed to the potential that increased printing velocities could diminish the amount of material being deposited, leading to a subsequent decline in the bonding between the layers.

The parameter that has the greatest influence on the flexural strength is the infill line multiplier. More precisely, the double infill line produces the highest flexural strength numbers, whilst the infill line multiplier 1 produces the lowest values. The infill patterns have the second highest impact on the final flexural strength. Utilizing a lines design yields superior flexural strength, while a grid pattern exhibits the lowest values of flexural strength. The triangle pattern is in between these two extremes.

In order to optimize the Signal-to-Noise (S/N) ratio and improve the consistency of flexural strength measurements, it is advisable to employ a double infill line, a lines infill pattern, a 25% infill percentage, and a printing speed of 25 mm/s. The parameters described are anticipated to result in the greatest level of consistency in the flexural strength of the specimens, as shown in Figure 10.

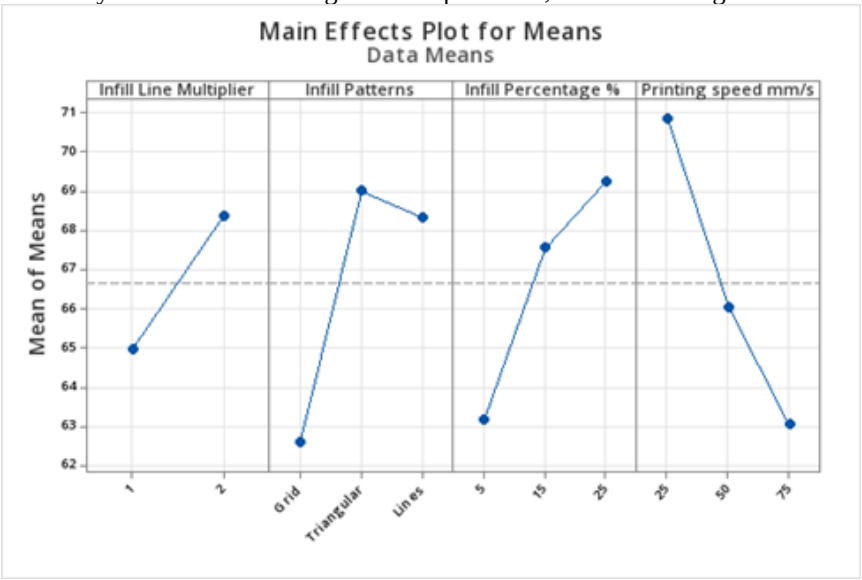

Figure 11. The primary effects of the processing factors on the flexural break stress of the produced specimens were analyzed using Taguchi's L18 array DOE. The average flexural break stress of the fabricated specimens is represented by the dashed gray line.

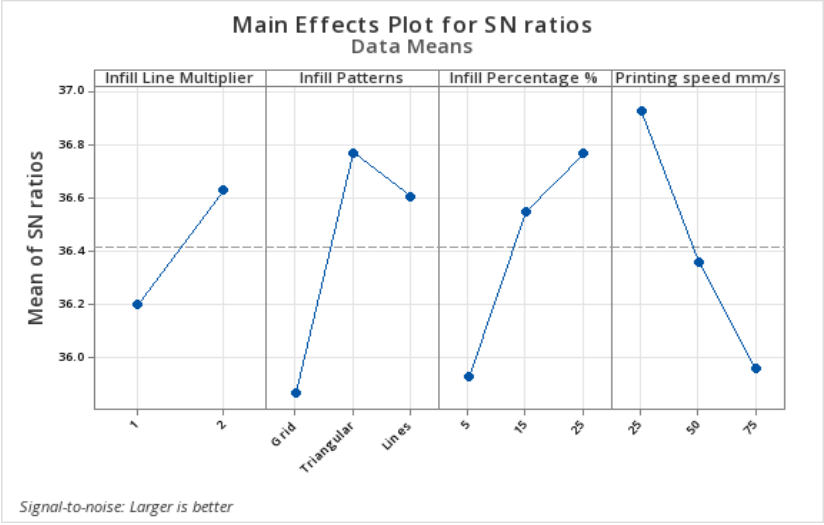

Figure 12. The graphs demonstrate the primary impacts of the processing parameters on the flexural break stress S/N ratio. The dashed gray line indicates the average S/N ratio of all the fabricated specimens.

The findings suggest that the flexural break stress is affected by the processing factors in a manner that is comparable to their impact on flexural strength. The printing speed has an equal impact on both the flexural break stress and flexural strength, as well as on the elastic modulus. It is worth mentioning that the printing speed of 25 mm/s achieved the highest maximum flexural break stress, as shown in Figure 11. The flexural fracture strength rises proportionally with the increase in the percentage of infill. The triangular infill design appears to produce superior results in terms of flexural break stress, whilst the lines pattern exhibits nearly identical performance. The grid infill pattern reduces the flexural break stress values. The infill line multiplier has a comparable impact on flexural strength, but it is the least significant factor. According to Figure 12, in order to get the highest Signal-to-Noise (S/N) ratio for flexural break stress, the processing parameters need to remain the same, except for the infill pattern which should be triangular.

Table 7. Analysis of Variance for Flexural Strength

Source	Seq SS	Contribution	Adj SS	Adj MS	F-Value	P-Value
Infill Line Multiplier	12.4723	49.24%	12.4723	12.4723	20.01	0.001
Infill Patterns	4.3362	17.12%	4.3362	2.1681	3.48	0.071
Infill Percentage %	0.5338	2.11%	0.5338	0.2669	0.43	0.663
Printing speed mm/s	1.7562	6.93%	1.7562	0.8781	1.41	0.289
Error	6.2335	24.61%	6.2335	0.6233		
Total	25.3320	100.00%				

Table 8. Analysis of Variance for Flexural break stress

Source	Seq SS	Contribution	Adj SS	Adj MS	F-Value	P-Value
Infill Line Multiplier	0.8326	4.23%	0.8326	0.8326	0.76	0.404
Infill Patterns	2.7621	14.03%	2.7621	1.3811	1.26	0.325
Infill Percentage %	2.2813	11.58%	2.2813	1.1406	1.04	0.389
Printing speed mm/s	2.8519	14.48%	2.8519	1.4260	1.30	0.315
Error	10.9642	55.68%	10.9642	1.0964		
Total	19.6921	100.00%				

The Analysis of Variance (ANOVA) for flexural strength and flexural break stress provides significant insights into the influence of various printing parameters on the mechanical properties of Nylon-Carbon Fiber composites. In the flexural strength analysis, the most critical factor proved to be the infill line multiplier, which showed a substantial contribution of 49.24% to the model with an F-value of 20.01, indicating a highly significant effect (P-value = 0.001). This suggests that the infill line multiplier greatly influences the composite's ability to resist bending forces, which is crucial for applications requiring high flexural strength. Conversely, other factors such as infill patterns, infill percentage, and printing speed demonstrated less impact. Infill patterns and printing speed showed some influence with F-values of 3.48 and 1.41, respectively, but their contributions were not statistically significant at conventional levels (P-values of 0.071 and 0.289, respectively). The infill percentage contributed minimally to flexural strength variations, as reflected by a low F-value of 0.43 and a non-significant P-value of 0.663, indicating that changes in percentage infill do not considerably alter the flexural strength within the tested range. For flexural break stress, the ANOVA results indicated a more evenly distributed but generally non-significant influence across all tested parameters. The highest contribution came from printing speed, contributing 14.48% with an F-value of 1.30 (P-value = 0.315), followed closely by infill patterns and infill percentage, which showed similar contributions and non-significant P-values. The infill line multiplier, despite being a significant factor in flexural strength, showed a minimal and non-significant effect on flexural break stress (P-value = 0.404). These findings suggest that while certain parameters significantly affect flexural strength, such as the infill line multiplier, their impact

on flexural break stress is less pronounced. This differentiation in parameter influence highlights the complexity of 3D printing settings on material properties, underscoring the need for careful selection and optimization of parameters based on the specific mechanical property requirements of the final product.

4. Conclusion

This study provides a detailed analysis of the mechanical properties of Nylon-Carbon Fiber composites manufactured using Fused Filament Fabrication (FFF). By examining tensile, compressive, and flexural strengths under various printing parameters, significant insights were gained into the optimization of these properties for industrial applications.

The tensile tests showed that the 'lines' infill pattern, when combined with a 15% infill density and a three-line multiplier, produced the highest tensile strength, enhancing the load-bearing capacity of the material. This configuration led to an optimal tensile strength of up to 18 MPa and a Young's modulus of 1.58 GPa, demonstrating that precise control over the infill parameters can lead to substantial improvements in performance. The consistency and reliability of these settings were validated by the Signal-to-Noise ratios, ensuring that the enhancements in mechanical properties are both significant and dependable.

In compressive strength tests, while the infill pattern and line multiplier impacted strength, their effects were less pronounced than in tensile strength tests. The optimal settings that favored higher infill percentages and specific infill patterns still provided a modest increase in compressive strength, with the best configurations achieving up to 35 MPa, indicating improved rigidity and load-bearing capacity under compression.

Flexural strength testing highlighted the critical role of the infill line multiplier, which substantially influenced the material's ability to resist bending forces. The best settings, involving a double infill line and specific speeds and patterns, led to a maximum flexural strength of 94 MPa. These parameters were crucial in distributing stress and strain across the composite during bending tests, thereby enhancing its structural integrity under flexural loads.

In summary, this research has systematically explored how the adjustment of key printing parameters can manipulate the mechanical properties of Nylon-Carbon Fiber composites in targeted ways. Each set of mechanical tests—tensile, compressive, and flexural—has its own set of optimal print settings, highlighting the need for a nuanced approach to the 3D printing of advanced composite materials. Future studies could further refine these findings by exploring the interaction effects between parameters and extending the analysis to include dynamic loading conditions and long-term material behavior. This would provide even deeper insights

into the practical applications of FFF technology in producing high-performance parts for aerospace, automotive, and other demanding industrial sectors.

References: 1. *M. S. Alsoufi, A. El-Sayed, and A. E. Elsayed*, How Surface Roughness Performance of Printed Part Manufactured by Desktop FDM 3D Printer with PLA+ is Influenced by Measuring Direction, Am. J. Mech. Eng., vol. 5, no. 5, pp. 211–222, 2017, doi: 10.12691/ajme-5-5-4. **2.** *A. Rashid*, Additive Manufacturing Technologies, CIRP Encycl. Prod. Eng., pp. 1–9, 2019. **3.** *S. Vyavahare, S. Teraiya, D. Panghal, and S. Kumar*, Fused deposition modelling: a review, Rapid Prototyp. J., vol. 26, no. 1, pp. 176–201, 2020, doi: 10.1108/RPJ-04-2019-0106. **4.** *K. Rajan, M. Samykano, K. Kadirgama, W. S. W. Harun, and M. M. Rahman*, Fused deposition modeling: process, materials, parameters, properties, and applications, vol. 120, no. 3–4. Springer London, 2022. doi: 10.1007/s00170-022-08860-7. **5.** *O. S. Es-Said, J. Foyos, R. Noorani, M. Mendelson, R. Marloth, and B. A. Pregger*, Effect of layer orientation on mechanical properties of rapid prototyped samples, Mater. Manuf. Process., vol. 15, no. 1, pp. 107–122, 2000, doi: 10.1080/10426910008912976. **6.** *K. M. Ashtankar, A. M. Kuthe, and B. S. Rathour*, IMECE 2013-63146, pp. 1–7, 2016. **7.** *L. Baich, G. Manogharan, and H. Marie*, Study of infill print design on production cost-time of 3D printed ABS parts, Int. J. Rapid Manuf., vol. 5, no. 3/4, p. 308, 2015, doi: 10.1504/ijrapidm.2015.074809. **8.** *K. Durgashyam, M. Indra Reddy, A. Balakrishna, and K. Satyanarayana*, Experimental investigation on mechanical properties of PETG material processed by fused deposition modeling method, Mater. Today Proc., vol. 18, pp. 2052–2059, 2019. **9.** *D. Yadav, D. Chhabra, R. Kumar Garg, A. Ahlawat, and A. Phogat*, Optimization of FDM 3D printing process parameters for multi-material using artificial neural network, Mater. Today Proc., vol. 21, pp. 1583–1591, 2020, doi: 10.1016/j.matpr.2019.11.225. **10.** *R. Srinivasan, W. Ruban, A. Deepanraj, R. Bhuvanesh, and T. Bhuvanesh*, Effect on infill density on mechanical properties of PETG part fabricated by fused deposition modelling, Mater. Today Proc., vol. 27, pp. 1838–1842, 2020, doi: 10.1016/j.matpr.2020.03.797. **11.** *E. V. De Toro, J. C. Sobrino, A. M. Martínez, and V. M. Eguía*, Analysis of the influence of the variables of the fused deposition modeling (FDM) process on the mechanical properties of a carbon fiber-reinforced polyamide, Procedia Manuf., vol. 41, pp. 731–738, 2019, doi: 10.1016/j.promfg.2019.09.064. **12.** *J. León-Becerra, M. Á. Hidalgo-Salazar, J. P. Correa-Aguirre, O. A. González-Estrada, and A. D. Pertuz*, Additive manufacturing of short carbon filled fiber nylon: effect of build orientation on surface roughness and viscoelastic behavior, Int. J. Adv. Manuf. Technol., vol. 130, no. 1–2, pp. 425–435, Jan. 2024, doi: 10.1007/s00170-023-12503-w. **13.** *F. Sedlacek and V. Lašová*, Additive Manufacturing of PA6 with Short Carbon Fibre Reinforcement Using Fused Deposition Modelling, Mater. Sci. Forum, vol. 928, pp. 26–31, Aug. 2018, doi: 10.4028/www.scientific.net/MSF.928.26.

Іоаніс Т. Христодулу, Василікі Е. Алексопулу, Ангелос П. Маркопулос,
Афіни, Греція

ЕКСПЕРИМЕНТАЛЬНЕ ДОСЛІДЖЕННЯ МЕХАНІЧНИХ ВЛАСТИВОСТЕЙ КОМПОЗИТІВ НЕЙЛОН-ВУГЛЕЦЕВЕ ВОЛОКНО, ВИГОТОВЛЕНИХ ІЗ ПЛАВКИХ НИТОК

Анотація. *Адитивне виробництво (АМ) – це галузь, яка швидко розвивається як у дослідницькому, так і в промисловому світі, оскільки дозволяє виробляти дуже індивідуальні та геометрично складні об'єкти. Найвідомішою технологією АМ для пластмас є виробництво з плавленої нитки (Fused Filament Fabrication, FFF), в якій термопластична нитка розплавляється і видавлюється через сопло на друкарську пластину. На якість надрукованих об'єктів впливають різноманітні параметри друку, такі як швидкість друку, щільність заповнення, малюнок заповнення,*

орієнтація побудови, висота шару тощо. У літературі вже існують ґрунтовні дослідження впливу параметрів друку на механічні властивості найпоширеніших термопластів, таких як ABS і PETG. Однак розробка сучасних термопластичних матеріалів, таких як нейлонові композити, армовані вуглецевими волокнами (Nylon-CF), вимагає подальшого дослідження впливу параметрів друку на ці композити. У даному дослідженні проведено поглиблену кореляцію всіх основних параметрів друку (малюнок заповнення, щільність заповнення, дворядкове заповнення і швидкість друку) з усіма основними механічними властивостями (міцність на розрив, міцність на стиск і міцність на вигин) нейлону з вуглецевим волокном (Nylon-CF). Випробування на розтягнення показали, що "лінійна" структура заповнення в поєднанні з 15% щільністю заповнення і трилінійним мультиплікатором забезпечує найвищу міцність на розтягнення, підвищуючи тримальну здатність матеріалу. Така конфігурація дозволила досягти оптимальної міцності на розрив до 18 МПа і модуля Юнга 1,58 ГПа, демонструючи, що точний контроль параметрів заповнення може призвести до значного поліпшення експлуатаційних характеристик. Послідовність і надійність цих налаштувань були підтверджені співвідношенням сигнал/шум, яке гарантує, що покращення механічних властивостей є значним і надійним. Таким чином, це дослідження системно вивчило, як регулювання ключових параметрів друку може цілеспрямовано впливати на механічні властивості композитів з нейлон-вуглецевого волокна. Для кожного набору механічних випробувань - розтягування, стиснення та згинання - є свій набір оптимальних параметрів друку, що підкреслює необхідність нюансованого підходу до 3D-друку передових композитних матеріалів. Майбутні дослідження можуть уточнити ці висновки, вивчивши ефекти взаємодії між параметрами і розширивши аналіз, включивши в нього динамічні умови навантаження і довгострокову поведінку матеріалу. Це дало б ще глибше розуміння практичного застосування технології FFF у виробництві високопродуктивних деталей для аерокосмічної, автомобільної та інших відповідальних галузей промисловості.

Ключові слова: *виробництво плавких ниток (FFF); нейлон-вуглецеве волокно (Nylon-CF); міцність на розрив; міцність на стиск; міцність на вигин.*

UDC 536:621.9 (075.8) **doi: 10.20998/2078-7405.2024.100.12**

LEVEREGING TECHNOLOGICAL HEREDITY TO INCREASE PRODUCTION EFFICIENCY OF FERROCERRAMIC PRODUCTS DURING FINAL MACHINING

Anatoliy **Usov** [0000-0002-3965-7611], Maksym **Kunitsyn** [0000-0003-1764-8922], Yuriy **Zaychyk** [0000-0002-8577-1095], Yuliia **Sikirash** [0000-0003-0853-582X]

National University "Odessa Polytechnic", Odessa, Ukraine
usov_a_v@op.edu.ua

Received: 22 March 2024 / Revised: 28 April 2024 / Accepted: 27 May 2024 / Published: 15 June 2024

Abstract. *The quality state of grinded surface of ferro ceramic products is formed under the influence of thermomechanical phenomena which occurs during final machining and depends on the technological conditions for workpiece procurement. The mathematical model was formulated to regulate and optimize thermomechanical processes during the acquisition of ferroceramic workpieces. This mathematical model describes thermomechanical processes during workpieces sintering. Thermomechanical processes have a direct influence on defects formation in the workpieces. Grinding can cause the appearance of burns, cracks, tensile stresses in the surface layers of the products. These defects can significantly spoil the quality of products during their operation. High thermal stress of diamond-abrasive processing brings thermophysical aspects as a dominating factor for quality characteristics of processed surface. Existing grinding methods for products made from ferrocerramic materials are not able to fully eliminate the defects in the surface layer. Such defects are inherited from preceding machining operations, particularly from workpiece procurement. Material structure itself is prone or defect occurrence due to micro-heterogeneities, packaging defects, dislocations, and structural transformations. Analysis of the thermomechanical processes that run inside the surface layer made it possible to formulate calculation dependencies for defining technological conditions for eliminating burns and cracks during grinding of ferrocerramic products. Device for automatic stabilization of thermomechanical characteristics that accompany grinding of ferrocerramic products. This is achieved through the selection of optimal technological conditions for machining of the products that have heredity inhomogeneities inside the surface layer. Thus, this approach helps to achieve maximum efficiency within required quality citeria.*
Keywords: *optimization; workpiece; grinding; surface quality; thermomechanical phenomena; model; defects; technological parameters; device.*

1. Introduction

Products from ferrocerramic materials are widely used in the energetics industry (in generators, electric drives, transformers, etc.) because of their wide range of magnetic properties. Unique combinations of electromagnetic properties make ferrites useful in other technical fields. The amount of their production in the world has reached millions of tons annually and keeps growing.

Thus, the improvement of technological processes for wastes recycling (including flawed products) of ferrite production is rather relevant because the amount of waste may be up to 30%. Recycling of wastes into usable half-finished products not only helps to optimize material consumption, energy, and production resources, but also helps to decrease the influence on the environment [1].

Technological loss is connected to loss of the material, half-finished products and usable products due to the imperfection of technological process and technological equipment (leakages, absence of trapping system, frequent failures, etc.). Flaw is connected to the deviations of the parameters of half-finished-products and usable products that overcome acceptable values. Flaw can be divided into 2 types: removable and unremovable. Recycling of the removable flaw into new products (or semi-finished products) requires additional operations connected with deep physical and chemical transformations. To recycle the unremovable flaw, we need additional operations that include shredding, thermal treating, chemical treating of the surface particles, etc. Technological wastes relate to the occurrence of side products during various technological operations (wastes from molding compounds, wastes from the machining operations, wastes from quality assurance stages, etc.) (fig.1). They also can be divided into two types: utilized into usable half-finished products; utilized into ecologically safe forms.

Attention of the researchers was paid to the process of supplying ferrites with quality characteristics during final machining operations [2] [3].

Research showed that sticking of the suspensions is happening in the acid or neutral environment.

Technological loss in the production of forming compounds (press-powders, pastes, and slips) like in the case with technological loss in production of powders is connected with leakages in technological equipment (drying-granulating, mixing, sifting, shredding, etc.). That's why the same methods for decreasing the loss same methods are used as for the powders.

During the production of forming compounds the flaw can be removed using two main approaches:

- burning of the bundle with the temperature of 400…600°C, followed by shredding of the obtained stock and repeating the preparation of the forming compound;
- repeated preparation of the forming compound without burning the bundle and utilizing auxiliary amount of the bundle or its separate components. For example, flawed press-powder can be repeatedly treated with water inside the attritor. The obtained suspension is used for making press-powder with vaporized drying approach.

The most widespread type of flaw during pressing of the granulated and usual powders is delamination – lateral or diagonal cracks that break workpiece consistency. The reasons for delamination can be the following:

- When pushing the workpiece out of press-form matrix two opposite processes may occur: expanding of the workpiece and squeezing of the matrix. As a result of these deformations cracks can appear alongside deformation borders.
- Incorrect construction of the press-form (e.g. absence of taper in the matrix from the output side) or its skewness during pressing results in irregular force drop which leads to additional stresses inside the workpiece during its removal out of the matrix. Excessively slow extraction of the workpiece (and especially stops during pressing out) can induce cracks. Thin walls and sharp transitions in the workpiece also contribute to crack appearance.

However, to solve this problem it is required to analyze the reasons of flaw appearance through the complete technological cycle of product manufacturing and formulate the recommendations for decreasing defects during each of the technological operations.

Technological wastes during powder manufacturing are caused by sticking of the suspension obtained through wet shredding on the walls of the technological equipment (vaporizing dryers, reactors, tubes) and forming of firm crusts, and big hard conglomerates during thermal treating of the stock.

Decreasing suspension sticking on the working surfaces of the technological equipment has important practical meaning. Suspension sticking can lead to the offset of chemical compound for ferrite powders of different series. That's why periodic equipment cleaning is required.

Size flaws may occur due to the increased resilient aftereffect in the workpiece in case of high resilience limit, incorrect construction or sizes of the press-form, unprecise powder doze or pressing modes violation (insufficient or excessive pressure). Scratches in the matrix lead to numerous risks for the workpiece surface. Low quality grinding of the puncheon working surface may result in the appearance of chips on workpiece edges.

Loss during sintering occur mainly because of flawed workpieces and can reach up to 20%. In oxide ceramic manufacturing the most common types of flaws during sintering are hidden delamination, insufficient sintering, over-burning, warping.

Control of the technological processes and their correction for various types of magnets has high importance. Problem of finding optimal conditions for sintering is rather relevant [1].

During the sintering of the ferroceramic products the process of consolidation and recrystallization runs faster at higher temperatures. But high temperature also contributes to defects in crystal cell. This means that ferrite crystals which are formed in such conditions will have defective structure. Defects in the crystal cell have significant influence on ferrite's durability. There is the reason to think that the

defects in the crystal cell may also have influence on magnetic properties of the ferrites.

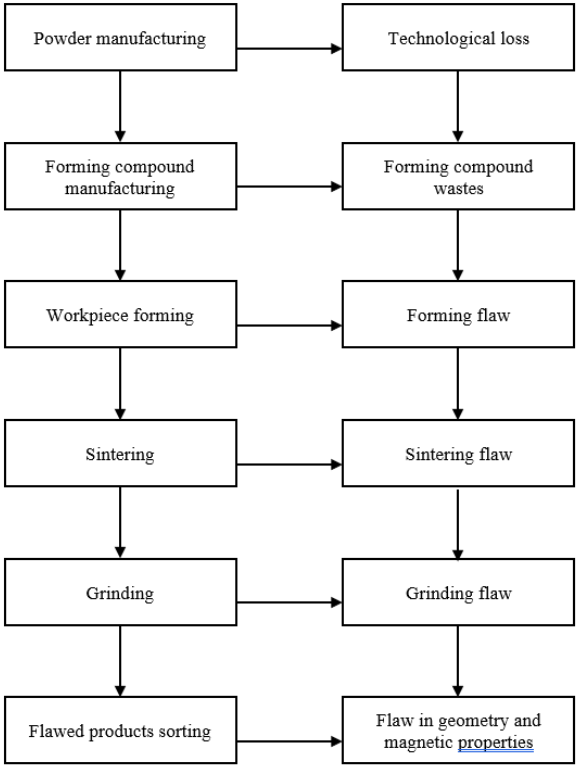

Fig. 1. Main types of wastes in ferrite products manufacturing.

Ferrite sintering is held in continuous furnaces. In order to create a closed optimal control system for sintering temperature it is required that information about the workpiece state have to be continuously sent to the control unit. This information consist of finite set of coordinate values of controlled object. At the same time we may investigate the current object state by the coordinates which are available for measuring.

The complexity of the processes occurring in the near-surface layer of a product subject to machining, as well as during the operation of these parts, makes it necessary to consider the influence of technological heredity both at the stage of obtaining the workpiece and on the final processing operations.

The most common finishing method is grinding, which ensures high precision and high productivity in the production of products. The heat tension of this type of processing affects the change in the thermophysical parameters of the processed materials (tensile strength, thermal conductivity). Therefore, the study of optimal thermomechanical characteristics in the processing zone did not take these factors into account.

Thus, the study and control of the thermomechanical state of workpieces and working surfaces of products made of ferro-ceramic materials during finishing operations, taking into account previous types of processing of products, in order to eliminate cracking and burn formation on the processed surfaces is the subject of this work.

2. Analysis of sources and problem description

The problem of improving the quality of the surface layer of sanded products is currently being solved using the following methods:

- selection of grinding modes that are rational for a given material and the corresponding characteristics of the tool are carried out [4];
- grinding wheels and belts with an intermittent working surface are used [5];
- automatic control systems for active cutting power are used [6];
- cutting fluids are recommended, which significantly reduces the heat stress of the grinding operation and thereby the likelihood of burns and cracks [7].

However, these methods, with the existing technology for manufacturing parts from ferro-ceramic materials, including in connection with the advent of composite materials, do not completely eliminate defects arising in the surface layer. This is facilitated by: inevitable fluctuations in allowance due to errors in previous machining operations [8]; micro-inhomogeneity of the material itself, characterized by grain size, packing defects, dislocations and structural transformations, warping of parts during thermal and similar processing; thermomechanical phenomena accompanying the grinding process and as a result of which burns, microcracks, structural transformations, residual stresses appear on the processed surfaces [9].

The high thermal intensity of diamond abrasive processing processes leads to the fact that the thermophysics of these processes is often dominant in the formation of the qualitative characteristics of the treated surface [10]. The lack of information about the thermomechanical state of the working surfaces of products made of ferro-ceramic materials during finishing operations does not allow to avoid the above-mentioned defects on the processed surfaces.

3. Research objectives

Study and control of the thermomechanical state of the working surfaces of products made of ferro-ceramic materials both during the receipt of workpieces and during finishing operations in order to eliminate cracking and burn formation on the processed surfaces.

Achieving this goal required setting and solving the following main task:

1. To formulate a mathematical model for optimizing and controlling thermomechanical processes when obtaining workpieces of ferro-ceramic products during sintering, describing thermomechanical processes in workpieces that affect the formation of defects and determine the control of technological parameters of sintering to eliminate these defects.
2. To Obtain calculated dependencies for determining the technological conditions for eliminating pinching and cracking on the working surfaces of ferro-ceramic products when processing them by grinding.

To develop a device for automatic stabilization of thermomechanical characteristics accompanying the grinding operation of ferro-ceramic products by selecting technological conditions for processing parts that have hereditary heterogeneities in the surface layer, ensuring maximum productivity while ensuring the required quality indicators.

4. Research methods

Theoretical studies were carried out using the thermophysics of mechanical and physical-technical processing processes, theories of thermoelasticity, an integrated approach of modern deterministic theories of fracture mechanics and methods for optimizing systems with distributed parameters, as well as numerical methods.

Let us consider the process of sintering a workpiece, described by the following relations [11]:

$$c\rho\frac{\partial T}{\partial t}=\frac{\partial}{\partial x}\left(\lambda(T)\frac{\partial T}{\partial x}\right),\ x\in(0,\ l),\ t\in(0,\ \infty), \quad (1)$$

$$T(x,\ 0)=T^{o}=const,\ \ x\in[0,\ l], \quad (2)$$

$$\lambda(T)\frac{\partial T}{\partial x}=\alpha[v(t)-T(l,t)],\ t\in\left[0,\overline{t}\right],\ 0<\overline{t}<\infty, \quad (3)$$

$$\frac{\partial T(0,t)}{\partial x}=-\frac{q}{\lambda(T)},\ t\in\left[0,\overline{t}\right], \quad (4)$$

here: T – temperature (°C); t – time; c – heat capacity coefficient; ρ – density; λ – thermal conductivity coefficient; l – surface layer thickness; x – workpiece movement coordinate inside continuous furnace; α – heat transfer coefficient; $v(t)$ – control; q – heat flow on workpiece's surface layer.

In the range of temperature variation $[T_1,\ T_2]$ function $\lambda(T)$ is positive and

according to the thermophysical properties of the material it has a finite derivative by T. Moreover, let's consider that inside the working temperature range T $\in$ [T_1, T_2] values of the function λ(T) are defined using the expression:

$$0 < \beta_1 \leq \lambda(T) \leq \beta_2, \quad (5)$$

Within the mentioned conditions system of equations (1) – (4) for each fixed value $v(t) \in V$ has generic solution.

According to the conditions of the problem, it is unacceptable that, under the influence of thermomechanical processes, the surface layer of the workpiece is heated to a temperature at which the functional properties of the surface layer are lost and thermal cracks form on the surface of the product.

Typically, workpieces use materials that break down brittlely when heated, without any noticeable deformation, or materials that transform into a plastic state under the influence of thermal stresses.

The problem of thermoelasticity in a quasi-static formulation and under the assumption that α_T is the coefficient of linear expansion and E - is the elastic modulus, do not depend on temperature and is solved analytically [8] [9].

Analysis of thermal stresses shows that, under the conditions of the problem under consideration, tensile stresses reach their greatest values in the workpiece at depth, and compressive stresses - on the surface. Taking into account the above, restrictions on thermal stresses in the workpiece can be written in the form:

$$\frac{\alpha_T E}{1-\psi}\left(-T(0,t) + \frac{1+3G}{l}\int_0^l T(\zeta,t)d\zeta - \frac{6G}{l^2}\int_0^l \zeta T(\zeta,t)d\zeta\right) \leq \sigma_1[T(0,t)], \quad (6)$$

$$\frac{\alpha_T E}{1-\psi}\left(T(0,t) - \frac{1-3G}{l}\int_0^l T(\zeta,t)d\zeta - \frac{6G}{l^2}\int_0^l \zeta T(\zeta,t)d\zeta\right) \leq \sigma_2[T(l,t)], \quad (7)$$

where $\sigma_1[T(0,t)] = \begin{cases} \sigma_p[T(0,t)] - \text{for brittle materials} \\ \sigma_{0.2}[T(0,t)] - \text{for flexible materials} \end{cases}$; $\sigma_2[T(0,t)] = \begin{cases} \sigma_c[T(l,t)] - \text{for brittle materials} \\ \sigma_{0.2}[T(l,t)] - \text{for flexible materials} \end{cases}$

ψ - Poisson coefficient; $\sigma_p(T)$, $\sigma_e(T)$, $\sigma_{0.2}(T)$ – tensile, compressive and yield strengths, respectively.

In addition to fulfilling inequalities (1) – (7), we will require fulfilling the limitation on the maximum temperature in the surface layer of the workpiece. It should not exceed, for example, the temperature of structural transformations T_s in the surface layer material, i.e.

$$T(l, t) \leq T_s . \quad (8)$$

Let us find the control $v^{\circ}(t) \in V$, $t \in [0, t^{\circ}]$, which transforms, in a minimum time t°, $0 < t^{\circ} < t^{-}$, the thermomechanical state of the surface layer, which is described by the system of equations (1) — (4) from the initial position (2) to a given final thermal position $\bar{T}(x)$ with a fixed accuracy:

$$\int_0^l \left[T(x,t°,v°) - \overline{T}(x)\right]^2 dx < \epsilon, \ \ \epsilon \geq 0$$

In such way, that for all $t \in [\varphi, t\ ^{\circ}]$, φ=const>0 inequations (6) – (8) will be fulfilled. To solve this problem we will use the approach of consecutive approximations [12]. Taking into account the "maximum principle" we get the following [13]:

$$m \leq T(x, t) \leq M, \tag{9}$$

where $M = \max \begin{Bmatrix} \max v(t), T° \\ t \in [0,t] \end{Bmatrix}, M = \min \begin{Bmatrix} \min v(t), T° \\ t \in [0,t] \end{Bmatrix}$. Let T_1=m, T_2=M, $\lambda_0 = \frac{\beta_1+\beta_2}{2}$.

The following itational process will be applied to the system of equations (1) – (4):

$$c\rho \frac{\partial T_{k+1}}{\partial t} - \lambda_0 \frac{\partial^2 T_{k+1}}{\partial x^2} = \frac{\partial}{\partial x}\left(\lambda(T_k)\frac{\partial T_k}{\partial x}\right), \tag{10}$$

$$T_{k+1}(x, 0)=T°, \ x \in (0, l), \tag{11}$$

$$\lambda_0 \frac{\partial^2 T_{k+1}}{\partial x^2} - \alpha[v(t) - T_{k+1}(x,t)]\Big|_{x=l} = [\lambda_0 - \lambda(T_k)]\frac{\partial T_k}{\partial x}\Big|_{x=l}, \tag{12}$$

$$\frac{\partial T_{k+1}}{\partial x}\Big|_{x=0} = -\frac{q}{\lambda(T_k)}. \tag{13}$$

We will look for a solution to problem (1) – (4) as the limit of solutions to problems (10) – (13). As function $\lambda(T)$ is positive and fulfills the expression (5) and has a derivative bounded by T at a range $[T_1, T_2]$, then for the arbitrary fixed control value $v(t)$ solutions T_{k+1} of the systems of equations (10) – (13) converge to the solution of system (1) – (4) when $k \to \infty$.

For the sake of simplicity of further expressions let's formulate system of equations (10) – (13) and bounds (6) – (7) in dimensionless units:

$$\alpha_0 = \frac{\lambda_0}{c\rho}, u = \alpha_T(v - T°), u^+ = \alpha_T(v^+ - T°), r = \frac{x}{l}, \theta = \alpha_T(T - T°), \tau = \frac{\alpha_0 t}{l^2}, \sigma_1^* = \frac{(1-\psi)\sigma_1}{E}, \sigma_2^* = \frac{(1-\psi)\sigma_2}{E},.$$

$$\theta_g = \alpha_T\left(T_{cp} - T°\right), \tilde{T} = \frac{\alpha_0 \bar{t}}{l^2}, B_i = \frac{\alpha l}{\lambda_0}, \tilde{\theta} = \alpha_T\left(\tilde{T} - T°\right), \frac{q}{\lambda_0} = q^*. \tag{14}$$

Then the problem of optimal nonlinear heating of the surface layer of the workpiece with restrictions on thermal stresses and the highest temperature is reduced to solving a system of linear ordinary differential equations:

$$\frac{dx}{d\tau} = A(\tau)x + B(\tau)u + D(\tau), \tau \in [0,T], x(0) = x_0 \neq 0_{RN}, \tag{15}$$

with bounds for phase variables and control values:

$$F_i(x, u, \tau) \leq 0, i = \overline{1,s}, \tag{16}$$

where $x = x(\tau) = (x_1(\tau), \ldots, x_N(\tau))$ – N-dimensional vector, $A(\tau)$, $B(\tau)$, $D(\tau)$ – known

matrices with the dimensions (*N*x*N*), (*N*x*1*), (*N*x1) correspondingly with piecewise continuous coefficients, $u = u(\tau) \in U$ – control.

The proposed approach to solving the nonlinear problem of thermal conductivity with restrictions was tested when checking for the adequacy of controlling the thermomechanical state of the working surfaces of products made of ferroceramic materials at the sintering stage.

A plate of $MnFe_2O_4$ alloy with a thickness of 2l = 0.2 m was sintered with an initial temperature T_0 = 200°C in modes in which sintering zone temperature has reached 11000°C. The maximum permissible temperature in the sintering zone at the furnace outlet should not exceed 7200°C for the minimum time, taking into account restrictions on thermal stress and temperature of the treated surface. The material $MnFe_2O_4$ is brittle. The temperature in the processing zone varied in the range [7200°C – 11500°C]. The dependence of the ultimate strength on temperature was specified in a table [14]:

Table 1. Tensile strength dependence from the temperature.

Temperature, °C		20	720	1050	1100	1150
Tensile strength, MPa	Compression	1500	850	470	310	210
	Extension	980	540	370	200	140

This dependence after the transition to dimensionless quantities, was approximated using the least squares method by nonlinear relations.

The dependence of the thermal conductivity coefficient on temperature was also specified in a table:

Table 2. The dependence of the thermal conductivity coefficient on temperature

Temperature,°C	20	200	500	600	700	800	900	1000
λ(T), W/m°C	10.05	15.07	18.84	20.5	22.1	24.2	26.3	28.05

For this dependance the same was applied: transition to dimensionless quantities, and approximation using the least squares method by nonlinear relations.

Figure 2 shows graphs of the dependences on the time of optimal control, surface temperatures and the main material of the workpiece after 6 iterations. The response time was 3.98 minutes, the optimal control has 135 switchings. Figures 3 and 4 show, respectively, graphs of the dependence of compressive and tensile strengths, as well as compressive and tensile thermal stresses on time under the optimal processing mode. As can be seen from fig. 3, the rate of temperature growth in the sintering zone is limited not only by tensile, but also by compressive thermal stresses. Traditionally, only tensile thermal stresses and restrictions on the sintering temperature of the workpiece were considered active.

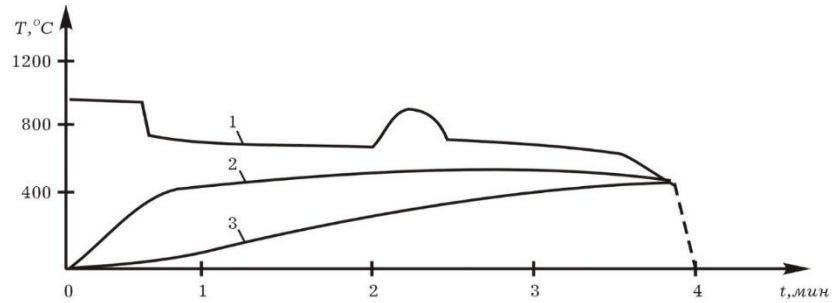

Fig. 2. Graphs of optimal control versus time: 1 – surface temperature, 2 – center temperature, 3 – temperature after 6th iteration.

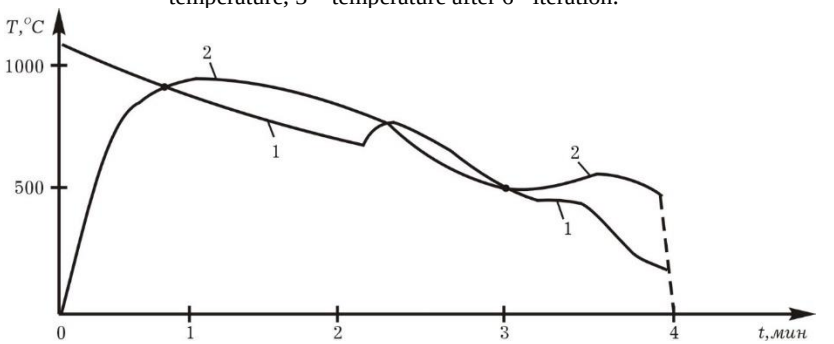

Fig. 3. Graphs of compressive (1) and tensile (2) strength versus time under optimal heating conditions.

As can be seen from Fig. 2, the heating rate limits not only tensile, but also compressive thermal stresses. Traditionally, only tensile thermal stresses and restrictions on the contact temperature of the workpiece surface were considered active.

Implementation of a model for optimizing and controlling thermomechanical processes when obtaining workpieces of ferro-ceramic products during sintering, which describes thermomechanical processes in workpieces, makes it possible to reduce the formation of defects and determine the control of technological parameters of sintering to increase the strength of ferrites.

The process of grinding ferroceramic products is accompanied by both thermal and mechanical phenomena, which, interacting with each other, determine the quality of the surface layer. A quantitative description of these phenomena requires the selection of certain models. Due to the interrelation and interdependence of phenomena and processes during the processing of ferro-ceramic products by grinding, it becomes obvious that the stress-strain state of the surface layer is determined mainly by temperature. If you use a model of a thermoelastic body that

reflects the relationship between mechanical and thermal phenomena at finite heat flows, you can make significant progress in research on the thermomechanics of phenomena accompanying the grinding process.

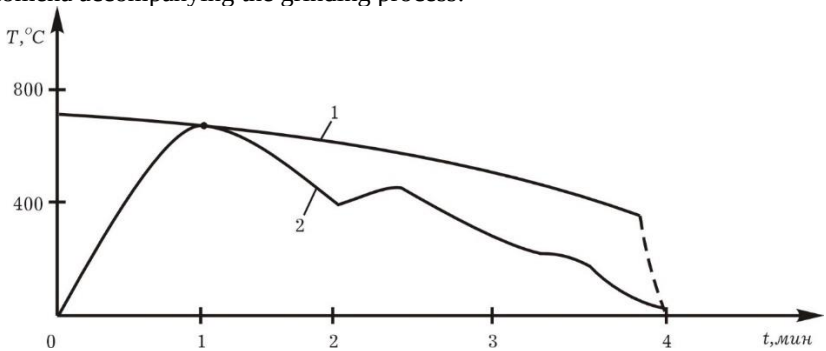

Fig. 4. Graphs of compressive (1) and tensile (2) thermal stresses versus time under optimal heating conditions.

For further studies of the kinetics of the formation of thermomechanical processes, we will use the following system of differential equations [15], which describes the interaction of the deformation field and the temperature field, as the main theoretical premise.

$$G\Delta\vec{U}_j + (\lambda_t + G)graddiv\vec{U}_j - \rho\frac{\partial^2\vec{U}_j}{\partial\tau^2} + P_j = \alpha_t\beta_t gradT, \quad (17)$$

$$\Delta T - \frac{1}{\alpha}\frac{\partial T}{\partial\tau} - \eta l\frac{\partial}{\partial\tau}div\vec{U}_j = -\frac{W}{\lambda} + C_q^{-2}\frac{\partial^2 T}{\partial\tau^2}, \quad (18)$$

where: λ_t, G - Lame constants; $\beta_t = 3\lambda_t + 2G$; ρ - density of the processed material: α_t - temperature coefficient of linear expansion of the metal; $a = \lambda / C_v$ – thermal diffusivity coefficient; λ – thermal conductivity coefficient; C_v - volumetric heat capacity; $\vec{U}(\Phi,\tau)$ – the total vector of displacements of the internal temperature Φ (*x, y*) of the surface layer under the influence of thermomechanical forces accompanying the grinding process: $l = 1 + \tau_r\,\delta/\delta$ (τ - relaxation time); $\eta = \alpha_t\beta_t T(\Phi, \tau) / \lambda$; W – power of the heat source; C_q is the speed of heat propagation in the processed material; τ – time; P_j - cutting forces;

$$gradT(x,y,z) = \frac{\partial T}{\partial x}\vec{i} + \frac{\partial T}{\partial y}\vec{j} + \frac{\partial T}{\partial z}\vec{k};$$

$$div\vec{U}_j = \frac{\partial U_x}{\partial x} + \frac{\partial U_y}{\partial y} + \frac{\partial U_z}{\partial z}.$$

The system of equations that determine the thermal and stress-strain state of the machined surface of parts during grinding includes [13]:

a) equation of unsteady thermal conductivity:

$$\frac{\partial T}{\partial \tau} = a^2\left(\frac{\partial^2 T}{x^2} + \frac{\partial^2 T}{y^2}\right) \quad (19)$$

b) Lamé elasticity equations in displacements:

$$\frac{\partial \theta}{\partial x}\cdot\frac{1}{1-2\mu} + \Delta\vec{U} = b^T\frac{\partial T}{\partial x}; \vec{U} = \frac{U}{2G}; \vec{V} = \frac{V}{2G}; \quad (20)$$

$$\frac{\partial \theta}{\partial y}\cdot\frac{1}{1-2\mu} + \Delta\vec{V} = b^T\frac{\partial T}{\partial y}; b^T = \frac{4G(1+\mu)}{1-2\mu}\alpha t; \quad (21)$$

c) initial conditions:

$$T(x, y, \theta) = 0; \quad (22)$$

d) bounding conditions for temperature and deformation fields:

$$\frac{\partial T}{\partial x} = -\frac{q(y,t)}{\lambda}, |y| < \alpha; \quad (23)$$

$$-\frac{\partial T}{\partial x} + jT = 0, |y| > \alpha; \quad (24)$$

$$\sigma_x(x, y, t)\Big|_{x=0} = \tau_{xy}(x.y.t)\Big|_{x=0} = 0; \quad (25)$$

e) conditions for discontinuity of the solution: for inclusions: for crack-like defects:

$$< \tilde{u} >= 0; < \sigma_x >\neq 0; \quad < \sigma_x >= 0; < \tilde{u} >\neq 0;$$
$$< \tilde{v} >= 0; < \tau_{xy} >\neq 0; \quad < \tau_{xy} >= 0; < \tilde{v} >\neq 0; \quad (26)$$

Taking into account the design features of wheels used for grinding the surfaces of ferro-ceramic products can be realized by satisfying the following boundary conditions:

$$q(y,t) = \frac{c\sqrt{\tau}}{\lambda}[H(y) - H(y - 2a^*)]\sum_{k=0}^{n}\sigma(y + kl - v_{kp}\tau), \quad (27)$$

where *H(y)* is the Heaviside function; *σ(y)* is the Dirac delta function; *n* is the number of grains passing through the contact zone during the time $\tau = \frac{\sqrt{Dt_{gr}}}{v_{kp}}$; λ is the thermal conductivity of the product material; $c\sqrt{\tau}$ — heat flow from a single grain; v_g, v_{kp}, t_{gr} grinding modes, 2a* — the length of the circle contact arc with the part; l* is the distance between the cutting grains. The maximum values of the instantaneous temperature T_M, from single grains to the constant component — T_K, were obtained theoretically and confirmed experimentally, which were used later as criteria for predicting the conditions for the formation of defects of the burn type and their depth.

The solution of the task made it possible to develop technological criteria for controlling the process of defect-free grinding of ferro-ceramic products on the basis of the established functional relationships between the properties of ferro-ceramic materials and the main technological parameters [16].

The quality of the processed surfaces will be ensured if, with the help of the controlling technological parameters we can select such processing modes, cutting fluids, and tool characteristics in a way that the current values of the grinding temperature *T(x,y,t)* and heat flow *q(y,t)*, stress σ*(M)* and grinding forces P_y, P_z, and

the coefficient of crack resistance K_{1C} will not exceed their limit values.

Realization of the system of limiting inequalities in terms of the values of the temperature itself and the depth of its distribution in the form:

$$T(x,y,\tau)=\frac{C}{2\pi\lambda}\sum_{k=0}^{n}H\left(\tau-\frac{kl}{v_{kp}}\right)H\left(\frac{L+kl}{v_{kp}}\right)\int_{r_1}^{r_2}f(x,y,\tau,\tau`)d\tau` \le [T]_M \quad (28)$$

$$T([h],0,\tau)=\frac{C}{2\pi\lambda}\sum_{k=0}^{n}H\left(\tau-\frac{kl}{v_{kp}}\right)H\left(\frac{L+kl}{v_{kp}}\right)\int_{r_1}^{r_2}\psi(x,y,\tau,\tau`)d\tau` \le [T]_M \quad (29)$$

$$T_k(0,y,\tau)=\frac{Cv_{kp}}{\pi\lambda\sqrt{v_g}}\int_a^{\tau}\int_{-l}^{l}\frac{\lambda(\eta,t)e^{\frac{(y-\eta)^2}{4(\tau-t)}}}{2\sqrt{\pi(\tau-t)}}\left\{\frac{1}{\sqrt{\pi(\tau-1)}}+\gamma e^{\gamma^2(\tau-t)}\left[1+\Phi\left(\gamma\sqrt{\tau-t}\right)\right]\right\}d\eta dt \le [T] \quad (30)$$

$$T_k^{max}(L,0)=\frac{Cv_{kp}\alpha}{\lambda l v_g^2}\sqrt{\frac{\alpha}{\pi}}\left[1-\exp\left(-\frac{v_g\sqrt{Dt_{gr}}}{\alpha}\right)\right] \le [T] \quad (31)$$

This allows to avoid the violation of the functional properties of products made of ferroceramics due to the elimination of structural changes from grinding burns and can serve as a basis for designing grinding cycles according to thermal criteria.

Processing of ferro-ceramic products without grinding cracks can be ensured if the stresses formed in the zone of intensive cooling are limited to limit values [17]:

$$\sigma_{max}(x,\tau)=2G\frac{1+\nu}{1-\nu}\alpha_i T_k \operatorname{erf}\left(\frac{x}{2\sqrt{\alpha\tau}}\right) \le [\sigma_{lc}] \quad (32)$$

In the case of the dominant influence of hereditary inhomogeneity in ferro-ceramic products on the intensity of formation of grinding cracks, it is necessary to use criteria, the structure of which includes determinate connections of technological parameters and the properties of the inhomogeneities themselves. As such, it is possible to use the limits of the stress intensity coefficient:

$$K=\frac{1}{\pi\sqrt{l}}\int_{-l}^{l}\sqrt{\frac{l+t}{l-t}}\{\sigma_x,\sigma_y\}dt \le K_{1c}, \quad (33)$$

or providing, with the help of controlling technological parameters, the limiting value of the heat flow, at which the balance of structural defects is preserved:

$$q^*=\frac{P_z v_{kp}\alpha_S}{\sqrt{Dt_{gr}}} \le \frac{\sqrt{3}\lambda K_{1C}}{Hl\sqrt{\pi l}\sigma}, \quad (34)$$

Conditions for flawless grinding can be realized using information about the structure of the processed material. Thus, in the case of the prevailing character of structural imperfections along the length of 2*l*, their regular arrangement relative to the contact zone of the tool with the part, it is possible to use as a criterion ratio the condition of equilibrium of the defect in the form:

$$l_0 < \frac{K_C^2}{x[GT_k(1+\nu)\alpha_t]^C}. \quad (35)$$

In this formula, the technological part is contained in the connection between the contact temperature T_K and the grinding conditions.

The given inequalities link the limiting characteristics of the temperature and

force fields with the controlling, technological parameters. They specify the area of a combination of these parameters that satisfy the obtained thermomechanical criteria. At the same time, the properties of the processed material are taken into account and the required product quality is guaranteed.

Based on the obtained criterion ratios, a device for stabilizing thermomechanical characteristics was developed to ensure the quality of the surface layer of ferrite parts during grinding, taking into account the maximum processing productivity (fig. 5). The device that controls the grinding machine 1 contains sensors 2 temperatures T_k and T_i, radial grinding force and thermoelastic stresses 3, intermediate amplifiers 4, 5 and 6, 10 integrating block 7, differentiating blocks 8 and 9, comparison body 10, setting device 11, block 12 of the control law, logical blocks 13 and 14 for selecting the control parameter and executive bodies, arithmetic blocks 15 and 16 for monitoring the current values of the burn depth depending on the time of thermal exposure and the current values of temperatures T_i and T_k and voltages, as well as executive bodies 20 17 , 18 and 19.

When controlling the grinding process by burn depth, the current values of contact and pulse surface temperatures and stresses in the grinding zone, coming from the output of sensor 2 to the input of the integrating unit 7, which integrates discrete temperature values, forming a continuous signal at the output, are amplified by auxiliary amplifiers 4, 5 and 6. After amplification, the signals arrive at the input of arithmetic blocks 15 and 16. In these blocks, the current value of the burn depth of the ground surface is determined depending on the temperatures T_k, T_i and voltages during the time of their thermal effect on the surface being processed, which is supplied to the inputs of the logical block 14 for selecting a control parameter, selecting the controlled parameter: surface temperature T_k, pulse temperature T_u or burn depth. and a differentiating block 9, which generates a signal at the output corresponding to the first or second time derivative of the signal from the output of block 16, allowing for control and prediction. After appropriate processing, the signals from the input of block 14 are compared by the comparison body 10 with the specified values from the device 11. The mismatch signals are sent to the input of block 12 of the control law, which takes into account the nonlinear dependence of temperatures T_i and T_k, burn depth on grinding factors, thermomechanical stresses σ_{max} (x,τ) and from its output through the intermediate power amplifier 4 - to the logical block 14 for selecting executive bodies, which selects executive bodies 17, 18 and 19 of the machine.

Stabilization of the burn depth and mechanical stresses allows you to control the quality of parts made of ferrites when processing them by grinding, significantly increasing their performance properties.

A device for automatic stabilization of thermomechanical stresses and quality characteristics of grinded parts, containing sensors for contact and pulse temperatures and radial grinding force, stresses, a power amplifier, a logical block

for selecting actuators, a control unit with intermediate amplifiers, a comparison body and a master device, characterized in that that, in order to stabilize the burn depth, it is equipped with arithmetic blocks connected in series to the outputs of the sensors for determining the current values of the burn depth from pulse and contact temperatures and a logical block for enabling a control parameter, the output of which is connected to the input of the comparison body, differentiating blocks, the inputs of which are connected to the outputs an arithmetic block for determining the burn depth from the contact temperature and an intermediate amplifier, and the output is connected to the input of the logical block for enabling the control parameter, an integrating block connected between the contact and pulse temperature sensors and an intermediate amplifier, the output of which is connected to the input of the logical block for enabling the parameter control, and a control law block whose inputs are connected to the comparison body and the master device, and the output is connected to the power amplifier.

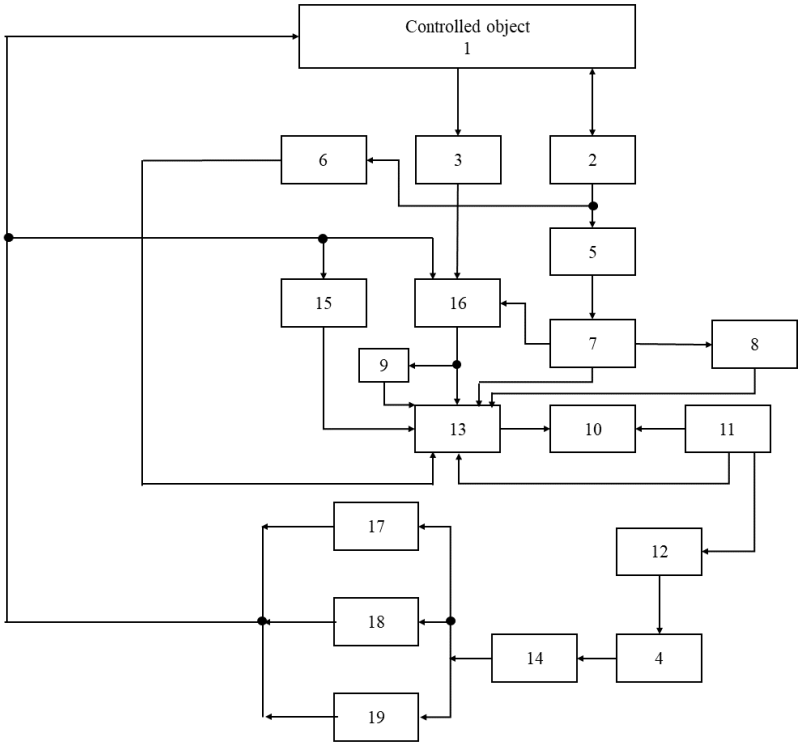

Fig. 5. A device for stabilizing thermomechanical characteristics to ensure the stability of the surface ball of ferroceramic parts when grinding to ensure maximum processing

productivity.

The initial data of the control object (grinding technological process) are [18]:

- Physical and mechanical characteristics of the processed material;
- Technical characteristics of processing equipment;
- Processing modes: depth of cut, speed of the workpiece, transverse feed, the purpose of which is determined from the conditions of limiting the grinding temperature and heat flow, stresses and grinding forces, crack resistance coefficient, which will not exceed their limit values.
- Characteristics of the selected tool (wheel), affecting the heat intensity of the processing process;
- The machining process is described by equations (1) – (6), a system of control relations (7) – (9) and thermoelastic stresses formed in the processing zone (15) – (16);
- Quality criteria for processed surfaces of products are the fulfillment of inequalities (20) – (23) – absence of functional changes in the properties of ferroceramics; inequalities (24) – (26) -- Processing of materials and alloys without grinding cracks.

5. Research results

As a result of the research carried out, a scientific and technical problem was solved consisting of establishing calculated dependencies to determine the influence of hereditary defects formed during the operation of obtaining a workpiece on the crack resistance of the surface layer during grinding and creating control over the thermomechanical state of the working surfaces of products made of ferro-ceramic materials during finishing operations, optimal technological processing conditions taking into account the accumulated damage and inhomogeneities of materials and alloys that are especially prone to crack formation during the grinding process, which is of great national economic importance for reducing defects in finishing operations and increasing the performance properties of ferroceramic parts [19].

6. Conclusions

The scientific novelty of the presented research lies in the establishment of calculated dependencies to determine the influence of hereditary defects formed during the production of workpieces from ferro-ceramic materials on the crack resistance of the surface layer during grinding and the creation of optimal technological processing conditions, taking into account the accumulated damage during sintering of workpieces and inhomogeneities in them, which create the

prerequisites to structural changes and cracking during the grinding process.

1. An analysis of the thermomechanical state of the surface layer of products made of ferro-ceramic materials of heterogeneous structure was carried out when obtaining workpieces. An optimal control of the thermomechanical state of the working surfaces of the workpieces was constructed, taking into account the nonlinearity of heat stress in the sintering zone, which made it possible to minimize defects in this operation and reduce the presence of structural defects affecting the strength of ferrites.
2. Technological criteria have been developed to control the process of defect-free grinding of ferro-ceramic products, which are implemented on the basis of established functional connections between the thermomechanical state of the processed materials and the main technological parameters.
3. A device for stabilizing thermomechanical characteristics was developed to ensure the quality of the surface layer of ferroceramic parts during grinding, taking into account the maximum processing productivity.

References: 1. *K. A. Dubrov and A. V. Usov*, Opredelenije ratsionalnykh tekhnologicheskikh parametrov bezdefectnoi obrabotki ferrokerramicheskikh izdelij., in Novyje i netraditsionnyje tekhnologii v resurso- i energosberezhenii, Odessa, 2006. **2.** *K. A. Dubrov, A. V. Usov and G. A. Oborskyi*, O putjah snizhenija jenergoemkosti mehanoobrabotki ferro keramicheskih materialov/, in Sovremennye problemy podgotovki proizvodstva, zagotovitel'nogo proizvodstva, obrabotki i sborki v mashinostroenii i priborostroenii, Kyiv-Svalyava, 2007. **3.** *A. V. Usov and K. A. Dubrov*, Tehnologicheskie vozmozhnosti snizhenija othodov pri proizvodstve ferro keramicheskih izdelij, №. 68, pp. 342–350, 2005. **4.** *F. V. Novikov and V. I. Polyanskyi*, Viznachennja umov pidvishhennja jakosti mehanichnoї obrobki za temperaturnim kriteriem, Perspektivni tehnologiї ta priladi, № 17, pp. 99–105, 2020. **5.** *O. V. Yakimov, A. V. Usov, P. T. Slobodyanyuk and D. V. Iorgachev*, Teplofizika mehanichnoї obrobki, Odessa: Astroprint, 2000, p. 256. **6.** *Y. M. Kusiy*, Naukovo-prikladni osnovi tehnologichnogo uspadkuvannja parametriv jakosti dlja zabezpechennja ekspluatacijnih harakteristik virobiv. Avtoreferat disertaciї na zdobuttja naukoogo stupenja dokt. tehnich. Nauk 131 Prikladna mehanika, Lviv, 2021, p. 44. **7.** *V. G. Lebedev, E. A. Lugovskaya and A. V. Ovcharenko*, Jeksperimental'nye issledovanija processa shlifovanija martensitno-starejushhej stali N18K9M5T, Visoki tehnologiї v mashinobuduvanni, vol. 1, № 27, pp. 69–78, 2017. **8.** *V. O. Dziura and P. O. Marushak*, Tehnologichni metodi zabezpechennja parametriv jakosti poverhon' til obertannja ta їh profilometrichnij kontrol', Ternopil: Palayanytsya, 2021, p. 170. **9.** *Novikov F.*, Optimisation of interrupted grinding parameters according to the temperature criterion, *"Cutting & Tools in Technological System"*, no. 98, pp. 59–72, 2023. https://doi.org/10.20998/2078-7405.2023.98.06 **10.** *S. Malkin and C. Guo*, Grinding Technology: Theory and Application of Machining with Abrasives, 2nd ed. New York, NY, USA: Industrial Press, 2008. **11.** A. Leblond and P. Hild, Mechanics of Materials and Structures: Thermomechanics, 1st ed. Cham, Switzerland: Springer, 2019. **12.** *F. P. Vasiljev*, Chislennye metody reshenija jekstremal'nyh zadach., Kyiv: Naukova dumka, 2009, p. 256. **13.** *B. D. Reddy*, Thermomechanics of Solids: A Dynamical Systems Approach, Computational Mechanics, vol. 54, no. 3, pp. 567–587, 2014. **14.** *R. B. Hetnarski and M. R. Eslami*, Thermal Stresses: Advanced Theory and Applications, 2nd ed. Dordrecht, Netherlands: Springer, 2009. **15.** *S. N. Atluri and A. M. Rajendran*, Modeling and Analysis of Thermal Stresses in Structures, Computational Mechanics, vol. 54, no. 4, pp. 827–841, 2014. **16.** *G. A. Oborskyi, A. F. Dashenko, A. V. Usov and D. V. Dmytryshyn*, Modelirovanie sistem, Odessa: Astroprint, 2013, p. 664. **17.** *Y. Aoyama, S. Morimoto, and Y. Yamada*, Analysis of Grinding Surface Residual Stress and Subsurface Cracks in Magnetic Alloys, Journal of Materials Processing Technology, vol. 209, № 7, pp. 3478–3485, 2009. **18.** *V. I. Pokhmurskyi and Y. I.*

Kryzhanovskyi, Mehanika rujnuvannja i micnist' materialiv, Lviv-Ivano-Frankivsk, 2006, p. 1193. **19.** *A. V. Yakimov*, Modelirovanie termomehanicheskih processov pri shlifovanii neodnorodnyh materialov, in Teplofizika tehnologicheskih processov, Kyiv, 2008.

Анатолій Усов, Юрій Зайчик, Максим Куніцин, Юлія Сікіраш, Одеса, Україна

ПІДВИЩЕННЯ ЕФЕКТИВНОСТІ ВИРОБНИЦТВА ФЕРРОКЕРАМІЧНИХ ВИРОБІВ НА ФІНІШНИХ ОПЕРАЦІЯХ З УРАХУВАННЯМ ТЕХНОЛОГІЧНОЇ СПАДКОЄМНОСТІ

Анотація. *Стан якості шліфованої поверхні ферокерамічних виробів формується під впливом термомеханічних явищ, що супроводжують фінішну операцію і залежить від технологічних умов одержання заготівки. Розроблено математичну модель оптимізації та управління термомеханічними процесами при отриманні заготовок феро керамічних виробів при спіканні, що описує термомеханічні процеси у заготовках, що впливають на формування дефектів та визначено управління технологічними параметрами спікання для усунення зазначених дефектів. Із застосуванням шліфування пов'язана поява в поверхневих шарах деталей припіків, тріщин, що розтягують напруги, що значно впливає на якість цих деталей, в процесі їх експлуатації. Висока теплова напруженість процесів алмазно-абразивної обробки призводить до того, що теплофізика цих процесів часто є домінуючою у формуванні якісних характеристик обробленої поверхні. Існуючі методи обробки шліфуванням деталей із ферокерамічних матеріалів не дозволяють повністю виключити дефекти, що виникають у поверхневому шарі. Цьому сприяють спадкові дефекти від попередніх операцій, зокрема при отриманні заготівлі; мікронеоднорідність самого матеріалу, що характеризується величиною зерна, дефектами упаковки, дислокаціями та структурними перетвореннями. Аналіз термомеханічних процесів, що протікають у поверхневому шарі дозволив отримати розрахункові залежності для визначення технологічних умов усунення припіко – та тріщиноутворення на робочих поверхнях ферокерамічних виробів при обробці їх шліфуванням. Розроблено пристрій для автоматичної стабілізації термомеханічних характеристик, що супроводжують операцію шліфування феро-керамічних виробів вибором технологічних умов обробки деталей, що мають у поверхневому шарі спадкові неоднорідності, що забезпечують максимальну продуктивність при забезпеченні необхідних показників якості.*

Ключові слова: *оптимізація; заготовка; шліфування; якість поверхні; термомеханічні явища; модель; дефекти; технологічні параметри; критерії; пристрій*.

UDC 621.9.048 **doi: 10.20998/2078-7405.2024.100.13**

PRELIMINARY STUDY OF THE AREAL ROUGHNESS PARAMETERS IN 3D PRINTING OF WORKPIECES OF PLA MATERIAL

István **Sztankovics** [0000-0002-1147-7475], Ziya **Mehdiyev** [0000-0001-7976-3411],

University of Miskolc, 3515 Miskolc-Egyetemváros, Hungary
istvan.sztankovics@uni-miskolc.hu

Received: 19 March 2024 / Revised: 26 April 2024 / Accepted: 26 May 2024 / Published: 15 June 2024

Abstract. *The field of production engineering is constantly expanding, as novel manufacturing procedures are being introduced and spread in the industrial environment. The creation of complex parts by the application of some kind of printing process is a relatively new method compared to the other traditional chip-removal processes. It can be applied in various fields, where the greatest advantage can be utilized, which is the lower restrictions on the geometry of finished parts. In this paper, the surfaces on 3D printed parts are being studied. The effect of the printing speed, layer height and nozzle temperature are analysed on the surface roughness of the experimental workpieces. The experimental setup plan is designed according to the full factorial design method. The results of this preliminary study are the general determination of the affecting factors on the surface roughness.*
Keywords: *3D printing; full factorial design; PLA; roughness height.*

1. Introduction

Additive Manufacturing (AM), also known as 3D printing (rapid prototyping) is mainly preferable technology in last decades because of it allowing the production of complex geometries with easier ways. The technology build parts by using layer-by-layer method that gets data from digital designs (stereolithography files), offering flexibility, customization, and cost-effectiveness in comparation with traditional methods [1–3]. In analysing materials used in 3D printing, Polylactic Acid (PLA) has high demand especially in desktop and hobbyist settings, as well as in industrial applications. PLA is a renewable, biodegradable thermoplastic made from natural resources such as corn starch or sugarcane. Its environmentally friendly properties combined with its low cost and ease of use, have made it a popular choice for AM. Because of its strong mechanical properties, PLA can be used for many types of purposes, such as tooling, end-use parts, and prototyping. On another side, PLA is a popular choice based on its compatibility with different 3D printing technologies, including Fused Deposition Modeling (FDM), Stereolithography (SLA), and Selective Laser Sintering (SLS). Its relatively low melting temperature minimal distortion during printing process, makes it an attractive option for both beginner and expert users [4–7]. In this

situation, understanding and controlling the surface quality of printed parts is an important factor. Surface roughness plays an important role in determining the practical and aesthetic properties of printed polymer materials. To achieve a better surface finish is critical for applications where smoothness, precision, and visual appeal are required. The optimized surface roughness in polymer printing is essential factor to ensure the success of printed parts in different applications such as rapid prototyping, product development, medical devices and consumer goods. By optimizing printing parameters and applying different post-processing techniques, manufacturers and designers can improve surface quality, and reduce defects, which unlock new possibilities for additive manufacturing [8–11].

There are numerous studies in the literature that explored the factors influencing surface roughness in 3D-printed polymers [12]. The performed research works help to shed light on the limitations and complexities of this critical aspect of AM. For instance, the research work [13] investigated that how different layer thickness values in 3D printing affect the surface qualities of wood flour/PLA filament. This research work investigated that how different layer thickness values in 3D printing affect the surface qualities of wood flour/PLA filament. Reducing layer thickness value improved surface roughness, while increasing it improves wettability. The results suggested that a layer thickness – 0.2mm is ideal for balancing surface quality and production time in 3D printed wood/PLA examples. In the next article [14], the impact of layer thickness parameter on the surface properties of 3D printed materials was analysed specifically for wood flour/PLA filament composites. In realized investigations, three circular textures were printed and tested under dry and lubricated conditions. The findings showed that texture size has a substantial impact on the coefficient of friction which texture T2 (texture diameter 1.5 mm) had the lowest friction under dry conditions, while T3 (texture diameter 2 mm) performed best under lubricated conditions at low speeds. Similar to the previous one, the paper [15] explored the influence of layer thickness on the surface properties of printed materials which were produced from wood flour/PLA filament. It highlighted the importance of surface coatings in improving mechanical properties and also discussed the applications of coated 3D printed parts in several industries. The study also shows the importance of understanding surface characterization, especially in the case of printed polymeric parts. The next work [11] analysed how the layer thickness parameter affects the surface qualities of printed parts. The study seeks to optimize printing conditions by modifying process parameters such as layer thickness, nozzle temperature, and infill density in order to improve surface quality, tensile strength, and hardness of printed specimens. The final results demonstrated the need for parameter adjustment to get the necessary mechanical and surface properties in mass production. With the similar purpose – the article [16] investigated the impact of layer thickness parameter on the surface

quality of polymer materials. In this research study, samples were printed with different layer height values (from 0.05 to 0.25) by using the "Creality Ender 3" printer. The obtained results showed that optimal parameters found at 0.15 mm and 0.20 mm for surface roughness and printing time. In addition, the paper [17] analysed the influence of different printing parameters on the surface properties of 3D printed denture base resins. And the study found that although printing orientation and post-curing time have little effect on the surface roughness, they have considerable effect on the hardness. 3D-printed denture base resins have reduced hardness than conventional heat-polymerized resins, however post-curing increases their hardness values. The placement of the parts to be printed also has an important factor in the result [18]. The geometry of the product significantly affects the resulting efficiency of the joint solution of the considered problems of technological process planning for additive manufacturing [19]. The following study [20] focused into the surface treatment of printed polymers using different coatings, focusing on visual aesthetics as well as environmental protection. Results showed that the characteristics of the substrate and the properties of the coatings have highly effect on the surface properties such as hydrophobicity, colour, gloss, and adhesion. In addition, understanding the relationship between substrate chemistry and coating composition is critical to achieve good surface finishes in additive manufacturing. The article [21] researched the influence of different fused filament fabrication 3D printing parameters on the printed surface of PLA polymers. The investigations were specifically focused on curved surfaces resembling hip prosthesis components. Performed ANFIS modelling demonstrated that layer height and nozzle diameter had a major impact on roughness, where smaller layer heights resulted in smoother surfaces. This study offered knowledge on optimizing 3D printing parameters to reduce surface roughness in complex, curved structures. The following study [22] compared the surface qualities of interim indirect resin restorations produced using CAD-CAM, 3D printing, and traditional methods. The observed results showed that 3D-printed resin restorations had similar flexural strength and micro-hardness to CAD-CAM-fabricated specimens, but much higher surface roughness. Studies suggested that 3D rapid prototyping technology is an appropriate option for the clinical production of provisional resin restorations. Additionally, the surface properties of ABS material printed by using fused deposition modelling were analysed in research work [23]. According to the gathered results, increased infill density and lower layer height parameters led to better surface roughness while increasing layer height results in rougher surface. Furthermore, a 0.06mm layer height and 100% infill density result in an optimum surface finish.

The main purpose of this study is to investigate the effect of different printing parameters, on the topography of FDM printed PLA parts. With analysing the results on the roughness, this research aims to provide a better understanding to optimize printing parameters to realize better surface quality for PLA parts.

2. Experimental conditions and methods

For the current research, all experiments were printed by using the "Qidi Tech X-CF Pro" 3D printer which is known for its high temperature and precise printing capabilities. The Qidi Tech X-CF Pro has a build volume of 300x250x300mm, which provides wide space for printing several complex geometries. With a heated build plate and a dual extrusion mechanism, this printer has the capability to print a wide range of filament types while providing optimal layer adhesion.

The printing material used in the production of all samples was PLA (biodegradable thermoplastic) which is known for its environmental friendliness and ease of use. This included nozzle temperature, printing speed, layer height, infill density, and etc which were set to get uniform printing results. Furthermore, the slicing software of the printer was used carefully to ensure that digital designs (in stereolithography file format) were accurately converted into physical items.

The experimental setup for this research work involved systematically changing printing parameters to investigate their impact on the surface roughness of printed PLA parts. Additionally, it should be also noted that the same PLA filament was used for all prints to eliminate material-related factors.

Table 1 illustrates the eight different experimental setups, where each of them is characterized by unique combinations of layer height (h_l), nozzle temperature (T_n), and printing speed (v_p).

The parameter combinations were selected based on their common use in 3D printing applications and their ability to affect surface roughness. By systematically changing the mentioned parameters and keeping other printing conditions constant, the main purpose was to analyse their individual effects on surface quality. The printed workpiece was designed to have a 6 mm x 6 mm flat surface. Each experimental setup was carried out two times, where the orientation of this flat surface changed: the to be studied surface was parallel to the base plate of the machine in the first case (hence this will be called “Horizontal” position) and it was perpendicular to the base plate in the second case (thus this will be called “Vertical” position). This resulted in 16 experimental setups overall.

After completing all the printing processes, all the samples were tested using a profilometry surface roughness test to evaluate their surface roughness. The necessary measurements were carried out after the experiments with an AltiSurf 520 three-dimensional topography measuring instrument using a triangulated laser probe.

Table 1 – Experimental setups

Setup	1	2	3	4	5	6	7	8
h_l [mm]	0.2	0.3	0.2	0.3	0.2	0.3	0.2	0.3

T_n [°C]	210	210	230	230	210	210	230	230
v_p [mm/s]	60	60	60	60	90	90	90	90

In this study, the following roughness parameters are measured and studied (ISO25178-2:2012):

- S_{10z} – Ten-point height [μm], the average value of the heights of the five peaks with the largest global peak height added to the average value of the heights of the five pits with the largest global pit height.
- S_{5p} – Five-point peak height [μm], the average value of the heights of the five peaks with the largest global peak height.
- S_{5v} – Five-point pit height [μm], the average value of the heights of the five pits with the largest global pit height.

Equations were worked out for the analysis using the form in Equation 1 according to the 2^3 full factorial design method. The y is the dependent value and k_i are the coefficients describing the effect of the different factors on the dependent value. O represents the orientation of the specimen. The independent variables are the layer height (h_l), nozzle temperature (T_n) and printing speed (v_p).

$$y(h_l, T_n, v_p)^O = k_0 + k_1 h_l + k_2 T_n + k_3 v_p + k_{12} h_l T_n + k_{13} h_l v_p + k_{23} T_n v_p + k_{123} h_l T_n v_p \quad (1)$$

3. Experimental results

The workpieces were printed out and the surface topography are measured for each setup. The resulted profiles were evaluated, and the studied parameters were recorded. These values are shown in Table 2 and 3.

Table 2 – Measurement results of horizontally printed specimens

Setup	1	2	3	4	5	6	7	8
S_{10z} [μm]	39.5	95.6	55.8	165.9	62.5	133.1	45.0	159.9
S_{5p} [μm]	24.2	37.9	30.8	54.6	24.2	52.6	22.9	37.4
S_{5v} [μm]	15.3	57.8	25.1	111.3	38.3	80.4	22.1	122.5

Table 3 – Measurement results of vertically printed specimens

Setup	1	2	3	4	5	6	7	8
S_{10z} [μm]	102.5	225.6	107.6	400.0	53.7	160.1	70.9	240.3

S_{5p} [μm]	42.8	82.5	50.2	163.6	27.5	79.5	28.9	126.6
S_{5v} [μm]	59.7	143.0	57.4	236.4	26.2	80.6	41.9	113.7

The formulas in the form of Equation 1 are determined for the calculation of the ten-point height of the roughness. Equation 2 shows the result for horizontally printed specimens and Equation 3 presents the formula, which determines the vertically printed parts.

During the study of the surface roughness, the peak height and pit height parameters are analysed by the application of their ratios with the total height of the roughness profile. In this way the structure of the produced surface can be characterized in 3D printing as well.

$$S_{10z}(h_l, T_n, v_p)^H = 595.5 - 7422h_l - 3.132T_n + 4.879v_p + 36.64h_lT_n + 38.57h_lv_p - \\ - 0.02417T_nv_p - 0.1608h_lT_nv_p \quad (2)$$

$$S_{10z}(h_l, T_n, v_p)^V = 8102 - 38530h_l - 39.13T_n - 79.11v_p + 190.9h_lT_n + 366.2h_lv_p + \\ + 0.3742T_nv_p - 1.77h_lT_nv_p \quad (3)$$

Table 4 – Calculated ratios of the roughness parameters (horizontally printed specimens)

Setup	1	2	3	4	5	6	7	8
S_{5p} /S_{10z} [-]	0.61	0.40	0.55	0.33	0.39	0.40	0.51	0.23
S_{5v} /S_{10z} [-]	0.39	0.60	0.45	0.67	0.61	0.60	0.49	0.77

Table 5 – Calculated ratios of the roughness parameters (vertically printed specimens)

Setup	1	2	3	4	5	6	7	8
S_{5p} /S_{10z} [-]	0.42	0.37	0.47	0.41	0.51	0.50	0.41	0.53
S_{5v} /S_{10z} [-]	0.58	0.63	0.53	0.59	0.49	0.50	0.59	0.47

$$S_{5p} / S_{10z}\ (h_l, T_n, v_p)^H = 18.54 - 64.82h_l - 0.07686T_n - 0.2821v_p + 0.2768h_lT_n + \\ + 1.051h_lv_p + 0.001236T_nv_p - 0.004647h_lT_nv_p \quad (4)$$

$$S_{5v} / S_{10z}\,(h_l, T_n, v_p)^H = -17.54 + 64.82h_l + 0.07686T_n + 0.2821v_p - 0.276h_lT_n - 1.051h_lv_p - 0.001236T_nv_p + 0.004647h_lT_nv_p \quad (5)$$

$$S_{5p} / S_{10z}\,(h_l, T_n, v_p)^V = -9.212 + 28.65h_l + 0.04614T_n + 0.1518v_p - 0.142h_lT_n - 0.4761h_lv_p - 0.000719T_nv_p + 0.002325h_lT_nv_p \quad (6)$$

$$S_{5v} / S_{10z}\,(h_l, T_n, v_p)^V = 10.21 - 28.65h_l - 0.04614T_n - 0.1518v_p + 0.1423h_lT_n + 0.4761h_lv_p + 0.000719T_nv_p - 0.002325h_lT_nv_p \quad (7)$$

The ratios of the peak and total heights and the ratios of the pit and total heights are shown in Table 4 for horizontally printed specimens by the application of the data in Table 2. Equation 4 and 5 show the worked-out formulas for the calculation of these. Table 5 contain the beforementioned ratios for vertically printed parts based on the values of Table 3. Equation 6-7 presents the deducted equations in form of Equation 1, which will be further used in the analysis.

4. Discussion

The analysis of the effect of the setup parameters on the studied roughness parameters started with the evaluation of the total height (S_{10z}). Figure 1 shows the results of the parts which were printed horizontally, while Figure 2 presents the outcomes on vertically printed parts. The first observation, which can be confirmed, is the high impact on the printing direction. The roughness values of the horizontally printed parts are almost half of the result of vertically printed parts at 60 mm/s printing speed, and also lower (but with a lesser extent) at 90 mm/s.

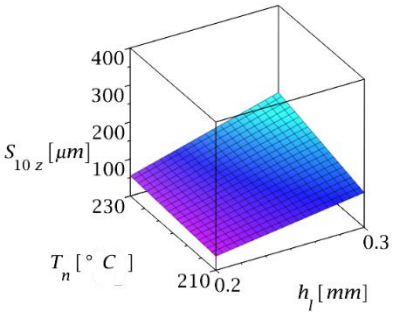

v_p = 60 mm/s

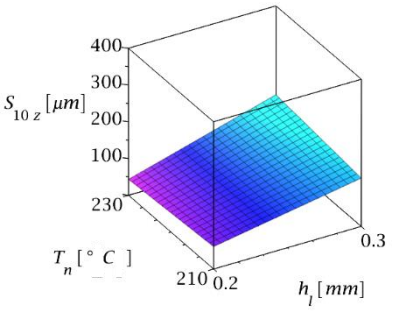

v_p = 90 mm/s

Figure 1 – Alteration of the S_{10z} on horizontally printed surfaces

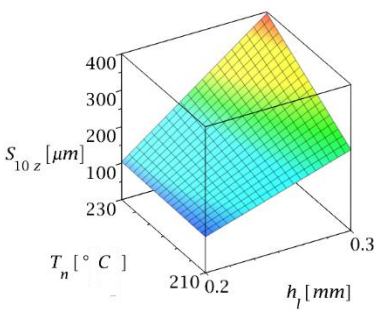

v_p = 60 mm/s

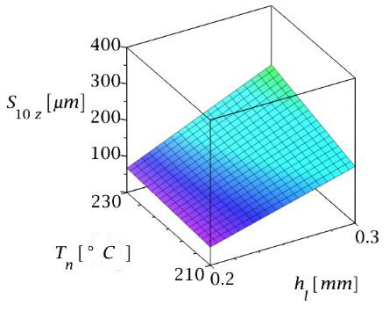

v_p = 90 mm/s

Figure 2 – Alteration of the S_{10z} on vertically printed surfaces

We identify based on the 16 setups, that increasing the layer height has a higher effect in vertical printing, while its have a lower increasing effect in horizontal printing. The previous statement can be easily seen, since the layer height means the periodicity of the profile in vertical printing, thus it has an increasing effect on the roughness. In horizontal printing, the layer hight should not have a direct effect on the roughness height, however its increasing effect can be observed here as well. Higher layer height alters the mechanism of the layering of the different material levels, which leads to a rougher surface. The nozzle temperature has also an increasing effect, because of the secondary plastic deformations, which occur in the before layered materials. Increasing the printing speed has no clear effect in horizontal printing, while it has a noticeable lowering effect in vertical printing. As we saw earlier, the contact characteristics between the previously layered sections and the recently printed material is important factor. If we increase the printing speed, we lower the contact time, which changes the secondary plastic deformations.

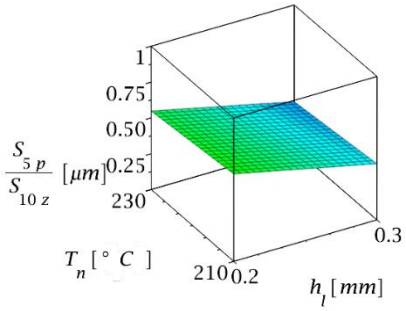

v_p = 60 mm/s

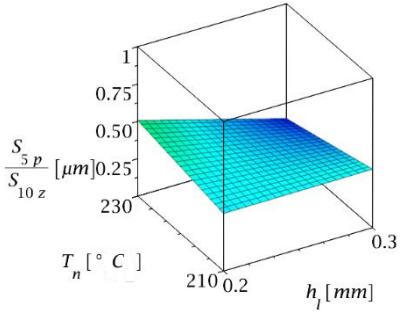

v_p = 90 mm/s

Figure 3 – Change of the peak to total height ratio on horizontally printed surfaces

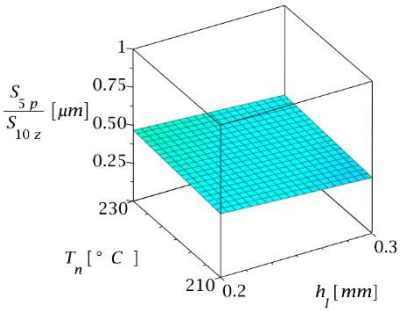

v_p = 60 mm/s

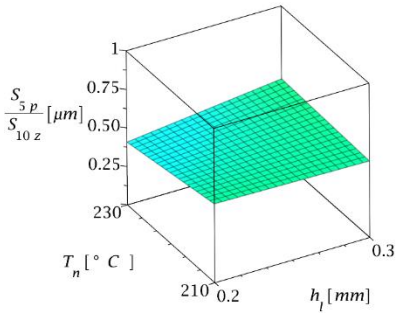

v_p = 90 mm/s

Figure 4 – Change of the peak to total height ratio on vertically printed surfaces

The study continued with the analysis of the beforementioned ratio parameters. Figure 3 and 4 shows the results of the ratios of the peak height and the total height in horizontally and vertically printed parts, while Figure 5 and 6 presents the pit height to total height ratios. Here we can also state that the printing direction has a significant effect on the composition of the total roughness height. The horizontally printed parts has higher pit heights while they have lower peak heights. This observation corresponds with the previously stated fact, that the horizontal printing has a lowering effect on the surface roughness. The characteristic of the surface profile changes as we alter the printing direction, which change leads to lower surface roughness. Among the analysed setup parameters, the layer height had the highest impact, which is followed by the printing speed in the point of view of the studied ratio parameters. It can be determined for a given application, which parameter setting would benefit more, if the task is to modify the surface topography characteristics. Higher peaks or higher pits can be achieved with the choice of the proper parameters.

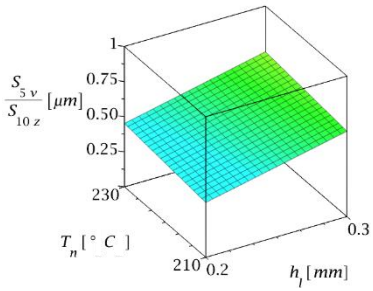

v_p = 60 mm/s

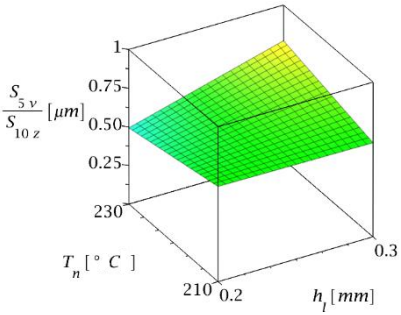

v_p = 90 mm/s

Figure 5 – Change of the pit to total height ratio on horizontally printed surfaces

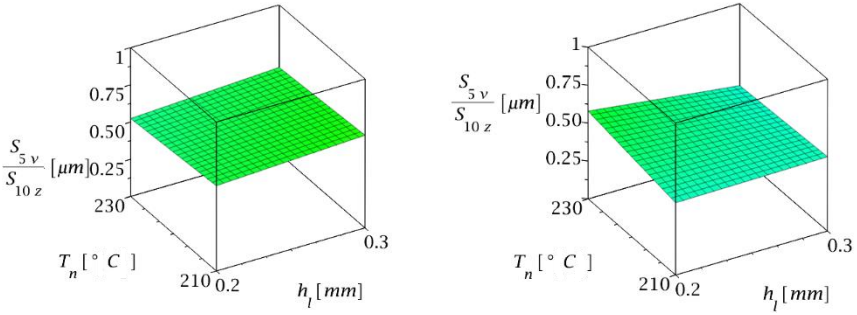

v_p = 60 mm/s v_p = 90 mm/s

Figure 6 – Change of the pit to total height ratio on vertically printed surfaces

5. Conclusions

In this paper, 3D printing experiments were carried out to study the surface roughness of differently orientated parts, which values play an important role in the quality of the products. The nozzle temperature, the printing speed and the layer height is changed to analyse their effect. In the study of the results the following observations can be highlighted:

- The roughness values of the horizontally printed parts are almost half of the result of vertically printed parts.
- Increasing the layer height has a higher effect in vertical printing, while its have a lower increasing effect in horizontal printing.
- Increasing the printing speed has no clear effect in horizontal printing, while it has a noticeable lowering effect in vertical printing.

References: 1. *Beaman, J. J., Bourell, D. L., Seepersad, C. C., & Kovar, D.* (2020). Additive manufacturing review: Early past to current practice. Journal of Manufacturing Science and Engineering, 142(11), 110812. **2.** *Kumar, L. J., Pandey, P. M., & Wimpenny, D. I.* (Eds.). (2019). 3D printing and additive manufacturing technologies (Vol. 311). Singapore: Springer. **3.** *Mehdiyev, Z., Felhő, C., & Maros, M. B.* (2022). Investigation on production parameters of additively manufactured ABS polymer gears. Cutting & Tools in Technological System, (97), 91–102. **4.** *Tümer, E. H., & Erbil, H. Y.* (2021). Extrusion-based 3D printing applications of PLA composites: a review. Coatings, 11(4), 390. **5.** *Leite, M., Fernandes, J., Deus, A. M., Reis, L., & Vaz, M. F.* (2018). Study of the influence of 3D printing parameters on the mechanical properties of PLA. **6.** *Camargo, J. C., Machado, Á. R., Almeida, E. C., & Silva, E. F. M. S.* (2019). Mechanical properties of PLA-graphene filament for FDM 3D printing. The International Journal of Advanced Manufacturing Technology, 103, 2423-2443. **7.** *Raj, S. A., Muthukumaran, E., & Jayakrishna, K.* (2018). A case study of 3D printed PLA and its mechanical properties. Materials Today: Proceedings, 5(5), 11219–11226. **8.** *Baran, E. H., & Erbil, H. Y.* (2019). Surface modification of 3D printed PLA objects by fused deposition modeling: a review. Colloids and interfaces, 3(2), 43. **9.** *Yadav, P., Sahai, A., & Sharma, R. S.* (2021). Strength and surface characteristics of FDM-based 3D printed PLA parts for multiple infill design patterns. Journal of The Institution of Engineers (India): Series C, 102, 197–207. **10.** *Mehdiyev, Z., Felhő, C., & Zoltán, K. P.* (2022). Investigation on 3D printing parameters of

PLA polymers for gear applications. In Vehicle and Automotive Engineering (pp. 654–664). Cham: Springer International Publishing. **11.** *Mani, M., Karthikeyan, A. G., Kalaiselvan, K., Muthusamy, P., & Muruganandhan, P.* (2022). Optimization of FDM 3-D printer process parameters for surface roughness and mechanical properties using PLA material. Materials Today: Proceedings, 66, 1926–1931. **12.** *Christodoulou, I. T., Alexopoulou, V. E., Karkalos, N. E., Papazoglou, E. L., & Markopoulos, A. P.* (2022). On the surface roughness of 3D printed parts with FDM by a low-budget commercial printer. Cutting & Tools in Technological System, (96), 52–64. **13.** *Ayrilmis, N.* (2018). Effect of layer thickness on surface properties of 3D printed materials produced from wood flour/PLA filament. Polymer testing, 71, 163–166. **14.** *Aziz, R., Haq, M. I. U., & Raina, A.* (2020). Effect of surface texturing on friction behaviour of 3D printed polylactic acid (PLA). Polymer Testing, 85, 106434. **15.** *Poornaganti, S., Yeole, S. N., & Kode, J. P.* (2022). Insights on surface characterization of 3D printed polymeric parts. Materials Today: Proceedings, 62, 3837–3848. **16.** *Bintara, R. D., Lubis, D. Z., & Pradana, Y. R. A.* (2021, February). The effect of layer height on the surface roughness in 3D Printed Polylactic Acid (PLA) using FDM 3D printing. In IOP conference series: materials science and engineering (Vol. 1034, No. 1, p. 012096). IOP Publishing. **17.** *Al-Dulaijan, Y. A., Alsulaimi, L., Alotaibi, R., Alboainain, A., Alalawi, H., Alshehri, S., ... & Gad, M. M.* (2022). Comparative evaluation of surface roughness and hardness of 3D printed resins. Materials, 15(19), 6822. **18.** *Garashchenko, Y., & Harashchenko, O.* (2022). Influence Of Determination Accuracy Of The Build Step On The Efficiency Of Adaptive Slicing Group Of Products For Layered Manufacturing. Cutting & Tools in Technological System, (97), 164–172. **19.** *Garashchenko, Y., Fedorovich, V., Ostroverkh, Y., Dašić, P., Anđelković, M., & Onalla, H.* (2023). Statistical Analysis of Deviations from the Correct Shape of Surface Depending on Product Orientation in Workspace of Additive Machine. Machines, 11(3), 348. **20.** *Žigon, J., Karož, M., & Pavlič, M.* (2020). Surface finishing of 3D-printed polymers with selected coatings. Polymers, 12(12), 2797. **21.** *Buj-Corral, I., Sánchez-Casas, X., & Luis-Pérez, C. J.* (2021). Analysis of AM parameters on surface roughness obtained in PLA parts printed with FFF technology. Polymers, 13(14), 2384. **22.** *Al-Qahtani, A. S., Tulbah, H. I., Binhasan, M., Abbasi, M. S., Ahmed, N., Shabib, S., ... & Abduljabbar, T.* (2021). Surface properties of polymer resins fabricated with subtractive and additive manufacturing techniques. Polymers, 13(23), 4077. **23.** *Sammaiah, P., Rushmamanisha, K., Praveenadevi, N., & Reddy, I. R.* (2020, December). The influence of process parameters on the surface roughness of the 3d printed part in FDM process. In IOP Conference Series: Materials Science and Engineering (Vol. 981, No. 4, p. 042021). IOP Publishing.

Іштван Станкович, Зія Мехдієв, Мішкольц, Угорщина

ПОПЕРЕДНЄ ДОСЛІДЖЕННЯ ПАРАМЕТРІВ ШОРСТКОСТІ ПОВЕРХНІ ПРИ 3D-ДРУКУ ЗАГОТОВОК З МАТЕРІАЛУ PLA

Анотація. *Сфера виробничої інженерії постійно розширюється, оскільки нові виробничі процедури впроваджуються і поширюються в промисловому середовищі. Створення складних деталей шляхом застосування певного процесу друку є відносно новим методом у порівнянні з іншими традиційними процесами виготовлення, пов'язаними з видаленням стружки. Він може застосовуватися в різних галузях, де найбільшою перевагою є менші обмеження на геометрію готових деталей. У цій роботі досліджуються поверхні на 3D-друкованих деталях. Проаналізовано вплив швидкості друку, висоти шару і температури сопла на шорсткість поверхні експериментальних заготовок. План експериментальної установки розроблений відповідно до методу повного факторного планування. Результатом цього попереднього дослідження є загальне визначення факторів, що впливають на шорсткість поверхні. У цій статті проведено експерименти з 3D-друку для дослідження шорсткості поверхні різноорієнтованих деталей, значення якої відіграють важливу роль у якості продукції. Тут можно констатувати, що напрямок друку має значний вплив на склад загальної висоти шорсткості. Горизонтально надруковані деталі мають більшу глибину ямок, тоді як вони мають*

меншу висоту піків. Це спостереження узгоджується з раніше встановленим фактом, що горизонтальний друк має знижувальний вплив на шорсткість поверхні. Характеристика профілю поверхні змінюється при зміні напрямку друку, що призводить до зниження шорсткості поверхні. Серед проаналізованих параметрів налаштування найбільший вплив має висота шару, за якою з точки зору досліджуваних параметрів співвідношення слідує швидкість друку. Для конкретного застосування можна визначити, яке налаштування параметрів принесе більше користі, якщо завданням є зміна характеристик рельєфу поверхні. Для аналізу їх впливу змінювали температуру сопла, швидкість друку та висоту шару. При вивченні результатів можна виділити наступні спостереження: значення шорсткості горизонтально надрукованих деталей майже вдвічі менші, ніж у вертикально надрукованих деталей; збільшення висоти шару має більший ефект при вертикальному друці, тоді як при горизонтальному – менший; збільшення швидкості друку не має чіткого ефекту для горизонтального друку, тоді як для вертикального друку має помітний ефект зниження.

Ключові слова: *3D-друк; повний факторний план; PLA; висота шорсткості.*

UDC 621.9.048 **doi: 10.20998/2078-7405.2024.100.14**

DETERMINATION OF THE SIZE OF MEDIUM GRANULES IN FREE ABRASIVE PROCESSING TECHNOLOGY AND THE SIZE OF THE RESERVOIR OF A MACHINE FOR VIBRATION PROCESSING OF PARTS

Andrii **Mitsyk** [0000-0002-3267-8065], Vladimir **Fedorovich** [0000-0001-7015-8653], Natalia **Kozakova** [0000-0002-1891-4615]

National Technical University «Kharkiv Polytechnic Institute», Kharkiv, Ukraine
Volodymyr.Fedorovych@khpi.edu.ua

Received: 29 March 2024 / Revised: 29 April 2024 / Accepted: 29 May 2024 / Published: 15 June 2024

Abstract. *It is noted that the process of vibration processing of parts is carried out by the relative movement and mutual pressure of granules of the medium and the parts being processed circulating in the oscillating reservoir. It is noted that the removal of defects from the surface of a part is carried out by the processes of microcutting and elastoplastic deformation. It is indicated that despite the effectiveness of vibration processing, its capabilities are limited to performing simple operations and have not been sufficiently studied. The effectiveness of vibration processing depends on a number of factors, among which the size of the medium granules and the size of the machine reservoir play a significant role. To determine these factors, the kinematics of the finishing and grinding process was considered, and the joint movement of the medium granule and the part was taken into account. The removal of microchips along the entire length of the machined surface during one period of oscillation of the machine reservoir and the damping properties of the material of the working medium used were also taken into account. It has been established that, depending on the shape of the part, its position and direction of movement in the reservoir, the angle of contact with the granules can vary from 0 to 90°. In this regard, cases of encounters between granules and parts are considered. It has been established that the unfavorable case of a meeting occurs at the right angle of their collision. It is concluded that the removal of microchips from the surface of parts is theoretically inversely proportional to the size of the medium granules. It has been determined that the increase in damping of the medium caused by a decrease in the size of the granules can be compensated by increasing the amplitude of the oscillations of the reservoir and the use of granules with a large specific gravity. The choice of granule size is also limited by the conditions of their access to the surfaces being treated, while the conditions for eliminating the possibility of granules jamming are met. It has been experimentally confirmed that the reservoir with a "U" – shaped cross-section turned out to be the best, due to the absence of stagnant zones in it. It has been established that as the cross-section of the reservoir increases, the productivity of the machine will decrease. Intensifying the process by increasing the amplitude is unacceptable, since this causes the appearance of deep defects on the treated surfaces. To increase processing efficiency, it is necessary to increase the volume of the reservoir by lengthening it, rather than increasing its cross-section.*

Keywords: *vibration treatment; granular medium; physical and technological parameters; contact angle; reservoir; productivity of vibration processing.*

1. Introduction

The process of vibration processing is accompanied by microcutting and elastoplastic deformation and is carried out due to the relative movement and mutual pressure of the granules of the working medium and the parts during their circulation movement in an oscillating reservoir [1].

Despite the effectiveness of vibration processing, its use until recently was limited to performing such simple operations as cleaning parts, removing burrs, and rounding sharp edges. The underestimation of the capabilities of this technological process is explained by the lack of knowledge about it [2].

The research carried out so far has involved solving particular problems of identifying the influence of one or a small number of factors on the efficiency of vibration processing. At the same time, ongoing comprehensive studies have shown that the effectiveness of vibration processing depends on many factors, the main ones of which include the size of the granules of the abrasive medium and the size of the reservoirs of machines for vibration finishing and grinding.

2. Features of the kinematics of the finishing and grinding process

To determine the above factors, it is necessary to consider the features of the kinematics of the process of vibration finishing and grinding, represented by the joint movement of a granule of the abrasive medium and the part. When considering the kinematics of the process, it is necessary to take into account the removal of microchips along the entire length of the machined surface during one period of oscillation and the damping properties of the material of the abrasive medium used [3, 4].

Granules of an abrasive medium with a mass of m_1 (Fig. 1, a), moving at a speed of V_{gr}, encounter a part with a mass of M on their way. In this case, the part can be either in a state of relative rest, or have counter or parallel movement at the speed of V_p part. At certain moments, the velocity vectors V_{gr} and V_p can make a certain angle.

The vector difference $\vec{V}_{gr} - \vec{V}_p$ represents the relative speed V_{gr} with which the interaction of granules and parts occurs. Depending on the shape of the part, its position in space and the direction of movement, the angle of contact with abrasive granules can vary from zero to 90º. Let's consider the most typical cases of abrasive granules meeting parts (Fig. 1).

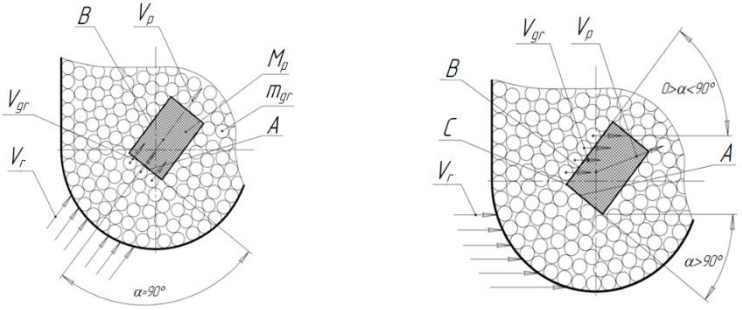

a b

Fig. 1.7. Diagram of the meeting of the part and the granules of the abrasive medium: (a) – at a right angle; (b) – at an acute angle

The most unfavorable case of granules meeting the surface being treated occurs at a right angle to their collision (Fig. 1, a). The wall of the machine's reservoir imparts movement to the granules at a speed of V_{gr} .The granules, when compacted, strike the surface of the part at a right angle. The average value of the force F_{imp} acting on the part during the collision with the granule can be expressed by the following formula:

$$F_{imp} = \frac{MV_{rel}(1+k)}{\tau}, \quad (1)$$

where M – is the mass of the part; V_{rel} – relative speed of granules and parts at the moment of impact; k – recovery coefficient, depending on the elastic properties of the part and the granule; τ – impact time.

The use of this formula is permissible, since the masses of the reservoir and granules after compaction, located between the wall and the surface, are large compared to the mass of the part.

3. Efficiency of vibration processing at different angles of impact of granules with the processed surface

The effectiveness of vibration processing when granules collide at right angles with the surfaces being processed is relatively low, since the abrasive granules are not so much removed as they are crushed by this surface, leaving micro-nicks on it.

This removal of metal from surface B occurs under unsatisfactory conditions. Abrasive granules slide along it with a small interaction force, which is determined only by the static pressure of the overlying layers of granules and parts. It is many times less than the forces arising at the surface A.

Other processing conditions occur at an impact angle other than 90º (Fig. 1, b). In this case, the impact on surface A has less elasticity. Surface B, which had not previously experienced impacts, also receives an oblique impact. During such a collision, the granules slide over both surfaces, removing chips.

The greatest destruction of the surfaces of the parts will occur in weakened areas of their perimeter, namely at the corners and edges (Fig. 1). In this position, corresponding to maximum destruction, there is rib C of the part.

4. Study of changes in the granule size of an abrasive medium and the effectiveness of its impact on the treated surface

With an increase in the mass of m abrasive granule, its kinetic energy increases, and consequently, the force that causes destruction and removal of surface layers of metal increases. However, an increase in the size of the granule, beyond certain limits, reduces the effectiveness of its impact on the part surface, as can be seen from the following.

Let us denote the size of the granule by d, the length of the surface of the part in contact with the granules by l, and the length of the granule sliding along the surface being processed by one oscillation by a.

To simplify the discussion, we represent the shape of the part in the form of a rectangular parallelepiped. Then the total length of the surface from which microchips will be removed during one oscillation of the reservoir can be expressed as

$$l_1 = a\frac{l}{d}. \tag{2}$$

For one of the part surfaces, with its linear dimension L perpendicular to the drawing plane, the surface from which chips will be removed is equal to:

$$l_2 = a\frac{l}{d}\cdot\frac{l_1}{d}. \tag{3}$$

From the resulting expression it follows that the dimensions of the processed surface for one relative movement of the granules, that is, for one period of oscillation of the machine reservoir, are inversely proportional to d^2.

You can choose the size of the granule so that it is equal to the value a, that is, $d_1 = a$. Then

$$l_1 = \frac{al}{d_1} = l, \quad (4)$$

that is, microchips are removed along the entire length of the surface. For the plane, we correspondingly find

$$l_2 = \frac{Ll}{d_1}. \quad (5)$$

Thus, the removal of microchips from the surface of the part is theoretically inversely proportional to the size of the granules of the working medium.

As the granule size decreases, the damping properties of the entire medium change. Therefore, with small sizes of abrasive granules, the length of the surface from which microchips can be removed during one period of oscillation of the reservoir will be significantly less than the calculated one.

An increase in the damping of the medium caused by a decrease in the size of abrasive granules can be compensated by increasing the amplitude of vibrations of the reservoir and using granules with the highest possible specific gravity [5].

From the practice of vibration processing it follows that the most suitable for processing complex-profile parts with internal planes, pockets, holes are granules of the working medium made of mineral ceramics TsM-332, the specific gravity of which is 3.93...3.95 g/cm^3. The choice of the size of such granules will be limited by the conditions of their access to the treated surfaces. In this case, the size of the granules should be selected to exclude the possibility of their jamming in the listed surface elements of the part.

Abrasive granules made from the TsM-332 material have a dense structure, high hardness and have shown great wear resistance, so they are most suitable for finishing operations. At the same time, they have a small grain size (1...3 μm), which, when used in grinding operations, leads to an increase in processing time, to speed up which it is advisable to add grinding powders of various grain sizes to the reservoir with an appropriate amount of a chemically active solution [6, 7].

When choosing materials for abrasive granules, abrasive granules from broken abrasive wheels, crushed granite and porcelain chips, as well as from mineral ceramics TsM-332 were studied. During the experiments, cylindrical samples made of steel 45 weighing up to 100 grams were processed. They had original purity classes of $Ra = 2.5$ μm to $Ra = 0.16$ μm.

The processing was carried out under constant vibration modes, amplitude $A = 2.0$ mm, frequency $\omega = 2200$ oscil/min, ellipse coefficient $K_A = 1.5 \pm 0.15$. The ratio of the volume of processed parts to the volume of abrasive granules was taken to be 1:3.

Experiments have established that grinding media made from broken abrasive wheels, crushed granite and porcelain chips are unacceptable for obtaining surfaces of high cleanliness classes. Therefore, for finishing processing, the use of TsM-332 mineral ceramics was proposed as an abrasive medium. It showed high durability: plates measuring 18×15×8 mm worked effectively for 700...800 hours. Their low wear made it possible to maintain the cleanliness of the environment in the reservoir and reduce the number of washes. A small amount of waste ensured higher grades of surface cleanliness. This was also facilitated by the small size of the grains from which the plates are made, – 1...4 μm.

When studying the influence of the weight and shape of abrasive granules and the amplitude of vibrations on the cleanliness of the surface, mineral-ceramic granules from the material TsM-332 were used, cylindrical in shape weighing 20...30 grams, rectangular in shape weighing 10, 7, 5 grams, respectively, and spherical in shape weighing 2...3 grams.

Before the experiments, all abrasive granules, with the exception of the spherical one, had their sharp corners and edges rounded. When processing steel samples 45 (eq. C45 DIN 10277) with mineral-ceramic granules, an alkaline chemically active solution was used.

Five samples from each batch of parts were measured and the average value Ra was calculated.

After the first tests, abrasive granules weighing 20...30 grams were excluded from further research, since they caused the appearance of a large number of micro-holes, the depth of which did not meet the requirements for cleanliness of processing.

Based on the research results, graphical dependencies were constructed (Fig. 2). It is clear from the dependencies that processing at all amplitudes gives a sharp decrease in roughness in the first hours of operation. Each amplitude corresponds to a certain achievable surface frequency. During further processing, the achieved value for a given amplitude remains constant.

A decrease in the vertical amplitude to $A_y = 0.5$ mm causes a sharp drop in the speed of rotational motion of the medium, which worsens the mixing of parts in the oscillating reservoir. Increasing the rotational effect in the reservoir is possible by increasing the oscillation frequency, for example, up to 2550 oscil/min. As a result, value Ra can be reduced to 0.5 μm.

To determine the possibilities of further reducing processing time, grinding and polishing experiments were carried out with the addition of various grinding powders. The material for them was normal electrocorundum with a grain size of 25, 8, 5, 3 and white electrocorundum with a grain size of M20. The amount of grinding powder in all experiments was 3 % of the reservoir volume.

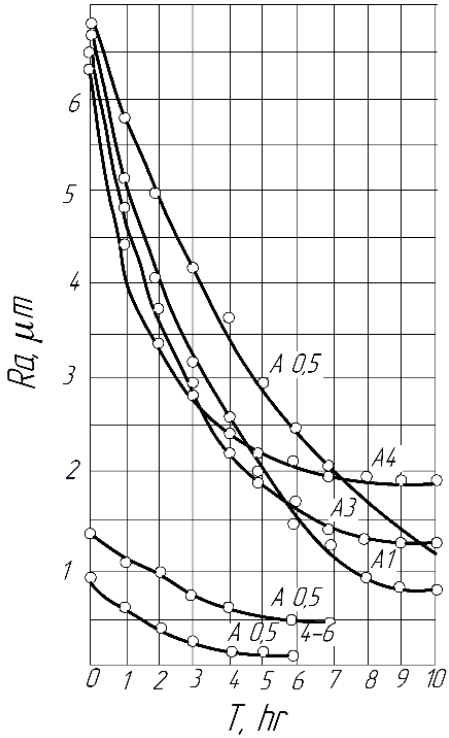

Fig. 2 Dependence of roughness Ra on amplitude A and processing time

In this series of experiments, plates made of mineral ceramics TsM-332 weighing 5...10 grams also served as abrasive granules. The volume ratio of parts and abrasive granules was taken to be close to that used to obtain high cleanliness classes, namely 1:4. The oscillation frequency for all experiments remained constant – 2140 oscil/min. The ellipse coefficient was taken to be 1.5, except when fine-grained M20 powders were used. The amplitude during the experiments varied

within 1...4 mm. The amount of alkaline solution was 3...3.5 % of the reservoir volume.

The solution and grinding powder were replaced every hour of operation of the vibrating machine. During the studies, the roughness of the processed surface was measured on a batch of samples every hour of processing. The dependence of the height of the roughness of the processed surface on the granularity of the powder, amplitude and processing time was obtained (Fig. 3).

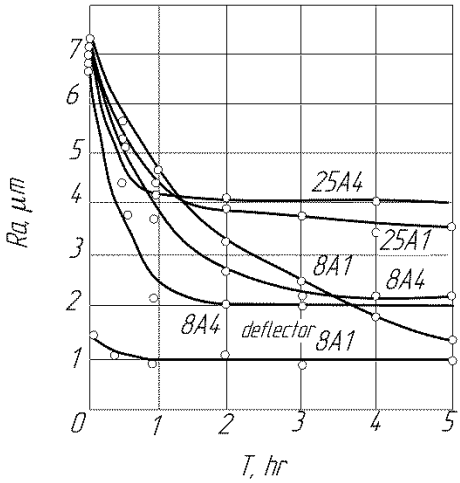

Fig. 3 Dependence of surface roughness Ra on the grain size of the grinding powder, amplitude and processing time

5. Research on Reservoir Sizing

The optimal dimensions of the reservoir have been experimentally determined. The "U" – shaped reservoir turned out to be the best in view of the absence of stagnant zones in it, as well as the possibility of installation in the internal space, intensifying the process of moving abrasive granules and machined parts, deflectors of the working medium of various shapes and sizes [8, 9].

The same conditions indicate that as the distance of granules and parts from the bottom and walls of the reservoir increases, their relative speeds decrease; layers of granules and parts, as they approach the center of the reservoir, are partially or

completely excluded from the zone of vibration influence of its walls. Processing of parts located in these layers stops.

To determine the optimal cross-sectional dimensions of the reservoir, a series of experiments were carried out.

The studies were carried out for three weight groups of abrasive granules: 2.5...3; 10; 30 grams. The velocity determination for each of them was carried out at amplitudes of A – 1, 2, 4 mm. The oscillation frequency for all experiments remained constant – 2140 oscil/min with an ellipse coefficient of $K_A = 1.5$.

Together with measuring the speed of the sensor-part, the speed of the reservoir was measured. Based on the ratio of these speeds, the damping of the medium was determined, that is, the degree of vibration damping. Graphic dependencies were constructed (Fig. 4), showing the change in the speeds of the sensors – parts at different distances from the reservoir wall.

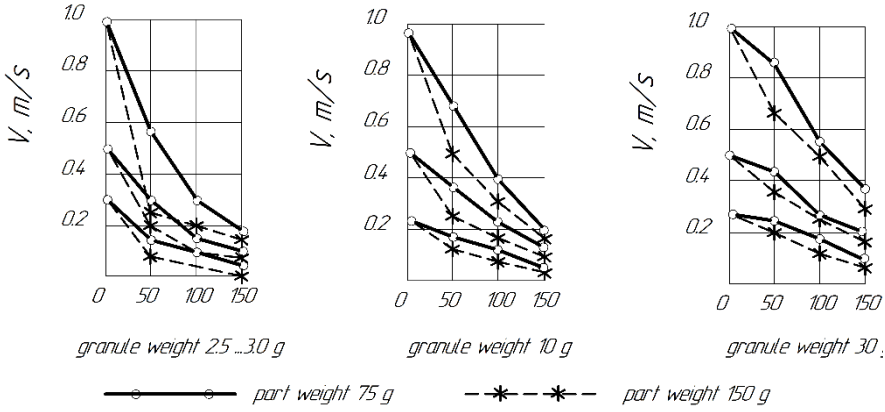

Fig. 4 Change in the speed of the sensor-part depending on its distance from the walls of the reservoir, the weight of the part, the amplitude and weight of the abrasive granule

The speed of heavy parts decreases more intensely than that of light ones. Under the same processing conditions, a heavy part has a lower speed than a lighter one. As the speed of the abrasive granules remains constant, the relative speed between them and heavier parts increases. The decrease in speed of a weighted part

occurs more slowly than the increase in its weight. This causes an increase in the mutual specific pressure of the granules and parts. This explains the faster processing of heavy parts compared to lighter ones.

Increasing the weight of abrasive granules also increases the efficiency of the processing process. This is explained by an increase in specific pressure due to an increase in the mass of the granule and a decrease in damping.

At the same time, it is noted that an increase in specific pressure can create conditions for the appearance of various defects on the surfaces being processed. At the same time, obtaining high frequency classes is difficult.

As the oscillation amplitude increases, the degree of damping of the medium decreases and the damping coefficients increase. For an amplitude of $A_y = 1$ mm, its smallest value is 0.11, and for an amplitude of $A_y = 4$ mm – 0.32. For the above processing conditions, the damping coefficient values ranged from 0.89 to 0.11.

When the frequency increased from 2040 oscil/min to 2500 oscil/min, the speed of movement of the sensors changed in the medium as follows (Table 1).

Table 1. Changing the speed of the sensor in an abrasive environment

Distance of the sensor from the wall, mm	Sensor speed, m/s at oscillation frequency, min		Speed increase, m/s
	2140	2500	
50	0.14	0.16	0.02
150	0.04	0.05	0.01

With large sections of the reservoir, the productivity of the machines will decrease despite the number of simultaneously processed parts. Intensifying the process by increasing the amplitude for finishing operations is not acceptable due to a significant increase in specific pressures in the layers of the medium close to the wall, as this causes the appearance of deep defects of great depth on the treated surfaces.

Measurements of the speed of the sensor placed in a reservoir with an increasing cross-section showed that its speed at a distance of 200 mm from the bottom is practically zero.

Thus, to increase processing productivity, it is necessary to increase the volume of the reservoir by lengthening it, rather than increasing its cross-section. This

explains the appearance of vibrating machines with two or more small-section reservoirs mounted on one vibrating platform.

Based on the conducted research, the following main conclusions can be drawn:

– a decrease in the degree of damping of the medium can be achieved by increasing the amplitude of oscillations of the reservoir;

– for vibrating machines intended for finishing operations, and therefore operating at small amplitudes, the most acceptable, as experiments have shown, should be considered reservoirs with a bottom radius of no more than 200 mm.

6. Conclusions

All the described experimental studies and their results form the basis for calculating the design parameters of vibration machines and designing technological processes for grinding and polishing operations for vibration finishing and grinding of parts of various types of metalworking industries.

Also, over the decades, the described developments have been successfully implemented at enterprises in various branches of mechanical engineering and instrument making, which indicates their high scientific level and practical relevance, which ensured the expansion of the fleet of modern metalworking machines and finishing and grinding technologies aimed at the process of effective mechanization of manual labor.

References: **1.** *Zhao Q, Sun Z, Guo B.* (2016) Material removal mechanism in ultrasonic vibration assisted polishing of micro cylindrical surface on SiC. Int. J. Mach. Tools Manuf. 103:28 39. https://doi.org/10.1016/j.ijmachtools.2016.01. 003 **2.** *Mitsyk A.V., Fedorovich V.A.* Ways of intensification of finishing by combining the schemes of energy effects on the working environment and parts (in Russian). Aerospace engineering and technology. Kharkiv, NAU im. M.E. Zhukovs'kogo «KhAI», 2011. № 6 (83). pp. 26 – 34. **3.** *Y. Chen, L. Pan, Zh. Yin, Y. Wu*. Effects of ultrasonic vibration-assisted machining methods on the surface polishing of silicon carbide, Volume 59, pages 7700–7715, 2024 https://doi.org/10. 1007/s10853-024-09661-x **4.** *Li, L., Kao, I.*, Experimental study of the impact of a vibrating wire on free abrasive machining as correlated to the modeling of vibration subject to an oscillating boundary condition. Journal of Manufacturing Science and Engineering, Transactions of the ASME, 143(5), 051006, 2021 https://doi.org/10.1115/1.4048637 **5.** *Bhagavat, S., Liberato, J.C., Chung, C., Kao, I.* Effects of mixed abrasive grits in slurries on free abrasive machining (FAM) processes. International Journal of Machine Tools and Manufacture , 50(9), pp. 843–847, 2010 https://doi.org/10.1016/j. ijmachtools.2010.04.006 **6.** Tools for machining parts with free abrasives (in Ukrainian): monografija / *M.O. Kalmykov, T.O. Shumakova, V.B. Strutins'kij, L.M. Lubens'ka*. Kyiv – Luhans'k: «Noulidzh», 2010. 214 p. **7.** *Mitsyk A.V., Fedorovich V.A., Ostroverkh Y.V.* Purpose and technological properties of granular media for vibration finishing and grinding processing. *Cutting & Tools in Technological System.* Kharkiv, NTU «KhPI». 2023. № 99. pp. 85 – 93. https://doi:10.20998/2078-7405.2023.99.10 **8.** *Opirskij B. Ja., Denisov P.D.* New vibrating machines (in Ukrainian). L'viv: Svit, 1991. 160 p. **9.** *Mitsyk A.V., Fadeev V.A., Fedorovich V.A.* Development of the

issues of kinematics and dynamics of finishing processes in an oscillating tank (in Russian). *Cutting & Tools in Technological System*. Kharkiv, NTU «KhPI», 2012. № 82. pp. 171 – 182.

Андрій Міцик, Володимир Федорович, Наталія Козакова, Харків, Україна

ВИЗНАЧЕННЯ РОЗМІРІВ ГРАНУЛ СЕРЕДОВИЩА У ТЕХНОЛОГІЇ ОБРОБКИ ВІЛЬНИМИ АБРАЗИВАМИ ТА РОЗМІРІВ РЕЗЕРВУАРА ВЕРСТАТА ДЛЯ ВІБРАЦІЙНОЇ ОБРОБКИ ДЕТАЛЕЙ

Анотація. *Відзначено, що процес вібраційної обробки деталей здійснюється відносним переміщенням і взаємним тиском циркулюючих в резервуарі, що коливається, гранул середовища та оброблюваних деталей. Зазначається, що видалення дефектів з поверхні деталі здійснюється процесами мікрорізання та пружнопластичного деформування. Вказано, що попри ефективність вібраційної обробки її можливості обмежені виконанням найпростіших операцій та недостатньо вивчені. Ефективність вібраційної обробки залежить від низки факторів, серед яких значну роль грають розміри гранул середовища та розміри резервуара верстата. Для визначення зазначених факторів розглянуто кінематику процесу оздоблювально-зачищувальної обробки, бралося до уваги спільне переміщення гранули середовища та оброблюваної деталі. Так само враховувався зйом мікростружки по всій довжині оброблюваної поверхні за один період коливання резервуара верстата і демпфуючі властивості матеріалу робочого середовища. Встановлено, що залежно від форми оброблюваної деталі, її положення та напрямки руху в резервуарі кут зустрічі з гранулами може змінюватись від 0 до 90°. У зв'язку з цим розглянуті випадки зустрічі гранул з оброблюваними деталями. Встановлено, що несприятливий випадок зустрічі відбувається під прямим кутом їхнього зіткнення. Зроблено висновок, що зйом мікростружки з поверхні деталей теоретично зворотно пропорційний розміру гранул середовища. Визначено, що підвищення демпфування середовища, викликане зменшенням розмірів гранул, можна компенсувати збільшенням амплітуди коливань резервуара і застосуванням гранул з великою питомою вагою. Вибір розміру гранул також обмежується умовами їх доступу до поверхонь, що обробляються, при цьому дотримуються умови виключення можливості заклинювання гранул. Експериментально підтверджено, що найкращим виявився резервуар «U» – подібної форми поперечного перерізу через відсутність у ньому застійних зон. Дано методику досліджень визначення оптимальних розмірів перерізу резервуара. Встановлено, що зі збільшенням перерізів резервуара продуктивність верстата знижуватиметься. Інтенсифікація процесу збільшенням амплітуди неприйнятна, оскільки це викликає появу на оброблюваних поверхнях глибоких дефектів. Для підвищення ефективності обробки необхідно збільшувати об'єм резервуара шляхом його подовження, а не збільшення перерізу.*

Ключові слова: *віброобробка; гранульоване середовище; фізико - технологічні параметри; кут зіткнення; резервуар; продуктивність віброобробки.*

CONTENT

Наукове видання

РІЗАННЯ ТА ІНСТРУМЕНТИ
в технологічних системах

Збірник наукових праць

Випуск № 100

Укладач *д.т.н., проф. І.М. Пижов*
Оригинал-макет *А.М. Борзенко*
Відп. за випуск *к.т.н., проф. Є.В. Островерх*

В авторській редакції

Матеріали відтворено з авторських оригіналів

Підп. до друку 12.06.2024.Формат 60х84 1/16. ПапірСоруРарег.
Друк - ризографія. Гарнитура Таймс. Умов.друк.арк. 10,93. Облік.вид.арк. 11,0. Наклад 30 прим.
1-й завод 1-100. Зам. № 1149. Ціна договірна.

Видавничий центр НТУ «ХПІ»
Свідоцтво про державну реєстрацію ДК № 116 від 10.07.2000 р.
61002, Харків, вул. Кирпичова, 2